

4th Asian Symposium on Materials Processing (ASMP 2015)



QIR

Lombok
Indonesia

10-13
August
2015

Organizing Committee

Symposium Chair

Prof. Hideshi Miura (Kyushu University, JAPAN)

General Chair

Prof. Masaaki Otsu (University of Fukui, JAPAN)

Dr. Gandjar Kiswanto (University of Indonesia, INDONESIA)

Co-General Chair

Prof. Ming Yang (Tokyo Metropolitan University, JAPAN)

Dr. Ario Sunar Baskoro (University of Indonesia, INDONESIA)

International Advisory Committee

Prof. Naoto Ohtake (Tokyo Institute of Technology, JAPAN)

Prof. Hiroshi Asanuma (Chiba University, JAPAN)

Dr. Gandjar Kiswanto (University of Indonesia, INDONESIA)

Prof. Ahmad Fauzi Mohd Noor (USM, MALAYSIA)

Dr. Zainuddin Sajuri (UKM, MALAYSIA)

Prof. Chaosuan Kanchanomai (Thammasat University, THAILAND)

Dr. Zainuddin Sajuri (Universiti Kebangsaan Malaysia, MALAYSIA)

Prof. Syoni Soepriyanto (Institute of Technology Bandung, INDONESIA)

Scientific & Program Committee

Prof. Yukio Miyashita (Nagaoka University of Technology, JAPAN)(Chair)

Dr. Sugeng Supriadi (University of Indonesia, INDONESIA)(Chair)

Dr. Yudan Whulanza (University of Indonesia, INDONESIA)

Dr. Jos Istiyanto (University of Indonesia, INDONESIA)

Prof. Nobuo Takeda (University of Tokyo, JAPAN)

Prof. Kenji Kaneko (Tokyo University of Science, JAPAN)

Prof. Masaaki Itabashi (Tokyo University of Science, Suwa, JAPAN)

Prof. Hideki Kyogoku (Kinki University, JAPAN)

Prof. Ikuo Ihara (Nagaoka University of Technology, JAPAN)

Prof. Masanobu Kubota (Kyusyu University, JAPAN)

Prof. Hiroyuki Kawada (Waseda Univeristy, JAPAN)

Prof. Toshio Hattori (Shizuoka Institute of Science and Technology, JAPAN)

Prof. Hiroshi Asanuma (Chiba University, JAPAN)

Prof. Koji Fujimoto (The University of Tokyo, JAPAN)

Dr. Tsutomu Murai (Japan Science and Technology Agency, JAPAN)

Prof. Masahiro Fukumoto (Toyohashi University of Technology, JAPAN)

Prof. Hironori Tohmyo (Tohoku Univeristy, JAPAN)

Prof. Shinji Ogiwara (Tokyo University of Science, JAPAN)

Prof. Satoshi Kobayashi (Tokyo Metropolitan University, JAPAN)

Prof. Shuichi Wakayama (Tokyo Metropolitan University, JAPAN)

Prof. Hiroki Akasaka (Tokyo Institute of Technology, JAPAN)

Prof. Ryo Matsumoto (Osaka University, JAPAN)

Prof. Hidemitsu Furukawa (Yamagata University, JAPAN)

Prof. Mikio Muraoka (Akita University, JAPAN)

Prof. Ming Yang (Tokyo Metropolitan University, JAPAN)

Dr. Miki Yamazaki (Hitachi, JAPAN)

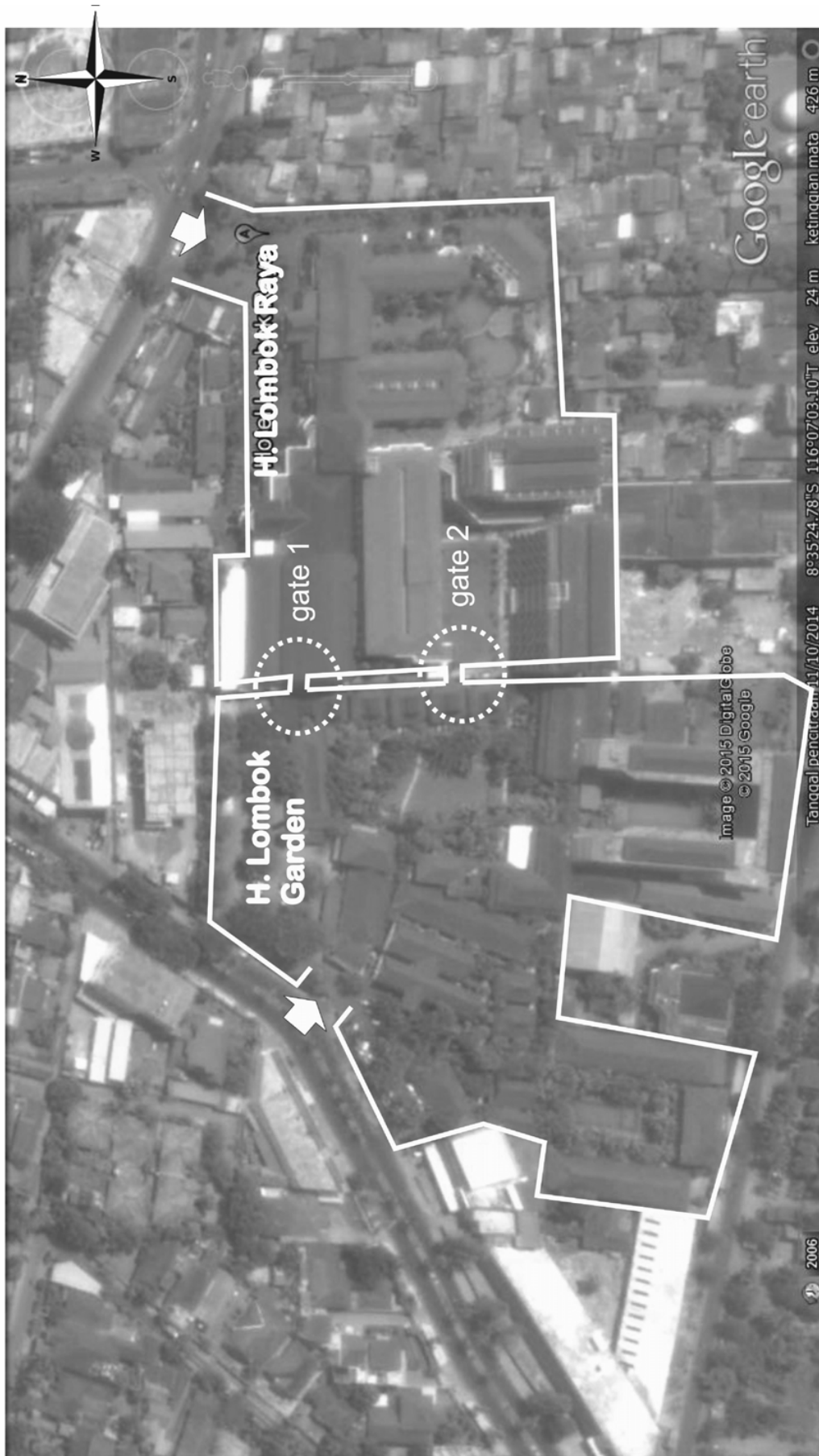
Prof. Wataru Nakao (Yokohama National University, JAPAN)

Symposium Secretary

Prof. Masato Okada (University of Fukui, JAPAN)

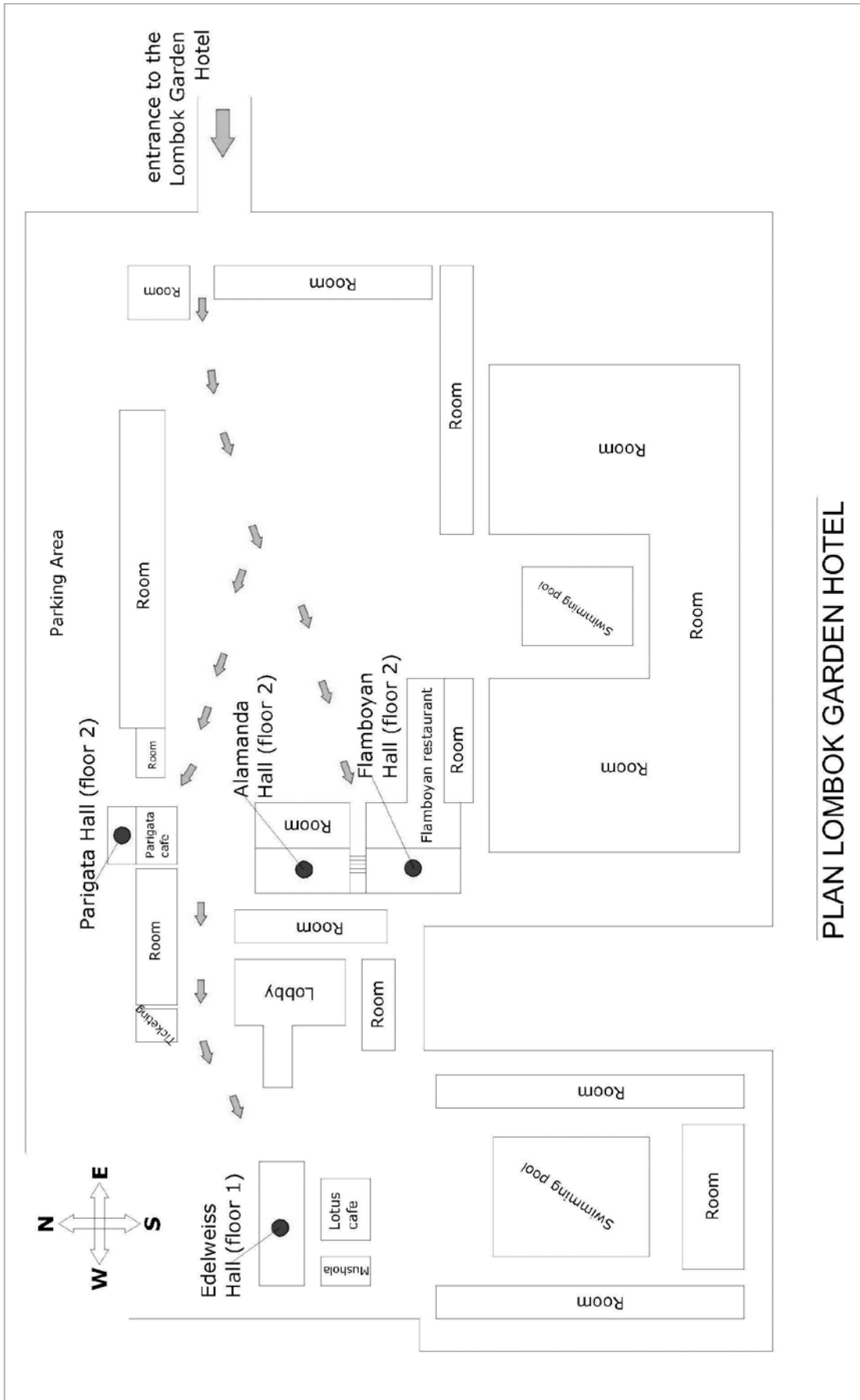
Ms. Herra Asta (University of Indonesia, INDONESIA)

ACTIVITY LOCATOR AND FLOOR PLANS

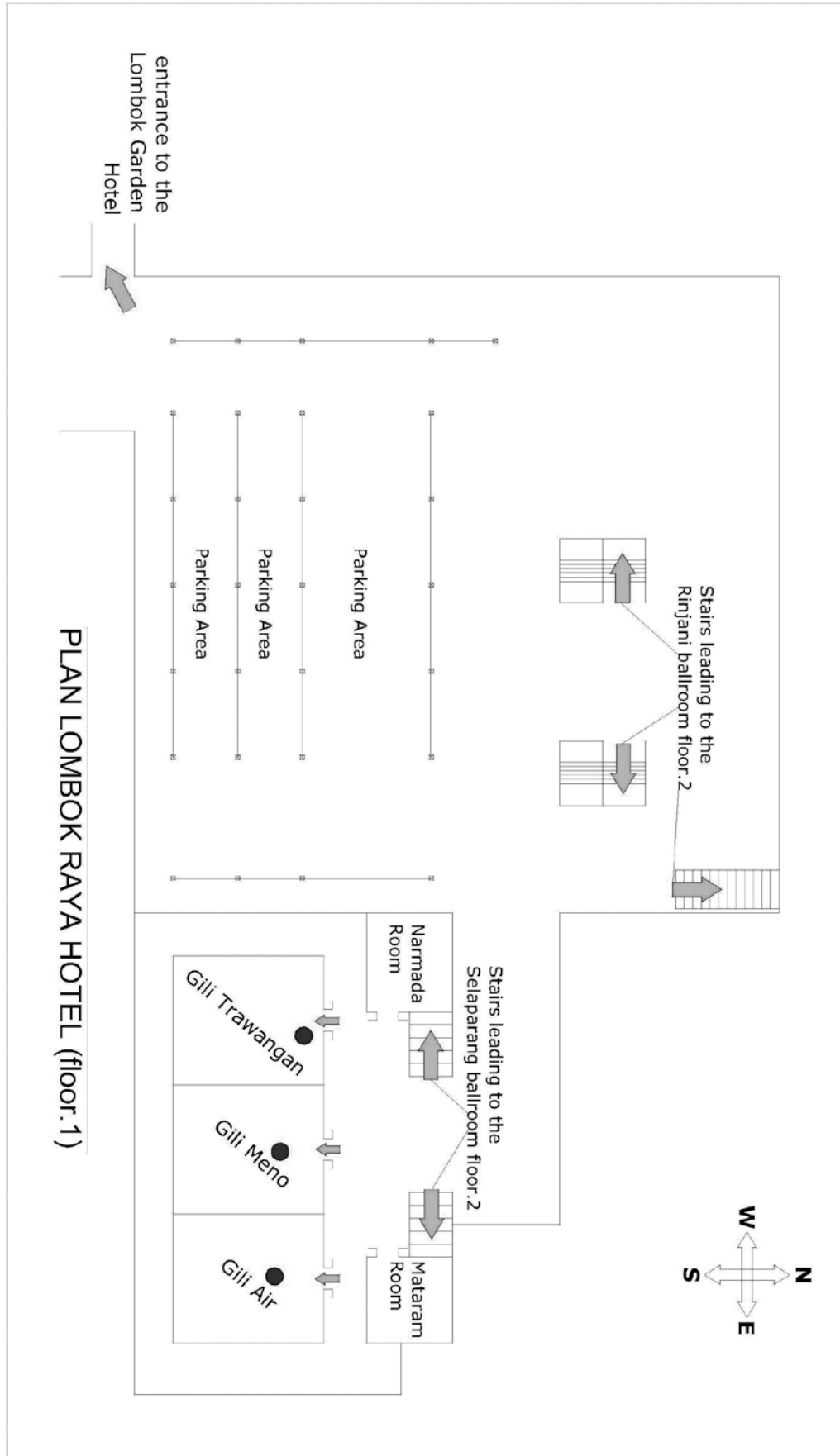


LAYOUT H. LOMBOK RAYA DAN H. LOMBOK GARDEN

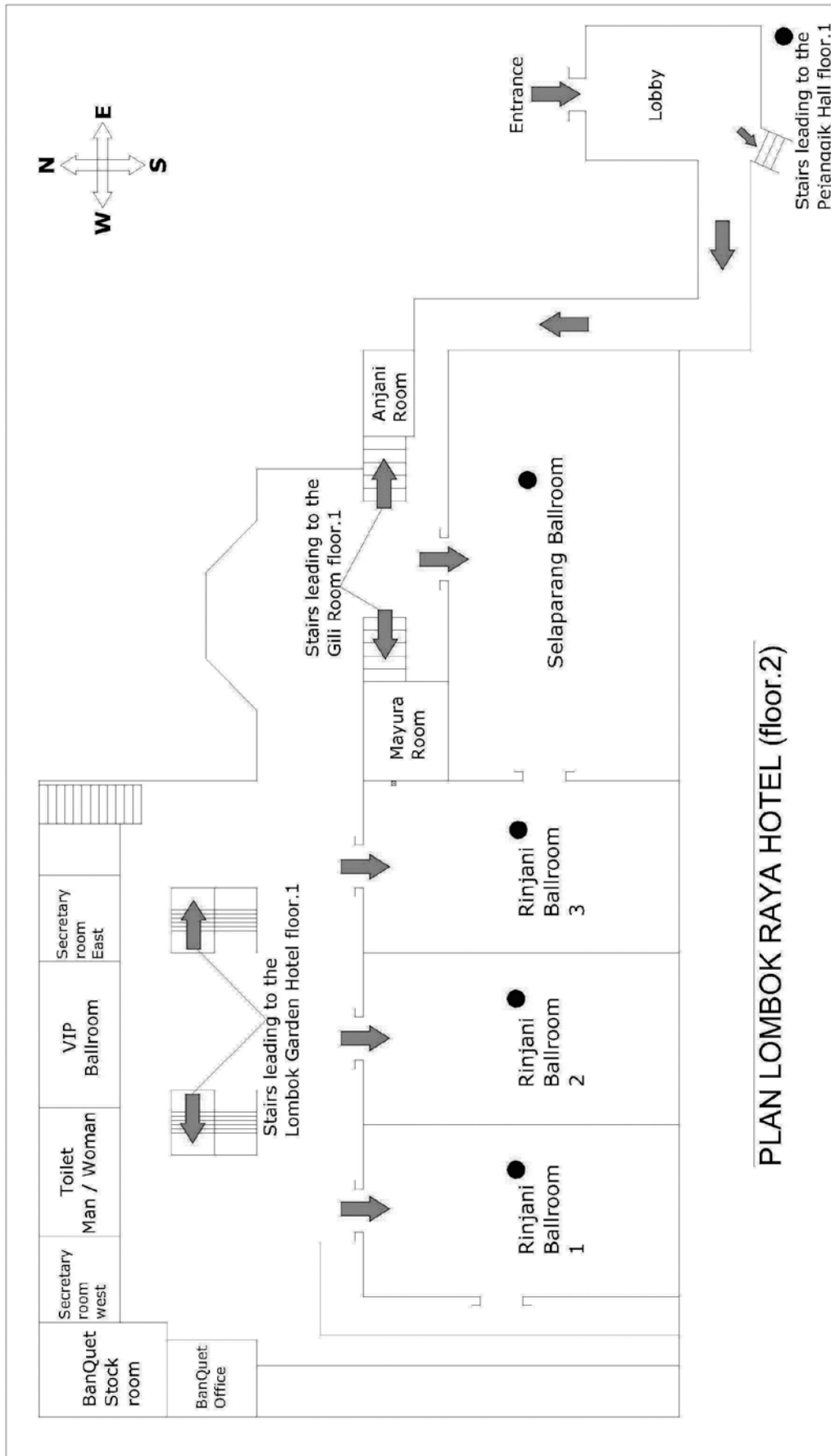
ACTIVITY LOCATOR AND FLOOR PLANS



ACTIVITY LOCATOR AND FLOOR PLANS



ACTIVITY LOCATOR AND FLOOR PLANS



PROGRAM AT GLANCE

Date	Time	Program	Venue
10 August 2015	04.00- 06.00 pm	Registration and Welcome Drink	Pre-function Hall
11 August 2015	07.30- 08.00 am	Registration	Pre-function Hall
	08.00- 08.40 am	Opening Ceremony	Rinjani Room I, II, III
	08.40- 09.00 am	Photo Session	
	09.00- 09.30 am	Keynote Speech 1	
	09.30- 10.30 am	Talk show: Serve the Country	
	10.30- 10.45 am	Coffee break	
	10.45- 12.00 am	Keynote Speech 2 and 3	
	12.00- 01.00 pm	Lunch	
	01.00- 03.00 pm	Poster Session	Pre-function Hall
		Exhibition	
		Parallel session	
	03.00- 03.30 pm	Coffee Break	Pre-function Hall
		Poster Session	
		Exhibition	
03.30- 05.00 pm	Parallel session	Meeting Rooms	
05.00- 07.00 pm	Poster Session	Pre-function Hall	
	Exhibition		
07.00- 09.00 pm	Banquette Dinner	Rinjani Room I, II, III	
12 August 2015	08.00- 10.00 am	Parallel session	Meeting Rooms
	10.00- 10.30 am	Coffee Break	Pre-function Hall
		Poster Session	
		Exhibition	
	10.30- 12.00 am	Parallel session	Meeting Rooms
	12.00- 01.00 pm	Lunch	Pre-function Hall
		Poster Session	
		Exhibition	
01.00- 03.00 pm	Parallel session	Meeting Rooms	
03.00- 03.30 pm	Coffee Break	Pre-function Hall	
	Poster Session		
	Exhibition		
03.30- 05.00 pm	Parallel session	Meeting Rooms	
05.00 - 06.00 pm	Closing Ceremony	Selaparang Room	
13 August 2015	08.00 am- 08.00 pm	Social Tour Lombok	

Table of Contents

IN-SITU NONINVASIVE HEAT FLUX EVALUATION BY ULTRASOUND FOR HIGH TEMPERATURE MATERIAL PROCESS MONITORING.	1
ELASTIC-PLASTIC FRACTURE TOUGHNESS OF EXTRUDED Mg-Al-Zn ALLOYS.	3
FABRICATION AND EVALUATION OF MICRO-STRUCTURED REACTION FIELD WITH VERTICALLY ALIGNED CARBON NANOTUBES FOR MICRO BIO-ANALYSIS DEVICE	5
IMPROVEMENT OF MECHANICAL PROPERTIES IN UNTWISTED CNT YARN BY PAA/DMSO DENSIFICATION TREATMENT.	7
EFFECTS OF PROCESSING CONDITIONS IN UNIDIRECTIONAL CARBON FIBER THERMOPLASTIC PREPREG TAPE LAYING USING NEAR INFRARED HEATER	9
ESTIMATION OF ELECTRICAL CONDUCTIVITY OF TiB ₂ /Al COMPOSITES WITH IMAGE ANALYSIS.	11
NEW MANUFACTURING METHOD OF PARTICLE INTERMETALLIC COMPOUND REINFORCED COMPOSITES	13
THE EFFECT OF ZrO ₂ ADDITION ON THE ELECTROCHEMICAL BEHAVIOR OF LOW-CARBON STEELS IN CrO ₃ -H ₂ SO ₄ ELECTROLYTE	15
PRODUCTION AND IMPROVEMENT OF CHARACTERISTICS OF SINTERED POROUS TITANIUM USING CAPSULE-FREE HIP METHOD	17
PROPOSAL FOR NEW FABRICATION METHOD OF GREEN COMPOSITE BY USING FRICTION STIR PROCESS.	19
INFLUENCE OF GRAIN SIZE ON PROCESS AFFECTED ZONE IN MICRO PIERCING.	21
REPLICATION OF ANTIREFLECTION STRUCTURE FOR SOLAR CELLS BY LASER-ASSISTED IMPRINTING.	23
SELECTIVE PATTERN-HARDENING OF AISI-SUS420/SUS430 MOLDS FOR MICRO-TEXTURING.	25
EVALUATION OF MAGNETIZATION FOR CANTILEVER SAMPLE USING MEMS DEVICE	27
FABRICATION OF MICRO-CHANNEL FROM THE POWDER BY PULSE ELECTRIC CURRENT SINTERING METHOD AND MARKED GRAPHITE DIE.	29
NUMERICAL STUDY ON EFFECTS OF MATERIAL INHOMOGENEITY AND GRAIN SIZE ON NECKING AND WRINKLING BEHAVIORS IN MICRO DEEP DRAWING OF METAL FOILS	31
TECHNICAL MILESTONE TO APPLY SELF-HEALING CERAMICS	33

BLANKING VIBRATION AND NOISE OF DIFFERENT TENSILE STRENGTH MATERIALS IN SCREW DRIVE SERVO PRESS BLANKING	35
BEHAVIOR OF ASYMMETRIC DEFORMATION OF ROD IN LOCALLY-LATERAL UPSETTING	37
DIRECT MEASUREMENT OF FRICTION FORCE DURING FORMING	39
MEASUREMENT OF TOOL TEMPERATURE IN BURNISHING USING DIAMOND TIP.	41
HIGH DENSITY OXYGEN PLASMA ASHING OF CVD-DIAMOND COATED END-MILLING TOOLS	43
FRONT AND REAR SIDES SIMULTANEOUS FORMING BY FRICTION STIR INCREMENTAL FORMING.	45
IN SITU OBSERVATIONS ON FRETTING WEAR BEHAVIOR OF PLASMA-SPRAYED HYDROXYAPATITE COATING	47
WETTABILITY BETWEEN GRAPHITE AND HIGH- TEMPERATURE LEAD-FREE SOLDER ALLOY	49
THE ROLE OF HYDROGEN IN HIGH RATE PLASMA NITRIDING OF MARTENSITE STAINLESS STEEL.	51
DEVELOPMENT OF TITANIUM FIBER/ALUMINUM MULTIFUNCTIONAL COMPOSITES.	53
PHASE-FILED SIMULATION OF ELEMENTARY PROCESS IN POWDER BED FUSION.	55
ESTIMATION OF FRICTIONAL PERFORMANCE OF LUBRICANTS FOR HOT FORGING OF STEEL BY CARIBRATION CURVES CONSIDERING HEAT TRANSFER IN RING COMPRESSION TEST	57
DEVELOPMENT OF HIGH SPEED TORSIONAL FATIGUE TESTING MACHINE FOR MULTIPLE SPECIMENSDEVELOPMENT OF HIGH SPEED TORSIONAL FATIGUE TESTING MACHINE FOR MULTIPLE SPECIMENS	59
GUIDED WAVE PROPAGATION IN WIRE CABLE UNDER TENSILE STRESS.	61
BEHAVIOR ON GENERATION AND PROPAGATION OF FATIGUE CRACK FOR WC-Co CEMENTED CARBIDES	63
A DEVICE OF GAS TRANSMISSION RATE FOR THIN FILMS IN A HYDROGEN STORAGE SYSTEM.	65
THE STUDY OF VARIANT SELECTION FOR SHAPE MEMORY EFFECT ON FE-MN-SI BASED ALLOY WITH EBSD.	67
CHARACTERISTICS OF METAL MATRIX COMPOSITES REINFORCED WITH PALM OIL FLY ASH FABRICATED BY USING STIR CASTING AND CENTRIFUGAL CASTING METHODS	69

MECHANICAL PROPERTIES OF AMORPHOUS CARBON FILMS DEPOSITED FROM CARBON ISOTOPE MATERIALS	71
EVALUATION OF ADHESIVE STRENGTH BETWEEN Ti-29Nb-13Ta-4.6Zr ALLOY AND SOL-GEL FABRICATED HYDROXYAPATITE FILMS.	73
ADHESION BEHAVIOR OF MECHANICALLY JOINED PARTS OF ALUMINUM ALLOYS.	75
DEVELOPMENT FOR HYDROGEN STORAGE Mg-Ti SOLID SOLUTION BY MECHANICAL ALLOYING	77
DEVELOPMENT OF DAMAGE DETECTION TECHNIQUE FOR SHEET-TYPE LITHIUM-ION BATTERIES USING ACOUSTIC EMISSIONS.	79
IMPACT RESISTANCE OF THE GLASSES INSTALLED NANO-LAMIRATED FILMS AND ARAMID FIBER CLOTH	81
INFLUENCE OF ANNEALING ON SHAPE MEMORY PROPERTY IN FE-MN-SI BASED ALLOY	83
FRICITION STIR INCREMENTAL FORMING OF ALUMINUM ALLOY SHEETS WITH BACK SUPPORT DIE	85
DEVELOPMENT OF CU-SN ALLOY WITH MECHANICAL ALLOYING.	87
FEM SIMULATION FOR TWO-DIMENSION CUTTING OF TITANIUM-ALLOY	89
CORROSION RESISTANCE OF Si-DOPED AMORPHOUS CARBON FILMS AGAINST NITRIC ACID	91
TENSILE AND FATIGUE BEHAVIORS FOR LIP-SEAL WELDS OF LIQUID LITHIUM PIPES AT ELEVATED TEMPERATURE.	93
EFFECT OF LOCAL PLASTIC PROCESSING ON FATIGUE STRENGTH OF STEEL PLATE WITH A HOLE	95

IN-SITU NONINVASIVE HEAT FLUX EVALUATION BY ULTRASOUND FOR HIGH TEMPERATURE MATERIAL PROCESS MONITORING

Shingo Isobe¹, Ikuo Ihara^{2*}, and Akira Kosugi¹

¹ Graduate Student, Nagaoka University of Technology, Nagaoka, 940-2188, Japan

² Dept. Mech. Eng., Nagaoka University of Technology, Nagaoka, 940-2188, Japan

* ihara@mech.nagaokaut.ac.jp

Keywords: Nondestructive measurement, Heat flux, Process monitoring, Ultrasound, High temperature

In materials processes at high temperature, it is often required to estimate temperature and/or heat flux of the processed materials and processing machines because such thermal parameters are closely related to the quality and reliability of final products. Such parameters are also indispensable to understand physical phenomena related to the thermal conduction and thermal resistance of heated materials. In addition, quantitative and real-time information on such parameters during materials processing are required to make accurate theoretical or computational analyses for material processes at high temperature. It is, therefore, strongly required to conduct in-situ measurements of temperature and heat flux for heated materials during high temperature processing. In particular, in-situ noninvasive monitoring of heat flux through the interface between two materials is quite attractive and could be beneficial for basic and practical researches of high temperature materials processing.

Ultrasound, due to its high sensitivity to temperature, has the potential to be an effective means for estimating thermal parameters of materials. Because of the advantages of ultrasonic measurements such as noninvasive and faster time response, ultrasound is expected to be a promising tool for measuring heat flux as well as temperature of heated materials. In this work, an effective ultrasonic thermometry providing simultaneous measurements of temperature and heat flux in a heated material is developed and its feasibility of conducting in-situ noninvasive monitoring of heat flux through the interface between two materials is examined through experiments with a single-side heated steel plate.

Temperature and heat flux determination by ultrasound

Considering that a material whose single side is heated by contacting with a hot material and assuming a one-dimensional temperature distribution in the single-side heated material, the transit time of ultrasound in the direction of the temperature distribution can be given by

$$t_L = \int_0^L \frac{1}{v(T(x))} dx \quad (1)$$

where L is the propagation distance of ultrasound, $v(T(x))$ is the ultrasonic wave velocity which is a function of the temperature T at a location x . Based on equation (1), the temperature distribution $T(x)$ near the heated surface can quantitatively be determined by the ultrasonic thermometry we had developed [1]-[3]. This method basically consists of ultrasonic pulse echo measurements and a finite difference analysis. It is noted that the temperature at the heated surface can be obtained by the method without any boundary conditions at the heating surface.

Heat flux q , that is a heat transfer rate per unit area in the x direction, is generally expressed by

$$q = -k \frac{\partial T}{\partial x} \quad (2)$$

where k is the thermal conductivity and $\partial T/\partial x$ is temperature gradient. If the thermal conductivity is known, the heat flux can be determined from the temperature gradient near the heating surface. Since the temperature gradient can be obtained from the temperature distribution determined by the ultrasonic thermometry, the heat flux at the heating surface is easily determined from the equation (2).

Experiment and result

Figure 1 shows a schematic of the experimental setup used. A steel plate of 30 mm thickness is used as the specimen and its bottom surface is heated by contacting with a copper plate of 30 mm thickness whose bottom is heated by a gas burner. To obtain a reference value of heat flux at the bottom

surface of the steel, a conventional thin film heat flux sensor is inserted into the boundary between the steel and copper plates. A longitudinal ultrasonic transducer of 5 MHz is installed on the top surface of the steel and ultrasonic pulse-echo measurements are made during heating. The transit times of the ultrasonic pulse echoes from the steel plate are precisely determined by taking a cross correlation of the pulse echoes and used for estimating the temperature distribution in the steel. Once the temperature distribution are determined by the ultrasonic method, heat fluxes are then determined from equation (2). **Figure 2** shows variations of estimated heat fluxes with elapsed time. It can be seen that heat flux increases just after heating starts and decreases after the heating stops. It is noted that the heat flux estimated by ultrasound agrees well with that estimated using the conventional heat flux sensor. A certain random error in the ultrasonic result is observed. It is basically caused by the fluctuation in the estimated temperature. In this paper, further discussion on the advantage of using the ultrasonic method for material process monitoring is made.

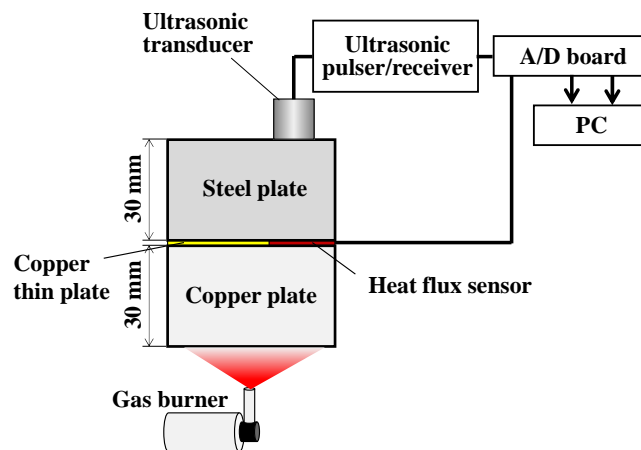


Figure 1 Schematic of the experimental setup.

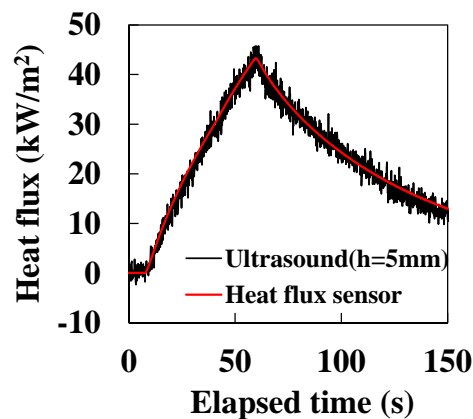


Figure 2 Variation of the estimated heat flux at the heating surface with the elapsed time.

Acknowledgment

Support from the JSPS Grant-in-Aid for Scientific Research (B) 25289238 are appreciated.

References

- [1] M. Takahashi and I. Ihara, Ultrasonic Determination of Temperature Distribution in Thick Plates during Single Sided Heating, *Modern Physics Letters B*, Vol. 22, No. 11(2008), pp.971- 976.
- [2] I. Ihara and T. Tomomatsu, In-Situ Measurement of Internal Temperature Distribution of Sintered Materials Using Ultrasonic Technique, *IOP Conf. Series: Materials Science and Engineering*, 18 (2011) 022008.
- [3] H. Yamada, A. Kosugi and I. Ihara, Non-Contact Monitoring of Surface Temperature Distribution by Laser Ultrasound Scanning, *Japanese Journal of Applied Physics*, Vol.50, No.7 (2011), 07HC06.
- [4] G. E. Myers: *Analytical Methods in Conduction Heat Transfer* (McGraw-Hill, New York, 1971) p. 262.

ELASTIC-PLASTIC FRACTURE TOUGHNESS OF EXTRUDED Mg-Al-Zn ALLOYS

Zainuddin Sajuri^{1*}, Noradila Abdul Latif¹, Junaidi Syarif²,
Yukio Miyashita³ and Yoshiharu Mutoh³

¹Department of Mechanical and Materials Engineering, Faculty of Engineering and Built Environment,
Universiti Kebangsaan Malaysia, 43600 UKM Bangi, Selangor, Malaysia

²Mechanical Engineering Dept., College of Engineering, University of Sharjah, PO Box:27272, Sharjah, UAE

³Department of Mechanical Engineering, Nagaoka University of Technology,
1603-1, Kamitomioka, Nagaoka, Niigata 940-2188, Japan

*sajuri@ukm.edu.my

Keywords: Elastic-plastic fracture toughness, ductile, *J*-integral, stretch zone, Mg-Al-Zn alloys

Introduction

Extruded Mg-Al-Zn alloys are categorized as ductile materials since the elongation to fracture is more than 15% [1]. Therefore, conducting *J*-integral test is preferable rather than the K_{IC} linear elastic fracture toughness test in investigating the fracture behavior and evaluating the plane strain fracture toughness value of these alloys. The objective of this study is to determine the elastic-plastic fracture toughness J_{IC} of extruded AZ31 and AZ61 magnesium alloys.

Experimental Procedures

The materials used in this study were extruded AZ31 and AZ61 magnesium alloys. A standard multiple specimens J_{IC} test method was performed to determine the J_{IC} -value of both alloys. Four fatigue pre-cracked single edge notched bend (*SENB*) specimens were used to develop a resistance curve (*R*-curve) for identifying J_{IC} -value of each material according to the *ASTM E1820* [2]. The method to determination of J_{IC} -value was based on the critical stretch zone that measured from the fracture surface as recommended by the *JSME S001* for obtaining J_{IC} -value [3].

Results and Discussion

The microstructures and nominal stress-strain curves of AZ31 and AZ61 are shown in Figs. 1 and 2, respectively. In Figure 1, AZ61 indicates smaller grain size than that of AZ31. Further, a higher twinning density has been observed in AZ31. The density of the twins in AZ61 was lower when compared with the AZ31. This might indicate an increased resistance to twinning deformation in AZ61. Meanwhile, the yield stress and tensile strength of AZ61 were higher compared to AZ31 as shown in Fig. 2. This was most probably due to high aluminum content in AZ61 which resulted in decreasing the grain size and increasing the β -phase volume that pinned the movement of dislocations and slips [4]. Figure 3 shows the load-load line displacement curves at different interrupted displacements of AZ31 and AZ61. The *J*-value was evaluated using the load-load line displacement and geometrical size of the specimen as $J = 2A/Bb$, where, *A* is the area under the curve, *B* is specimen thickness and *b* is the remaining crack ligament. The ductile crack growth size (Δa) and the critical stretch zone width ($SZWC$) of the break-opened specimen were then measured from the *SEM* micrograph. The *J*-value, Δa and $SZWC$ were summarized in Table 1. All these values were then used to develop the

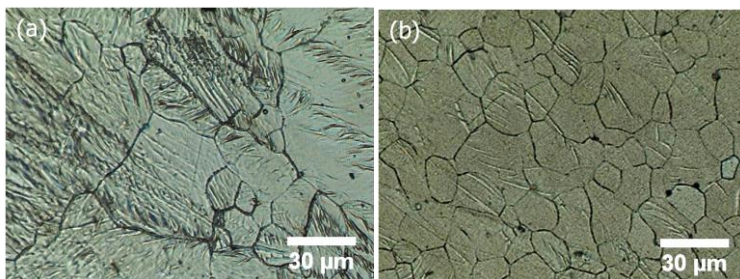


Figure 1 Microstructures of (a) AZ31 and (b) AZ61

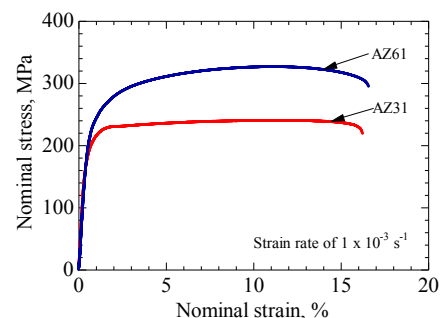


Figure 2 Nominal stress-strain curves of AZ31 and AZ61

R-line and stretch zone line on the *R*-curve as shown in Figure 4. From the *R*-curve, the J_{IC} -values of extruded AZ31 and AZ61 magnesium alloys were found at 18.8 and 24.7kJ/m², respectively.

Conclusion

J-integral was used to determine the elastic-plastic fracture toughness J_{IC} of extruded AZ31 and AZ61. The determination of J_{IC} for both Mg-Al-Zn alloys was based on the interception of stretch zone line and *R*-curve. The J_{IC} of extruded AZ31 and AZ61 Mg alloys were 18.8 and 24.7kJ/m², respectively.

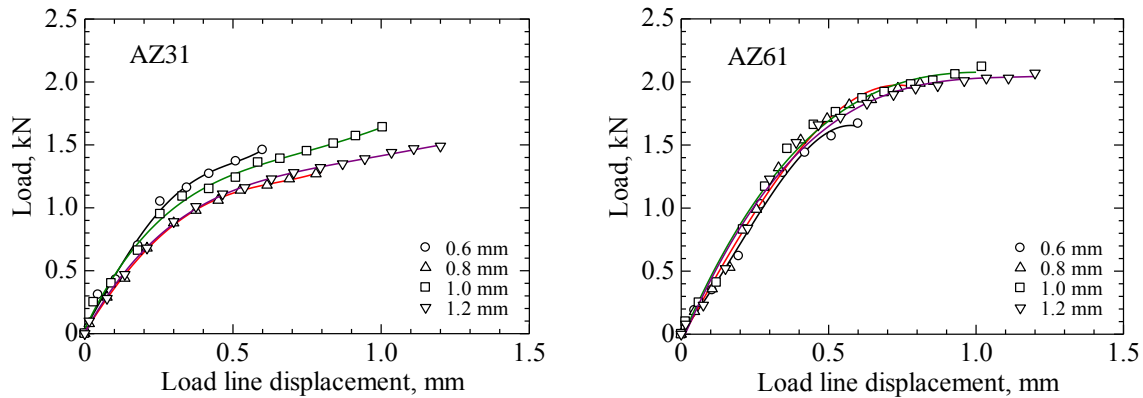


Figure 3 Load-load line displacement curves at different interrupted displacements for AZ31 and AZ61

Table 1 *J*-value, crack growth size and critical stretch zone width of AZ31 and AZ61

Interrupted displacement (mm)	AZ31				AZ61			
	0.6	0.8	1.0	1.2	0.6	0.8	1.0	1.2
<i>J</i> (kJ/m ²)	20.8	25.1	41.7	47.8	25.1	39.7	53.6	67.1
Δa (mm)	0.122	0.227	0.329	0.428	0.066	0.178	0.286	0.404
SZWC (mm)	0.081	0.089	0.092	0.092	0.047	0.051	0.056	0.054

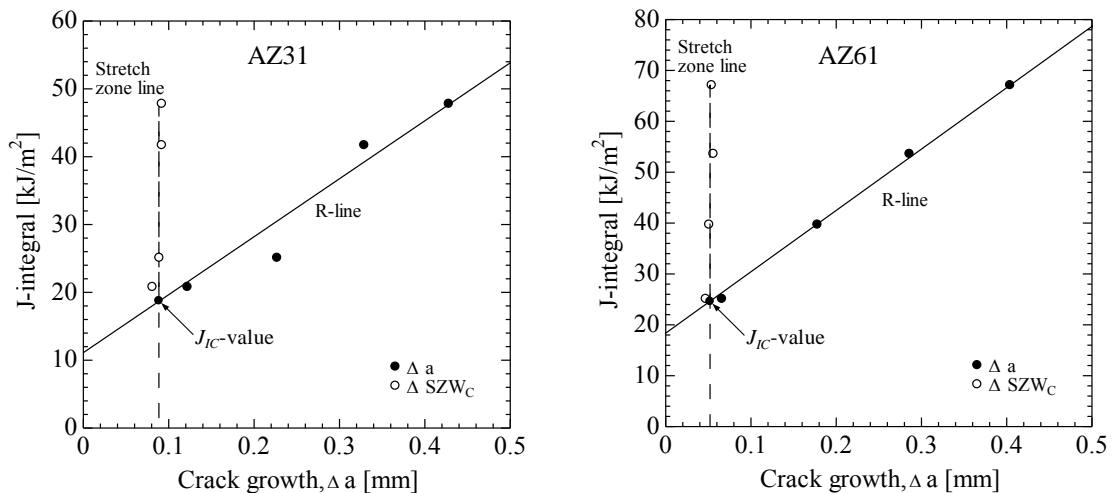


Figure 4 J_{IC} determinations for AZ31 and AZ61 using *R*-curves

Acknowledgement

The authors acknowledge the supports from the Universiti Kebangsaan Malaysia, Ministry of Higher Education Malaysia (ERGS/1/2011/TK/UKM/02/9) and Nagaoka University of Technology.

References

- [1] T. Yokoyama, Impact tensile stress-strain characteristics of wrought magnesium alloys, *Strain*, 39-4 (2003), 167-175.
- [2] ASTM E1820 Standard Test Method for Measurement of Fracture Toughness (2007)
- [3] JSME S001 Standard Method of Test for Elastic-Plastic Fracture Toughness, J_{IC} (1981)(In Japanese)
- [4] M. S. Dargusch, K. Pettersen, K. Nogita, M. D. Nave, G. L. Dunlop, The effect of aluminium content on the mechanical properties and microstructure of die cast binary magnesium-aluminium alloys, *Materials Transactions*, 47-4 (2006), 977-982.

FABRICATION AND EVALUATION OF MICRO-STRUCTURED REACTION FIELD WITH VERTICALLY ALIGNED CARBON NANOTUBES FOR MICRO BIO-ANALYSIS DEVICE

Yuma Suzuki^{1*}, Ewelina Pabjańczyk-Wlazole², Tetsuhide Shimizu¹, Ming Yang¹

¹*Advanced Materials and Processing Engineering Laboratory (AMPEL),
Graduate School of System Design, Tokyo Metropolitan University,*

²*Department of Material and Commodity Sciences and Textile Metrology, Lodz University of Technology*

* yuma-suzuki@ed.tmu.ac.jp

Keywords: Micro bio-analysis device, Carbon Nanotubes, Photolithography, Protein adsorption, Ultraviolet Spectrometry

Micro bio-analysis device (MBD), such as micro Total Analysis Systems (μ -TAS) and Lab-on-a-chip (LOC), is demanded to realize a rapid and high sensitivity diagnosis of biomolecules (for instance, viruses and proteins) [1]. The reaction field with micro structures in MBD can offer larger specific surface area (surface areas per volume) and reduction of diffusion distance which improves detection sensitivity and reaction efficiency [2]. Carbon nanotubes (CNTs) are one of nanomaterials with chemical stability and high aspect ratio which brings in high specific surface area [3]. Furthermore, for distinct control of micro structural dimensions in the reaction field, the fabrication of micro pattern array by combining CNTs synthesis and photolithography has been attracting significant attention. However, designs of the structure and the surface of micro-structured reaction field have not been investigated. In this work, we fabricated the reaction field with micro structure array by patterning metal catalyst with photolithography and synthesizing vertically aligned CNTs (VACNTs). For high detection sensitivity and reaction efficiency in MBD, the influence of structure dimensions and zeta potential on protein adsorption and diffusion time was investigated.

Patterned-VACNTs structures were synthesized by ultraviolet photolithography and catalytic thermal CVD (Chemical Vapor Deposition). Fig.1 shows the fabrication process for patterned VACNTs. Silicon (Si) wafer was used as substrates. First, positive photoresist was coated on the substrate by spin coater and ultraviolet light was exposed to resist-coated substrate covering a photomask. After developing photoresist, metal catalysts, aluminum (Al) and iron (Fe), was deposited in sequence by sputtering. Coated photoresist was removed by organic solvent and VACNTs was synthesized on metal catalysts by CVD.

The protein adsorption on the reaction field with patterned-VACNTs structures was evaluated by ultraviolet spectrometry. First, 20 μ l bovine serum albumin (BSA) solution was dropped on the reaction field. Then, the sample was incubated 15 and 30 minutes for protein diffusion and adsorption on the reaction field. In this method, the reflectivity of protein-adsorbed reaction field was measured and we compared reflectivity the wavelength of 205 nm which protein adsorbs [4] for various dimension of patterned-VACNTs structure.

Fig. 2 shows the patterned-VACNTs structures on the substrate. VACNTs structures with different pattern dimensions were fabricated. Protein adsorption on VACNTs structures was characterized by ultraviolet spectrometry (See Fig. 3). The results indicated that the adsorbed amount and time of protein depend on the structure dimensions and the zeta potential of VACNTs structures. Wider structural pitch tends to adsorb more proteins with shorter time. On the other hand, narrower pitch tends to adsorb more proteins longer time. The balance between structural dimensions and zeta potential is one of important issues for designs of the reaction field with high detection sensitivity and reaction efficiency.

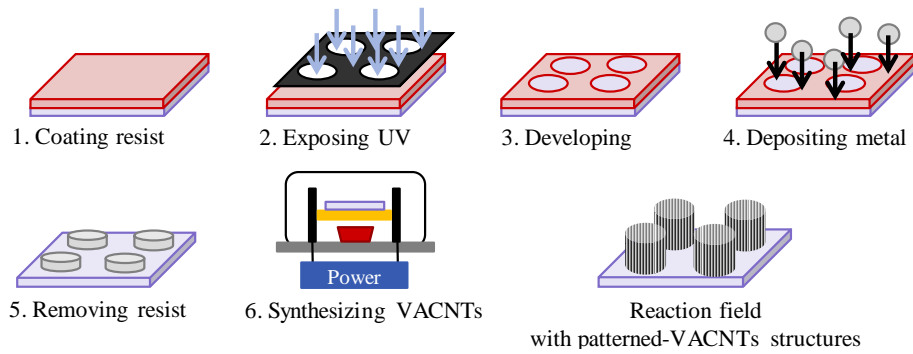


Figure 1 Schematic image of the fabrication process for patterned VACNTs

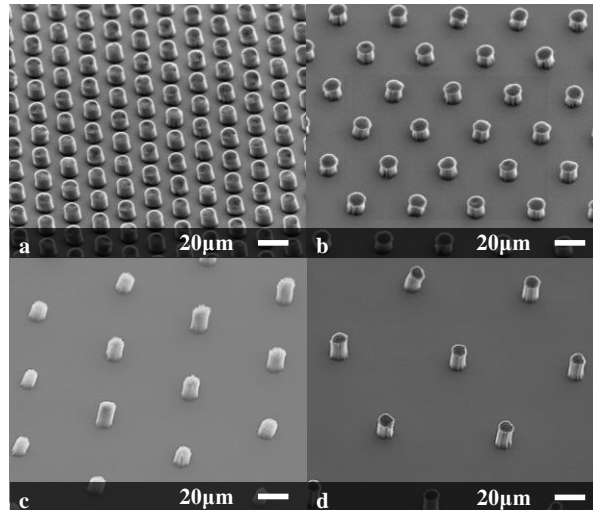


Figure 2 SEM images of patterned-VACNTs structures with various dimensions.
 (a) Structural diameter (D) is $10\ \mu\text{m}$ and structural pitch (P) is $10\ \mu\text{m}$.
 (b) $D = 10\ \mu\text{m}$, $P = 30\ \mu\text{m}$ (c) $D = 10\ \mu\text{m}$, $P = 50\ \mu\text{m}$ (d) $D = 10\ \mu\text{m}$, $P = 70\ \mu\text{m}$

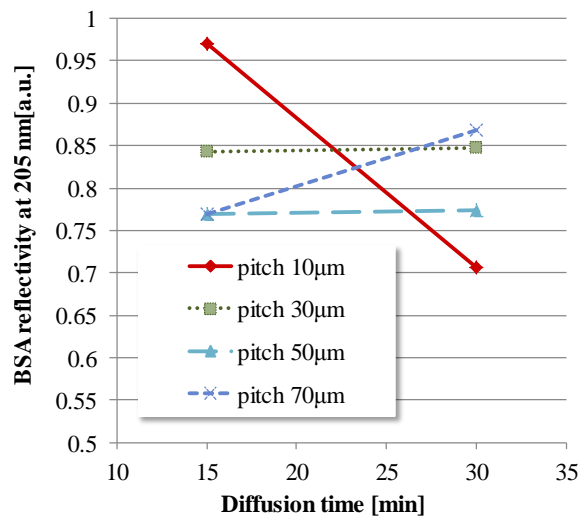


Figure 3 BSA reflectivity at the wavelength of 205 nm in the reaction field with patterned-VACNTs structures

References

[1] Emmanuel Delamarche, David Juncker, Heinz Schmid, Microfluidics for Processing Surfaces and Miniaturizing Biological Assays, *Advanced Materials*, 17 (2005), pp. 2911-2933.
 [2] Sang Won Han, Seulah Lee, Juree Hong, Eunji Jang, Taeyoon Lee, Won-Gun Koh, Mutiscale substrates based on hydrogel-incorporated silicon nanowires for protein patterning and microarray-based immunoassays, *Biosensors and Bioelectronics*, 45 (2013), pp. 129–135.
 [3] Ming Yang, Yakuya Yabe, Katsumi Uchiyama, Fabrication of Micro Device for Rapid and High-Sensitive Bio-Analysis, *Journal of Solid Mechanics and Materials Engineering*, 7-2 (2013), pp. 199-205.
 [4] Robert K. Scopes, Measurement of protein by spectrophotometry at 205 nm, *Analytical Biochemistry*, 59-1 (1974), pp. 277-282.

IMPROVEMENT OF MECHANICAL PROPERTIES IN UNTWISTED CNT YARN BY PAA/DMSO DENSIFICATION TREATMENT

Tae Sung Kim¹, Kaoru Sugano¹, Atsushi Hosoi², Hiroyuki Kawada^{3,*}

¹ Graduate student, Department of Applied Mechanics, Graduate School of Fundamental Science and Engineering, Waseda University, 3-4-1 Okubo, Shinjuku, Tokyo 169-8555, Japan

² Assistant Professor, Department of applied Mechanics and Aerospace Engineering, Waseda University, 3-4-1 Okubo, Shinjuku, Tokyo 169-8555, Japan

³ Professor, Department of applied Mechanics and Aerospace Engineering, Waseda University, 3-4-1 Okubo, Shinjuku, Tokyo 169-8555, Japan

*Corresponding.author: kawada@waseda.jp, Tel:+81-3-5286-3261, Fax:+81-3-5273-2667

Keywords: CNT yarn, tensile properties, densification treatment, heat stretching, polymer solution

INTRODUCTION

Carbon nanotube (CNT) is increasingly applied as a reinforcement of polymer matrix composite because of extremely high mechanical properties. Among several forms of CNT reinforcement, continuous CNT yarn, which is fabricated by drawing Multiwall Carbon Nanotubes (MWCNTs) continuously from vertically aligned MWCNT arrays, can be a next-generation reinforcement which enables the use of CNTs in the macro-scale. Strength development mechanism of CNT yarn is thought to depend on the interactive force such as the van der Waals forces between CNTs. Therefore, improvement of stress transfer capability is required for the enhancement of CNT yarn. There have been various methods to enrich the interaction between CNTs. Especially densification treatment using a polymer solution is thought to be an effective and simple method. However, the tendency of the effective polymer for densification treatment is not fully understood. There is still a lot of room for improvement in selecting polymers. In this study, we fabricated untwisted CNT yarn which has higher mechanical properties than other CNT yarns. Untwisted CNT yarn was polymer treated for the purpose of densification. Then, we selected polymer considering its molecular structure and physical property. Furthermore, applying heat stretching treatment in addition to densification treatment, mechanical properties of untwisted CNT yarn was improved.

MATERIALS

Untwisted CNT yarn is fabricated by passing CNT sheets through a die. Figure 1 shows a schematic view of drawing untwisted CNT yarn. CNT sheets are drawn continuously from vertically aligned MWCNT arrays. MWCNTs are synthesized on the Si wafer substrate by atmosphere pressure chemical vapor deposition (AP-CVD). The diameter of fabricated CNT yarn is about 35 μm .

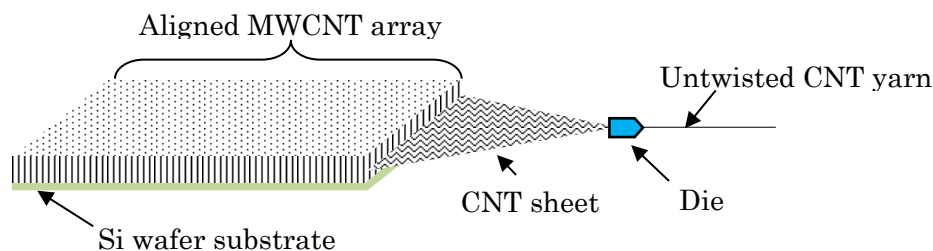


Figure 1 Schematic view of drawing untwisted CNT yarn.

EXPERIMENTAL

Polymer treatments are conducted to CNT yarns for the purpose of densification. First, CNT yarn is immersed in Polyacrylic acid/ Dimethyl sulfoxide (PAA/DMSO) solution with the condition of 60°C for 3 hours. After that, polymer treated CNT yarn is dried for 1 hour at 150°C to evaporate DMSO in it. Then, CNT yarn is applied 150mN load, which is less than 10 % of braking force, and heat stretching treatment is conducted.

RESULTS AND DISCUSSIONS

Figure 2 shows Weibull distributions of CNT yarn strength obtained by single fiber tensile test. Here, 'Untreated', 'PAA' and 'PAA-T' denotes untreated CNT yarn, PAA/DMSO treated CNT yarn and heat stretching treated CNT yarn after PAA/DMSO treated, respectively. In the case of 5 wt% PAA solution concentration, tensile strength of CNT yarn is improved from 0.90 GPa up to 2.35 GPa by densification and heat stretching treatment. Young's modulus is increased from 60.9 GPa to 172 GPa in 7 wt% PAA solution concentration. Figure 3 shows SEM images of CNT yarn surface. There is some disarray of constituent CNTs on the surface of polymer treated CNT yarn (Figure 3 (a)). On the other hand, the orientations of constituent CNTs are by heat stretching treatment (Figure 3 (b)). Contact area between CNTs was increased, and interactive force of CNTs and mechanical properties of CNT yarn was highly improved.

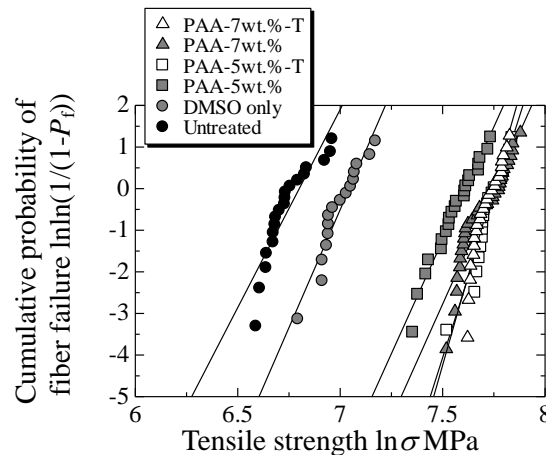


Figure 2 Comparison of mechanical properties for treated fibers.

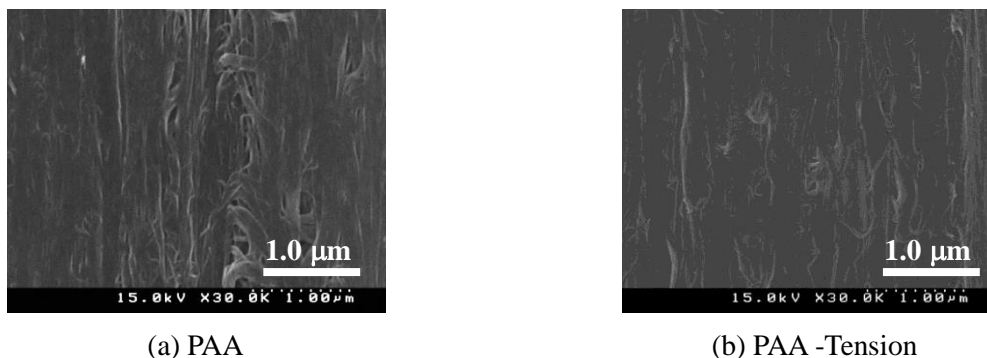


Figure 3 SEM images of the surface morphology of PAA/DMSO treated fibers.

Conclusion

In this study, untwisted CNT yarn was polymer treated using Poly acrylic acid/Dimethyl sulfoxide (PAA/DMSO) solution for the purpose of densification. As a result of single fiber tensile test, strength and Young's modulus of PAA/DMSO treated CNT yarn were drastically increased. Furthermore, as a result of heat stretching treatment in addition to densification treatment, strength and Young's modulus of CNT yarn was improved up to 2.35 GPa, 172 GPa respectively. After observation of CNT yarn surfaces using SEM, disarray of CNTs with heat stretching treatment was remedied. Contact area between CNTs was increased, and interactive force of CNTs and mechanical properties of CNT yarn was highly improved.

References

- [1] Jiang KL, Li QQ, Fan SS. Spinning continuous carbon nanotube yarns. *Nature* 2002; 419 (6909): pp. 801.
- [2] Sugano K, Kurata M, Kawada H. Evaluation of mechanical properties of untwisted carbon nanotube yarn for application to composite materials. *Carbon* 2014; 78: pp. 356-365.

EFFECTS OF PROCESSING CONDITIONS IN UNIDIRECTIONAL CARBON FIBER THERMOPLASTIC PREPREG TAPE LAYING USING NEAR INFRARED HEATER

Daiki TANABE^{1,*}, Kazuaki NISHIYABU², Tetsusei KURASHIKI¹

¹Dept. of Management of Industry and technology, Graduate School of Eng., Osaka University

²Dept. of Mechanical Engineering, Faculty of Science and Eng., Kinki University

* d-tanabe@mit.eng.osaka-u.ac.jp

Keywords: ATL, CF/PA6, CFRTP, Near infrared heating, Interlaminar shear strength

Automated thermoplastic tape laying (ATL) is a high-potential manufacturing method for continuous fiber reinforced thermoplastic composites which can ensure operational safety even in highly loaded components such as aircraft wing skins and fuselages or construction large scaled structures [1]. This method often uses computer-controlled robotics to lay one or several layers of carbon fiber thermoplastic tape onto a mold, and should be optimized some processing parameters such as heating, pressing and feed speed and so on. Though the final aim of this study is to manufacture composite laminates made from tapes pre-impregnated with unidirectional carbon fiber reinforcement and a thermoplastic matrix, this study focuses on thermal distribution and joining strength in a laying process of unidirectional carbon fiber reinforced thermoplastic tape. The tape are commonly heated up to the melting temperature by various heating sources including heated roller, hot gas torch, near-infrared light lamp and diode laser and so on [1, 2]. A near-infrared heater has some advantages such as rapid start-up speed, suitable for heating of carbon fiber and low cost. However, the heating characteristic is influenced significantly by position of the heater and feed rate of prepreg tape, thus it is necessary to optimize these heating parameters. Therefore, it is important for the thermoplastic prepreg tape laying process to investigate the heating and consolidation behavior. This study aimed to predict the optimum processing condition for thermoplastic tape laying. The material used for the experiment was carbon fiber reinforced polyamide 6 prepreg tape (TenCate, CETEX[®] TC910). This prepreg tape has unidirectional construction with a resin content of $V_f=58\text{vol.}\%$ and a thickness of $t=0.16\text{mm}$.

Figure 1 shows appearance of the tape laying machine authors made originally. This tape laying machine has the near infrared heater (Heraeus, ZKB600/80G) as source of heating and the pressure rollers. The heater has two tungsten filament as heating source, and it is suitable as the heater of CFRTP prepreg tape because the absorbed fraction is high into black body as carbon fiber. The pressure rollers are heated rapidly to any temperature by a induction heating equipment (Hidec Co., Ltd.). This tape laying process is divided into the three steps. Firstly, the prepreg tapes are heated by the near infrared heater. Then, the matrix polymer of prepreg tapes is melted rapidly. Secondly, two prepreg tapes are welded by pressing using pressure rollers. Finally, the laminated tape is cooled down. Two fine thermocouple (ANBE SMT Co., Ltd., KSG-40-100-100, type K) were bonded on the prepreg tape surface to investigate the fusion behavior. Two prepreg tapes with 50mm in width were inserted to pressure roller at the angle of $\theta_{CF}=60^\circ$. The fiber direction of two prepreg tapes and the feed direction is same direction. The angle of the near infrared heater was fixed at $\theta_H=30^\circ$, and the feed speed was changed from $v=14\text{mm/s}$ from to $v=28\text{mm/s}$. The heating behavior of the surface of prepreg tape was measured by fine wire thermocouples using a temperature measuring instrument (Graphtech Co., Ltd., midi LOGGER GL200A). The images of joint surfaces peeled off after joining were imported with a scanner device (Epson Co., Ltd., ES-7000H). The welding surfaces were also observed with a microscope to investigate the fusion joining interface. The single lap shear strength test was carried out to evaluate a joint strength by using universal testing machine (SHIMAZU Co., Ltd., AG-50kN XDplus). Figure 3 shows appearance of single lap joining test specimen. Before the testing, aluminum tabs were bonded to end of specimens with epoxy adhesive. The cross-head speed was $v=0.5\text{mm/min}$.

Figure 2 shows the change of surface temperature of CF/PA6 prepreg tape at $v=14\text{mm/s}$. The temperature of pressure roller was $T_R=30^\circ\text{C}$. The temperature of prepreg tapes were increased with increasing the x-coordinate. When the prepreg tapes were cooled down quickly, the tapes were contacted pressure rollers. Also, when the distance of heater was $x_H=50\text{mm}$ and $x_H=60\text{mm}$, the

temperature was over $T=225^{\circ}\text{C}$. This temperature is melting temperature of PA6 polymer. The maximum temperature was increased with decreasing the distance between heater and pressure rollers (x_H). It was also revealed that the range of heating was increased with decreasing the distance of heater. From these results, it is considered that the proper distance of the heater is from 50mm to 60mm.

Figure 3 shows the result of single lap shear strength test. The lap shear strength (τ_{ap}) and the maximum load (P_{max}) were increased with decreasing the distance between heater and pressure roller (x_H). The feed speed was $v=14\text{mm/s}$, the lap shear strength and maximum load were higher than $v=24\text{mm/s}$ because the matrix polymer of prepreg tapes melted sufficiently.

From these results, the effects of processing conditions such as number and position of infrared heaters, feed speed and temperature of pressure roller on the laying behavior of prepreg tape were revealed to obtain the proper processing parameters.

Table and Figure

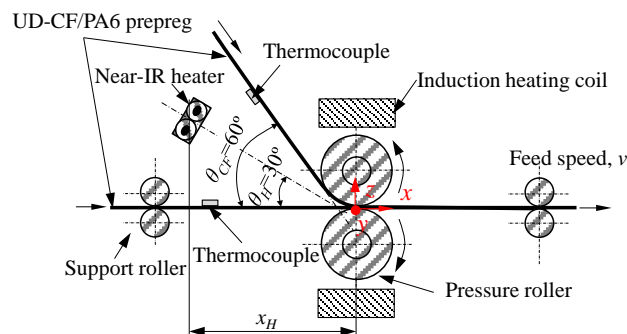


Figure 1 Appearance of ATL machine.

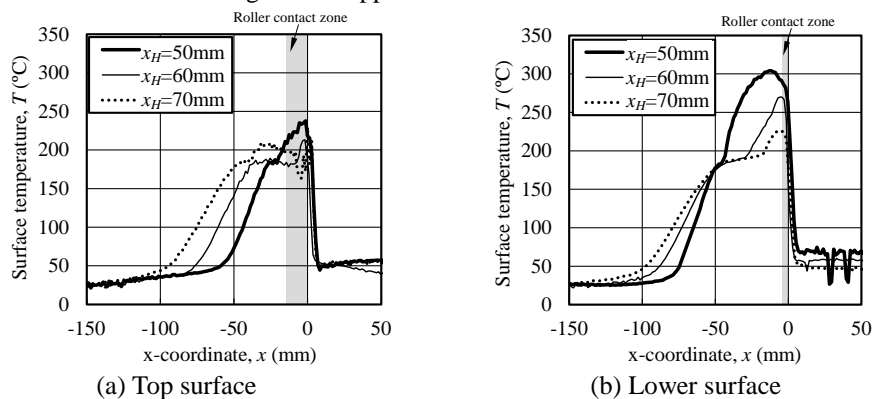


Figure 2 Change of surface temperature of CF/PA6 prepreg tape at $v=14\text{mm/s}$.

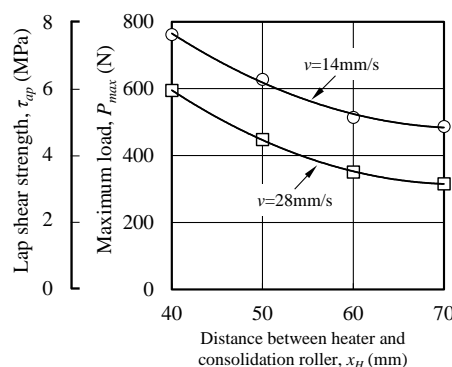


Figure 3 Result of single lap shear strength test of CF/PA6 laminated tapes.

References

- [1] C.M. Stokes-Griffin, P. Compston, A combined optical-thermal model for near-infrared laser heating of thermoplastic composites in an automated tape placement process, *Composites Part A: Applied Science and Manufacturing*, In Press, Corrected Proof, Available online 14 August 2014.
- [2] Z. Qureshi, T. Swait, R. Scaife, H.M. El-Dessouky, In situ consolidation of thermoplastic prepreg tape using automated tape placement technology: Potential and possibilities, *Composites: Part B* 66 (2014) 255–267.

ESTIMATION OF ELECTRICAL CONDUCTIVITY OF TiB₂/Al COMPOSITES WITH IMAGE ANALYSIS

Kenjiro Sugio^{1*}, Nariaki Kawano², Takaaki Hirose², Yong-Bum Choi¹ and Gen Sasaki¹

¹Division of Materials and Production Engineering, Institute of Engineering, Hiroshima University, 1-4-1, Kagamiyama, Higashi-Hiroshima, Hiroshima 739-8527, Japan

²Department of Mechanical Science and Engineering, Graduate School of Engineering, Hiroshima University, 1-4-1, Kagamiyama, Higashi-Hiroshima, Hiroshima 739-8527, Japan

*Corresponding ksugio@hiroshima-u.ac.jp

Keywords: electrical conductivity, image analysis, particle dispersibility

In the present study, it was aimed at the development of the software that is possible to calculate the effective electrical conductivity of aluminum-based particle-dispersed composites from the actual microstructure image by performing conduction simulation. However, the electrical conductivity calculated with the microstructure image is supposed to be not equivalent to the electrical conductivity measured with experimental method, such as four-terminal method, because microstructure image is a two-dimensional information though the experimental conductivity is obtained from three-dimensional microstructure. It is not well studied on the relationship between two-dimensional and three-dimensional electrical conductivity. Therefore, statistical relationship between three-dimensional and two-dimensional electrical conductivity were investigated by performing conduction simulation.

First, a three-dimensional particle distribution was created in the simulation cell, and the electrical conductivity in three-dimension was calculated. Then, the sequential two-dimensional cross-sections were cut out from the three-dimensional particle distribution. The electrical conductivity for each cross-section was calculated. Electrical conductivity of Al, TiB₂, SiC and Al₂O₃ were set to 40.0, 11.1, 0.01 and 1.0×10^{-18} ($10^6/\Omega/m$), respectively. Three-dimensional cell was divided into $100 \times 100 \times 100$ elements, and electrodes whose size is $100 \times 100 \times 5$ are added to the both sides. The size of elements was $2 \times 2 \times 2$ (μm). Diameter of reinforcing particles was $10 \mu m$, and their dispersibility were changed by using uniform random number and changing standard deviation of normalized random number. Two-dimensional cross-section which cut out from the three-dimensional cell was divided into 100×100 elements, and electrodes whose size is 100×5 were added to the both sides. The degree of dispersion of the particles in the cross-section was evaluated by two-dimensional local number (LN2DR) [1]. The potential difference between left and right sides set as 0.05V in three and two dimensions. Finite volume method was used to calculate the steady state of electrical potential distributions. Calculations were stopped when the average variation of potential in each elements is smaller than 10^{-13} . Electrical conductivity was calculated from the potential distribution of the steady state.

Fig. 1 shows the electrical conductivity of three-dimensional cell and two-dimensional cross-sections in 20vol.%TiB₂/Al composite where TiB₂ particles were uniformly distributed. Open circles indicates the electrical conductivity of the two-dimensional cross section which is extracted from the three-dimensional cell. The horizontal axis represents the position of the cross section. The particle arrangement of typical two-dimensional sections are shown in the figure. Broken line indicates the average electrical conductivity of the two-dimensional cross-sections and each electrical conductivity (open circle) is not apart from the average (broken line) in the case of uniform random distribution. Solid line indicates the electrical conductivity of the three-dimensional cell, and the average value of two-dimensional

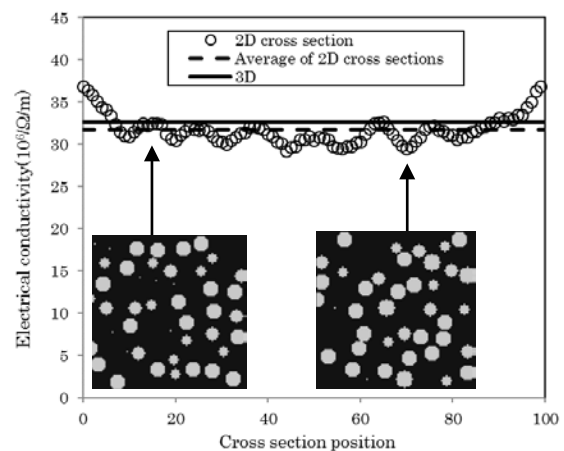


Fig. 1 Relation of electrical conductivities of 3D and 2D cross section in uniform random distribution of 20vol.%TiB₂ particles.

cross-sections is slightly lower than the three-dimensional value. Series of calculations with uniform random distribution were carried out by changing the kind of the reinforcement (TiB₂, SiC, Al₂O₃) and the volume fraction (5% to 50%). Fig. 2 shows a summary of those calculations. Closed circle indicates electrical conductivity of three-dimensional cell dispersing the TiB₂ particles, and open circles indicates the average electrical conductivity of the two-dimensional cross-sections. The average electrical conductivity of two-dimensional cross-sections is lower than that of three-dimensional cell, and the difference increase with increasing volume fraction. Electrical conductivity of Al and TiB₂ were 40.0 and 11.1 (10⁶/Ω/m), respectively, and the difference is not so large. Therefore, there is no large difference between three-dimensional and two-dimensional electrical conductivity in case of TiB₂ particles. Meanwhile, electrical conductivity of SiC and Al₂O₃ were 0.01 and 1.0×10⁻¹⁸ (10⁶/Ω/m), respectively, and difference against Al is too large. This possibly enhanced difference between three-dimensional and two-dimensional electrical conductivity in case of SiC and Al₂O₃. Fig. 3 shows results of the calculation by changing the dispersibility of the TiB₂ particles. The horizontal axis is LN2DR_{var} which can represent dispersibility quantitatively. If LN2DR_{var} is 7, gravity centers of dispersed particles are arranged in uniform random distribution. If LN2DR_{var} increases, clustering tendency of the particles increases. Filled markers indicates the three-dimensional electrical conductivity, and open markers indicates the average of the two-dimensional electrical conductivity. The difference between two-dimensional and three-dimensional electrical conductivity is constant in each volume fraction even when dispersibility is changed. This means that it is not necessary to consider the dispersibility when converting the two-dimensional conductivity to three-dimensional conductivity. In addition, the same trend was seen in the case of SiC and Al₂O₃ particles. Table 1 shows list of correction value for converting two-dimensional electrical conductivity to three-dimensional electrical conductivity. Although maximum correction value for TiB₂ is 105.45%, maximum correction value for SiC and Al₂O₃ is about 171%.

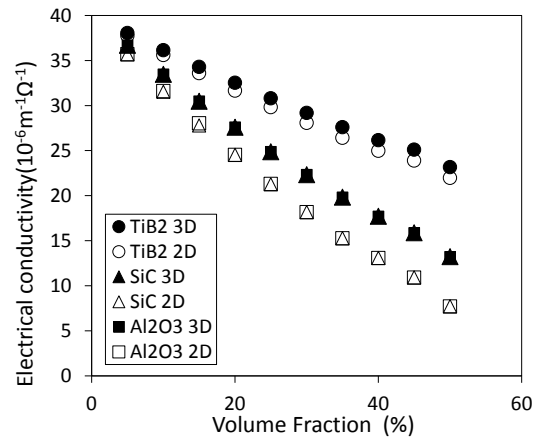


Fig. 2 Relation of electrical conductivities of 3D and 2D cross section in uniform random distribution of TiB₂, SiC and Al₂O₃ particles.

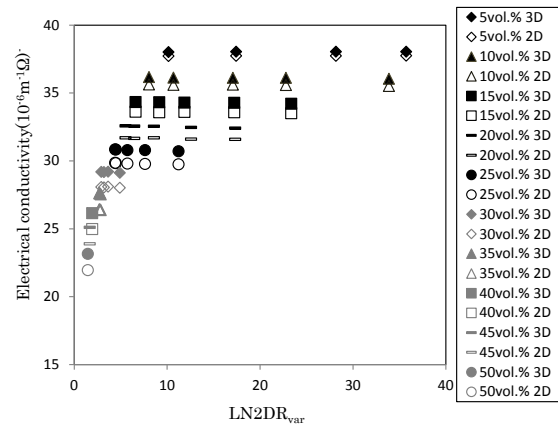


Fig. 3 Relationship between electrical conductivities and dispersibility of TiB₂ particles.

Table 1 List of correction value (%) for converting 2D electrical conductivity to 3D electrical conductivity.

	σ_p/σ_{Al}	5vol.%	10vol.%	15vol.%	20vol.%	25vol.%	30vol.%	35vol.%	40vol.%	45vol.%	50vol.%
TiB ₂	0.2775	100.80	101.49	102.10	102.72	103.32	103.95	104.45	104.70	105.07	105.45
SiC	2.5×10 ⁻⁴	102.87	106.27	109.67	112.65	117.27	122.41	129.74	135.29	145.20	171.04
Al ₂ O ₃	2.5×10 ⁻²⁰	102.85	105.89	108.78	112.53	116.84	122.94	129.87	135.47	145.64	171.83

References

[1] K. Sugio et. al., Evaluating Spatial Distribution Randomness of Overlap Permissive Second Phase in Three- and Two-Dimensions, Mater. Trans., 48(2007) pp. 2762-2767.

NEW MANUFACTURING METHOD OF PARTICLE INTERMETALLIC COMPOUND REINFORCED COMPOSITES

Yongbum Choi^{1*}, Zhefeng Xu¹, Kenjiro Sugio¹, Kazuhiro Matsugi¹, Gen Sasaki¹

¹ Division of Materials and Manufacturing, Graduate School of Engineering, Hiroshima University, 1-4-1 Kagamiyama, Higashi-Hiroshima, Hiroshima 739-8527, Japan

*Corresponding. ybchoi@hiroshima-u.ac.jp

Keywords: *Intermetallic, Composites, Porosity, Infiltration and reaction method.*

Conversion to aluminum alloy from cast iron materials has been increasing. And advanced features of the aluminum alloy are demanded. Due to this, composites which are strengthened with ceramic particles in aluminum alloy are developed. It is applied in practical for brake disk and piston in mobile parts in the industrial field [1]. Generally, manufacturing methods of a ceramic particles dispersed composite include Powder metallurgy process [2], Stir casting [3] and squeeze casting method [4], etc.

A new process in this study is proposed to fabricate an aluminum alloy matrix composite dispersed with refining intermetallic compound particles by using the reaction between porous nickel and molten aluminum alloy. The objective of this study is to investigate the effects of the specific surface area on the intermetallic compounds formed in the composites by infiltration and reaction method. Therefore, the research investigated on the reaction of porous nickel and molten Al alloy, the amounts of the intermetallic compounds by different specific surface area of porous nickel and the aspect ratio of intermetallic compounds under $1250\text{m}^2/\text{m}^3$, $2800\text{m}^2/\text{m}^3$, $5800\text{m}^2/\text{m}^3$ and $> 5800\text{m}^2/\text{m}^3$, respectively. A366 alloy in ASTM, which composition of Al-12Si-1Ni-1Cu-1Mg (mass %), was used as matrix. Preform was porous nickel (Toyama Sumitomo Electric Co., Ltd.). Volume ratio of porous nickel is 4~6vol.%. Porous nickels with four different kinds of specific surface areas (a: $1250\text{ m}^2/\text{m}^3$, b: $2800\text{ m}^2/\text{m}^3$, c: $5800\text{ m}^2/\text{m}^3$ and d: $> 5800\text{ m}^2/\text{m}^3$) were used in the experiment to examine the reactive behavior of the intermetallic compound. Infiltration and reaction method was used to fabricate the composites. Temperature of molten Al alloy and applied pressure to molten Al alloy were 973K and 0.1MPa.

Figure 1 shows microstructure of Al matrix composites dispersed intermetallic compound with specific surface area of porous: a) $1250\text{ m}^2/\text{m}^3$, b) $2800\text{ m}^2/\text{m}^3$, c) $5800\text{ m}^2/\text{m}^3$ and d) $>5800\text{ m}^2/\text{m}^3$. As a result of observing the microstructure of the composites manufactured using four kinds of porous nickel, on the whole, the intermetallic compound were distributed inside matrix by the reaction of a porous nickel and aluminum. However, the microstructure observed from the composites fabricated with low specific surface area (in figure 1(a) $1250\text{ m}^2/\text{m}^3$) that almost all porous nickel were changed to intermetallic

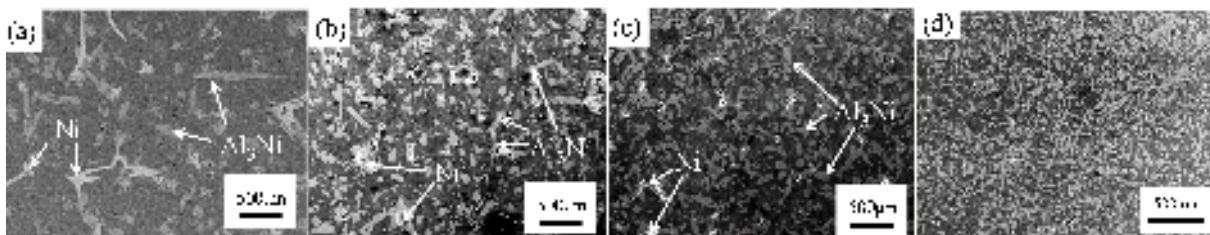


Figure 1 Microstructure of Al matrix composites dispersed intermetallic compound composites

compound. Area fraction of the generated intermetallic compound is about 15%. In addition, the portion which remains as porous nickel body without delamination from the porous surface was also observed. However, the area fraction of the un-reacted nickel was 2.8%. And most of the fine Al_3Ni intermetallic compounds (below 0.1mm^2 calculated area) were homogeneously dispersed inside matrix. But shape of the needle-like Al_3Ni was observed too. And numerous pores were observed in the composites. The microstructure when specific surface area is high (in figure 1(d) $>5800\text{ m}^2/\text{m}^3$), more fine intermetallic compounds were distributed as compared with other materials in figure 1(a), (b) and (c). The fine intermetallic compounds increased with increasing specific surface area of porous nickel. In addition, based on the figure 1(d). Area fraction (%) of intermetallic compound Al_3Ni was about 28.2%, which is almost twice comparison with figure 1(a). Furthermore, the area fraction of un-reacted nickel reached a minimum value of 0 % when the specific surface was $>5800\text{ m}^2/\text{m}^3$. The results indicate that higher the specific surface area of porous nickel is, larger the contact surface with molten Al is, and it provided further reaction of nickel with Al.

As shown, figure 2 is the porosity in Al matrix composites dispersed intermetallic compound according to the variation of the specific surface area of porous nickel. Porosity in porous nickel, it was occurred by initial polymer foam to fabrication of porous nickel. Polymer foam can be removed from the metal/polymer by heat-treatment. Pore was remained by the hollow struts inside porous nickel. Porosity in porous nickel is different by specific surface area. The porosity inside porous nickel decreased by the increasing a specific surface area of porous nickel. Although there was almost similar porosity in the composites infiltrated with porous nickel of three different specific surface area, pore size in the composites infiltrated with high specific surface area is smaller than those with low specific surface area. The general porosity trend in both porous nickel and matrix is reducing with the increasing of the specific surface area at the same fabrication conditions, and the minimum porosity is about 0.17% in the matrix and 0.19% in the porous nickel of $>5800\text{ m}^2/\text{m}^3$ since with the reduction of the porous thickness accelerated the reaction between Ni and Al and delamination caused by the difference of thermal expansion coefficient with nickel, which is a great reduction of defect in the composites as well.

References

- [1] Y. B. Choi, G. Sasaki, K. Matsugi, S. Kondoh, O. Yanagisawa, Low pressure casting process of FeCrSi/A366.0 alloy composites and their characterization. *Key Eng. Mater.* 326-328(2006), pp.1741-1744
- [2] M.H. Lee, Y.B. Choi, K. Sugio, K. Matsugi, G. Sasaki, Effect of aluminum carbide on thermal conductivity of the unidirectional CF/Al composites fabricated by low pressure infiltration process. *Compos. Sci. Technol.*, 97(2014), pp.1-5.
- [3] H. Izadi, A. Nolting, C. Munro, D. P. Bshop, K. P. Plucknett, A. P. Gerlich, Friction stir processing of Al/SiC composites fabricated by powder metallurgy. *J. Mater. Proc. Technol.*, 213. 11(2013), pp.1900-1907.
- [4] V. Bharath, N. Madev, V. Auradi, S.A. Kori, Preparation of 6061Al- Al_2O_3 MMCs by stir casting and evaluation of mechanical and wear properties. *Proc. Mater. Sci.*, 6(2014), pp. 1658-1667

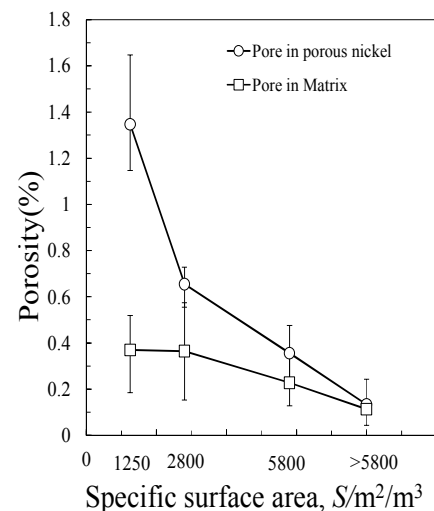


Figure 2 Porosity of Al_3Ni , intermetallic compound and Un-reacted nickel.

THE EFFECT OF ZrO₂ ADDITION ON THE ELECTROCHEMICAL BEHAVIOR OF LOW-CARBON STEELS IN CrO₃-H₂SO₄ ELECTROLYTE

Kazuma Hashimoto¹, Kenjiro Sugio^{1*}, Gen Sasaki¹, Asep Ridwan², Aditianto Ramelan²

¹*Division of Materials and Manufacturing, Graduate School of Engineering, Hiroshima University, 1-4-1 Kagamiyama, Higashi-Hiroshima, Hiroshima 739-8527, Japan*

²*Department of Materials Engineering, Faculty of Mechanical and Aerospace Engineering, Bandung Institute of Technology, Bandung, Indonesia*

*Corresponding. ksugio@hiroshima-u.ac.jp

Keywords

Electrodeposited Cr, Nanocomposite coating, Zirconia particle, Polarization behavior, Electrophoretic deposition

Hard chromium coating is mainly used to improve the surface performance of pistons, brake disks, and gears. In the future, better abrasion resistance and better corrosion resistance of hard Cr coating are demanded. Previous studies showed that co-deposition of ceramic particles such as Al₂O₃/SiC in Cr coating improved these characteristics¹⁾. The Cr-ZrO₂ composite coating is one of the prospective candidates for this purpose. However, the effect of ZrO₂ addition on the electrochemical behavior of carbon steels in CrO₃-H₂SO₄ electrolyte is unknown. In this study, the polarization behavior of low carbon steel in CrO₃-H₂SO₄ electrolyte with ZrO₂ addition was investigated.

Low-carbon steels with the size of 1 cm×1 cm were prepared for the substrate. The specimens were covered with thermoset polymer and were polished by waterproof abrasive paper from #200 to #2000. The electrolytes consisted of CrO₃ (250g/L) and H₂SO₄ (2.5g/L), and the additive amount of ZrO₂ particles was varied from 0 g/L to 2.0 g/L. The average size of ZrO₂ particles was 30 nm. The cyclic voltammetry measurements were carried out by VersaSTAT-300 (Princeton™ Applied Research). A saturated calomel electrode was used as the reference electrode. The potential scanning rate was 0.5mV/s from -1.5V to 0.6V.

Fig. 1(a) shows the polarization curves of each ZrO₂ amount. The shape of polarization curve was changed by the addition of ZrO₂ particles. Polarization point can be confirmed by the plot of the potential versus logarithmic value of the absolute current. Polarization point was shifted higher by the addition of ZrO₂ particles. Fig. 1(b) summarizes the polarization potential at different ZrO₂ density. The polarization potential approaches to zero with increasing the amount of ZrO₂. This suggests that the corrosion resistance was improved by the addition of ZrO₂ particles. Fig.1 (c) shows the cathodic polarization curves for the deposition of Cr-ZrO₂. The vertical axis is current value between -0.1 and 0A and the horizontal axis is potential value between -0.6 and -0.4V. The slope of the plot indicates electrical conductivity of the cathode including the substrate and the plated film. The slope become gentler with increasing the amount of ZrO₂, and this means that addition of ZrO₂ particle decrease electrical conductivity of the

plated film. Reductive reaction without ZrO_2 stopped rapidly around $-0.52V$ as shown in Fig 1(c). In contrast, reductive reaction stopped gently around $-0.45V$, when ZrO_2 was included in solution. This suggests that reductive reaction continued after the end of reductive reaction of Cr. Fig.2 shows the specimen after each experiment. The gloss of the surface decreased with the amount of ZrO_2 particles. This suggests that ZrO_2 particles were introduced into the coating. Previous study showed that hydrogen ion was adsorbed on ZrO_2 particles and they were positive charged in strong acidity. The positive charged ZrO_2 particle were reacted at the cathode. Fig.3 shows optical microscope images of the specimens after each experiment. The particle size was bigger by the addition of ZrO_2 . And lattice defect concentration decreased by the addition of ZrO_2 . But it did not depend on the amount of ZrO_2 . This suggests that ZrO_2 improve mechanical characteristic of Cr coating.

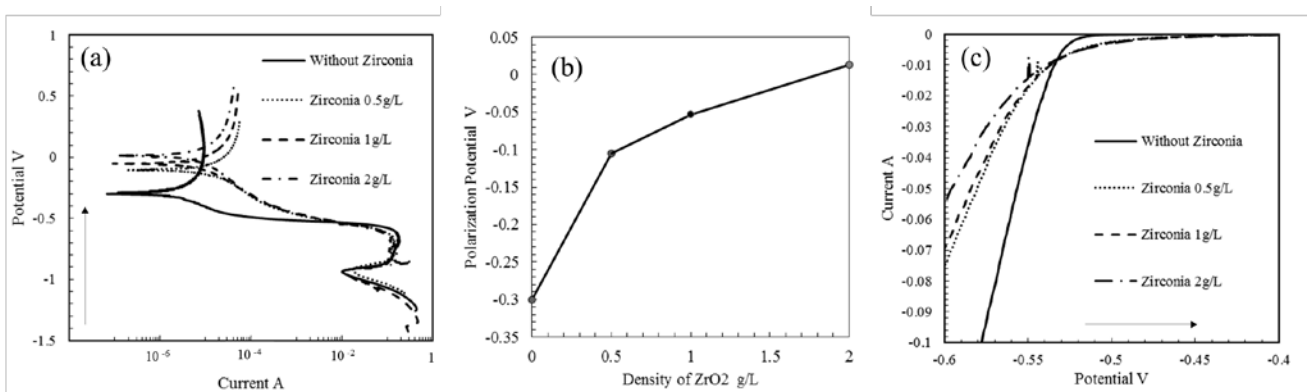


Figure 1: (a) Polarization curves on each ZrO_2 density, (b) polarization potential versus ZrO_2 density and (c) cathodic polarization curves on each ZrO_2 density.

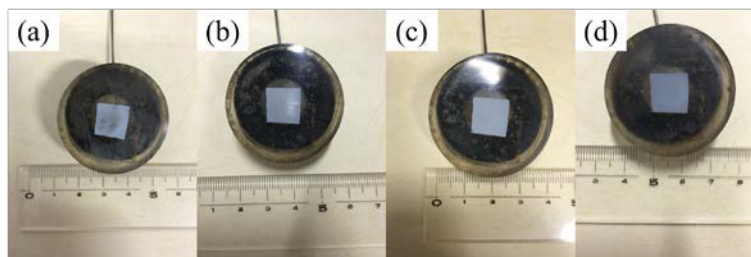


Figure 2: Specimens after plating. (a) 0 g/L, (b) 0.5 g/L, (c) 1.0 g/L and (d) 2.0 g/L ZrO_2 particles were included in the electrolytes.

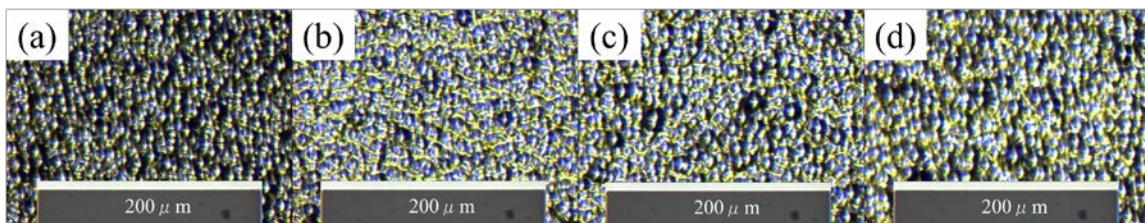


Figure 3: Optical microscope images of the specimens after plating. (a) 0 g/L, (b) 0.5 g/L, (c) 1.0 g/L and (d) 2.0 g/L ZrO_2 particles were included in the electrolytes.

Reference

1. Jifeng Gao, Jinping Suo, Preparation and characterization of the electrodeposited $Cr-Al_2O_3/SiC$ composite coating, Applied Surface Science 257 (2011), pp.9643– 9648

PRODUCTION AND IMPROVEMENT OF CHARACTERISTICS OF SINTERED POROUS TITANIUM USING CAPSULE-FREE HIP METHOD

Shuichi MASHINO¹, Takuji OKABE^{2*}

¹ Graduate Student, Hiroshima Institute of Technology, 2-1-1 Miyake, Saeki-ku, Hiroshima 731-5193, Japan

² Department of Mechanical Systems Engineering, Hiroshima Institute of Technology, 2-1-1 Miyake, Saeki-ku, Hiroshima 731-5193, Japan

*okabe@cc.it-hiroshima.ac.jp

Keywords: Capsule-free hot isostatic pressing, Sintering, Porous material, Porosity, Titanium

1. Introduction

Porous materials are seen as new lightweight, functional materials with properties such as low density and large surface area [1]. However, these materials also have problems such as low mechanical strength and inconsistent porosity. The production of sintered porous materials by capsule-free hot isostatic pressing (HIP) is capable of simultaneous control of both mechanical strength and porosity [2]. An additional feature of this method is that it does not necessarily require a foaming agent. In this study, we produced sintered porous titanium using the capsule-free HIP method and attempted to improve material characteristics by investigating the effects of capsule-free HIP on the sintered compacts.

2. Experimental Procedure

First (Experiment 1), commercial titanium powders (99.5% purity, -350 mesh, 4 g) were placed in a 15-mm diameter die and compacted using a hydraulic hand pressing machine (uniaxial compaction loads: 4.9, 9.8, 14.7, 19.6, and 24.5 kN). The green compacts were then sintered using the capsule-free HIP method at a holding temperature of 1523 K, under an argon gas atmosphere, at a holding pressure of 150 MPa, for a holding time of 1 h. In addition, the green compacts were sintered by electric furnace at the relatively low temperature of 873 K, under an argon gas atmosphere, at normal pressure, for a holding time of 1 h. The pre-sintered compacts were then subjected to the capsule-free HIP treatment under the same conditions as described above. The characteristics of the sintered compacts were evaluated by microstructure observation (optical microscope; OM), component analysis (X-ray diffraction), porosity measurement (image analysis software), density measurement (Archimedes method), and compression test (universal testing machine).

Next (Experiment 2), commercial titanium powders (99.5% purity, -150 mesh, 4 g) were classified by sieves having meshes of 106 and 150 μm . Using the sieved powders ($\leq 106 \mu\text{m}$ and $106 - 150 \mu\text{m}$), experiments and evaluations were performed as described for Experiment 1.

3. Results and Discussion

Experiment 1: Examples of OM images of the sintered compact surfaces are shown in Fig. 1. Measurement of mean porosity at the surface and relative density (i.e., bulk density to true density) for Ti: 4.51 Mg/m^3 are shown in Fig. 2. These figures show that the sintered compact that was subjected to the direct capsule-free HIP treatment definitely has some pores, but the porosity is much lower than that of the pre-sintered compacts. The relative densities of the direct HIPed compacts are more than 70%, indicating that these compacts have generally low porosity. Conversely, the compacts that were pre-sintered have porosities that are more than twice those of the direct-HIPed ones, and the relative densities are 55 % – 65 %, indicating a significant density reduction. The experimental results show that pre-sintering is effective in the production of sintered porous compacts using the capsule-free HIP method. The shapes of most pores are rounded, which indicates that the pores were formed isotopically by the high-temperature, high-pressure gas of the HIP treatment, leading to an improvement of mechanical strength by the relaxation of stress concentrations. In such processing conditions, however, large variation of characteristics was confirmed. Therefore, it was necessary to investigate its improvement.

Experiment 2: The results of the capsule-free HIP treatment after pre-sintering are shown in Fig.

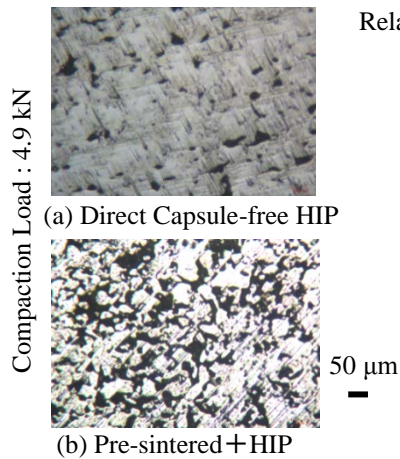


Fig. 1. OM images of sintered porous compacts at surface (Experiment 1).

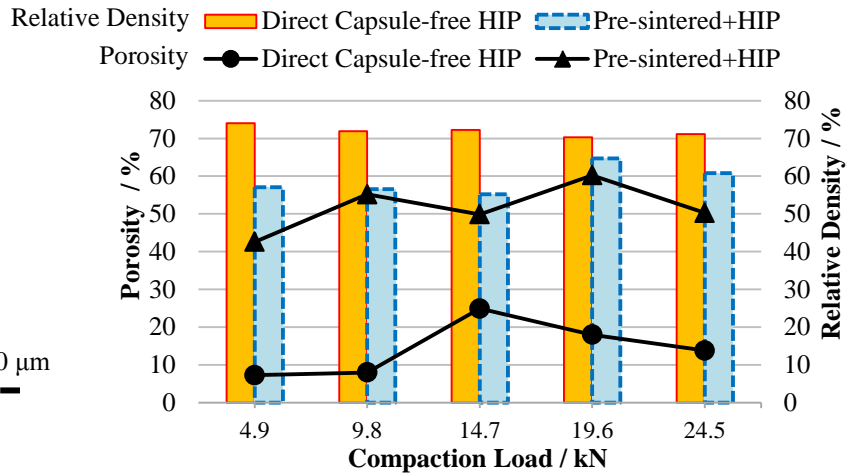


Fig. 2. Porosity at surface and relative density of sintered porous compacts (Experiment 1).

3 for various compaction loads. This result shows that these compacts have porosity that is equivalent to the pre-sintered ones in Experiment 1 (Fig. 2). Moreover, porosity decreases and density increases with increasing compaction load. The variation of porosity with processing conditions is relatively subdued compared with Experiment 1. This trend is attributed to the effect of homogenization of the particle size of raw powders. Therefore, homogenization of the green compact is expected to lead to an improvement of characteristics of the sintered compacts. Mean porosity measurements at the cross section are shown in Fig. 4. The measurement points were at three locations (top, side and center) on the cross section. From this result, the locational variation of porosity is large inside the sintered compact. In particular, the center portion is densified, and its porosity is reduced to about half that of the surface. This trend was confirmed in all processing conditions. However, it is necessary to investigate the cause and countermeasures.

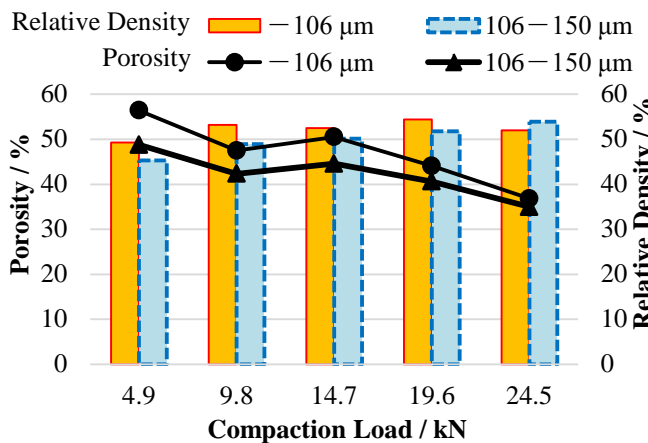


Fig. 3. Porosity at surface and relative density of sintered porous compacts (Experiment 2).

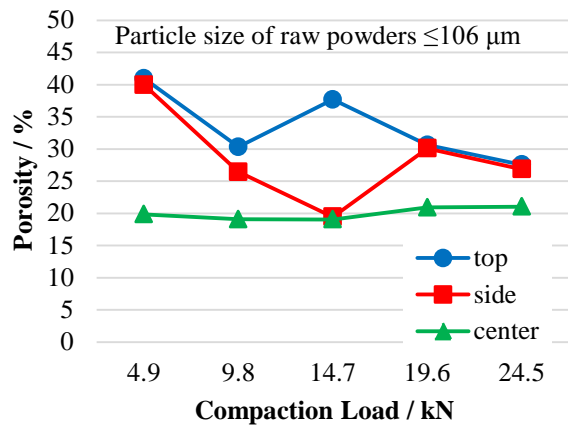


Fig. 4. Porosity on cross section of sintered porous compacts (Experiment 2).

4. Conclusion

Sintered porous titanium produced by capsule-free HIP method after pre-sintering at a relatively low temperature with a short holding time, had high porosity. These sintered compacts showed some improvement of characteristics by homogenization of the green compact, but the center portion of the sintered compact was densified, and its porosity was reduced.

References

- [1] S. Suzuki, J. L. Martin, H. Utsunomiya, H. Nakajima, Plastic Deformation Processes of Lotus-Type Porous Metals, *Journal of the JSTP*, **52**(2011), pp. 206-211.
- [2] T. Takahashi, K. Matsumaru and K. Ishizaki, Production and Sintering Mechanism of Open-Pore Porous Materials by Using Hot Isostatic Press (HIP), *J. Jpn. Soc. Powder Powder Metallurgy*, **55**(2008), pp. 170-176.

PROPOSAL FOR NEW FABRICATION METHOD OF GREEN COMPOSITE BY USING FRICTION STIR PROCESS

Tairyu Yamashita¹, Yuhei Kurabe², Yukio Miyashita^{3,*}, Yuichi Otsuka³ and Hisashi Hori⁴

¹ Graduate Student, Graduate School of Engineering, Nagaoka University of Technology, Japan

² National Institute of Technology, Ishikawa College, Japan

³ Nagaoka University of Technology, 1603-1 Kamitomioka, Nagaoka, Niigata, 940-2188, Japan

⁴ Nippon Light Metal Co., Ltd., Japan)

*Corresponding Author: miyayuki@mech.nagaokaut.ac.jp, Tel: +81-258-47-9704

Keywords: Green composite, Friction stir process, Bamboo fiber, HDPE, Tool

Introduction

Composite material by using reinforcement of natural fiber is called green composite. Green composite has advantages in recyclability and environmental friendly. However, the mechanical property can be easily degraded during the fabrication process by thermal degradation in natural fiber used as reinforcement [1]. In the present study, friction stir process was applied as a lower heat input process to fabricating green composite material in order to avoid occurrence of thermal degradation in reinforcement of natural fiber. Bamboo fiber and high-density polyethylene (HDPE) were used as reinforcement and matrix in the present study. A new method to providing the reinforcement into the matrix without pre-machining is proposed.

Experimental Procedures

Materials used for the matrix and the reinforcement was HDPE and bamboo fiber. Physical and mechanical property for HDPE is shown in Table 1. Bamboo fiber used in the present study is shown in Fig.1. Specimen size of HDPE was 100 mm × 40 mm with thickness of 5 mm. Bamboo fibers were mixed with resin to form a cylindrical shape with 4.1 mm in the diameter and 15 mm in the height, then it was inserted into the tool. Friction stir process was used to mixing the matrix and the reinforcement in order to fabricate green composite in the present study. Preparing groove or hole is necessary as a pre-machining process in friction stir process in usually. However, those machining processes decrease productivity and result in increasing production cost. In this study, a new method is proposed as a friction stir process without pre-machining process. It is expected in the present process proposed that reinforcement is pushed out from the tool during the process and is broken to be fine with tool traveling. The fine fiber broken was stirred with the matrix by rotating of the tool and then green composite is fabricated. Schematic of the tool is shown in Fig.2. The tool has pin with M10 screw. The reinforcement was filled into a hole in the pin. In the friction stir process, tool tilt angle was 0° and rotating direction of the tool was counterclockwise. Friction stir process experiments were carried out at conditions of 600 rpm - 15 mm/min (rotating speed - traverse speed), 600 rpm - 45 mm/min and 1200 rpm - 15 mm/min. In the present process, rotating tool was inserted into the matrix until 4 mm depth from surface of the specimen with plunging speed of 15 mm/min, then the tool moved with certain traverse speed.

Table 1 Physical and mechanical property of HDPE.

Young's modulus, GPa*	1.18
Tensile strength, MPa*	31.9
Thermal conductivity, W/mk	0.24
Glass transition temperature, °C	-90
Melting temperature, °C	137
Crystallinity, %	70
Melt viscosity, Pa·s	6×10 ²
Shear velocity(140°C), s ⁻¹	10 ²

*at crosshead speed: 1.0mm/min

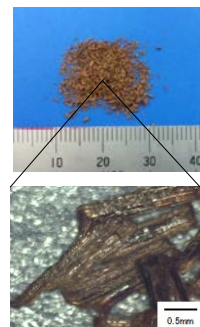


Fig.1 Bamboo fiber used.

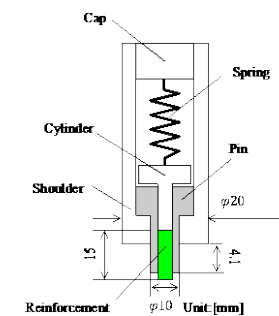


Fig.2 Tool used for friction stir process.

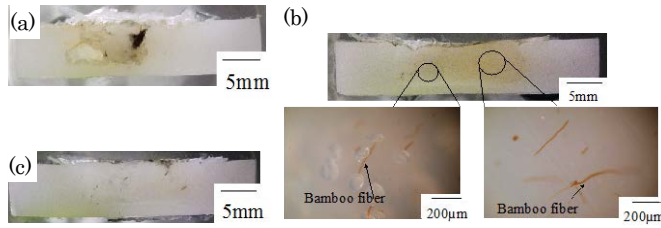


Fig.3 Observation for cross section of the stir zone applied with (a) 600 rpm – 45 mm/min, (b) 600 rpm – 15 mm/min and (c) 1200 rpm – 15 mm/min.

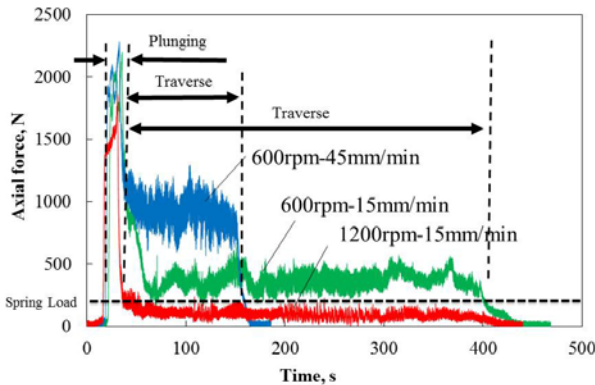


Fig.5 Axial force acting in the tool during the process.

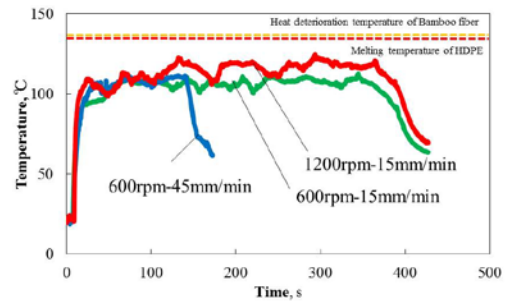


Fig.4 Temperature change during the process.

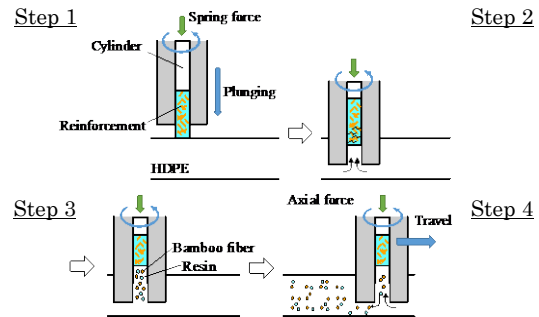


Fig.6 Schematic illustration of fabricating process of green composite by using friction stir process proposed in the present study.

Result and discussions

Figure 3 shows observation of cross section of the stir zone. According to the figures, the reinforcement was stirred into the matrix in all three conditions applied. According to observation of the stir zone from the top surface, bamboo fibers were oriented following rotation of the tool. Shape of the bamboo fiber bundle changed from 1200 to 350 μm in length and 350 to 15 μm in diameter by the stirring process. Figure 4 shows results of temperature measurement during the process. Temperature was measured by using a thermocouple attached inside the tool at 1 mm from tip of the tool. According to Fig. 4, the maximum temperatures measured in each condition were lower than the melting temperature of HDPE and also lower than the temperature inducing thermal degradation of mechanical property in bamboo fiber. Figure 5 shows change in axial force acting in the tool during the process. The axial force increased at the beginning of the process, then that decreased and reached to the constant value. The degradation of the axial force occurred due to softening and flowing of the material due to friction stirring. In Fig.5, spring force for pushing the reinforcement out is indicated as a dashed line. In case of that the friction stir process was carried out with condition of 1200 rpm - 15 mm/min, the axial force at the steady state was lower than the spring force. On the other hands, in other two conditions, the axial forces at the steady state were higher than the spring force. However, the reinforcement was pushed out from the tool into the matrix, even the axial force was higher than the spring force. According to the results shown in above, friction stir process conducted in the present study was considered as schematically shown in Fig. 6. The material was started to move by friction stirring and then flowed into the tool and broke the fiber. The fiber was flowed out from the tool and mixed in the matrix with traverse of the tool, then resulted in fabricating green composite.

Summary

Green composite of HDPE matrix and bamboo fiber reinforcement was successfully produced by the friction stir process proposed in the present study without pre-machining process. Bamboo fiber bundle was broken and mixed with the matrix by flowing of HDPE during the process. The maximum temperature observed during the process was lower than the melting temperature and the temperature inducing thermal degradation of mechanical property in bamboo fiber.

Reference

- [1] S. Ochi, H. Takagi and R. Niki, Mechanical Properties of Heat-Treated Natural Fibers, J. Soc. Mat. Sci., Japan, 51, 10 (2002) pp.1164-1168.

INFLUENCE OF GRAIN SIZE ON PROCESS AFFECTED ZONE IN MICRO PIERCING

Tomomi Shiratori^{1*}, Shizuka Nakano², Yohei Suzuki¹, Masahito Katoh²,
Naoko Sato², Takafumi Komatsu¹, Ming Yang³.

¹ Komatsuseiki Kosakusho Co. LTD., ² National Institute of Advanced Industrial Science and Technology,
³ Tokyo Metropolitan University

*shiratori@komatsuseiki.co.jp

Keywords: Piercing, Punching, Fine-grain, Sheared surface, EBSD

Control technologies of material grain size had been developed for austenitic stainless steel SUS304. It is well known that the material has a tendency to increase the tensile strength and decrease the elongation for smaller grain size. There have been a number of studies on micro piercing and basic stamping characteristics for austenitic stainless steel SUS304 with fine-grained micro structure [1,2]. There are few investigations on the correlation of stability of sheared surface and grain size in micro piercing [3]. We have been investigating that stability of starting point of fractured surface becoming smaller when choosing the average grain size of 3.0 μm [3]. However, the mechanism has not yet been elucidated. Purpose of this study is that understanding the effects of grain size on process affected zone from middle step of micro piercing.

To reveal phenomena, we selected the experimental conditions: punch diameter of $\phi 0.08\text{mm}$, material thickness of 0.10mm and as a result, aspect ratio of 1.25, clearance between punch and die are set by 2.5 μm , which is 2.5% of the material thickness. Average grain sizes of material are 7.5 μm for normal material, 1.5 μm and 3.0 μm for fine-grained material. Mechanical properties are shown in Table 1. Desk top stamping unit (SSI-01) is produced with BISAIKAKOH KENKYUSHO shown in figure 1 (a), and the motions are controlled by servo motor and the maximum stamping force is 10kN. Micro piercing die was produced for the experiment shown in Figure 1 (b). The die has a nano-meter accuracy stage embedded in under of the die tool. It is possible to control the relative position between punch and die in nano-meter scale to obtain concentric position. Process affected zones of middle step of micro holes were observed by FE-SEM and measured by EBSD (Electron Back Scattered Diffraction). EBSD investigation area of middle step of hole is 65 μm (x axis) and 120 μm (y axis) with 0.15 μm pitch analysis. Process affected zones are investigated by EBSD phase map and EBSD KAM (Kernel Average Misorientation) map.

Figure 2 shows the SEM BSE image of cross section of middle step of micro piercing. Process affected zones are presented along a line from punch edge to die edge for each material. Figure 3 (a) shows the EBSD Phase maps from grain sizes 1.5 μm to 7.5 μm . During micro piercing, austenitic stainless SUS304 is able to transform the phase to strain-induced martensitic. When transform is progressing, the phase changes from face-centered cubic (fcc, γ phase) to body-centered cubic (bcc, α phase). Martensitic phase in grain size 7.5 μm looks hackly and slanted to 45 degrees direction, long and wide grains are appeared. Slip line of 45 degrees direction is induced by shear strain. Martensitic phase in grain size 3.0 μm is smoother in comparison to grain size 7.5 μm . It is considered that grain size is strongly related to strain-induced martensitic transformation. Martensitic phase in grain size 1.5 μm is more expansive and smoother than grain size 3.0 μm . It relates tensile strength. When the grain size is smaller, strain-induced martensitic is becoming smooth and expand expansive. Figure 3 (b) shows the EBSD KAM map from grain size 1.5 μm to 7.5 μm . Misorientation angle is investigated in this map and this angle is known to correspond to plastic strain [4,5]. Misorientation angle 5 degrees area (Color : Red) for grain size 7.5 μm expand from punch edge to die edge. 45 degrees slip line and 5 degrees misorientaion areas are clearly correlated. It is said that misorientation angle 5 degrees area is related to local plastic strain. Misorientation angle 5 degrees area in grain size 3.0 μm looks more expansive than 7.5 μm . Misorientation angle 5 degrees area in grain size 1.5 μm is expender than 3.0 μm . Area for misorientation angle 5 degrees depends on grain size and tensile strength. If grain sizes are smaller, area for misorientation angle 5 degrees becomes more expansive with stronger tensile strength.

Investigated results show that the process affected zones in micro piercing of middle step of

piercing, strain-induced martensitic phase and misorientation angle are strongly related to grain size.

Table and Figure

Table 1 Characteristics of material

Grain Size [μm]	1.5	3.0	7.5
Tensile strength [MPa]	875	845	803
0.2%Proof stress [MPa]	599	504	433
Elongation [%]	45.8	49.5	56.6
<i>n</i> Value	0.31	0.37	0.43
Vickers hardness [HV]	261	227	191

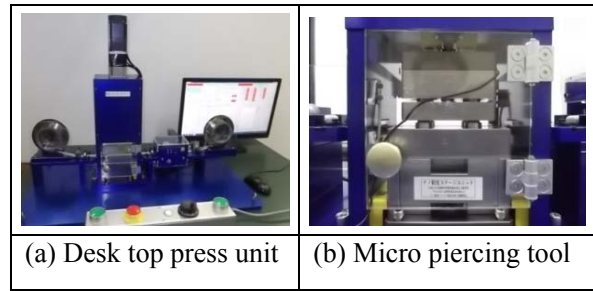


Figure 1 Experiment tools

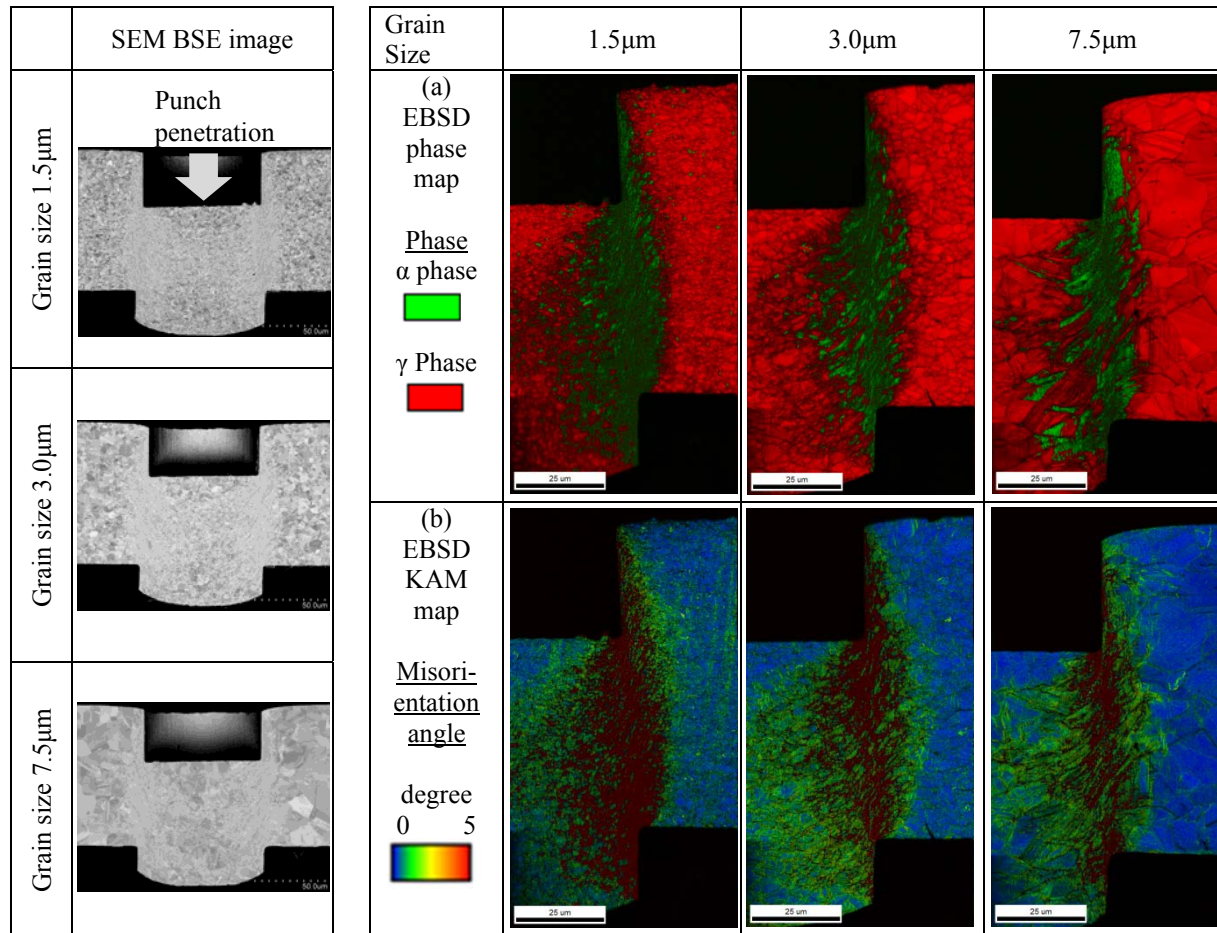


Figure 2 SEM BSE image

Figure 3 EBSD Phase map and KAM map

References

- [1] T. Komatsu, T. Matsumura & S. Torizuka, Effect of grain size in stainless steel on cutting performance in micro-scale cutting, *Int. J. Autom. Tech.*, 5-3(2011), pp. 334-341.
- [2] T. Komatsu, H. Kobayashi, S. Torizuka, & S. Nagayama, Micro hole piercing for ultra fine grained steel, *Int. J. Autom. Tech.*, 6-6(2011), pp. 802-808.
- [3] T. Shiratori, S. Nakano, Y. Suzuki, M. Katoh, M. Yang, T. Komatsu, Influence of grain size on sheared surface in micropiercing, *J. JSTP*, 56-652(2015), pp. 401-506
- [4] M. Kamaya, A. J. Wilkinson, J. M. Titchmarsh, Measurement of plastic strain of polycrystalline material by electron backscatter diffraction, *Nucl. Eng. Des.*, 235 (2005), pp. 713–725.
- [5] Masayuki Kamaya, Measurement of local plastic strain distribution of stainless steel by electron backscatter diffraction, *Materials characterization*, 60 (2009), pp. 125-132.

REPLICATION OF ANTIREFLECTION STRUCTURE FOR SOLAR CELLS BY LASER-ASSISTED IMPRINTING

Keisuke Nagato^{1,2*}, Yuki Yajima¹, Ken Takahashi¹, Tetsuya Hamaguchi¹, Masayuki Nakao¹

¹The University of Tokyo, ²JST PRESTO

*nagato@hnl.t.u-tokyo.ac.jp

Keywords: *Replication, Solar cells, Laser-assisted imprinting*

Nanoimprinting is a promising candidate, in which large-area polymer surfaces are replicated by using nanostructured mold with high throughput and low cost. However, in the conventional thermal nanoimprinting, entire of polymer and mold should be heated and cooled across the glass transition temperature of the polymer. Therefore, the cycle time is limited [1]. To date, we have proposed a laser-assisted replication technology as a breakthrough the cycle time limitation [2]. The laser is irradiated to the surface of the mold and only the surface of the polymer is heated and filled into the nanostructure of the mold, and then the replicated polymer is cooled by heat conduction to the inside of the mold and the polymer immediately after the laser irradiation.

The laser-assisted roller imprinting is applied to the roller imprint method [3]. A polymer film is pressed by a glass roller and a Ni roll mold. The laser is irradiated to the Ni mold surface through the glass roller and the polymer film. The surface of the mold is directly heated by the laser and the nanostructure is thermally replicated to the polymer surface. The laser is scanned onto the contacted area and the continuous replication of large-area polymer is performed.

On the other hand, the surface of solar cell reflects the light with Fresnel reflectance principle [4]. We propose that the light-incorporation efficiency is increased with covering a polymer film with an antireflection structure. The increase of efficiency leads to the enhancement of the actual generation efficiency.

A subwavelength-sized antireflection structure was replicated on a 75- μm -thick polymethylmethacrylate (PMMA) film by the laser-assisted roller imprinting. The Ni mold of the structure was fabricated by electroplating using an anodic-alumina nanohole array [5]. The average pitch and depth of the inverted-conical structure of Ni mold were about 150 and 300 nm, respectively. The image inserted in Fig. 1 shows a scanning electron microscopy (SEM) image of the replicated conical structure. We measured the reflectivity of the imprinted surface using a spectrophotometer (CM-2600d, Konica Minolta Sensing, Inc.). Figure 1 shows the reflectivities of the flat PMMA surface and the imprinted surface. The reflectivity of the imprinted surface, about 0.5%, was drastically lower than that of the flat surface, about 4%, over the entire range of visible wavelength.

The enhancement of solar cells using the antireflection-structured film was demonstrated. The solar cell used was LR0GC02 from Sharp Co. (40 \times 60 mm²). When measuring the property, the reverse side of the PMMA film was attached on the cell using glycerin with the same refractive index as PMMA (1.4–1.5). A fluorescent light, FL20SSW/18 from TOSHIBA CO., was set at 110 mm above the solar

cells. As shown in Fig. 2, the maximum generation power was increased for 4% when the antireflection-structured film was attached. This result can be simply discussed with the effect of the antireflection properties of the surface of the attached film. Because the antireflection structure has an advantage that the reflectivity is low throughout the various incident angle of the light, the attachment of the antireflection structure on solar cells leads to the enhancement of the power generation.

In summary, we demonstrated the replication of the antireflection structure on PMMA film using laser-assisted roller imprinting technique and enhancement of the power generation of solar cells. The increase, 4%, of the generation corresponded to the decrease of the reflectivity of the PMMA film. The laser-assisted roller imprinting is a promising method of the mass fabrication of antireflection film of solar cells because of the advantages of high throughput and large area.

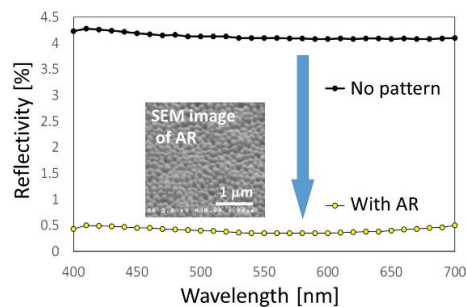


Figure 1. Reflectivity of flat and antireflection-structured PMMA films. Inserted figure shows a tilted-view SEM image of antireflection structure.

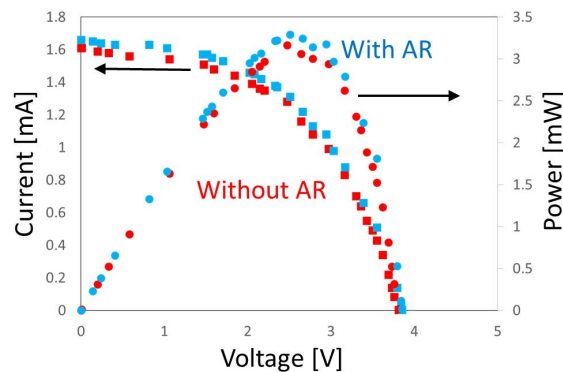


Figure 2. Current-voltage and power-voltage properties of solar cells covered by flat and antireflection-structured PMMA films.

References

- [1] K. Takahashi, K. Nagato, T. Hamaguchi, M. Nakao, High-speed replication of light-extraction structure with thermal roller nanoimprinting, *Microelectron. Eng.* in press.
- [2] K. Nagato, K. Takahashi, T. Sato, J. Choi, T. Hamaguchi, M. Nakao, Laser-assisted replication of large-area nanostructures, *J. Mater. Process. Technol.* 214 (2014), pp.2444-2449.
- [3] K. Nagato, K. Takahashi, M. Nakao, Thermal roller nanoimprinting –multilayered structures, laser-assisted replication–, 14th International Conference on Nanoimprint and Nanoprint Technology (NNT).
- [4] S.-J. Liu and C.-T. Liaw, Fast fabrication of nano-structured anti-reflection layers for enhancement of solar cells performance using plasma sputtering and infrared assisted roller embossing techniques, *Opt. Express* 20 (2012), pp. 5143-5150.
- [5] T. Yanagishita, K. Yasui, T. Kondo, Y. Kawaomoto, K. Nishio, H. Masuda, Antireflection polymer surface using anodic alumina molds with tapered holes, *Chem. Lett.* 36 (2007), pp.530-531.

SELECTIVE PATTERN-HARDENING OF AISI-SUS420/SUS430 MOLDS FOR MICRO-TEXTURING

Tatsuhiko Aizawa^{1*}, Istiroyah², Yoshio Sugita³

¹Shibaura Institute of Technology, ²Brawijaya University, ³YS-Electric Industry, Co. Ltd.

*taizawa@sic.shibaura-it.ac.jp.

Keywords: Micro-texturing, Plasma nitriding, Stainless steels, Solid solution hardening

INTRODUCTION

Micro-texturing has grown to be one of the most important die-and-mold technologies to improve the surface properties and functions of metallic and plastic products. The conventional micro-milling and micro-EDM [1, 2] require for huge amount of leading time to fabricate the micro-textured molds and dies. Non-traditional micro-texturing method is proposed with aid of the high density plasma nitriding process [3-5]. Its key principle in manufacturing lies in the selective pattern-hardening of molds, where the unprinted part of mold surface is selectively nitrided and hardened with other printed parts remaining un-nitrided. In the present study, this key technology is experimentally demonstrated by using the patterned AISI-SUS420 and SUS430 specimens. Their un-masked surfaces are nitrided to have the hardness higher than 1200 HV; while, the hardness of masked surfaces, which are not essentially nitrided, remain as they are before nitriding. Besides the hardness testing, SEM and EDX are utilized to discuss the relationship between the selective pattern-hardening and the inner nitriding process.

EXPERIMENTAL PROCEDURE

This plasma-nitriding assisted micro-texturing method consists of three processes as shown in Fig. 1. 1. At first, an original mask-pattern is printed on the surface of mold-die by using the dispenser. Selection of plastic primer inks to endure in the nitriding condition becomes essential to make micro-patterning onto the surface of tool steel and stainless steel substrates. In second, the substrate materials are plasma-nitrided to have sufficient hardness without change in the contents of chromium and iron elements and with less damage onto the substrate material surface. Finally, this nitrided surface is mechanically polished to remove the un-nitrided patterns and the residual inks and to form a negative micro-texture against the initially printed micro-pattern.

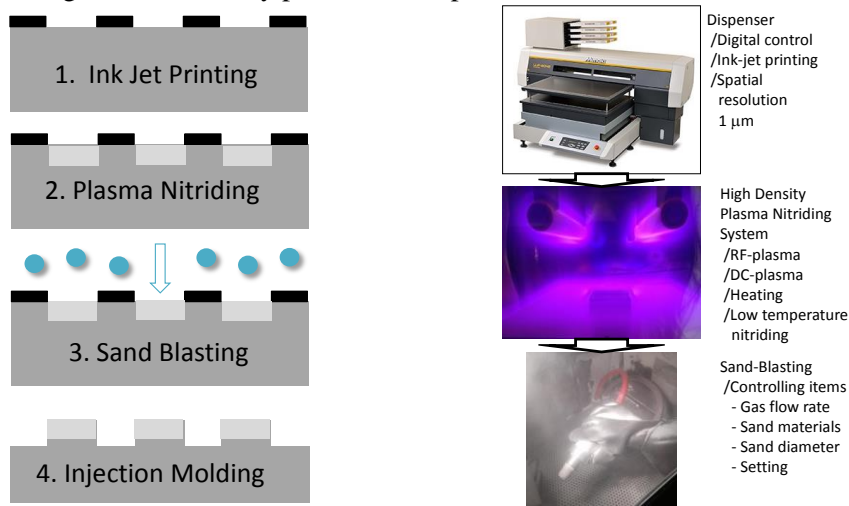


Fig. 1: Plasma nitriding assisted micro-texturing method.

EXPERIMENTAL RESULTS and DISCUSSION

In order to demonstrate that the original masking pattern should be homogeneously transformed into

the hardness profile pattern, a single square region was only left unprinted at the center of AISI-SUS420 type J2 specimen as shown in Figure 2 a). That is, the whole surface except for a square region at the center of specimen was printed as a mask. Figure 2b) compares the hardness profiles measured both in the lateral and longitudinal directions across the mask. The applied indentation load was constant, 1 N or 100 g in weight. Less significant difference was seen in both hardness profiles; i.e. the hardness in the un-masked regions is 1400 Hv, and, it remains to be 200 Hv in the masked region. The steep change of hardness across the edge of masks reveals that the unmasked regions are nitrided to have much higher hardness than matrix hardness of AISI-SUS420 stainless steels. On the other, the masked regions are free from infiltration of nitrogen atoms into matrix. Hence, the hardness map in the nitrided specimen corresponds to the masking pattern. Hence, the masked regions are easy to be removed and dug into the depth by the sand blasting; the un-masked regions have sufficient hardness not to be mechanically removed. Owing to this selective pattern hardening, the micro-textured AISI420/430 stainless steel molds are fabricated by the procedures in Fig. 1 even without use of mechanical milling or micro-EDM.

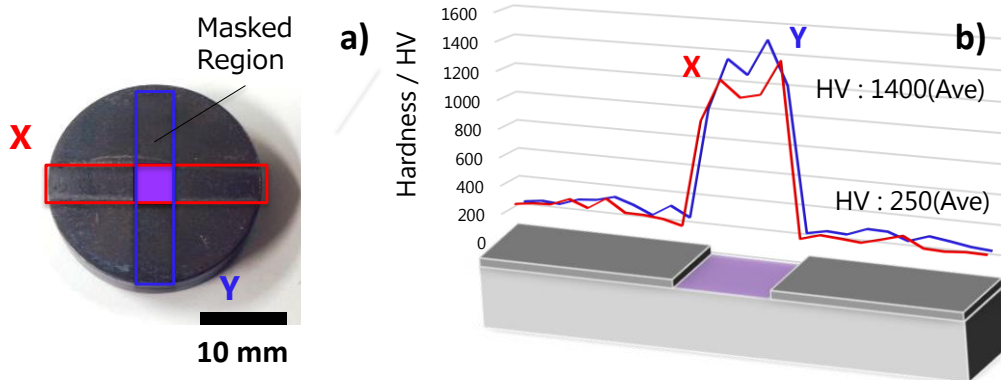


Fig. 2: Selective pattern hardening via the high density plasma nitriding onto the un-masked surfaces. a) Masked specimen, and, b) Hardness profile in the x- and y-directions on the specimen.

CONCLUSION

Non-traditional micro-texturing method is proposed to fabricate the micro-textured molds and dies for injection molding of micro-patterned plastic parts and for stamping to micro-patterned metallic parts. The final micro-patterns on the products are controllable by the initial CAD data for ink-jet printing onto the surface of stainless steel molds and dies. This initial micro-pattern is transformed by the low temperature plasma nitriding to the hardness profile. The patterned regions have lower hardness or nearly the same hardness of matrix. The bare surface except for this initial patterns has higher hardness than 1400 Hv. This hardness profile results in the micro-texturing by the sand-blasting. Then, the initial micro-pattern turns to be a micro-texture into the molds and dies.

References

- [1] B. Denkena, J. Koehler, J. Laestner, "Efficient machining of micro-dimples for friction reduction," Proc. 7th ICOMM, 2012; 85-89.
- [2] Y. Jiang, W.S. Zhao, X.M. Kang, L. Gu, "Adaptive control for micro-hole EDM process with wavelet transform detecting method," Proc. 6th ICOMM, 2011; 207-211.
- [3] T. Aizawa, T. Yamaguchi, "High-density plasma nitriding assisted micro-texturing onto martensitic stainless steel mold-die," Proc. IWMMF2014, 2014; 31-37.
- [4] T. Katoh, T. Aizawa, T. Yamaguchi, "Plasma assisted nitriding for micro-texturing onto martensitic stainless steels," Manufacturing Review. 2 (2015).
- [5] T. Aizawa, T. Yamaguchi, "Plasma nitriding assisted micro-texturing into martensitic stainless steel molds for injection molding," Proc. 4M/ICOMM (2015) 454-459.

EVALUATION OF MAGNETIZATION FOR CANTILEVER SAMPLE USING MEMS DEVICE

Takuya Maetani¹, Junpei Sakurai¹, Mizue Mizoshiri¹, Seiichi Hata^{1,*}

¹ Graduate School of Nagoya University, Japan

*Corresponding Author: hata@mech.nagoya-u.ac.jp

Keywords: MEMS, magnetic material, relative permeability, cantilever, combinatorial method

INTRODUCTION

The combinatorial method [1] is a useful method for the searching of the novel materials or optimize the composition of alloy materials. In this method, it is studied how to fabricate the library and how to evaluate the characteristics. The library that has different compositions or fabrication conditions could synthesize by using sputtering or laser molecular beam epitaxy with the moving masks to limit the deposition area. In the recent work, we proposed the Combinatorial New Facing Targets Sputtering and the Combinatorial Arc Plasma Deposition [2]. These thin film deposition methods could fabricate composition gradation library. There are several high throughput evaluation methods such as fatigue hydrogen storage characteristics [3].

Magnetostrictive materials have gained attention because of the features that are high power, fast response, and contactless actuation. Magnetostriction and relative permeability are important characteristics to determine the performance of the sensors and actuators with magnetostrictive materials. However, conventional evaluation method of the magnetostriction and relative permeability took a lot of time. In this research, we proposed the high throughput evaluation method of relative permeability using with the MEMS device.

FABRICATION PROCESS

The MEMS device for evaluation of relative permeability consists of the cantilever samples, vibrating electrode and pickup coil as shown in figure 1. The evaluation substrate has vibrating electrode and pickup coil. The sample substrate and the evaluation substrate are fabricated differently, and then bonded these two parts.

Figure 2 shows the fabricated evaluation substrate. The detail of the fabrication process is shown in figure 3. The fabrication process of evaluation substrate starts with cutting Si substrate in dimension of 30 mm × 30 mm. The Si substrates are ultrasonically rinsed with acetone, ethanol and DI water and baked on a hot plate. Then a bottom electrode layer of Au/Cr is sputtered on the patterned negative photoresist (ZPN-1150, Zeon Inc.) using RF magnetron sputtering machine. This is shown in figure 3(a). Next, lift-off process is done with acetone using an ultrasonic shaker for one minute. This is shown in figure 3(b). Next, polyimide based positive photoresist (PW-1500, Toray Industries Inc.) is patterned as an insulating layer. Then polyimide is nitride for the 340°C in the nitride atmosphere as shown in figure 3(c). Next, top electrodes of Au/Cr are sputtered on the patterned negative photoresist using RF magnetron sputtering machine. This is shown in figure 3(d). Next, lift-off process is done with acetone using an ultrasonic shaker for one minute. Then, acryl based negative photoresist (THB-151N, JSR Inc.) is patterned as the mold for the electroforming as shown in figure 3(e). Next, 25 μm thick Au is electroformed as shown in figure 3(f). The condition of current density is 0.8A/dm². Next, 5 μm thick In is electroformed as shown in figure 3(g). The condition of current density is same as Au electroforming. Finally, electroforming mold is removed using THB-S2 (JSR Inc.) on a hot plate (80 °C for 10 minutes) as shown in figure 3(h).

EXPEIMENT AND RESULT

To confirm the principle of measurement using evaluation substrate, magnetization of magnetic material is evaluated. Figure 4 shows the experimental setup. The sample is vibrated 20 μm amplitude by using a piezo actuator in the proximity of the pickup coil in static magnetic field, which is applied by using a Helmholtz coil. Then, induced electromotive force is produced to the pickup coil.

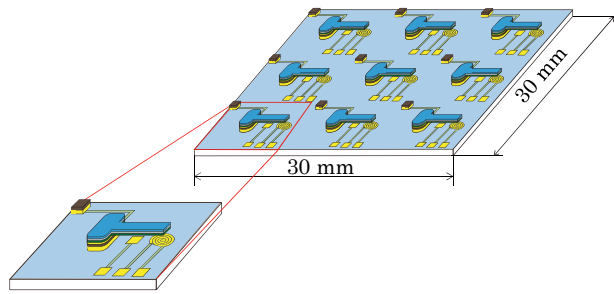


Figure 1. The overview of the device

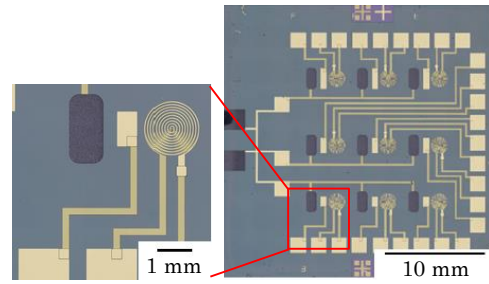


Figure 2. Photo of evaluation substrate

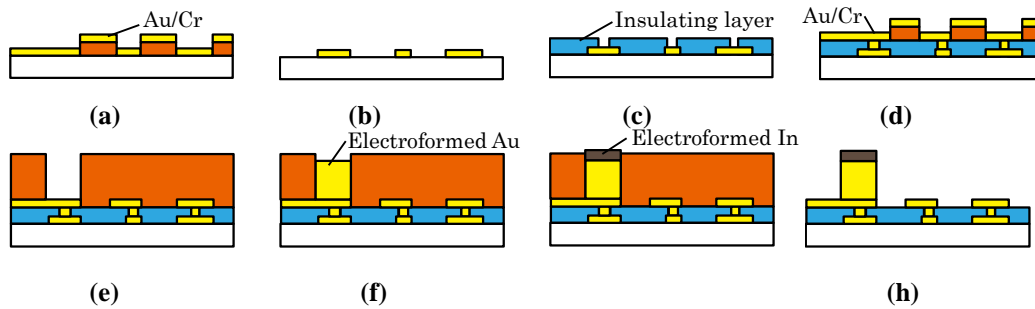


Figure 3. The fabrication step of evaluation substrate

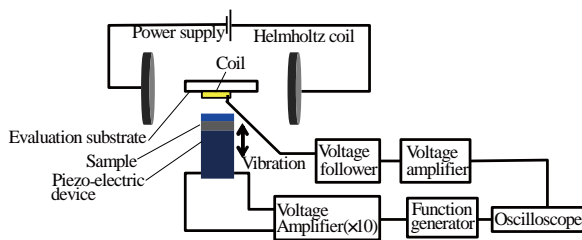


Figure 4. The experimental setup

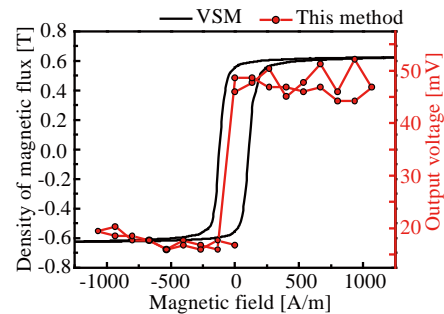


Figure 5. The magnetization curves measured by using with VSM and this method

To compare the measurement result of magnetization, evaluation substrate and vibrating sample magnetometer (VSM) were used. The evaluation sample ($\text{Fe}_{32.0}\text{Ni}_{55.3}\text{Cr}_{12.7}$) is fabricated by using New Facing Targets Sputtering on the $10\text{ mm} \times 10\text{ mm}$ glass substrate, then annealed at 773 K in the vacuum. Figure 5 shows the measurement result. The result of using evaluation substrate is similar to the result of using VSM. This result suggests the possibility of high throughput measurement for magnetism. However, it could not transfer the voltage to the magnetism in this method, it is necessary compared the output voltage to the reference material such as Ni.

CONCLUSIONS

In this research, the evaluation method of magnetism is studied. The evaluation substrate is fabricated successfully. The magnetization of $\text{Fe}_{32.0}\text{Ni}_{55.3}\text{Cr}_{12.7}$ was evaluated by using VSM, which is a conventional measurement method, and evaluation substrate. The magnetization curves measured by two methods are similar. There is possibility that this measurement method could apply to the combinatorial material searching method.

References

- [1] X.-D. Xiang, X. -D. Sun, G. Briceho, Y. Lou, K.-A Wang, H. Chang, W. G. Wallace Freedman, S.-W. Chen, P. G. Schultz, A Combinatorial Approach to Materials Discovery, *Science* 268 (1995), pp.1738-1740
- [2] S. Hata, R. Yamauchi, J. Sakurai and A. Shimokohbe, Combinatorial Arc Plasma Deposition of Thin Films, *Jpn. J. Appl. Phys.* 45 (2006), pp.2708-2713
- [3] A. Ludwig, J. Cao, A. Savan, M. Ehmman, High-throughput characterization of hydrogen storage materials using thin films on micromachined Si substrates, *J. Alloys and Compounds*, 446-447 (2007), pp.516-521

FABRICATION OF MICRO-CHANNEL FROM THE POWDER BY PULSE ELECTRIC CURRENT SINTERING METHOD AND MARKED GRAFITE DIE

Satoshi Kishimoto¹ and Yutaka Kagawa²

¹National Institute for Materials Science, ²National Institute for Materials Science

*KISHIMOTO.Satoshi@nims.go.jp

Keywords: *Spark plasma sintering method, micro-channel, micro-pattern, Ion milling, Low melting point glass.*

There are a lot of investigations to fabricate the micro-channel for sensors. To fabricate the micro-channel, the electron beam lithography [1], photo-lithography [2], micro-milling and nano-imprint [3] have been utilized. However, these methods need expensive equipment and long process. In this study, a rapid fabricating method using pulse electric current sintering (Spark plasma sintering: SPS) method has been developed.

One surface of a graphite punch (10mm diameter) was polished and patterns of micro-channel were fabricated on the polished surface by an ion milling. Using this punch, low melting point glass powder is sintered by SPS (Sumitomo, SPS-515). The surface of the punch with micro-channel and fabricated specimen was observed by a scanning electron microscope (SEM), and an optical micro-scope.

Figure 1 (a) shows a fabrication process of graphite punches by ion milling. A mask of same metal wires of 100micro-meter diameter is placed on the polished surface of graphite punch. Argon ion shower is exposed unto the mask. After removing the mask, micro-pattern is fabricated. Figure 1 (b) shows a substrate with micro pattern fabrication process, low melting point glass ($ZnO \cdot Bi_2O_3 \cdot B_2O_3$) and Al powder was sintered by pulsed electric current sintering (temperature: 460°C, holding time: 10 minutes).

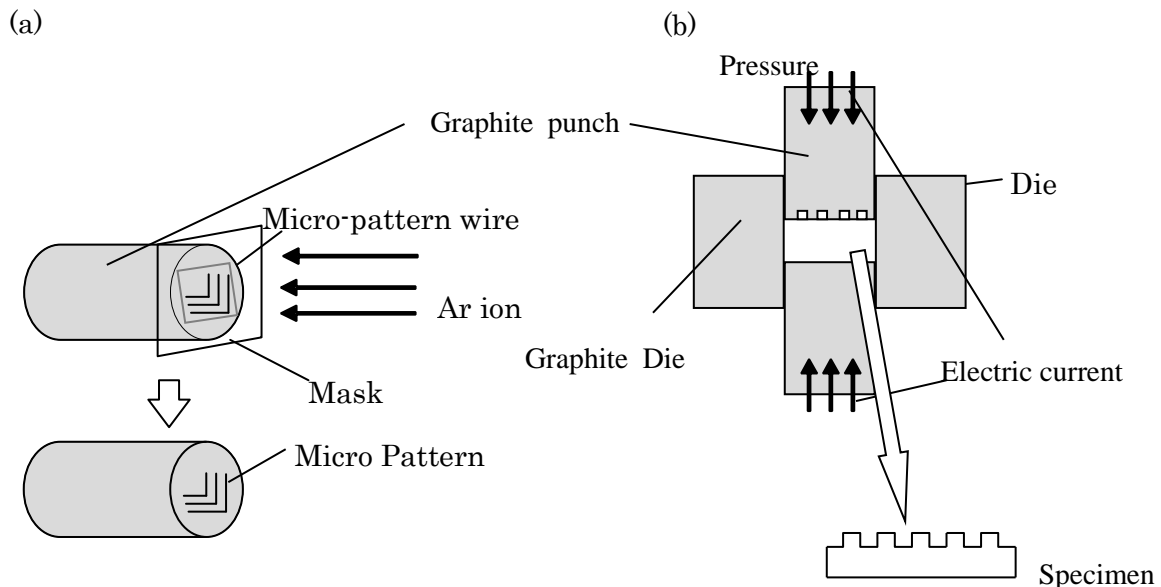


Figure 1 Micro-pattern fabrication process, (a): Graphite punch with micro-pattern fabrication process and (b): Substrate with micro-pattern fabrication process.

Figures 2 show the photographs of the scanning electron microscope images of graphite punch of lower magnification: (a) and the higher magnification: (b). Figures 3 show the photographs of the scanning electron microscope images of sintered low melting point glass surfaces. Figure 3 (a) shows a lower magnification image and (b) shows a higher magnification image. These photographs indicate a micro-cannel patterns with 100 micro meter width can be fabricated by this method.

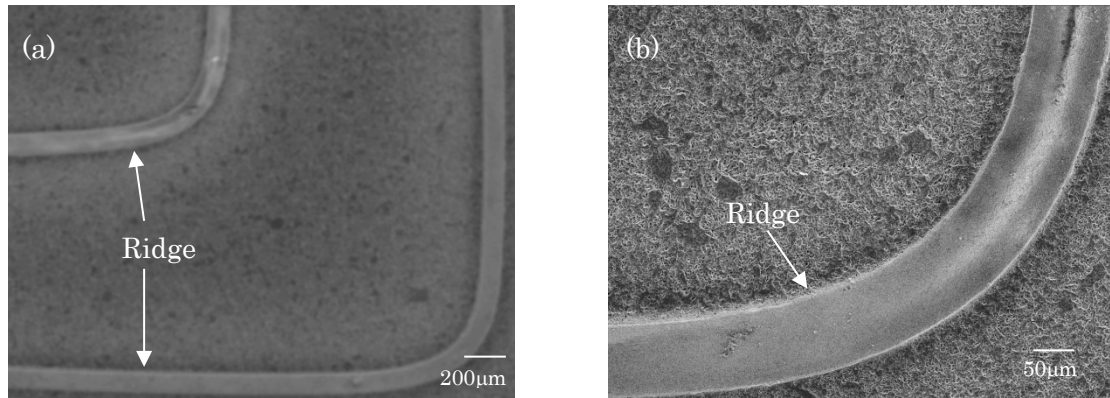


Figure 2 Scanning electron microscope images of graphite punch, (a) : lower magnification and (b) : higher magnification.

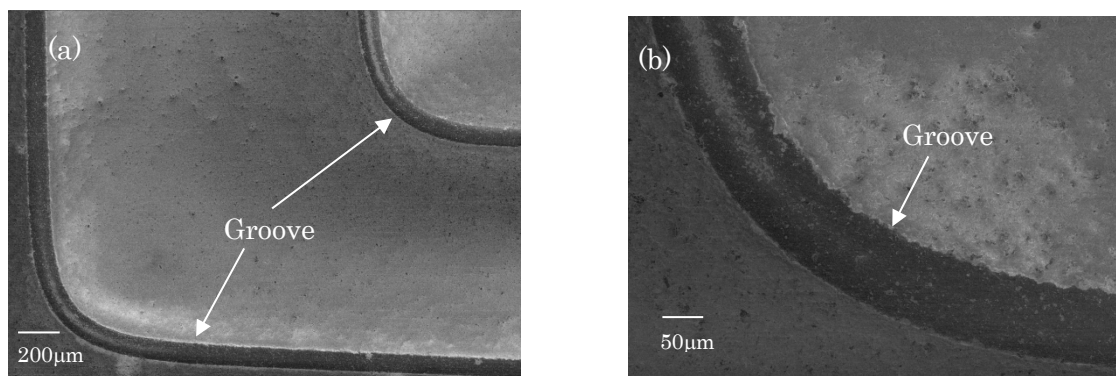


Figure 3 Scanning electron microscope image of sintered low melting point glass surface, (a) : lower magnification and (b) : higher magnification.

References

- [1] Kishimoto, S., Egashira, M., and Shinya, N., "Micro-creep deformation measurement by a Moiré method using electron beam lithography and electron beam scan", *Opt. Eng.*, Vol. 32, (1993), pp. 522-526.
- [2] Nam, Y., Kim, M. and Kim T., "Pneumatically controlled multi-level microchannel for separation and attraction of microparticles", *Sensors and Actuators B*, Vol. 190, (2014), pp. 86-92.
- [3] Tang, M. J., Xie, H. M., Zhu, J. G., Li, X.J., and Li, Y. J., "Study of moiré grating fabrication on metal samples using nanoimprint lithography", *Opt. Express.*, Vol. 20, (2012), pp. 2942-2955.

NUMERICAL STUDY ON EFFECTS OF MATERIAL INHOMOGENEITY AND DRAWING OF METAL FOILS

Tsuyoshi Furushima^{1*}, Kenta Takahashi¹, Ken-ichi Manabe¹

¹ Dept. Mechanical Engineering, Tokyo Metropolitan Univ., Japan

*furushima-tsuyoshi@tmu.ac.jp

Keywords: Material inhomogeneity, Micro deep drawing, Necking, Wrinkling

1. Introduction

Micro metal forming with metal foils has been focused on in technical applications such as electronic devices, medical equipment, sensor technologies, and optoelectronics. The miniaturization of components takes place problem of size effects due to grain size and surface roughness on inhomogeneous deformation. In particular, the surface roughening of metal foils may affect not only local problem such as accuracy of products and frictional condition but also global deformation behavior such as necking behavior [1]. Therefore, prediction of inhomogeneous deformation such as free surface roughening, friction and necking behaviors is very important in micro metal forming for metal foils with ultra thin thickness. From these backgrounds, we have proposed mesoscopical inhomogeneous finite element method considering mesoscopical material inhomogeneity for prediction of free surface roughening, necking and wrinkling in micro deep drawing process.

2. Mesoscopical inhomogeneous finite element method

In this model, grain size and variation in flow stress of each grain as aspect of mesoscopic material information were considered. A commercial FE code of LS-DYNA ver. 971 was used. **Figure 1** shows the mesoscopical inhomogeneous FE model of micro deep drawing. To model grain shape, Voronoi Tessellation was utilized in this model [2]. In the micro deep drawing, punch diameter of 944 μm and thickness of 50 μm are used. As boundary conditions of micro deep drawing, quarter model were given. For each grain, different flow stress was input. The modified Swift's flow stress equation as shown in Eq. (1) considering material inhomogeneous parameter α_i was used for each grain.

$$\sigma_{eq} = \alpha_i F(\varepsilon_0 + \varepsilon_{eq})^n \quad (i=1,2,\dots,k) \quad (1)$$

The probability distribution of the α_i value in the FE model is divided into k classes for mesoscopical inhomogeneous FE material modeling. In this model, the class k was 7. **Table 1** and **2** show the mechanical properties and α_i values and their standard deviations of blank used in this analysis. In this study, a homogeneous model and inhomogeneous models with grain size of 2, 10 and 20 μm were given to investigate the effects of inhomogeneity and grain size on micro deep drawability. In addition, the effects of drawing ratio DR=1.80, 1.91, 2.01 and 2.12 and blank holder force on micro deep drawability were investigated numerically.

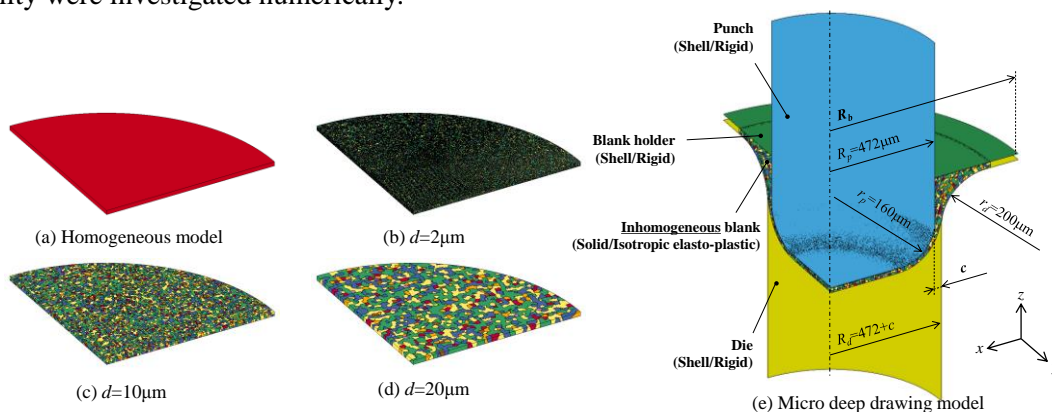


Figure 1 Mesoscopical inhomogeneous FE model of micro deep drawing.

Table 1 Mechanical properties of blank in FE analysis

's modulus E /GPa	Poisson's ratio ν	Yield stress σ_y /MPa	K -value K /MPa	n -value n	Initial equivalent strain ϵ_0
197	0.3	526	1570	0.29	0.03

Table 2 α -values and their standard deviations

	α_1	α_2	α_3	α_4	α_5	α_6	α_7	σ_α
Condition	0.7	0.8	0.9	1.0	1.1	1.2	1.3	0.11

3. Results and discussion

Figure 2 shows the comparison of strain distribution in thickness direction between homogeneous model and inhomogeneous model with grain size of 2 and 20 μ m under condition of DR=1.91 and BHF=48N. The necking did not occur under condition of grain size of 2 μ m and homogeneous model. However, the necking caused by local deformation occurs at cup radius under grain size of 20 μ m. **Figure 3** shows the effect of grain size on limiting drawing ratio (LDR) diagram obtained from various DR and BHF. As a result, it is found that the LDR and wrinkling limit decrease with increasing grain size. These tendency obtained from the inhomogeneous simulation are in good agreement with that of previous experiment [3]. From these results, we clarify the importance of the simulation considering material inhomogeneity in micro metal forming.

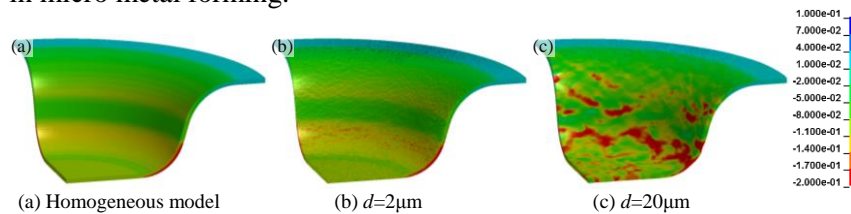


Figure 2 Comparison of strain distribution in thickness direction under fracture limit condition.

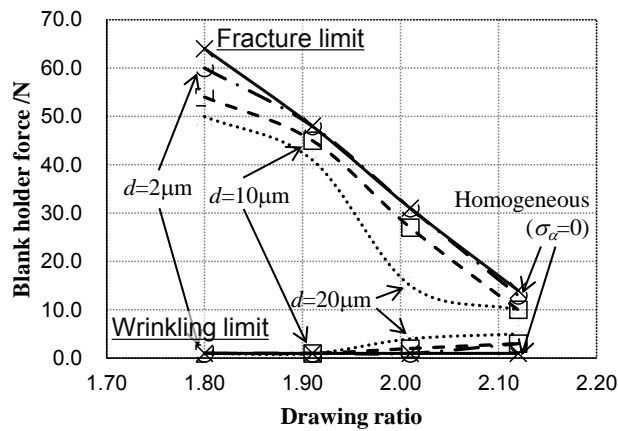


Figure 3 Effect of grain size on limiting drawing ratio (LDR) diagram obtained from various DR and BHF.

4. Conclusion

In this study, we have proposed mesoscopical inhomogeneous finite element method considering mesoscopical material inhomogeneity for prediction of free surface roughening, necking and wrinkling in micro deep drawing process. As a result, the LDR and wrinkling limit decrease with increasing grain size. Therefore, the importance of the simulation considering material inhomogeneity in micro metal forming was clarified.

References

- [1] T. Furushima, H. Tsunozaki, K. Manabe, S. Alexandrov, Ductile fracture and free surface roughening behaviors of pure copper foils for micro/meso-scale forming, *Int. J. Mach. Tools. Manuf.*, 76 (2014), pp. 34-48.
- [2] T. Furushima, K. Manabe, S. Alexandrov, Mesoscopical inhomogeneous material modeling for micro metal forming, *AIP Conf. Proc.*, 1618 (2014), pp. 331-334.
- [3] F. Vollertsen, Effect of the deep drawing diagram in micro forming, *Prod. Eng. Res. Devel.*, 6 (2012), pp11-18.

TECHNICAL MILESTONE TO APPLY SELF-HEALING CERAMICS

Wataru NAKAO^{1,2*}

¹Institute of Advanced Sciences, Yokohama National University, 79-5, Tokiwadai, Hodogaya-ku, Yokohama, 240-8501, Japan

² Faculty of Engineering, Yokohama National University

*wnakao@ynu.ac.jp

Keywords: *High Temperature, Structural Materials, Jet Engine, Ceramics based Composite, Car Engine*

Self-healing materials are designed by using novel structural material concept, in which the chemical reaction is exploited as a function like creature. The novel concept has received large interest; many researchers have made a large effort to develop the advanced self-healing materials, e.g., self-healing polymer [1], self-healing concrete [2], and self-healing alloys [3].

Fiber reinforced self-healing ceramic (shFRC) [4] is one of attractive self-healing materials and has been anticipated to be the candidate materials for turbine blade. As the turbine blades are employed in high temperatures from 600 °C to 1500 °C, the shFRCs should be developed by adjusting the chemical reaction to be suitable to the service conditions. Moreover, more complex structure compared with ordinary composites must be controlled to maximize the chemical reaction to the strength recovery effects. Therefore, the actualization of turbine blades using shFRC will not be attained without the adequate strategy to solve the retained technical issues.

Considering the situation, the present author established the roadmap including to the technical milestones, as shown in Fig.1, in which the technical readiness level [5] is employed as the vertical axis. The first stage is to actualize the concept of fiber-reinforced self-healing ceramics as the real material. Furthermore, in the stage, the development of the advanced shFRC which satisfied the required performances for the application, i.e., the material design concept of shFRC is established. The second stage is to summarize the process factors of shFRC which exhibit the excellent performance with small scatter. In order to reach the goal of the second stage, it is necessary to determine the basic processing of shFRC, and to investigate the shFRC performance with the variation of the processing parameters. The subsequent stages are evaluation the performance of the shFRC components, and to enhance the accuracy of the processing.

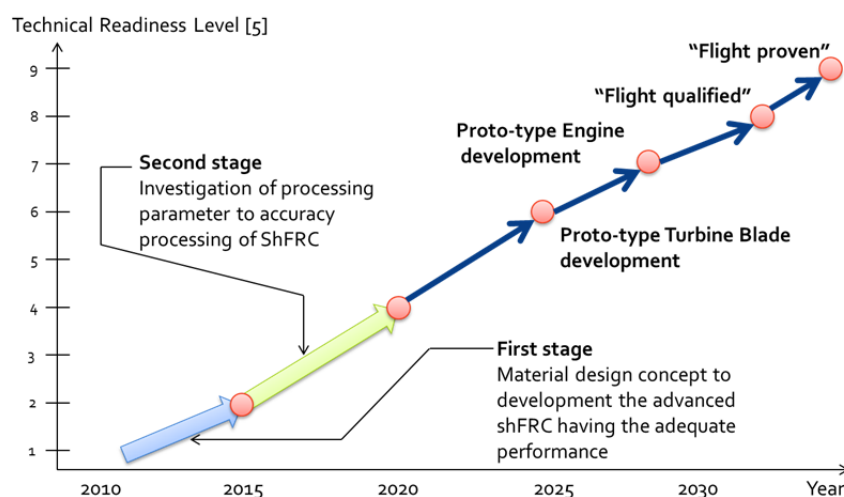


Figure 1 Technical readiness level roadmap of shFRC turbine blade for jet engines

Recently the present author and co-workers succeeded to the first milestone in the first stage, where the first mile stone was defined that the self-healing rate and high temperature strength are satisfied to the required performances of the middle pressure turbine blade used at temperatures from 1000 °C to

1200 °C. Some critical material design strategies to enhance self-healing ability and mechanical properties were found through the development of shFRC with the required performance. One of the strategies is employment of the heterogeneous interlayer. 50wt% TiSi₂-SiC heterogeneous interlayer leads to the adequate self-healing behavior, by which the developed shFRC can heal completely the introduced crack at 1000 °C for 10 min. The healing rate is superior to the every crack propagation except critical fracture expected in the middle pressure turbine application. Also it was found that pre-stressed fiber bundle coating enhances the total mechanical performance of shFRC, because the defects in fiber bundle became the critical fracture resource in the proto-type shFRC. Employing the process, the stiff interlayer, such as 50wt% TiSi₂-SiC heterogeneous interlayer, can be used. As a result, it was succeeded that the new type of shFRC having 7 times higher strength than that of proto-type shFRC was developed. As the strength is higher than the design stress of Ni superalloy turbine blade, the developed it is confirmed that the developed shFRC has the adequate performance to the middle pressure turbine blade.

References

- [1] S. R. White, N. R. Sottos, P. H. Geubelle, J. S. Moore, M. R. Kessler, S. R. Sriram, E. N. Brown and S. Viswanathan, Autonomic healing of polymer composite, *Nature*, 409 (2001), pp. 794-797.
- [2] A. García, E. Schlangen, M. Van De Ven, and D. Van Vliet, Induction heating of mastic containing conductive fibers and fillers, *Materials and Structures/Materiaux et Constructions*, 44[2], 2011, pp. 499-508.
- [3] S. M. He, N. H. van Dijk, M. Paladugu, H. Schut, J. Kohlbrecher, F. D. Tichelaar, and S. van der Zwaag, In situ determination of aging precipitation in deformed Fe-Cu and Fe-Cu-B-N alloys by time-resolved small-angle neutron scattering, *Physical Review B*, 82 (2010), pp.174111-174129
- [4] W. Nakao, D. Maruoka, S. Ozaki, M. Nanko, and T. Osada, Advanced Ceramic Composite Using Self-Healing and Fiber-Reinforcement, *Mechanical Properties and Performance of Engineering Ceramics and Composites IX*, (2015), pp. 187-193.
- [5] Department of Defence, Technology Readiness Assessment Deskbook, https://www.skatelescope.org/public/2011-11-18_WBS-SOW_Development_Reference_Documents/DoD_TRA_July_2009_Read_Version.pdf

BLANKING VIBRATION AND NOISE OF DIFFERENT TENSILE STRENGTH MATERIALS IN SCREW DRIVE SERVO PRESS BLANKING

Tomohiro MURAKAMI^{1,*}, Ming YANG²

¹Polytechnic University, ²Tokyo Metropolitan University

*murakami@uitech.ac.jp

Keywords: *tensile strength, blanking noise, break through, screw drive servo press*

1. INTRODUCTION

There is a noise reduction effect in low speed blanking by screw drive servo press, especially in low-strength metals [1]. But it is said that the noise reduction effect is not admitted by stainless steel and high tensile steel [2]. A blanking noise is occurred to blanking vibration [3]. And a blanking vibration is related to blanking tool life. Therefore it is necessary to grasp how the materials influences blanking noise and blanking vibration. In this study, we investigated the relationship between the tensile strength of materials, the noise and blanking vibration, in screw drive servo press blanking.

2. Experimental procedure

We used a screw drive servo press (KOMATSU HCP3000: 800kN) in this experiment. The size of blanking is 40mm×40mm, Corner radius is 1mm, and die clearance is 5% to the thickness of 1mm. We defined the blanking speed as the punch speed just before breaking. Under the blanking speed $V=15\text{mm/s}$ as the usual blanking speed and $V=0.5\text{mm/s}$ as the low-speed blanking, we compared copper (C1100), mild steel (SPC), stainless steel (SUS304) and high tensile steel (SPFC). Specimen's thickness is 1mm and the size is 80mm×80mm. Blanking noise and the location of the punch was measured by measurement devices indicated in **Figure 1**.

3. Results

Figure 2 indicates the tensile strength and the breaking load at the blanking. The Breaking load is proportional to the tensile strength. **Figure 3** indicates the location of the punch and the sound pressure when blanking SPC. t_2 is the breaking time. The distance of p_2 - p_3 is the break through distance.

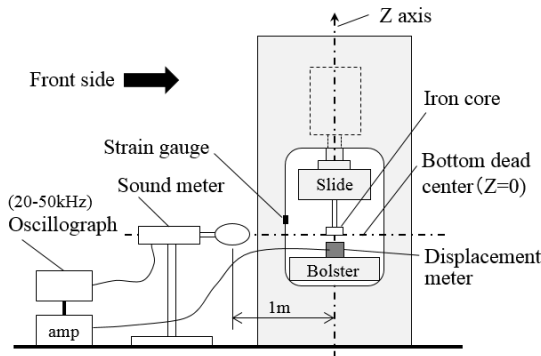


Figure 1: Position of measurement devices

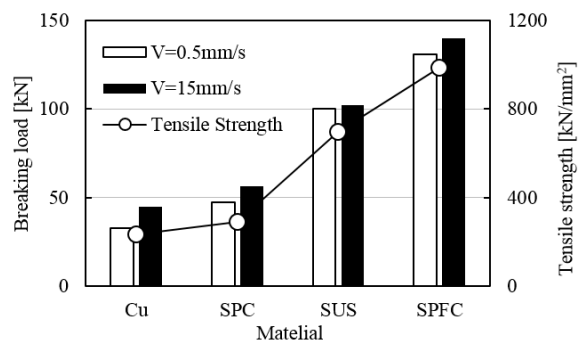


Figure 2: Breaking load in the Blanking

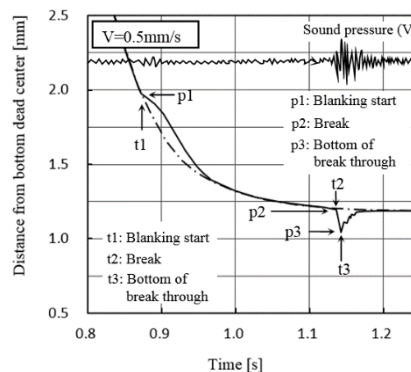
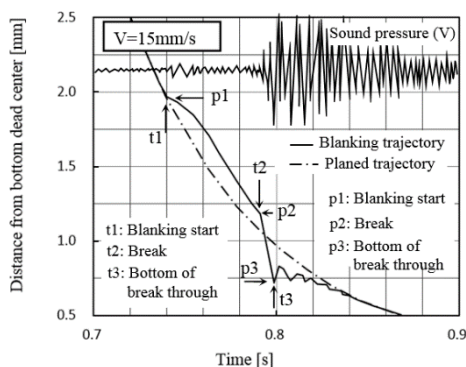


Figure 3: Punch trajectory and Sound pressure in the blanking speed $V=15\text{mm/s}$ and $V=0.5\text{mm/s}$

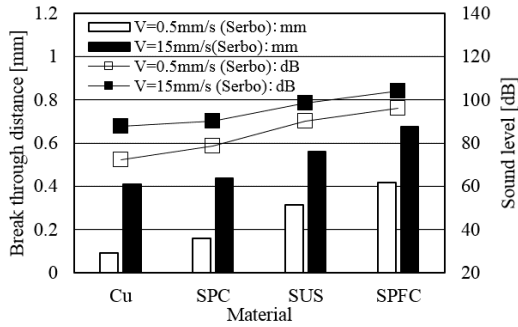


Figure 4: Break through distance and Sound level

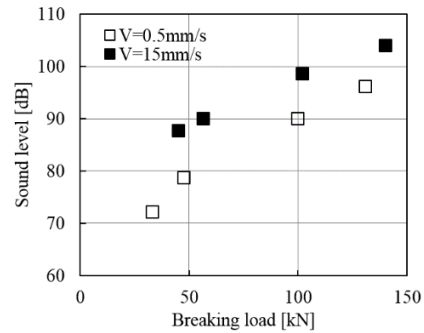


Figure 5: Relation between breaking load and Sound level

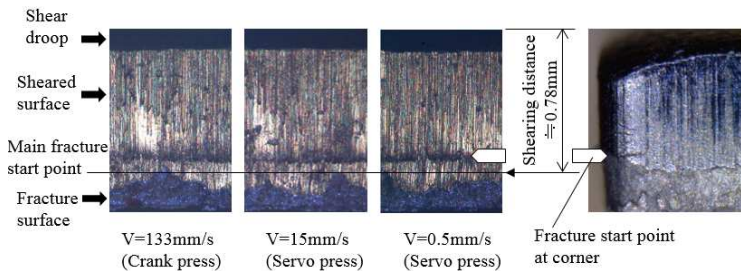


Figure 6: Sheared edge of SPC

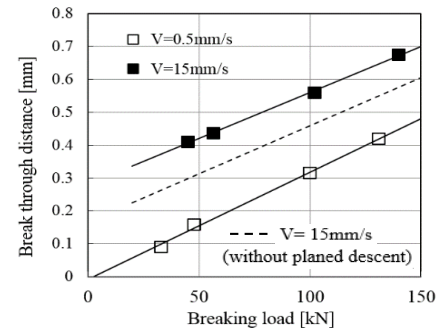


Figure 7: Relation between breaking load and Break through distance

From Figure 3, we can confirm that the blanking noise was caused by break through. **Figure 4** indicates the break through distance and the sound level. Both the break through distance and the sound level are big at V=15mm/s. The break through distance is proportional to the material strength. And the sound level is proportional to the break through distance. The correlation coefficient of the break through distance and the sound level is 0.95.

4. Consideration

Figure 5 indicates a relation between the breaking load and the sound level in blanking. The sound level is proportional to the breaking load. But the sound level of V=15mm/s was bigger than V=0.5mm/s. As shown in **Figure 6**, in spite of different blanking speed and different breaking load, the shearing distance of SPC were almost same 0.78mm. It was the same with the other materials. It suggests that a factor besides the breaking load influences blanking noise. **Figure 7** indicates a relation between the blanking load and the break through distance. Even if the breaking load decreases, a line of V=15 mm/s doesn't pass 0mm. The difference between the line of V=15 mm/s and the line of V=0.5mm/s is more than 0.2 mm. In the break through distance, press slide is descended along planned trajectory. We call it "planned descent". Planned descent is the descent distance between t₂-t₃ in a planned trajectory on figure 3. The broken line on figure 7 indicates the figure which deducted plan descent from the line of V=15 mm/s. We considered that unknown factor hides in blanking vibration of V=15 mm/s. And the break through distance of V=15mm/s became big by this unknown factor. As shown in **Figure 3**, before deviation of punch position is canceled, breaking of V=15 mm/s has occurred. Therefore we're inferring that this unknown factor is related to control-system of screw drive servo press.

5. Conclusion

We confirmed that the breaking load is proportional to the tensile strength of materials, and the break through distance is proportional to the breaking load. And we confirmed that the blanking noise was caused by break through. But, in spite of the same breaking load, the sound level and the break through distance of V=15mm/s was bigger than V=0.5mm/s. It suggests that unknown factor hides in blanking vibration. We're inferring that this unknown factor is related to control-system of servo press.

References

- [1] Chieko Yamagata, Masaaki Otsu, Kouzou Osakada, JSTM spring meet of 2002, (2002), pp.161-162.
- [2] Tomohiro Murakami, Press Technology, vol41-4 (2003), pp. 28-33.
- [3] Kazuki Aoi, Journal of JSTM, vol22-251 (1981), pp. 1188-1193.

BEHAVIOR OF ASYMMETRIC DEFORMATION OF ROD IN LOCALLY-LATERAL UPSETTING

Takashi Nomura¹, Nguyen Sinh Con¹, Kazuhito Asai¹, Kazuhiko Kitamura^{1*}

¹Nagoya Institute of technology

*Corresponding. kitamura.kazuhiko@nitech.ac.jp

Keywords: *Lateral upsetting, Material flow, Tooling, Asymmetry*

1. Introduction

Remarkable progress in cold forging has recently brought manufacture of various products with an asymmetric and complicated shape. To achieve higher accuracy of these products efficiently, appropriate preforms at a previous step are required in multiple-step cold forging. Ishikawa et al.¹⁾ has proposed how to make an asymmetric product using synchronized a motion of servo-press with a robot handling a billet. Kuboki et al.²⁾ has bended a band in plain by incremental stamping using a flexibly inclined and triangle punch. In both sophisticated methods, lower forming load using a simpler shaped tool extremely contributes to economic manufacturing. In this paper, a punch with appropriate nose shape and punch arrangement are investigated experimentally and numerically to promote asymmetric material flowing under lower forming load in locally-lateral upsetting of a bar.

2. Lateral upsetting outlines

Figure 1 shows the diagram of the locally-lateral upsetting. In this test, a punch compressed the intermediate position of a round billet. This billet is set to 0°, 15°, 30°, 45° of the angle between the billet axis and the punch width direction.

Material of a punch and a die is die steel for cold forging (quenched and tempered, 60 HRC). This punch has a cylindrical nose with the thicknesses of 6, 8, and 12 mm and the nose radii of 3, 4, and 6 mm, respectively. The width of the punch is 50 mm. The punch is finished by lapping and the surface roughness is 0.2 μm Rz. Compression ratios are 20%, 30%, 40%, and 50%. The stroke is 10 mm when the compression ratio is 50%.

The punch pushes the billet at a speed of 1.0 mm/s using a hydronic press that is supported with four rigid columns. Compression load measured load cell of a back punch.

The billet material is 99.7% aluminum as annealed. The billet has diameter of 20 mm and length of 40 mm. It has a yield point of 45 [MPa] and the yield stress can be approximated by $Y = 115\varepsilon^{0.26}$ [MPa] ($0.1 \leq \varepsilon \leq 0.7$). Lubrication used beef fat (75%) and graphite (25%). The coulomb's frictional coefficient μ of 0.06 were measured by ring compression test under the lubricated condition.

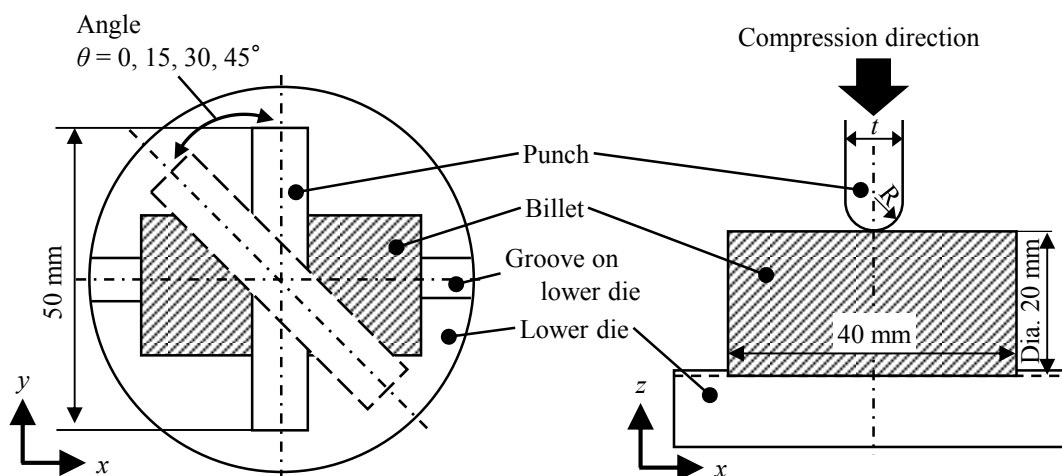


Figure 1 The diagram of the locally-lateral upsetting.

In this test, the billet end surfaces are shifted in the y -axis direction. This shift ratio S_y is calculated y -distance y_d is divided by 20 mm of initial diameter. The shift ratio S_y as meant asymmetry after forging is estimated by measuring the shift distance of the billet after the test.

3. The punch-setting angle θ and billet on locally-lateral upsetting

This test was investigated the influence on the material behavior by angles. The billet axis was x -axis, and vertex axis of the punch was y -axis. A punch used 8 mm of thickness and 4 mm of nose radius. **Figure 2(a)** shows shift ratio by punch-setting angle θ and stroke. $\theta = 0^\circ$ didn't shift of any stroke. $\theta = 15^\circ$ and 30° , the shift ratio was increased gradually with increasing stroke. When stroke is 10 mm, shift ratio is 4 and 10%, respectively. When θ is 45° and 4 mm stroke, shift ratio reached 5%. Furthermore, when it pushed punch, rapidly shift ratio is increased. When the stroke is 10 mm, shift ratio reached 29%. As the result, larger punch-setting angle θ is effective in shifting the both end of the billet. The material can flow to the punch thickness direction when the punch-setting angle θ increases.

When punch-setting angle θ is 45° , it was investigated the influence on the material behavior to the different radii of curvature. The punch thicknesses used 6, 8 and 12 mm and nose radii of 3, 4 and 6 mm, respectively. **Figure 2(b)** shows the shift ratio by different punch thickness and stroke. The shift ratio indicates until stroke is 5 mm. The shift ratio was 15% at the stroke 10 mm when the punch-nose radius. The shift ratio is large without regard to stroke when the punch with nose radius of 6 mm is used. Finally, the shift ratio reaches 36% at stroke 10 mm. As these results, the shift ratio S_y can increase when the larger punch-nose radius and the larger punch-setting angle θ is used. Thus, the asymmetric pre-form can be obtained in the locally-lateral rod upsetting by these simple punches.

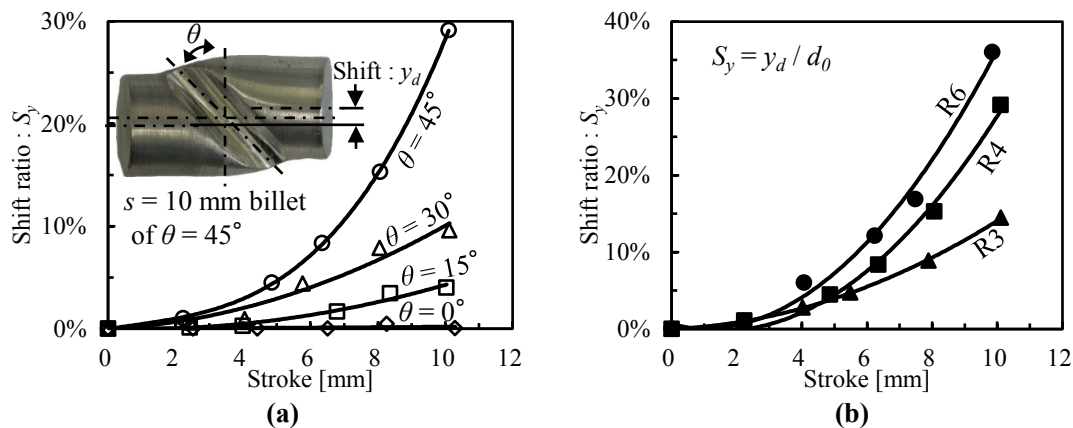


Figure 2 Shift ratios after tests. (a) Different the punch-setting angle θ in the punch thickness of 8 mm. (b) Different radii of curvature in the punch-setting angle $\theta = 45^\circ$.

4. Conclusion

Influence of the punch-nose radius and the punch-setting angle on the behavior of asymmetric deformation of rod was experimentally investigated in locally-lateral upsetting of the rod. The following results were obtained:

- 1) The shift ratio S_y of the asymmetric pre-form increased with punch-setting angle increasing. The maximum S_y reached 29% when the compression ratio was 50% using the cylindrical punch with the punch-setting angle of 45° .
- 2) The shift ratio S_y of the asymmetric pre-form increased with the punch-nose radius increasing. The maximum S_y reached 36% when the compression ratio was 50% using the cylindrical punch with the punch-nose radius of 6 mm.

References

- [1] Takashi Ishikawa, Wang Xin-yun, Nobuki Yukawa, Yoshinori Yoshida, Takuya Sukeda, Incremental forming using servo-press and robot, Proc. 5th JSTP-ISPF, (2009), pp. 41-46.
- [2] Takashi Kuboki, Armad Azrie, Yingjun Jin, A new incremental in-plane bending of thin sheet metals for micro machine components by using a tiltable punch, CIRP, Manufacturing Technology, 63(2014), pp. 249-252.

DIRECT MEASUREMENT OF FRICTION FORCE DURING FORMING

Takehiko Makino^{1*}, Yuya Yogo², Toshinari Michimoto², Yohei Takamori²

¹ Department of Mechanical Engineering,

Nagoya Institute of Technology, Gokiso-cho, Showa-ku, Nagoya, 466-8555 Japan

² Nagoya Institute of Technology, Gokiso-cho, Showa-ku, Nagoya, 466-8555 Japan

* makino.takehiko@nitech.ac.jp

Keywords: *Forming, Friction force, Direct measurement, Laser reflection*

Abstract

Information about distribution and change in friction during forming is required to construct a prediction model. The small deflection of a thin part fabricated at the other side of a flat tool surface is detected using laser reflection to decompose the normal and horizontal (frictional) forces. The locus of laser reflection on a detector showed both components. The values estimated from the locus were fairly close to the measured forces.

Introduction

The forming process, especially small-scale forging [1], is strongly affected by friction between the tool and material. Usually, the friction state is estimated by comparing the results of the load required to perform the forming process and the load calculated by the finite element method with constant friction coefficients. The information about distribution and change in friction during forming is required to construct a prediction model. Various methods for direct measurement of friction force during forming have been reported. The pressure-pin method [2] detects the friction force using an inclined pin placed in the cavity of the tool. In this method, the material tends to occupy the cavity, and the friction force between the pin and tool cavity (commonly unknown) must be subtracted from the measured force. In the friction sensor method [3], the deflection of a thin part of the tool surface is measured by the strain gauges attached to the flat plate connected to the thin part. However, the thin part of this method becomes relatively large in area because the deflection is still detected by the strain gauges. The objective of the present study is to develop a method for direct friction force measurement during small-scale forming using laser reflection.

Apparatus and method

In the proposed method, a small thin part (diameter: 2.0 mm, thickness: 0.42 mm) with a protrusion was fabricated at the other side of a flat tool surface by electric discharge machining. The small deflection of the thin part during forming is detected by two laser beams reflected by two mirrors attached to the pin glued to the protrusion, as shown in **Figure 1**. The loci of the laser enlarged by the optical lever were detected by two position sensitive detectors (PSDs, Hamamatsu Photonics S5990-01) placed at both sides of the tool. The calibrations for each direction are performed using the two-axis press designed for this study (**Figure 2**). For calibration, the small pin (diameter: 2.0 mm, height: 3.2 mm, material: SKH) is placed on the thin part and compressed and tensioned simultaneously by the vertical and horizontal presses, respectively, as shown in **Figure 3**.

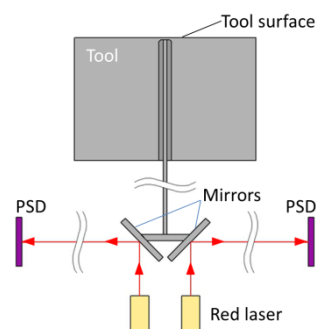


Figure 1 Principle of direct friction measurement.

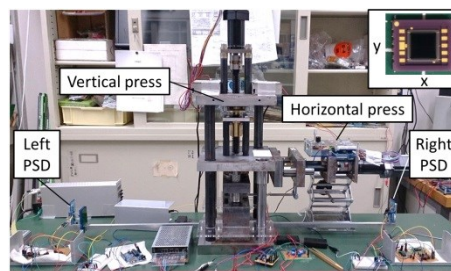


Figure 2 Two-axis press and two PSDs.

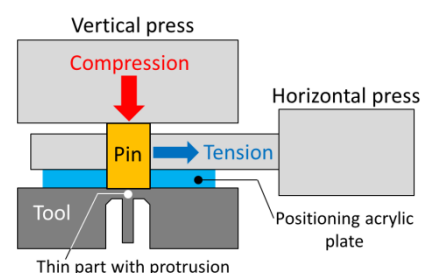


Figure 3 Schema of the calibration.

Results

Figure 4 shows the results of the calibration (1) with loading normal and horizontal forces applied separately. In this case, (a) after the normal force reached the maximum value of 400 N, (b) the horizontal force is applied while retaining the normal force. After the horizontal force reached the predetermined value of 100 N, the horizontal force is released. The horizontal axis scale (time) for (a) and (b) is the same. After the horizontal force becomes zero, the normal force is released. Fig. 4 (c) shows that the locus on the left PSD moves in an upper-right direction from the origin (indicated by “O” in the figure) and then turns almost 90° to a lower-right direction at “P.” This movement corresponds to the sequence of loading until the horizontal force reaches the predetermined value. During unloading, the locus retraces the route conversely. Fig. 4 (d) indicates that the locus on the right PSD moves from the origin to the lower-left. However, the loci due to the normal and horizontal forces overlap each other.

Figure 5 shows the results of the calibration (2) with loading normal and horizontal forces applied simultaneously. In this case, as the normal force increases, the horizontal force is applied. In Fig. 5 (c), the turning appears at “P” when the horizontal force is applied. While the horizontal force is at a constant value, the displacement in the locus due to the horizontal force continues.

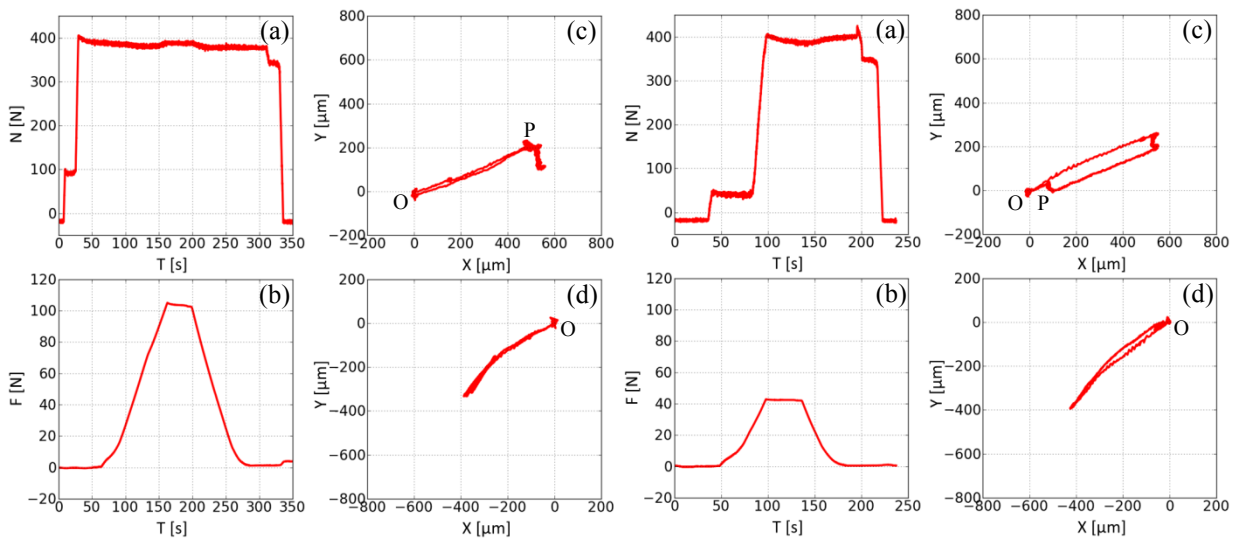


Figure 4 Results of the calibration (1). (a) Normal force, (b) horizontal force, (c) locus on the left PSD, (d) locus on the right PSD.

Figure 5 Results of the calibration (2). (a) Normal force, (b) horizontal force, (c) locus on the left PSD, (d) locus on the right PSD.

Discussion

Logically speaking, the normal and horizontal forces need to be decomposed by the vertical loci of the laser using two PSDs. However, the locus on the left PSD represents both components that can be decomposed. Analysis of Fig. 5 (c) showed that the normal and horizontal forces estimated from the locus (35 N and 311 N) were fairly close to the measured forces (36 N and 279 N, respectively).

Conclusion

The direct friction force measurement apparatus developed in this study decomposes the normal and friction forces applied at a flat tool surface.

Acknowledgement

This work was supported by JSPS KAKENHI Grant Number 24560130.

References

- [1] Makino, T., Dohda, K., Ishitani, A., Zhang, H., “Anisotropy of plastic deformation in micro/meso-scale metal forming -development of testing method”, Transactions of NAMRI/SME, 37(2009), pp. 330-340.
- [2] Van Rooyen, G. T., Backofen, W. A., “Friction in cold rolling”, Journal of the Iron and Steel Institute, 186 (1957), pp. 235-244.
- [3] Yoneyama, T., Takahashi, M., “Development of a Friction Sensor and Measurement in Aluminum Hot Extrusion”, Journal of Japan Society for Technology of Plasticity, 521(2004), pp. 82-470.

MEASUREMENT OF TOOL TEMPERATURE IN BURNISHING USING DIAMOND TIP

Masato Okada^{1*}, Masayoshi Shinya², Hidetake Tanaka³, Naoki Asakawa⁴, Masaaki Otsu¹

¹ University of Fukui, ²Graduate School of Natural Science and Technology, Kanazawa University

³Sophia University, ⁴ Kanazawa University

*Corresponding author: okada_m@u-fukui.ac.jp

Keywords: Surface finishing, Burnishing, Diamond tipped tool, Tool temperature, Two-color pyrometer

Introduction

Diamond burnishing is a micro-plastic forming method which uses a diamond-tipped tool to generate smooth surfaces and work-hardened layers [1]. It offers a high level of processing efficiency relative to grinding and does not require dedicated equipment because it can be performed using the same machine tools as those that are commonly used for cutting. In diamond burnishing, the tool temperature at the burnishing point is an important factor determining the degree of diamond tip wear and the target surface quality. With the burnishing process, however, it is difficult to measure the tool temperature because the amount of heat and the size of the heated portion are very small. Furthermore, because the diamond tip is an electrical insulator, a tool-work thermocouple configuration cannot be applied. To overcome this, a method of measuring the temperature of the diamond burnishing tool using a two-color pyrometer with an optical fiber is proposed. In addition, the influence of the burnishing conditions on tool temperature is investigated.

Experimental method and conditions The setup for measuring the tool temperature is shown in Fig. 1. The inner circumferential surface of the cylindrical workpiece, rotated by the main spindle of the lathe, was targeted. The tool temperature was measured using a two-color pyrometer with an optical fiber, developed by the authors. This pyrometer offers a high response speed and a small measurement area under non-contact conditions and eliminates the influence of the emissivity of the target by using the ratio of the output voltages from two different infrared detectors [2]. The infrared rays emitted from the burnishing point of the diamond tip are accepted by the rotated probe, a small stainless tube housing an optical fiber, which is fixed to the workpiece in the radial direction. The collected rays are transmitted to the other optical fiber, attached to the pyrometer, through a non-contact coupling. Thus, the infrared rays are transmitted to the pyrometer at that instant when the burnishing point, the rotated probe, and the optical fiber attached to the pyrometer are all aligned on the same axis. An accelerometer was mounted on the shank of the burnishing tool to detect the micro vibrations caused by the diamond tip passing the rotated probe. The experimental conditions are listed in Table 1.

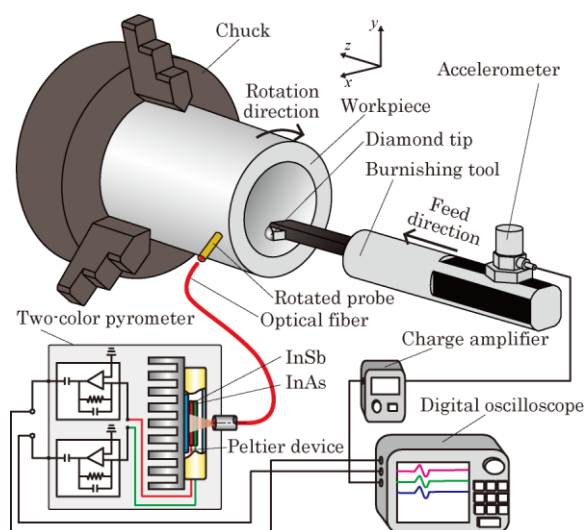


Fig. 1 Experimental setup

Table 1 Experimental conditions

Tool	Diamond tipped tool DT2D1, Sugino Machine Ltd.
Workpiece	Hardened stainless steel JIS SUS420J2 53HRC Ra = approx. 1.0 μ m
Burnishing speed	$v_b = 100, 150, 200$ m/min
Thrust force	$F_t = 90, 140, 180$ N
Feed rate	$f = 50$ μ m/rev
Lubrication	Dry

Experimental results and discussions In a case of the using a new tip, as shown in Fig. 2 (a), the output voltage from the pyrometer, for which the lower-limit measurable temperature is approximately 150°C, was not observed even when $v_b = 200$ m/min and $F_t = 180$ N. Subsequently, the output was observed in accordance with the increase in the burnishing length, and the output waveforms from the two-color detector, shown in Figs. 3 (a) and (b), were obtained when the tip wore as shown in Fig. 2 (b). Thus, the tool was at a low temperature of 150°C or less in the primary stage, but the tool temperature increased with the tool wear. Fig. 3 (c) also shows the output from the accelerometer. Given the output from the accelerometer, it can be assumed that the burnishing point passes the rotated probe at approximately $\tau = 4.5 - 12$ s. The temperature during this period is shown in Fig. 3 (d). The tool temperature ranged from approximately 235°C to 305°C. It can be assumed that this distribution occurred as a result of the slight change in the actual tool temperature during each revolution and the change in the sliding condition as the diamond tip passes the stainless tube.

Figures 4 (a) and (b) show the influence of the thrust force and burnishing speed on the tool temperature. The tool temperature was defined as the mean value of the five maximum temperatures under each condition. These measured values were obtained when the tool wore as shown in Fig. 2 (b). The tool temperature increased with an increase in the burnishing speed and thrust force, and the strong influence of these burnishing conditions on the tool temperature was observed.

Conclusions The infrared energy radiating from the contact area between the diamond tip and workpiece can be obtained by fixing the optical fiber in the rotated probe. The tool temperature during burnishing, which increases with the tool wear, can be measured by using the proposed method. Moreover, it can be concluded that the burnishing speed and thrust force greatly influence the tool temperature, and these results show that it is important to take the thermal effect on burnishing characteristics into consideration.

Acknowledgements The authors acknowledge the financial support for this study by the Machine Tool Engineering Foundation and the Mazak Foundation. The authors also indebted to Sugino Machine Limited for their technical support.

References

- [1] Mieczysław Korzynski, Modeling and experimental validation of the force-surface roughness relation for smoothing burnishing with a spherical tool, *International Journal of Machine Tools and Manufacture*, 47 (2007), pp. 1956-1964.
- [2] Masato Okada, Akira Hosokawa, Ryutaro Tanaka, Takashi Ueda, In-process monitoring of tool temperature in end milling by newly developed compact two-color pyrometer, *Proceedings of the 8th International Conference on Progress of Machining Technology*, (2006), pp. 281-284.

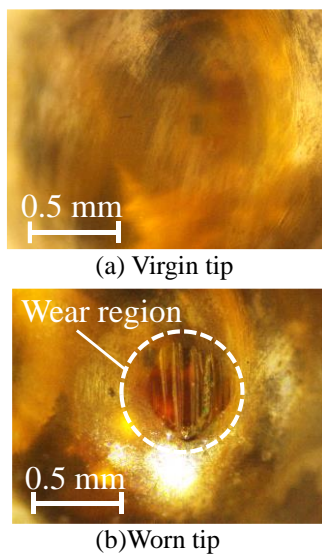


Fig. 2 Enlarged view of tip

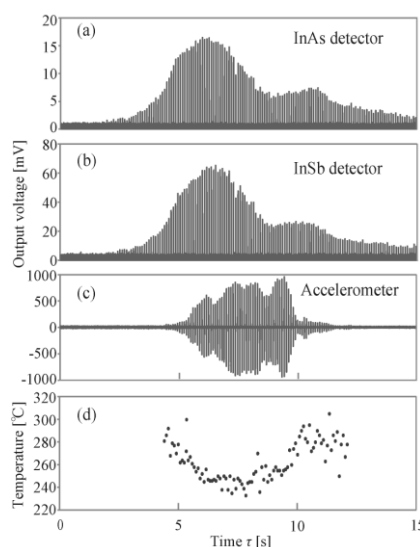


Fig. 3 Output waveform and temperature

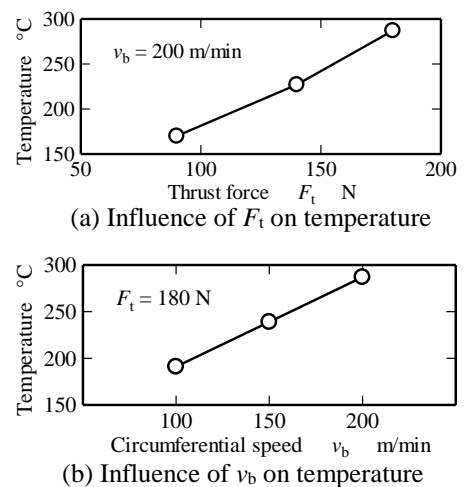


Fig. 4 Influence of burnishing conditions on temperature

HIGH DENSITY OXYGEN PLASMA ASHING OF CVD-DIAMOND COATED END-MILLING TOOLS

E.E. Yunata¹, K. Yamauchi¹, T. Aizawa^{1*}

¹Shibaura Institute of Technology

*Corresponding. taizawa@sic.shibaura-it.ac.jp.

Keywords: Plasma technology, Oxygen plasmas, Ashing, Etching, CVD-diamond coated tools

INTRODUCTION

CVD-diamond coated end-milling tools have been utilized for dry machining of carbon fiber reinforced plastic components and parts in the airplanes and automobiles [1]. Although they have high hardness even against the dry machining, they often suffer from chipping and wear in practice. Since the tool substrate is made from WC (Co) and the designed tooth geometry is shaped into this tool, it must be recycled and reused as a diamond-recoated tool by complete ashing the used diamond coatings without significant loss of tool substrate materials [2-4]. In the present paper, high density oxygen plasma ashing system is developed to make perfect ashing of CVD-diamond coatings within one hour. The ashing rate of 10 to 15 $\mu\text{m}/\text{h}$ is much faster by 10 to 30 times than the conventional oxygen processes. Optimum processing conditions are obtained to minimize the tool substrate damage and to reduce the tooth diameter shrinkage. The effect of plasma processing parameters on the ashing behavior is also discussed by the on-line quantitative plasma diagnosis.

EXPERIMENTAL PROCEDURE

The present high density oxygen plasma ashing system consists of the vacuum chamber, the plasma generator, the control unit, the carrier gas supply, and the plasma diagnosis instrument. The chamber is neutral in electricity; RF dipole electrodes and DC-bias work independently to generate RF and DC plasmas, respectively. A standard experimental set up is summarized as follows. The base pressure is less than 5×10^{-3} Pa, and pure oxygen gas (purity; 99.99%) is only used as a carrier gas. RF voltage, DC bias, and pressure are varied in a range from 100 V to 250 V, from -400 V to -600 V, and from 25 Pa to 100 Pa, respectively.

A hollow-cathode device is also employed in this system to control the external plasma condition to etching. As shown in Fig. 1 a), the generated RF-plasma is confined in this hollow so that higher ion and electron densities are attained for ashing the DLC- and diamond films [5]. The diamond-coated tool shown in Fig. 1 b) is placed in the center of hollow tube; the same DC-bias is applied to both the hollow and the tool. Under this set-up, the tool is rotated with the constant rotational speed of 6 to 10 rpm to make uniform ashing of diamonds on the whole tooth surfaces of tools. The above experimental set-up of tools into the hollow has significant influence on the ashing behavior in practice.

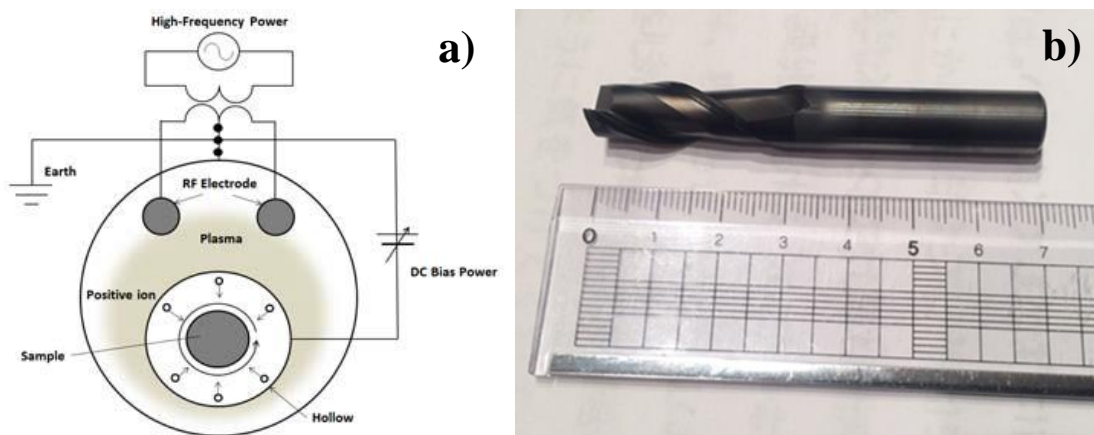


Fig. 1: Experimental procedure for oxygen plasma ashing. a) Ashing system, and, b) Specimen.

EXPERIMENTAL RESULTS and DISCUSSION

The RF-voltage has more importance on the oxygen plasma state, which is confined in the hollow tube. In this experiment, this RF-voltage was reduced from 250 V to 100 V with keeping the DC bias by -500 V. As shown in Fig. 2 a), the whole tool surface just after ashing is covered by thin grey-colored film, which is easy to be broken away by ultrasonic cleansing. Any oxide layers were never left on the polished surface; as shown in Fig. 2 b), small tints were seen just after light cleansing. Figure 2 c) depicts the microscopic image of top tooth edge. The original small holes were dotted on the tooth surface; they were made by chemical treatment before diamond coating as a nucleation site of diamond films. The initial WC (Co) tooth surfaces are recovered by the present plasma ashing condition.

The outer diameter (D_m) of top tooth after ashing was measured and compared to the calculated one (D_c) by subtracting the coating thickness from the outer diameter of coated top tooth. If D_m is much less than D_c , the tooth edge and surface is significantly removed to lower the tool substrate life in recycling. Hence, $D (= D_c - D_m)$ plays an important parameter to evaluate the microscopic damage of tool tooth. Under this ashing conditions, $D = 1 \mu\text{m}$. No significant defects and damages were seen in this condition.

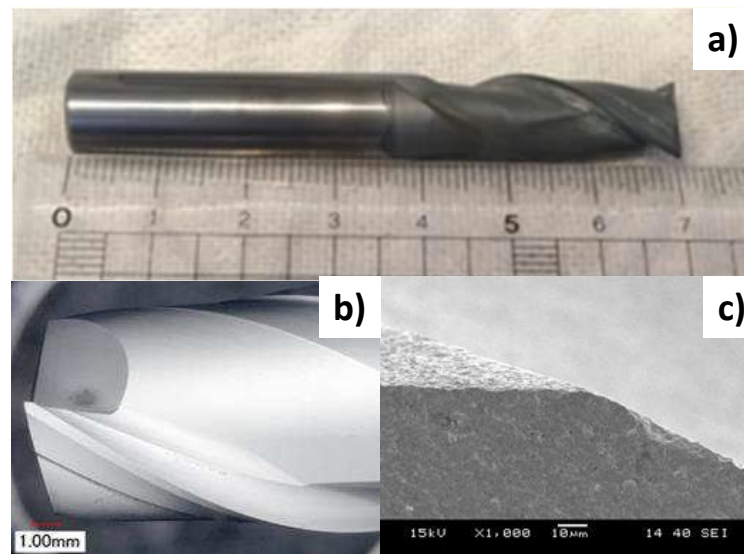


Fig. 2: Ashed specimen by the present method. a) Outlook of ashed CVD-diamond coated tool, b) A top tooth of ashed tool after cleansing, and c) SEM image of tooth edge.

CONCLUSION

Perfect ashing of the used CVD-diamond coating without any damage and defects onto the WC (Co) substrates is completed by the present high density oxygen plasma ashing with use of the hollow cathode device. Direct control of the RF voltage as well as the DC-bias leads to optimization of ashing process condition not to cause the over-oxidation of WC (Co) substrate but to make perfect removal of diamond coatings. Short leading time by 3.6 ks or 1 h in the present ashing process is also attractive to tooling companies which often suffer from long ashing time over 20 hs.

References

- [1] R. Hasegawa, "Cutting tool for aircraft and applications," *Journal of Japan Society for Precision Engineering*, 75 (8) (2009) pp. 953-957.
- [2] E.E. Yunata, T. Aizawa, "High density oxygen plasma micro-texturing into CVD-diamond coated dies for micro-embossing", *Proc. 10th 4M-ICOMM2015*. (2015) pp. 460-465.
- [3] E.E. Yunata, T. Aizawa, "Micro-texturing into DLC/diamond coated molds and dies via high density oxygen plasma etching", *Manufacturing Review* (2015) (in press).
- [4] K. Yamauchi, E.E. Yunata, T. Aizawa, "High density oxygen plasma ashing of used CVD diamond coating for recycling of WC (Co) tools," *Proc. IFMM-2015* (2015, May, Toyama) (in press).
- [5] E.E. Yunata, T. Aizawa, D.J.H. Djoko Santjojo, "Characterization of hollow cathode plasma for etching and ashing processes," *Proc. 8th SEATUC Conference* (2014, UTM, Johor Balu, Malaysia) CD-ROM.

FRONT AND REAR SIDES SIMULTANEOUS FORMING BY FRICTION STIR INCREMENTAL FORMING

**Masaaki Otsu^{1,*}, Seiya Ichikawa², Takayuki Muranaka³, Hidenori Yoshimura⁴,
Ryo Matsumoto⁵, Masato Okada⁶**

¹Professor, University of Fukui, 3-9-1 Bunkyo, Fukui, 910-8507, Japan

²Graduate Student, University of Fukui, 3-9-1, Bunkyo, Fukui, 910-8507, Japan

³Associate Professor, Fukui National College of Technology, Geshi, Sabae, 916-8507, Japan

⁴Associate Professor, Kagawa University, Saiwaicho 1-1, Takamatsu, 760-8521, Japan

⁵Associate Professor, Osaka University, 2-1 Yamadaoka, Suita, 565-0871, Japan

⁶Lecturer, University of Fukui, 3-9-1 Bunkyo, Fukui, 910-8507, Japan

*Corresponding Author: otsu@u-fukui.ac.jp

Keywords: Friction Stir Incremental Forming, Sheet Metal Forming, Aluminum Alloy Sheet, Front and Rear Sides Simultaneous, Forming Accuracy

1. Introduction

The authors have developed friction stir incremental forming (FSIF) method for flexible forming non-ferrous sheet metals without dies [1]. In conventional incremental sheet metal forming, double side incremental forming was developed to increase shape variety and improve forming accuracy [2]. In this study, double side friction stir incremental forming machine is developed. The formability, formable working conditions, forming accuracy and sheet thickness direction by single and double side friction stir incremental forming were investigated.

2. Experimental method

A forming equipment was developed originally. Appearance of developed equipment is shown in Figure 1 and schematic illustration is shown in Figure 2. Two sets of XYZ axes and a spindle are equipped. A schematic illustration of double side friction stir incremental forming is drawn in Figure 3. A sheet metal is clamped at the edge part by a blank holder, and formed by the two forming tools from upper and lower surface simultaneously.

The diameter of the forming tools was 6 mm and the top shape of the tool was hemispherical. AISI AA5052 aluminum alloy sheets were used for specimen. The size of the sheet was 100 mm x 100 mm and the thickness was 0.5 mm. The sheets were formed into frustum of pyramidal shape with a height of 10 mm. The tool rotation rate ω , feed rate v and wall angle θ were changed and formable working conditions, thickness distribution and forming accuracy were studied.

3. Experimental results

3.1 Formable working conditions

The tool feed rate was fixed to $v = 1000$ mm/min, and the tool rotation rate ω and wall angle θ were changed to obtain the formable working conditions for both single and double side friction stir incremental forming. The obtained formable working conditions were plotted in Figure 4. Open circle marks mean the forming was succeeded without fracture. Cross marks indicate the sheet was fractured and forming was failed.

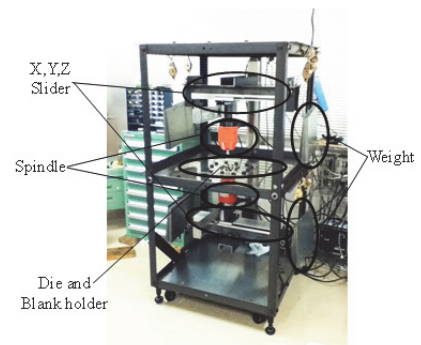


Figure 1 Appearance of forming equipment

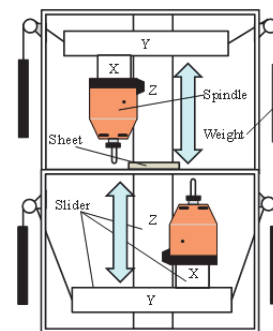


Figure 2 Schematic illustration of double side friction stir incremental forming equipment

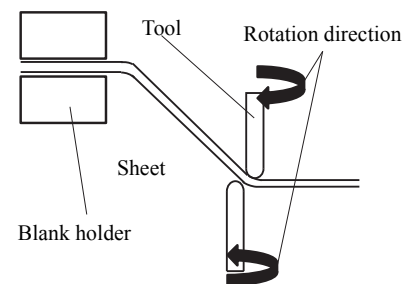


Figure 3 Schematic illustration of double side forming

The minimum wall angle by single side friction stir incremental forming was $\theta = 25^\circ$ and that by double side friction stir incremental forming was the same. This means the formability by single side forming and double side forming was equal. However, the area of formable working conditions at low tool rotation rate by double side forming was wider than that by single side forming. This reason is considerable that the friction stirring phenomenon occurred easily due to clamping sheet by two tool.

3.2 Cross-sectional shape of formed sheets

After forming with a height of 5 mm by both single and double side forming, the cross-sectional shape of formed sheets was measured by a laser displacement sensor. Comparison among ideal and formed by single and double tool is shown in Figure 5.

In a case of single side forming, actual wall angle was more than 40° , although the objective wall angle was $\theta = 40^\circ$. This reason is considerable that there are no counter supports, the sheet was elastically bent and the corner part between flange and conical part could not be formed sharply.

In a case of double side forming, the corner part between flange and conical part was formed more sharply than the single side forming case and forming accuracy was improved significantly.

3.3 Thickness distribution

Thickness distribution of formed sheets were measured. The obtained thickness distributions were plotted in Figure 6. The initial sheet thickness is 0.5 mm. Since the wall angle is $\theta = 40^\circ$, the theoretical wall thickness at the conical part calculated by sine law is 0.321 mm.

In a case of single side forming, thickness changes gradually and the minimum thickness was 0.403 mm. On the other hand, in a case of double side forming, the inclination of thickness change is steeper than that of single side forming and the thickness is closer to the ideal one. The minimum thickness was 0.215 mm and this is smaller than the ideal one.

4. Conclusions

The original forming machine for double side friction stir incremental forming was developed. Aluminum alloy sheets were formed by single and double side friction stir incremental forming, and formable working conditions, formed shapes and sheet thickness distributions were compared. Formabilities of single and double side forming were equal. However, in a case of double side forming, the area of formable working conditions was wider, the forming accuracy was higher and the sheet thickness distribution is closer to the ideal one than those of single side forming.

References

- [1] Otsu, M., Ichikawa, T., Matsuda, M., Takashima, K., Friction Stir Incremental Forming of Aluminum Alloy Sheets, Steel Research International, 81-9(2010), pp. 942 - 945.
- [2] Yongjun, W., Ying, H., Cao, J., Reddy, V.N., Experimental Study on a New Method of Double Side Incremental Forming, Proceedings of MSEC_ICM&P2008 (2008), 72279.

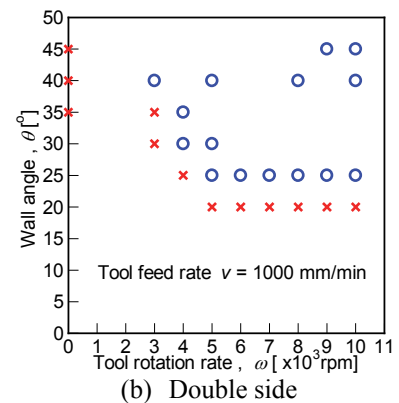
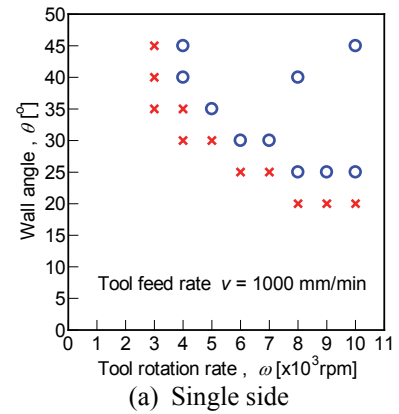


Figure 4 Formable working conditions ($v = 1000$ mm/min)

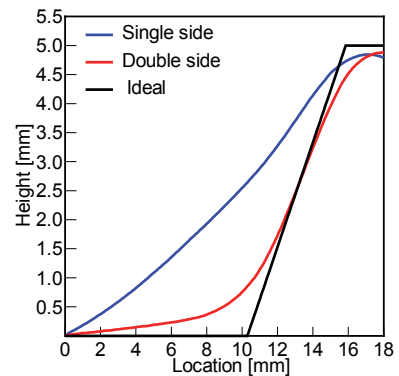


Figure 5 Comparison among formed and ideal cross-sectional shape

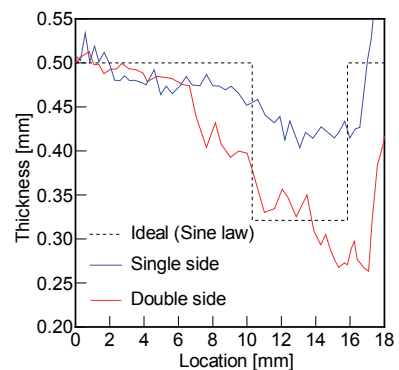


Figure 6 Distributions of formed and ideal thickness

IN SITU OBSERVATIONS ON FRETTING WEAR BEHAVIOR OF PLASMA-SPRAYED HYDROXYAPATITE COATING

Yuichi OTSUKA^{1*}, Yukio MIYASHITA², Yoshiharu MUTOH³

¹ Associate Professor, Department of System Safety Nagaoka University of Technology, 1603-1 Kamitomioka Nagaoka, Niigata 940-2188 Japan

² Associate Professor, Department of Mechanical engineering, Nagaoka University of Technology, 1603-1 Kamitomioka Nagaoka, Niigata 940-2188 Japan

³ Executive director / vice president, Nagaoka University of Technology, 1603-1 Kamitomioka Nagaoka, Niigata 940-2188 Japan

*Corresponding Author:otsuka@vos.nagaokaut.ac.jp, Tel:+81-258-47-9575, Fax+81-258-47-9573,

Keywords

Hydroxyapatite, plasma-spray, coating, interface mechanics, fretting fatigue, fretting wear

Introduction

This study aims at observing the effects of delaminations in Hydroxyapatite coating on wearing behavior of artificial human bones in situ. Plasma-sprayed Hydroxyapatite (HAp) coating has been widely used as bonding between human bone with artificial metallic implants in order to smoothly transmit loads during gaits. However, the HAp coating is susceptible to be failed due to brittle fracture, fatigue cracks, wears by fretting or corrosion etc. Wear particles made by fretting is also concerned due to its possibility of activating inflammations at surrounding organs, which leads to loosening of implants or subsequent failures of the implants. Delaminations in HAp coating interface can accelerate the wearing behavior in fretting fatigue. Therefore, in-situ observation tests of fretting fatigue of HAp coating were conducted.

Experimental Methods

Figure 1 shows the dimensions of testing specimen and contact pad. Testing specimen is made by T-6Al-4V and contact pad is made by artificial cancellous bone (porous poly propylene 50 cpf, Avicel, Japan). Table 1 shows mechanical properties of the artificial cancellous bone. HAp coating is deposited on the side surface of specimen by atmospheric plasma-spraying method. The side surfaces of HAp coating are subsequently polished by using emery papers from # 120 to # 1200 in order to observe the pass of delaminations with ease.

Fretting fatigue testing was conducted by using hydraulic fatigue testing machine(LMV3049, Saginomiya, Japan) with confocal laser microscope (OLS1100, Olympus, Japan).Testing condition was; $\sigma_{max} = 150\text{MPa}$, stress ratio $R = 0.1$, contact pressure $P_c = 30\text{MPa}$, respectively.

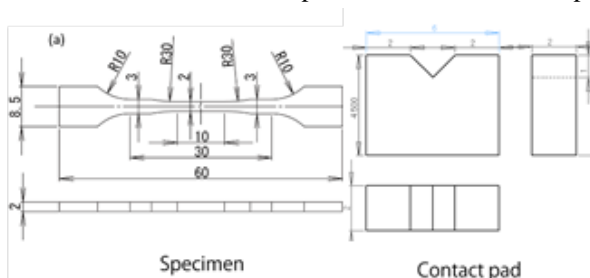


Fig. 1 Geometry of fretting testing specimen. (a) Specimen (b) contact pad

Table 1 Mechanical properties of artificial cancellous bone(PP)

Compressive strength (MPa)	Young's modulus (MPa)	Density (g/cc)
48	1469	0,80

Results and discussions.

Figure 2 shows the delamination pass after $N= 2X 10^6$ cycles. At initial stage vertical cracking at the edge of contact pads occurred due to stress concentrations by fretting contact. Delaminations initiated from the root of vertical crack and then delamination grew to the center part of contact regions. Figure 3 shows the SEM picture of the edge of delaminations after testing. The wear debris were found at the resion adjacent to the edge of delaminations even in the cases of positive loading ratio. Figure 4 shows delamination growth history and figure 5 shows delamination growth rate, respectively. Delamination growth curve seems to be divided into two regions. In first region (delamination length was less then $700 \mu\text{m}$), growth rate decreases with increasing delamination length. The phenomenon can be dominated by stress singularity at the edge of interface where intensity at the edge was higher than the one at the subsequent interface cracks. In second region (delamination length was more then $700 \mu\text{m}$),the slope of growth rate was more decreased. Its mechanism is not clear but the wear particle effects or changes in stress singularity are possible mechanism.

Summary

This study aims at observing the effects of delaminations in Hydroxyapatite coating on wearing behavior of artificial human bones in situ. HAp coating was delaminated and subsequently wear particle was observed at the interface between contact pad with HAp coating. The changes in the rigidity by delamination seems to promote wear behavior of HAp coating with contact pad. Fretting fatigue behaviors in Simulated body fluid is going to be observed by the same system(references are omitted).

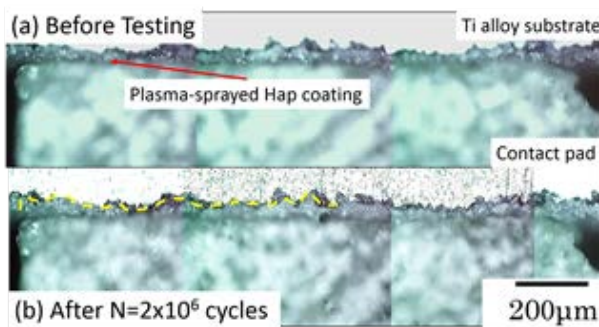


Figure 2 Observations of delamination behavior of HAp coating during fretting fatigue

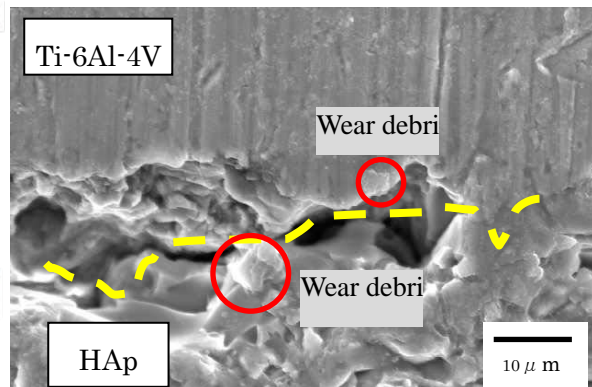


Figure 3 Wear debris at the tip of interface delamination

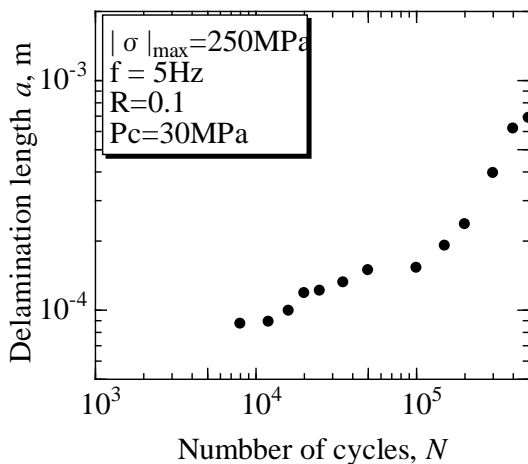


Figure 4 Delamination growth plot in fretting fatigue test. Dleamination initiated at $N=8 X 10^3$

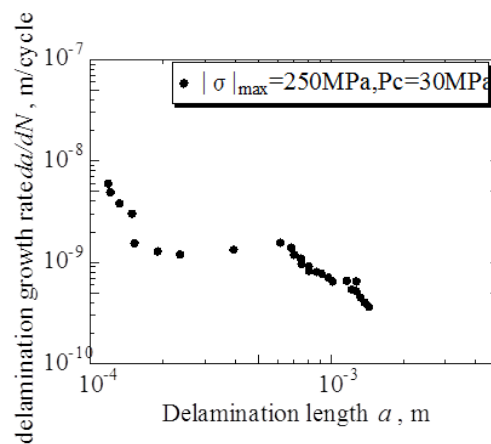


Figure 5 Delamination growth rate vs delamination length. Delamination growth rate decreases with increasing delamination length.

WETTABILITY BETWEEN GRAPHITE AND HIGH- TEMPERATURE LEAD-FREE SOLDER ALLOY

Gen Sasaki^{1*}, Kunihiro Nakata¹, Kenjiro Sugio¹

¹Graduate School of Engineering, Hiroshima University

*gen@hiroshima-u.ac.jp

Keywords: Composites, High-Temperature Lead-Free Solder, Wettability, Reactivity, Graphite

Although the development of lead-free solder metals at high-temperature over 473K is urgent study, the alternative alloy used in conventional use is not yet developed. Sn, Bi, Zn base alloys are considered as the candidate materials in previous studies. However, these alloys have many problems on the ductility, the wettability, the long-term reliability (mechanical properties and thermal fatigue properties) at the high-temperature, the reliability of the joining under the vibration environment and so on. On the other hand, some of the authors have developed the lead-free fuse [1, 2]. From the point of view about easy control of the melting point, electrical conductivity, the fusing, the corrosion resistance and good joining ability, Zn-Sn alloy was selected as the base metal. In previous study [3], lead free Zn-Al-Sn alloy was developed using s-orbital energy level in order to satisfy both the tensile strength of 200MPa and the elongation of 5%. One of suitable composition is Zn-10wt%Al-2wt%Sn (Zn-10Al-2Sn) alloy. But this planning value of strength and elongation for this alloy is still lower than that of Pb base alloy. Especially, the low elongation and inferior properties on thermal fatigue failure is fatal defects. Therefore, the addition of carbon short fiber to alloy is one of good idea for improving these properties because of the effect of pull-out of fiber from matrix alloy and the improvement of the thermal fatigue failure by suppressing the thermal expansion. Particularly, vapor grown carbon fiber (VGCF) is promising materials for the dispersant in matrix alloy, which shows good mechanical properties and high-cost performance. On the other hand, the chemical reaction between alloy and carbon fiber during preparation of the composites may affect the microstructure and the mechanical properties. Therefore, the wettability and the reactivity between the molten alloy and graphite sheet with (002) plane in a surface, which is a same plane for surface of VGCF, is investigated in this study.

The Zn-10Al-2Sn alloy was obtained by mixing of the each pure element metals at 1023K, and then poured water cooled copper die. Graphite sheet was bonded to stainless steel plate with circle form and was used for the substrate of dropping test. The condition of dropping test was at 1023K in Ar atmosphere, and keeping time after dropping was 5, 10 and 30min. The contact angle was measured by $\theta/2$ method. Microstructure was observed by optical microscopy and EPMA.

Figure 1 show XRD analysis of graphite sheet used in this study. XRD analysis shows only (002) and (004) planes in graphite. It shows the surface of graphite consists from only (002) plane, which is very similar with VGCF.

Figure 2 shows the droplet of molten Zn-10Al-2Sn alloy on graphite sheet at 1023K in argon atmosphere as increasing contact time after dropping. Figure 3 shows the time dependence of contact angle between Zn-10Al-2Sn alloy and graphite sheet at 1023K. The contact angle between graphite sheet and Zn-10Al-2Sn alloy is 115-120 degree, which indicates this system has low wettability, which shows the interface between the graphite and the alloy seems to have low interfacial strength. As increasing time, the contact angle decreased for 1-4 degree, which means the chemical reaction between alloy and graphite. Figure 3 shows the microstructure between alloy and graphite. Gap was observed at the interface between alloy and graphite. In equilibrium phase diagram between Zn-C, Al-C and Sn-C, only Al reacts with C to form Al_4C_3 . As Al_4C_3 is dissolved by water and humidity, it seems the gap sign of the existence of Al_4C_3 . On the other hand, the microstructure of alloy parts shows two-phase, which is dendritic Al base parts and Zn base parts. Sn was distributed in Zn base parts. This structure is similar to monolithic Zn-10Al-2Sn alloy, and the effect of this reaction on properties seems to be small.

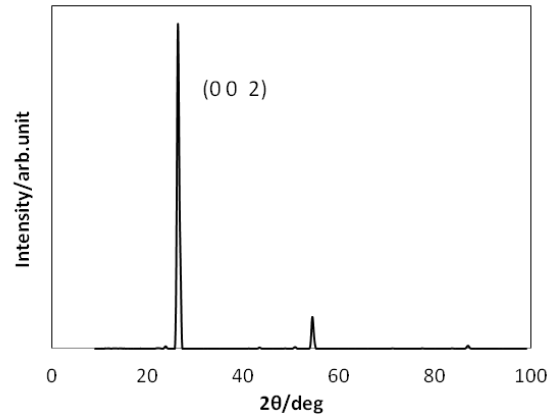


Figure 1 XRD analysis of surface of graphite sheet.

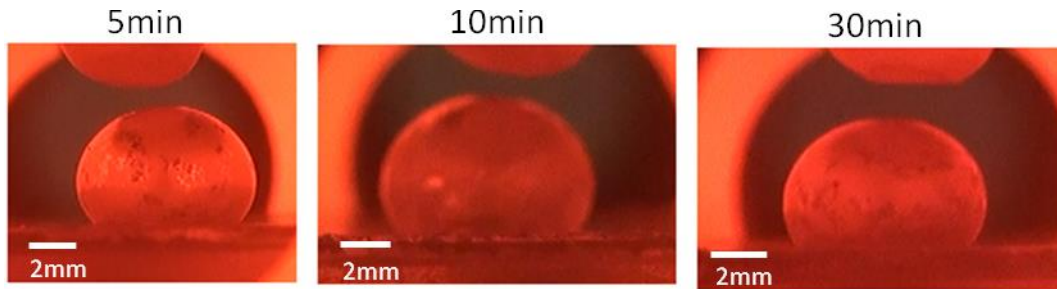


Figure 2 Configuration of droplet of molten alloy on graphite as a function of holding time after dropping.

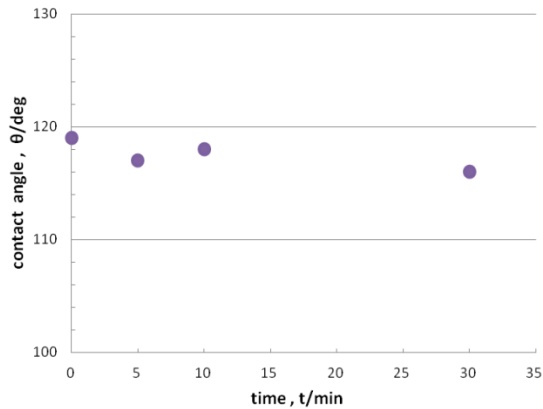


Figure 3 Contact angle of droplet on graphite as a function of holding time after dropping.

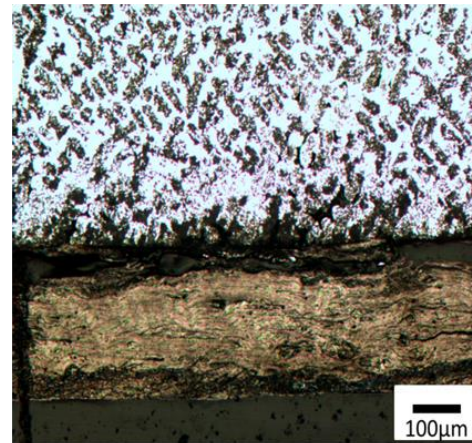


Figure 4 Microstructure around the interface between droplet and graphite sheet by optical microstructure. Holding time is 30 min.

References

- [1] K. Matsugi, Y. Iwashita, Y. B. Choi, G. Sasaki, K. Fujii, Long Time Stability of Pb-Free Sn-9Zn Elements for AC-Low Voltage Fuse Performance, *Materials Transactions* 52,2, (2011), pp753-758
- [2] K. Matsugi, Y. Saki, Y. B. Choi, G. Sasaki, K. Suetsugu, K. Fujii, Control of Electrical and Thermal Properties on Sn-50Zn Alloy by 8vol% Al₂O₃ Addition for Pb-Free AC Low Voltage Fuse Elements, *Materials Transactions* 54, 2, (2013), pp. 231-237
- [3] K. Matsugi, K. Terada, S. Furukawa, Y.B. Choi, G. Sasaki, K. Suetsugu, Design of Zn-Al-Sn Alloys as Lead-Free Solders for High Temperature Application and Their Characteristics, *J. JFS*, 86, 3, (2014), pp216-222
- [4] G. Sasaki, M.H. Niu, K. Sugio, Y.B. Choi, K. Matsugi, Development and Mechanical Properties of High Temperature Lead Free Solder Composites, *Abs of The 11th China-Japan Joint Conf. on Composite Materials (CJCC-11)* (2014)

THE ROLE OF HYDROGEN IN HIGH RATE PLASMA NITRIDING OF MARTENSITE STAINLESS STEEL

D.J. Santjojo^{1*}, T.Aizawa², Istiroyah¹

¹CRC-ASMAT Brawijaya University, ²Shibaura Institute of Technology

*dsantjojo@ub.ac.id.

Keywords: High rate plasma nitriding, surface reaction, hydrogen plasma, metastable nitrogen

INTRODUCTION

High concentration of nitrogen with nearly constant profile toward the nitriding front end cannot be explained with conventional nitriding mechanisms. Complex reactions on the surface of the substrate during the nitriding process produce large amount of certain nitrogen species which can be diffuse easily into the substrate. Analysis of optical emission spectroscopy data combined with Langmuir probe measurement data showed that inclusion of hydrogen in the plasma leads to high density ion production. The high density ion contains of metastable state nitrogen and NH species reacting to produce reactive nitrogen ion and atoms. The hydrogen atoms played important role in the complex reactions with the metastable nitrogen and the NH.

EXPERIMENTAL PROCEDURE

Specimens for this study were produced by means of a RF-DC Plasma nitriding system (Fig.1a). The martensitic steel used was AISI 420 which was cut and shiny polished into 5 mm thick silinders with a diameter of 10 mm. Investigation on the role of hydrogen in the high rate plasma nitriding was carried out by a combination of optical emission spectroscopy and Langmuir probe measurement (Fig.1b). Composition of elements of the nitride subsurface layer of the specimens was obtained from auger electron spectroscopy (AES) measurements. The Composition of elements to the depth was acquired by serial measurements of subsequent surface etching.

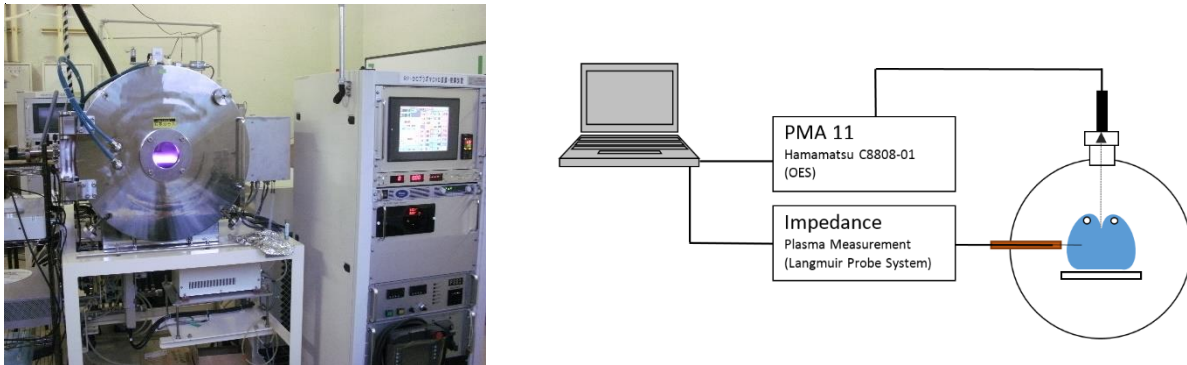


Fig. 1: a) Plasma nitriding system; b) A combination of OES and Langmuir probe measurement.

EXPERIMENTAL RESULTS and DISCUSSION

High rate plasma nitriding was estimated from depth profile auger electron spectroscopy. A high nitrogen concentration (40%) profile was found almost constant up to 3 μm . This was produced by means of a mixture of hydrogen and nitrogen plasma nitriding. The role of hydrogen was investigated by comparing the result with the one produced using nitrogen plasma only (Fig.2) The active species for steel nitriding are the metastable state nitrogen such as $\text{N}_2(A^3 \Sigma_u^+, \vartheta)$ or vibrationally excited states such as $\text{N}_2(X^1 \Sigma_g^+, \vartheta)$. The active species cannot be observed directly from the OES spectra. However,

indirect observation is possible by investigating transitions of the second positive at 337, 358 and 370 nm which is related to the N_2^* and the first negative $N_2^+(B^2\Sigma_u^+ \rightarrow X^2\Sigma_g^+)$ at 391 and 427 nm which related to the N_2^+ . Other important state of the plasma in the nitriding mechanism is the NH species which is found at 336 nm (Nagamatsu,2013).

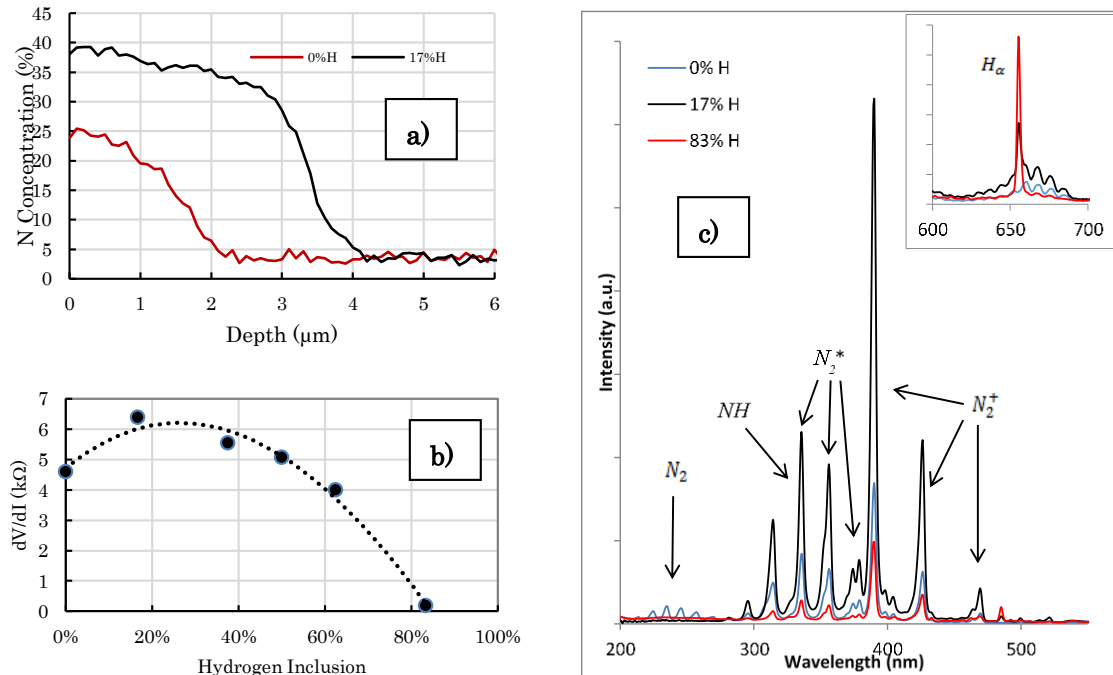


Fig. 2: a) AES depth profile data; b) Plasma electrical resistance as a function of hydrogen inclusion; c) OES spectra of nitrogen plasma and nitrogen-hydrogen plasma.

CONCLUSION

Our study concludes that the high rate nitriding is governed and controlled by dynamic of nitrogen and hydrogen species in the plasma. The dynamic of the mixed gas plasma depends on the inclusion of hydrogen in the nitrogen plasma. OES and Langmuir probe measurement suggest that low concentration of hydrogen plasma (17%) contains a large density of positively charge species which are N_2^* , N_2^+ and NH complexes. Intermediate species exist in the plasma reaction and emit observable radiation. The species react on the surface producing high concentration of high energy atomic nitrogen which diffuse into the metal uniformly.

References

- [1] Alphonsa, A. Chaini, P.M Roale, B. Ganguli, P.I John, A study of martensitic stainless steel AISI 420 modified using plasma nitriding, Surf. Coat. Technol., 150, 2002.
- [2] Pinedo C. E., Waldemar A. Monteiro, On the kinetics of plasma nitriding a martensitic stainless steel type AISI 420, Surf. Coat. Technol, 179, 2004.
- [3] Yun-tao Xi, Liu Dao-xin, han Dong, Improvement of erosion-corrosion resistance of AISI 420 stainless steel by low temperature plasma nitriding, Appl. Surf. Sci., 258, 2008.
- [4] Santjojo D.J., et.al, Formation of Expanded Martensite In Plasma Nitrided AISI420 Stainless Steel, Proceeding SEATUC 8th Symposium, Malaysia, 2013.
- [5] Nagamatsu H., et.al, Steel nitriding by atmospheric pressure plasma jet using N₂/H₂ mixture gas, Surface & Coatings Technology, 225,2013.

DEVELOPMENT OF TITANIUM FIBER/ALUMINUM MULTIFUNCTIONAL COMPOSITES

¹, S. Yamaguchi ², T. Mochizuki ², T. Yanaseko ² and Suprianto³

¹ Professor, Chiba University, 1-33 Yayoicho, Inage-ku, Chiba-shi, Chiba, 263-8522 Japan

² Graduate student, Chiba University, 1-33 Yayoicho, Inage-ku, Chiba-shi, Chiba, 263-8522 Japan

³Lecturer, University of Sumatera Utara, Medan 20155 Indonesia

*Corresponding Author: asanuma@faculty.chiba-u.jp, Tel: +81-43-290-3201

Keywords: Multifunctional, Metal Matrix Composites, Innovative Processing, Interphase, Aluminum

Introduction

Asanuma et al. have developed a simple temperature and strain sensor by embedding surface surface-oxidized nickel (NiO/Ni) fiber in an aluminum matrix in the previous work [1]. In this study, two more useful functions, that is, heating and actuation were tried to be added in addition to temperature sensing and strain sensing by using surface-oxidized titanium fiber by making use of its higher electrical resistance and lower thermal expansion coefficient compared with those of nickel fiber.

Experimental

Pure aluminum plates of 0.2 mm thickness, 8 mm width and 30 mm length were used as matrix. A 0.01 mm thick copper foil was used as insert. Titanium fiber of 0.15 mm diameter and 99.5% purity was used as functional fiber. It was oxidized at 1073 K for 1.8 ks in the air in an electric furnace to obtain the surface-oxidized (TiO₂/Ti) fiber. These materials were consolidated by the IF/B method [1], which can be briefly explained as following. The TiO₂/Ti fiber was arranged in the U-grooves made on the aluminum plate laminated with the copper insert, and they were covered with another matrix aluminum plate without U-grooves to make unsymmetrical configuration for actuation. These piled-up materials were hot-pressed under the condition of 853 K, 1.36 MPa and 0.3 ks in a low vacuum.

Results and discussion

A SEM image of a cross section of the composite embedded with the TiO₂/Ti fiber is given in Figure 1. It shows that the TiO₂/Ti fiber can be embedded in aluminum matrix without fracture of the surface oxide layer when it is hot-pressed under the condition of 823 K, 1.36 MPa and 0.3 ks in a low vacuum. The relation between the temperature obtained by the embedded TiO₂/Ti fiber and the surface temperature of the active composite measured with an external thermocouple is given in Figure 2, which shows good coincidence of the temperatures even after deformation of the active composite up to higher than 450K. According to the result, it is clear that the curvature of the active composite can be monitored by the temperature measurement with the embedded fiber. The relation between the electrical resistance of the embedded TiO₂/Ti fiber and the surface temperature of the active composite is given in Figure 3.

This shows an almost linear relationship between them, which means that the curvature of the active composite can be monitored also by the resistance measurement though it includes the both effects of the temperature increase as well as the strain reduction. Figure 4 shows the curvature change of the active composite during the fifth heating and cooling cycle between room temperature and 813K. According to the result, the embedded fiber is working as a heater for actuation and its monitoring. In addition, the shape of the composite at room temperature is reproducible even after the thermal cycle up to 813 K. Figure 5 shows the curvature change of the active composite during the thermal cycle up to 493 K. It shows that the curvature of the active composite during the thermal cycle up to about 490 K can change without hysteresis.

Conclusions

The results obtained in this study are as follows:

- (1) The oxide layer formed on the titanium fiber at 1073 K for 1.8 ks in the air remains unbroken during the composite fabrication by the IF/B method.
- (2) The embedded titanium fiber works as a heater for actuation and a sensor for temperature and deformation monitoring.
- (3) The composite shape at room temperature is reproducible even after thermal cycle up to 813 K.
- (4) The curvature of the composite during the thermal cycle up to 493 K changes without hysteresis.

References

- [1] H. Asanuma, The Development of Metal-Based Smart Composites, JOM, 52-10 (2000), pp. 21-25.

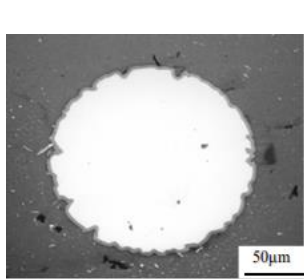


Fig. 1 SEM image of a cross section of the composite.

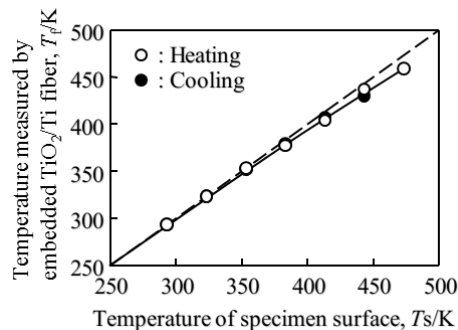


Fig. 2 Relation between the temperature measured by the embedded fiber and that of specimen surface measured with an external thermocouple.

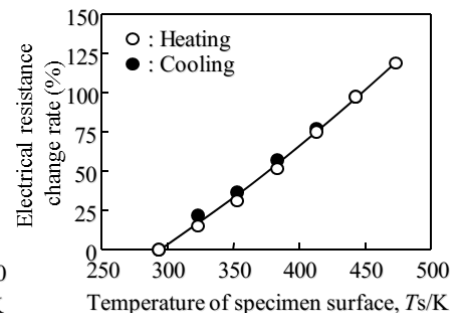


Fig. 3 Relation between the electrical resistance change rate of the embedded fiber and the temperature of specimen surface.

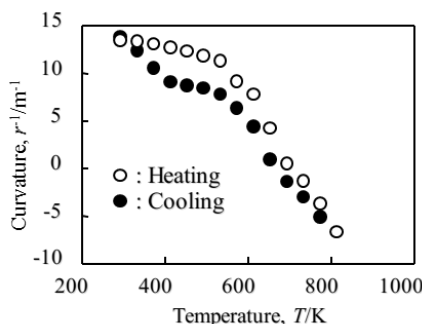


Fig. 4 Curvature change of the active composite during the fifth thermal cycle between room temperature and 813K.

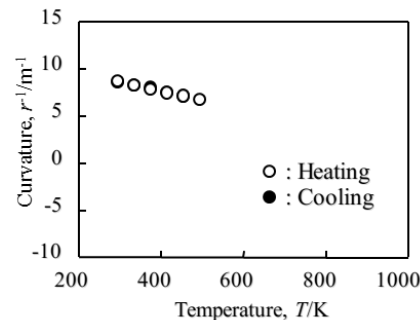


Fig. 5 Curvature change of the active composite during the thermal cycle up to 493 K.

PHASE-FIELD SIMULATION OF ELEMENTARY PROCESS IN POWDER BED FUSION

Kazunari Shinagawa

Faculty of Engineering, Kagawa University

shina@eng.kagawa-u.ac.jp

Keywords: *powder, simulation, phase-field method, discrete-element method, selective beam melting*

Introduction

Powder bed fusion, a 3D printing technique, is expected to be a new way of manufacturing by its ability to produce high value-added products or supply wide variety of parts in small quantities. Considering the benefits, optimizing the manufacturing conditions may become more important with increasing the practical applications. Manufacturing conditions, determined by empirical laws, have been mostly obtained through trial and error. A general law which can be applied to different materials and machines will be desired. This study aims to establish a method for analyzing the fusion process of metal powder particles to optimize the conditions of the selective beam melting process in a rational manner. The author has developed a combined phase-field/discrete-element method (PFM/DEM) to simulate both shrinkage and grain growth behavior in powder compacts during sintering [1]. In this paper, PFM/DEM is applied to melted particles, and an elemental fusion process is simulated as the first step of the study.

Numerical method

In PFM, the migration of interface between particles is computed with minimizing the interfacial energy. Combining with DEM, the force acting between particles (which stems from the surface tension) is evaluated in the phase field by taking into consideration the surface curvature. Note that the force consists of two terms. The first term is a compressive force directly acting on the contact plane between particles, while the second one is an imaginary compressive force converted from the outward force at the neck tip. As for the simulation of solid state sintering, the position of the neck tip can be easily detected in the phase field because the neck between particles is the grain boundary as well, where the phase-field variable changes sharply. For liquid phase, melted particles do not have the grain boundary, but low grain boundary energy with different phase-field variables is given to adjoining particles, for finding the position of the neck by searching the change in phase-field variable. The resultant forces are transferred into DEM to compute the motion of particles.

Calculation condition and result

As in the previous study [1], a two-dimensional model was used in the simulation. The grid points of 200x200 with an interval of $\Delta x = \Delta y = 2$ were generated for the finite difference method to conduct the phase-field simulation. A model of powder having size distribution with the mass

median diameter of 40 and the geometrical standard deviation of about 1.4 was prepared in the grid by using random number generation. In the central circular region with a diameter of 240 in the grid, the particles were assumed as liquid phase, and a large value of interface mobility as well as a small value of the grain boundary energy was set. On the assumption that the outer region is affected by heat, the solid state sintering was simulated for the surrounding particles.

Figure 1 shows an example of the calculated results. The particles in the central region fused together with time t , while the sintering process with grain growth was observed in the other region. In Fig. 1(c), rounded pores can be seen in a glob of liquid phase. The liquid phase seemed to shrink a little apart from the outer region.

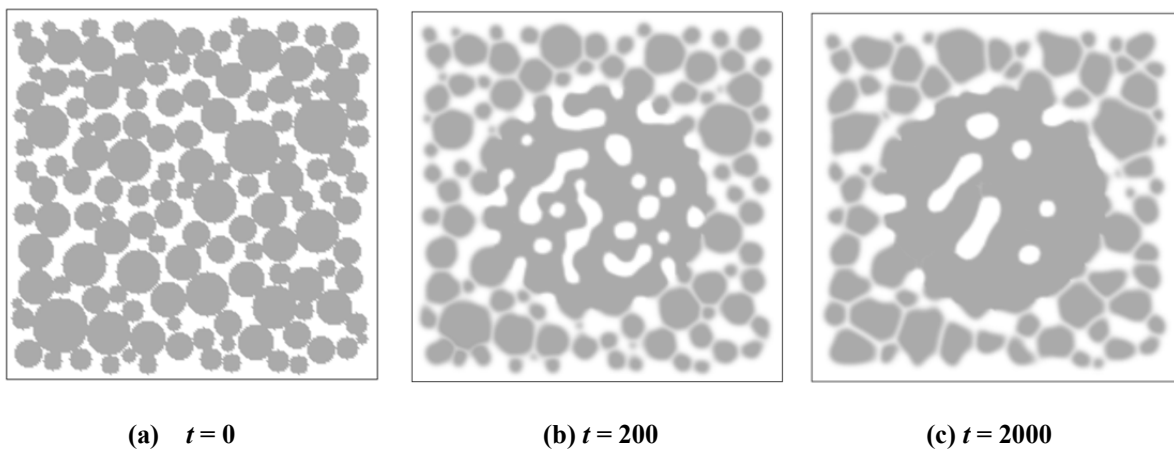


Figure 1 Calculated result

Summary

By using a PFM/DEM combined method, the formation of a glob of liquid phase was calculated in a two-dimensional simplified simulation, as the first step of the numerical study on powder bed fusion. Other factors of selective beam melting, including scanning operation, will be introduced into the present method, and the whole process of powder bed fusion will be simulated in the next study.

Acknowledgements

This work was supported by Grants-in-Aid for Scientific Research (B) (No. 26289273) from Japan Society for the Promotion of Science.

References

- [1] K. Shinagawa: Simulation of grain growth and sintering process by combined phase-field/discrete-element method, *Acta Materialia*, **66**(2014), pp. 360-369.

ESTIMATION OF FRICTIONAL PERFORMANCE OF LUBRICANTS FOR HOT FORGING OF STEEL BY CALIBRATION CURVES CONSIDERING HEAT TRANSFER IN RING COMPRESSION TEST

Kazuhito Asai¹, Kazuhiko Kitamura^{1*}

¹ Dept. of Engineering physics, Electronics and Mechanics, Nagoya Institute of Technology, Gokiso-cho, Showa-ku, Nagoya 466-8555, Japan,

* Corresponding Author: kitamura.kazuhiko@nitech.ac.jp, Tel:+81-52-735-5351, Fax:+81-52-735-5442

Keywords: (Tribology, friction, hot forging, testing method, lubricant)

1. Introduction

Higher performance lubricants are required to improve die life in hot forging of steel. The frictional performance of these lubricants has been often estimated by ring compression test. A low-speed hot-ring compression test¹⁾ was proposed to be helpful in classifying the tribological performances of lubricants in hot forging of steel. By this test, high performances lubricants could be selected, which showed low-frictional coefficient and high heat-resistance performance. To use more precise values of these frictional coefficients, calibration curves considering heat transfer between a billet and dies are determined by FEM analysis. In this report, frictional coefficients under poor-lubricated condition are estimated by the low- and high-speed hot-ring compression test.

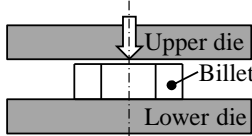
2. FEM analysis conditions of ring compression test

The conventional cold-ring compression test is widely used and roughly analyzed under an isothermal condition as shown in **Table 1 (a)**. A ring billet is made of 0.45% carbon steel, and a commercial data base of this steel is used in FEM analysis. The temperature of this billet and dies is 20°C. The billet has dimensions of 10 mm in height, 15 mm in internal diameter, and 30 mm in outer diameter. A coulomb's frictional coefficient μ between dies and the billet is calculated when reduction in height Re is 50% and compression speed is 2.0 mm/s.

Table 1 (b) shows an analysis condition of hot-ring compression test considering heat transfer. Billet temperature is 1100°C before compression. Mechanical press takes 0.1 s and hydraulic press takes 8.0 s for this test with 50% reduction in height. These testing times are input in FEM analysis. A heat transfer coefficient²⁾ α between the billet and the open air is $0.1 \text{ kW}\cdot\text{m}^{-2}\cdot\text{K}^{-1}$, and α between the dies and the air is also $0.1 \text{ kW}\cdot\text{m}^{-2}\cdot\text{K}^{-1}$. By considering the oxide thickness of the billet after heating, α between the dies and the billet is $12.5 \text{ kW}\cdot\text{m}^{-2}\cdot\text{K}^{-1}$. The emissivity²⁾ of the billet or the die is 0.7.

An adiabatic condition of hot-ring compression test is also referred as shown in **Table 1 (c)**, namely the heat transfer coefficient between the billet and the dies is neglected under this condition.

Table 1 Analysis conditions for hot ring compression test of steel

	<p>(b) Considering heat transfer for hot-ring compression test</p> <table border="1" style="width: 100%; border-collapse: collapse;"> <tr><td>Billet</td><td>0.45% carbon steel, 1100°C</td></tr> <tr><td>Dies(Upper/Lower)</td><td>Consider heat transfer, R.T.</td></tr> <tr><td>Compression time</td><td>8.0 s (Hydraulic press)</td></tr> <tr><td>($Re=50\%$)</td><td>0.1 s (Mechanical press)</td></tr> <tr><td>Heat transfer coefficient</td><td></td></tr> <tr><td>a) Billet - Air, Dies - Air</td><td>0.1 kW/m²K</td></tr> <tr><td>b) Dies - Billet</td><td>12.5 kW/m²K</td></tr> <tr><td>Emissivity (Dies and Billet)</td><td>0.7</td></tr> </table>	Billet	0.45% carbon steel, 1100°C	Dies(Upper/Lower)	Consider heat transfer, R.T.	Compression time	8.0 s (Hydraulic press)	($Re=50\%$)	0.1 s (Mechanical press)	Heat transfer coefficient		a) Billet - Air, Dies - Air	0.1 kW/m ² K	b) Dies - Billet	12.5 kW/m ² K	Emissivity (Dies and Billet)	0.7		
Billet	0.45% carbon steel, 1100°C																		
Dies(Upper/Lower)	Consider heat transfer, R.T.																		
Compression time	8.0 s (Hydraulic press)																		
($Re=50\%$)	0.1 s (Mechanical press)																		
Heat transfer coefficient																			
a) Billet - Air, Dies - Air	0.1 kW/m ² K																		
b) Dies - Billet	12.5 kW/m ² K																		
Emissivity (Dies and Billet)	0.7																		
<p>(a) Cold-ring compression test (Isothermal condition)</p> <table border="1" style="width: 100%; border-collapse: collapse;"> <tr><td>Billet</td><td>0.45% carbon steel, R.T</td></tr> <tr><td>Original height: internal diameter: out side dia.</td><td></td></tr> <tr><td>= 10 mm : 15 mm : 30 mm</td><td></td></tr> <tr><td>Dies(Upper/Lower)</td><td>Non-consider heat transfer, R.T</td></tr> <tr><td>Frictional coefficient</td><td>Coulomb's friction μ</td></tr> <tr><td>Reduction in height Re</td><td>50%</td></tr> <tr><td>Compression speed</td><td>2.0 mm/s</td></tr> </table>	Billet	0.45% carbon steel, R.T	Original height: internal diameter: out side dia.		= 10 mm : 15 mm : 30 mm		Dies(Upper/Lower)	Non-consider heat transfer, R.T	Frictional coefficient	Coulomb's friction μ	Reduction in height Re	50%	Compression speed	2.0 mm/s	<p>(c) Adiabatic condition for hot-ring compression test</p> <table border="1" style="width: 100%; border-collapse: collapse;"> <tr><td>Heat transfer coefficient</td><td></td></tr> <tr><td>b) Dies - Billet</td><td>0 kW/m²K</td></tr> </table>	Heat transfer coefficient		b) Dies - Billet	0 kW/m ² K
Billet	0.45% carbon steel, R.T																		
Original height: internal diameter: out side dia.																			
= 10 mm : 15 mm : 30 mm																			
Dies(Upper/Lower)	Non-consider heat transfer, R.T																		
Frictional coefficient	Coulomb's friction μ																		
Reduction in height Re	50%																		
Compression speed	2.0 mm/s																		
Heat transfer coefficient																			
b) Dies - Billet	0 kW/m ² K																		

3. Estimation of frictional coefficient in hot-ring compression test

Figure 1 shows a relationship between a decrease in an internal diameter and a coulomb's frictional coefficient μ by hot-ring compression test. Under a poor-lubricated condition μ indicates 0.3 or more for low-speed hot-ring compression tests when the hydraulic press is used. Calibration curves for hot-ring compression the test leads the different μ from μ determined with the calibration curves for cold-ring compression test. It is necessary to calculate more appropriate calibration curves for hot-ring compression test. The calculation considers temperature, compression speed, and heat transfer.

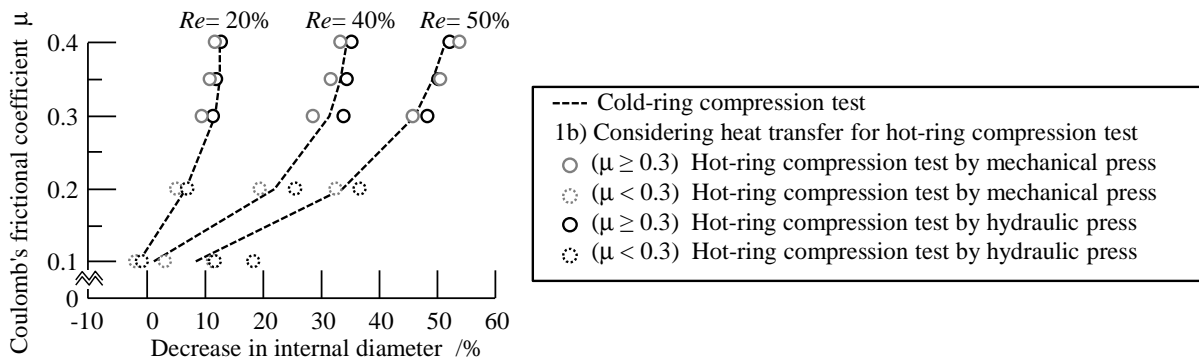


Figure 1 Calibration curves of ring compression test with considering heat transfer

Figure 2 shows the relationship between a decrease in an internal diameter and a coulomb's frictional coefficient μ without considering heat transfer in hot-ring compression test. These frictional coefficients μ are close to μ that is estimated with considering heat transfer because the test takes for short time using mechanical press. The frictional coefficients calculated with considering heat transfer are different from μ that is calculated without considering heat transfer because this test takes for long time using hydraulic press. The billet temperature can decrease when the test takes for long time in low-speed hot-ring compression test. Particularly, the temperature of the billet near the dies can fall down to be low. Material flow is locally difficult because the material is strengthened by cooling. It is also important to consider the material strength in the analysis of hot-ring compression test.

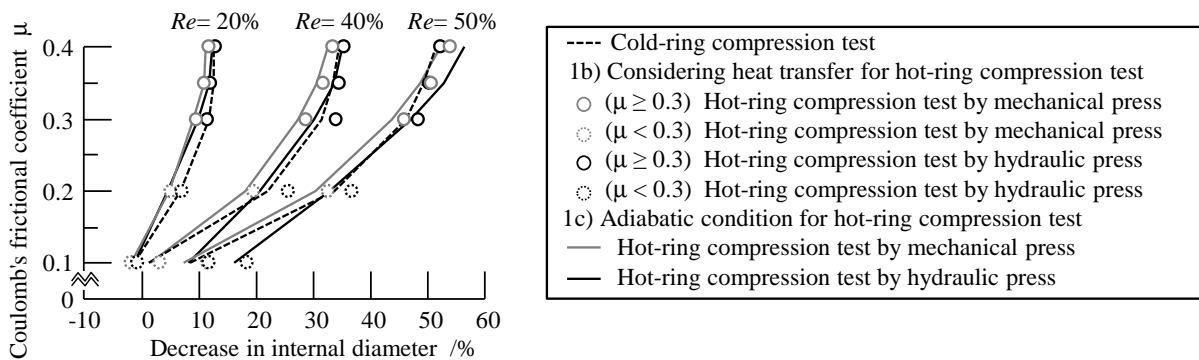


Figure 2 Calibration curves with and without considering heat transfer

4. Conclusion and outlook

Calibration curves for hot-ring compression test were calculated with considering heat transfer under a poor-lubricated condition. The billet temperature, heat transfer coefficient, compression speed directly influenced on increasing in material strength by cooling of the ring billet. To obtain the more appropriate calibration curves, it is necessary to consider influence of lubricant on heat transfer under a well-lubricated condition in hot forging.

References

[1] Kazuhito Asai, Kazuhiko Kitamura, Estimation of frictional property of lubricants for hot forging of steel using low-speed ring compression test, 11th ICTP2014, Procedia Engineering 81 (2014), pp. 1970-1975.
 [2] Nobuki Yukawa, Yoshihiro Nakashima, Takahiro Ishiguro, Eiji Abe, Modeling of heat transfer coefficient of oxide scale in hot forging, 11th ICTP2014, Procedia Engineering 81 (2014), pp.492-497.

DEVELOPMENT OF HIGH SPEED TORSIONAL FATIGUE TESTING MACHINE FOR MULTIPLE SPECIMENS

Katsunori TAKEZAWA¹, Noriyasu OGUMA^{2,*}, Mai FUKAMI³ and Masanori KONTANI³

¹ Graduate Student, Graduate School of Science and Engineering, University of Toyama, Gofuku 3190, Toyama-shi, Toyama 930-8555 Japan

² Professor, Faculty of Engineering, University of Toyama, Gofuku 3190, Toyama-shi, Toyama 930-8555 Japan

³ Engineer, Tohshin Seiki Co., Ltd., Ha 18 Terai, Nomi-shi, Ishikawa 923-1121 Japan

oguma@eng.u-toyama.ac.jp, Tel&Fax: +81-76-445-6776

Keywords: Torsional fatigue, Displacement controlled, Rotating-reciprocating-swinging conversion, Sliding friction, Multiple specimens

Introduction

Torque transmission shafts, rolling bearings, coil springs and so on are important elements to dynamic mechanical device. It is known that fatigue destruction of these mechanical elements occurs mainly under shear stress. Therefore it is important to clarify fatigue strength characteristics of the material used for these mechanical elements under shear stress from design aspect. However, most of tests to grasp fatigue characteristics have been performed under normal stress in rotating bending tests or axial loading fatigue tests. This is because the torsion testing machine which is low-priced and can be efficiently tested is not widely popularized. In these circumstances, we aimed for the development of the compact torsion fatigue testing machine in which four specimens can be tested at high speed at the same time to efficiently accumulate torsional fatigue data on materials for machine structures. And the validity of the torsion fatigue testing machine developed was estimated by the inspection of the torsional angle of specimens and the fractographic observation of fracture surfaces of the failed specimens in torsional fatigue testing.

Driving mechanism of torsional testing machine

The developed testing machine uses an electric motor as a drive source, and has a rotating-reciprocating conversion and a reciprocating-swinging conversion mechanism. A schematic diagram of the former mechanism is shown in Fig. 1. Its mechanism consists of an eccentric shaft, a connecting rod and a piston. Figure 2 is a schematic diagram of the latter one. Its mechanism consists of a piston, link pins and four wheels. Specimens are fixed on the center of the wheels and twisted by swing of the wheels. To set up several loading levels for the specimens, each wheel has plural pin holes where the distances are different from center. However, since connecting the two wheels on a single link pin, the stress level can be tested at one time is two conditions. Needle roller bearings are press-fitted in the pin holes for reduction of gaps and friction. Contact portions of the component parts with relative movement of the testing machine are rolling contact and so as to suppress the heat generation due to friction.

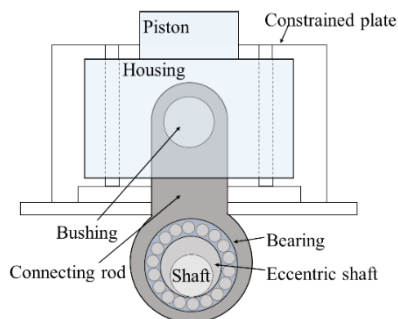


Figure 1 Rotating-reciprocating conversion mechanism

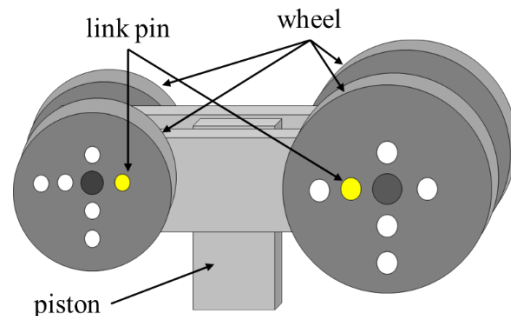


Figure 2 Reciprocating-swinging conversion mechanism

Function confirmation of torsional testing machine

First, the relationship between the operating frequency and the temperature rotating-reciprocating conversion mechanism was examined to evaluate fever due to friction. Temperature measured points were around the bearing, the bushing and housing. Temperature measurement was carried out a step-up idling method using a thermocouple. As a result of the

measurement, the temperature at any points became gradually higher with the increase of the operating frequency, and the temperature in the vicinity of the bearing was the highest temperature. The temperature was stabilized at 304 K with operating frequency 50 Hz. Thus we concluded that this testing machine can operate by a frequency range to 50 Hz.

Next, the swinging angles of the wheels were confirmed to evaluate the test accuracy. The swinging angle was calculated by measuring the displacement of the reflection plate which was attached to the wheel shaft by a laser displacement meter. Figure 3 shows the swinging angles of the wheels obtained in each hole position by inserting the link pin and the design value. In the figure, two kinds of plots in the same hole numbers are meant to be respective data of the two wheels. The measurement results obtained at all of the hole positions fell within less than 5 % of errors from design values. Therefore we judged that the intended dynamic functions of this testing machine could be reproduced.

Then, the torsion angle of specimen was confirmed to evaluate the test accuracy. The torsional angle of specimen was also measured using the laser displacement meter. Measurement points were three positions of near the chuck portions and the center of the specimen. Figure 4 shows the measured torsional angle of the specimen. Also the designed torsion angle is indicated by a solid line. The measurement values fell within less than 1 % of error from design values.

Based upon the foregoing, we succeeded in development of the torsional fatigue testing machine which can conduct fatigue tests for multiple specimens at high speed.

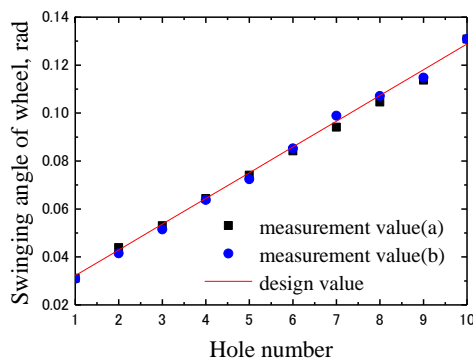


Figure 3 Swinging angle of wheels obtained in each hole position and design value

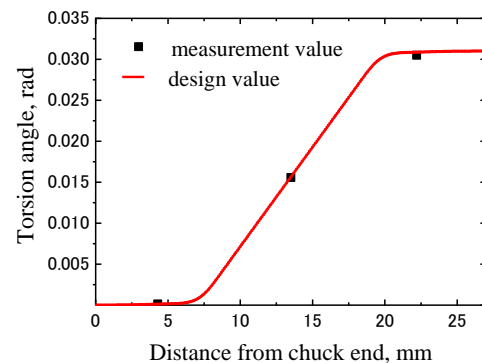


Figure 4 Measured value and design value of torsion angle of specimen

Torsional Fatigue Test

Torsion fatigue tests of JIS-S45C material were performed by means of the developed testing machine in the room atmosphere without any control of temperature and humidity. Diameter of the chuck portion is 10 mm, and the parallel portion for dumbbell-shaped specimen is 3 mm. It is provided with two fillets in order to reduce the stress concentration. The stress concentration factor of this specimen in torsion is given as 1.049 from FEM analysis. Example of photo image of a crack generated in the specimen at stress level of $\tau_a = 705$ MPa, $N = 3.0 \times 10^4$ cycles is indicated in Fig. 5. It was confirmed that fatigue crack was generated in the axial direction and perpendicular thereto a circumferential direction of the specimen due to shear stress. Exact fatigue life is currently under consideration on the basis of the changes in the torsional angle data, because the rate of the changes of torsional angle is found to vary depending on the relationship between the measurement position of torsional angle and the crack generating position.



Figure 5 Example of photo image of a crack generated in the specimen

Conclusions

Torsional fatigue testing machine in which four specimens can be tested at high speed at the same time was developed. This testing machine can be operated up to a load frequency of 50 Hz. Result of verification of the torsional angle of specimen, the accuracy was less than 1 % of the design value. In addition, as results of the torsional fatigue tests, fatigue cracks were generated in the axial and circumferential direction, it was confirmed that the shear stress was dominated fatigue fracture.

GUIDED WAVE PROPAGATION IN WIRE CABLE UNDER TENSILE STRESS

Takuma MATSUO^{1*} and Shunsuke OZONO¹

¹*School of Science and Technology, Meiji University*

**matsuo@meiji.ac.jp*

Keywords: Wire cable, Guided wave, Nondestructive testing, Wavelet transform, Group velocity

Wire cables are widely used for mechanical and structural components. To evaluate the damage and degradation of a wire cable, a nondestructive inspection technique utilizing guided waves is desirable. However, calculating the propagation mode in wire cables is difficult because they consist of twisted threads. In our previous study, we examined the guided-wave propagation in a wire cable with no tensile force [1]. We found that the group velocity and amplitude dispersion were not similar to those of a rod. Moreover, the guided waves were mainly propagated in threads where the input signal was excited. In the present study, we experimentally evaluated the propagation of guided waves under tensile stress.

The propagation behavior of guided waves under tensile stress was first evaluated using the experimental setup shown in Fig. 1. Guided waves were produced and detected by a pair of PZT transducers (PAC, R50 α). The transducers were installed on the wire-cable surface, separated by 600 mm. Step signals of 300 V was applied to one of the transducers, and a guided wave was excited. The guided wave was detected by the other transducer and fed to the oscilloscope via a pre-amp and 100-kHz high-pass filter. The wire cable a fiber core wound with seven strands. The core and strands were composed of twined steel wires. The tested wire cable was made of SUS304 and had an outer diameter of 3.0 mm [2]. Under these conditions, the amplitude of the signal had dispersion because the contact force of the threads in the wire cable was not constant. On the other hand, the detected waveforms were constant in the wire cable with tensile force. According to the wavelet contour maps of the detected waves, the propagation mode of the guided waves was similar to the longitudinal and flexural modes of a rod. These modes were denoted as the L-like mode and F-like mode. Figure 2 shows the change in the maximum amplitude of the L-like mode packet. These data were detected using the positions of the transducers for which the maximum amplitude signal was detected with no tensile stress. The maximum amplitude decreased as the tensile force increased. This trend was caused by the contraction of the cross section, which caused the contact among the neighboring

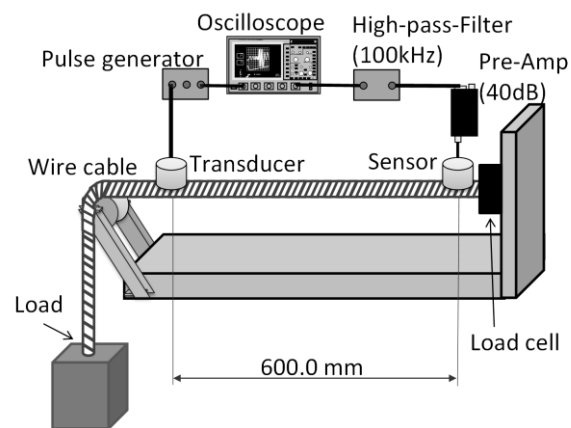


Fig. 1 Experimental setup for detecting guided wave propagated on wire cable with tensile stress.

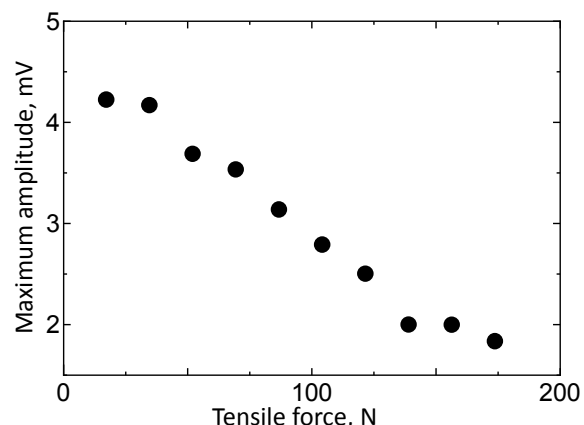


Fig. 2 Change in peak-to-peak amplitude of longitudinal-like mode packet as a function of tensile load.

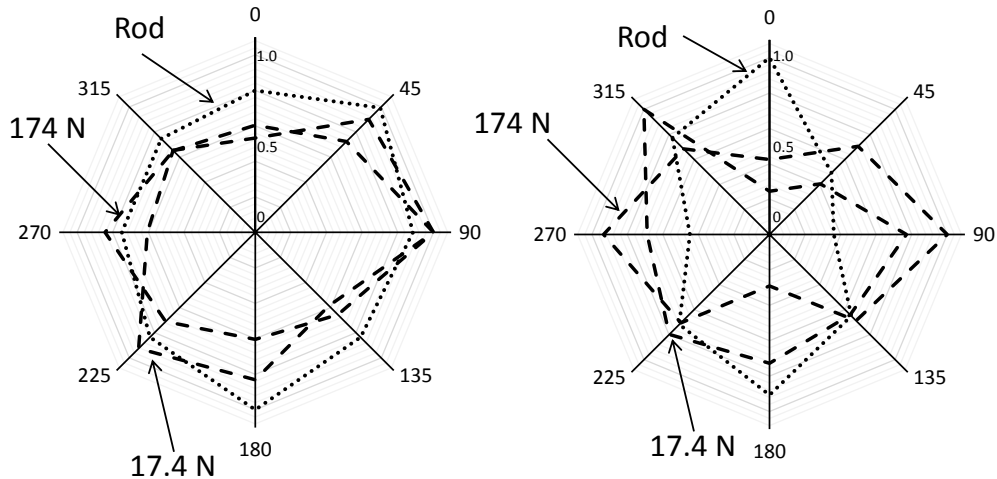


Fig. 3 Normalized maximum-amplitude profiles for the L-like (left) and F-like (right) modes. The out-of-plane displacement for the L-like mode was almost constant, whereas the displacement for the F-like mode had angular dependence and changed as a function of the axial distance from the excitation point. This change was according to the thread on which excitation transducer was mounted. These characteristics were similar to those of an elastic wave in a rod [3].

unit strands in the wire to be more greatly influenced by the increasing tensile-stress intensity.

The out-of-plane displacement of each mode was examined. Figure 3 shows normalized maximum-amplitude profiles for the L-like (left) and F-like (right) modes. The out-of-plane displacement for the L-like mode was almost constant, whereas the displacement for the F-like mode had angular dependence and changed as a function of the axial distance from the excitation point. This change was according to the thread on which excitation transducer was mounted. These characteristics were similar to those of an elastic wave in a rod [3].

Next, the relationship between the defect area and the amplitude of the guided wave was evaluated. Three types of 10-mm ϕ wire cable with different defect areas were compared, and the amplitude of the transmitted wave was measured. The experimental setup was the same as that shown in Fig. 1; however, a defect was added in the center of the wire cable. Figure 4 shows the relationship between the cross-sectional loss and amplitude loss for the L-like mode. Here, the black circles indicate the average results and solid bar indicated the dispersion of the data. The amplitude loss of the L-like mode and defect size exhibited a relationship; however, dispersion of the amplitude occurred. It was determined that the contact between the sensor and thread was not constant.

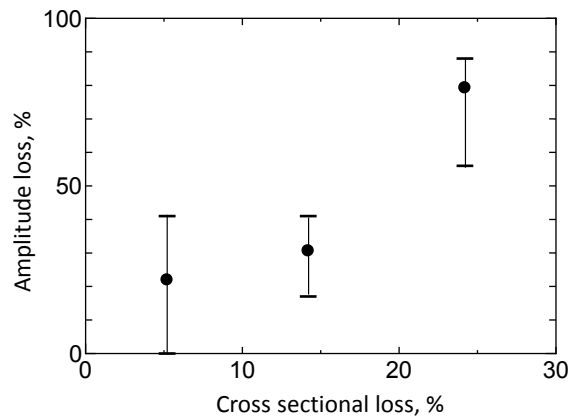


Fig.4 Relationship between cross-sectional loss and amplitude loss for L-like mode.

References

[1] Matsuo, T. and Seshime, A., Elastic Wave Propagation in Wire Cable for Corrosion Monitoring and Evaluation, Corrosion Engineering, 63-11(2014), pp.456-461.
 [2] Ono, S., Kougaku-no-Suugaku (Mathematics for Engineers), AGNE Gijutsu Center, 2005, p.5 (in Japanese).
 [3] Rose, J., Ultrasonic Waves in Solid Media, Cambridge University Press, 1999.

BEHAVIOR ON GENERATION AND PROPAGATION OF FATIGUE CRACK FOR WC-Co CEMENTED CARBIDES

Hiroko MIKADO^{1,2}, Shingo KAWAMURA² and Noriyasu OGUMA^{3,*}

¹ Graduate Student, Graduate School of Science and Engineering, University of Toyama, Gofuku 3190, Toyama-shi, Toyama 930-8555 Japan

² Engineer, Machinery and Engineering Group, YKK Corp., Yoshida 200, Kurobe-shi, Toyama 938-8601 Japan

³ Professor, Faculty of Engineering, University of Toyama, Gofuku 3190, Toyama-shi, Toyama 930-8555 Japan

* oguma@eng.u-toyama.ac.jp, Tel&Fax: +81-76-445-6776

Keywords: WC-Co cemented carbides, Fatigue crack generation, Fatigue crack propagation, Grain size, Crack growth pass

Introduction

It is well known that WC-Co cemented carbides have excellent wear resistance. Taking advantage of its characteristics, the material is used for cutting tools and dies. However, the tools or dies in some cases leading to fracture failure in cracking or chipping during use. Therefore it is important to grasp the fatigue crack growth resistance because of the brittle material. In this study, in order to examine the influence of WC grain size exerting the fatigue crack generation and its propagation, rotating bending fatigue tests and short crack growth tests were performed using WC-Co cemented carbides specimens with three grades WC grain-sizes. The plane specimens and the artificially defect specimens were used for the tests respectively.

Specimen and Experimental Procedure

The materials used in this study were WC-13%Co cemented carbides with different WC grain sizes. They are labeled as fine-grained WC (average grain size of 0.45 μ m), medium-grained WC (0.76 μ m) and coarse-grained WC (1.08 μ m), respectively. Figure 1 shows the shape and dimensions of specimens. Diameter of the critical portion for the hourglass type specimen is 3 mm, and the round notch radius is 10 mm. The stress concentration factor of this specimen in bending is given as 1.04. Figure 1(a) indicates the plane specimen, and (b) indicates the micro-defect specimen. For the latter, the artificial defect with a length of 80 μ m, a width of 20 μ m and a depth of 40 μ m was introduced into the center of the specimen by laser beam machining.

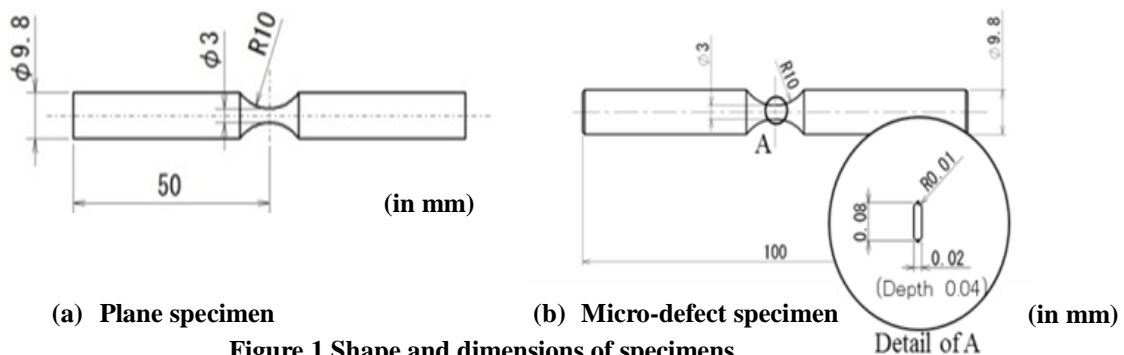


Figure 1 Shape and dimensions of specimens

Rotating bending fatigue tests were performed by means of a cantilever-type rotating bending fatigue testing machine in the room atmosphere without any control of temperature and humidity. Frequency of cyclic load applied 5-15 Hz. To evaluate the rate of fatigue crack growth of a micro surface crack, the fatigue tests were interrupted at constant intervals to obtain replicas of the specimen surface. The crack lengths recorded on the replicas were measured using an optical microscope.

Experimental results

Figure 2 shows the experimental *S-N* characteristics for three grades of WC grain specimens. From this figure, the fatigue life for the specimens of finer WC grain-size was longer. An example of SEM

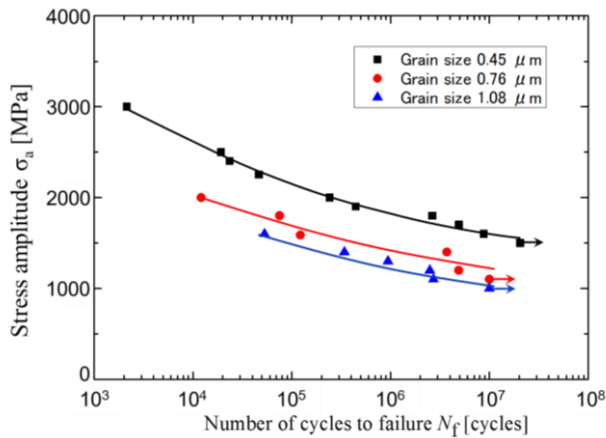


Figure 2 S-N characteristics for WC-Co cemented carbides

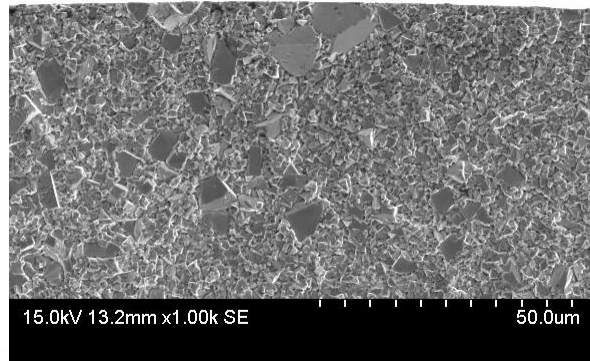


Figure 3 SEM image of the fracture surface for coarse-grained WC specimen at $\sigma_a = 1100\text{MPa}$

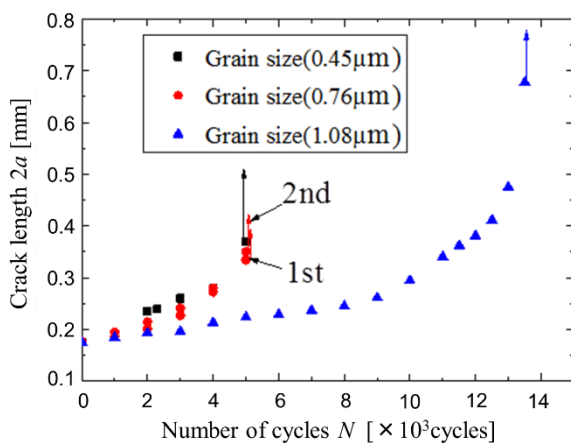


Figure 4 Crack growth behavior tested at $\sigma_a = 600\text{MPa}$

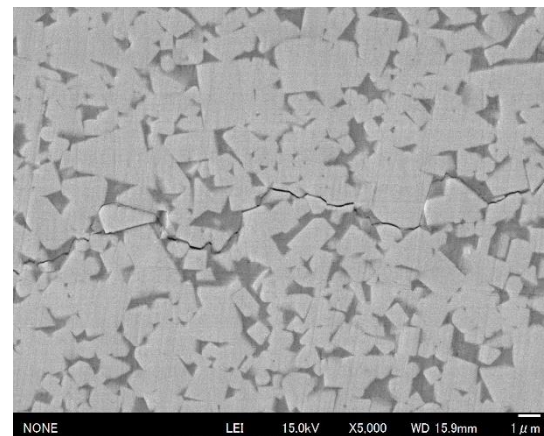


Figure 5 Crack propagation path appeared on the surface for coarse-grained WC specimen

observation of the fracture surface for coarse-grained WC specimen is shown in Fig. 3. It is found that the crack initiation sites were relatively large WC grain in the surface. The crack origin of all the failed specimens were such a large WC grain. Therefore it can be considered that the fatigue life depends on an existence probability of large WC grain.

Figure 4 indicates the increase of crack lengths of the specimen surfaces shown in Fig. 1(b) as a function of number of cycles from the results of the micro surface crack growth tests. As can be seen from Fig. 4, the crack growth rate for the specimen of rougher WC grain-size was lower. The observation photograph of crack propagation path of the surface for coarse-grained WC specimen is shown in Fig. 5. The fatigue crack grows mainly along the WC/WC boundary or WC/Co boundary with avoiding the WC grains.

Considering by comparing the results of the above two types of experiment, the crack propagation life of fine-grained WC alloy is short, and its crack generation life is much longer. On the contrary, the crack propagation life of coarse-grained WC alloy is long, and its crack generation life is not so long. Thus the finer WC grain size to be suitable to improve the fatigue strength of WC-Co cemented carbides.

Conclusions

- (1) The results of rotating bending fatigue tests, the fatigue life of the finer grained WC-Co cemented carbides was improved.
- (2) According to the results of crack propagation tests, the crack propagation life of the coarse grained WC-Co alloy was longer. Thus the fatigue life of WC-Co cemented carbides is estimated to be governed to the crack generation life.
- (3) From the two types of experiment, it is concluded that the finer WC grain size to be suitable to improve the fatigue strength of WC-Co cemented carbides.

A DEVICE OF GAS TRANSMISSION RATE FOR THIN FILMS IN A HYDROGEN STORAGE SYSTEM

Hiroki Mano^{1,*}, Mitsuo Notomi²

¹*Graduate Student, Department of Mechanical Engineering, Meiji University, 1-1-1 Higashi-mita, Tama-ku, Kawasaki, Kanagawa, 214-8571 JAPAN*

²*Professor, ditto*

*ce42076@meiji.ac.jp

Keywords: *Gas transmission rate, Hydrogen storage amount, Measuring device, Thin film, Carbon based material*

Introduction

Hydrogen storage materials, which are represented by hydrogen storage alloys and/or carbon based materials, have attracted a great deal of attention. Although hydrogen storage alloys have high hydrogen storage density per unit volume, their hydrogen storage density per unit mass is low due to their weight, and they have inferior cycling characteristics. Carbon based materials possess light weight, high specific surface area and nanopores which are valuable in hydrogen adsorption and the materials have excellent cycling characteristics due to the physical adsorption that depends on temperature and/or pressure change monotonically. In addition the materials show high adsorption performance at low temperature under high pressure and they alone can't really adsorb at room under atmospheric one.

One of the solutions for increasing the adsorbing amount is that the materials are wrapped in thin films of which hydrogen permeation depends on temperature and/or pressure change non-monotonically. If hydrogen permeation of the films has changed dramatically at a point of temperature and/or pressure, the materials with the thin films could control the amount for the temperature and/or the pressure. Hirotsuki et al.[1] prepared the samples of Mg-Formate powder sealed with the laminated film, originated Teflon tape with Silicon adhesive and sputtered Pt as a catalyst, and they have reported that sealing with it improves hydrogen absorption amount of the Mg-Formate; while that of the commercial its powder is 0.297 wt.% at 298 K at 2.0 MPa, that of the sample is 0.424 wt.% at the same conditions. Since the Mg-Formate also adsorbs hydrogen with the physical adsorption as with the carbon based materials, it can be expected that the hydrogen storage system with the materials shows higher hydrogen storage property through the improvement of the thin films. We have considered using the laminated films which are composed of polymer and metal for the thin films, and we need to measure correctly hydrogen transmission rate and storage amount of the thin films alone at the same time. The purpose of this study was development of such a measuring device for inventing the hydrogen storage system.

Design of the gas transmission rate measuring device

Gas transmission rates of films are determined according to JIS K 7126-1 (Plastics - Film and sheeting - Determination of gas transmission rate - Part 1: Differential - pressure method)[2]. Figure 1 shows system diagram of the gas transmission rate measuring device which we designed on the basis of the JIS without a valve, a tank and a pressure sensor written in red lines. Measurement section is divided into high pressure side (HS) and low pressure side (LS) by a specimen, the laminated film. We introduce test gas into HS and calculate the gas transmission rate with pressure change in LS by the following equation.

$$GTR = \frac{V_c}{R \times T \times A \times P_u} \times \frac{dp}{dt} \quad (1)$$

GTR : Gas transmission rate[mol/(m²·s·Pa)], *V_c* : Volume of LS[l], *T* : Test temperature[K], *P_u* : Pressure of HS[Pa], *A* : Area of transmission[m²], *dp/dt* : Pressure change of LS per unit time[Pa/s], *R* : 8.31×10³[L · Pa/(K · mol)]

Furthermore, we divided the measurement section in two parts, measurement system (MS) and sample system (SS), by a valve written in red line, and we added a pressure sensor to MS for measuring the hydrogen storage amount. It is based on JIS H 7201[3]. We can calculate the theoretical value of pressure in MS plus SS using ideal gas law with volume and former pressure in MS and volume in SS. Hydrogen storage amount is obtained by comparing pressure in MS plus SS when it is equilibrium state after proceeding transmission and the theoretical value.

In addition, we added a tank to MS to avoid pressure decrease of HS due to gas transmission from HS to LS. Entire assembly drawing of the gas transmission rate measuring device based on the above is shown in Figure 2; left is a front view and right is a side view. In order to inhibit tubes deformation, each valve is fixed on a panel, the lower flange is fixed on a table and a flexible tube is used for a part of connecting pump.

Conclusion

We designed the gas transmission rate measuring device which can also measure hydrogen storage amount for thin films, and this device was designed to combine the principle of JIS K 7126-1 and H 7201. Next, we will evaluate some polymer thin films with this device and eventually develop the hydrogen storage system with the films and carbon based materials.

References

- [1] Shota Hirotaki, Mitsuo Notomi, Hydrogen absorption property of Magnesium Formate by spillover at the ambient temperature, TMS2015, March 18/2015
- [2] JIS K 7126-1, Plastics-Film and sheeting-Determination of gas-transmission rate-Part 1: Differential-pressure method, (2006), pp. 1-6
- [3] JIS H 7201, Method for measurement of pressure-composition-temperature (PCT) relations of hydrogen absorbing alloys, (2007), pp,1-7

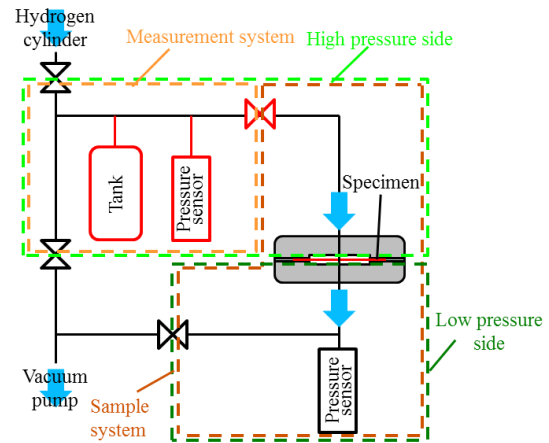


Figure 1 System diagram of the gas transmission rate measuring device

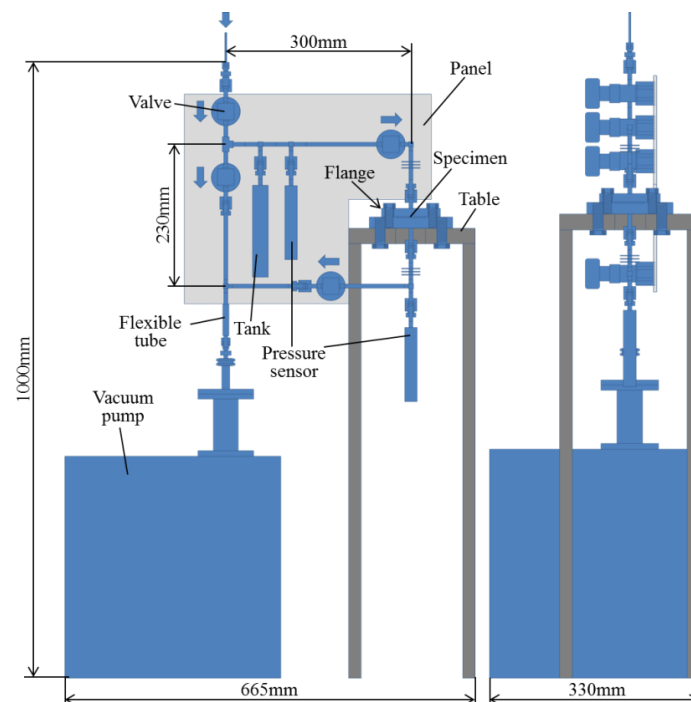


Figure 2 Entire assembly drawing of the gas transmission rate measuring device

THE STUDY OF VARIANT SELECTION FOR SHAPE MEMORY EFFECT ON FE-MN-SI BASED ALLOY WITH EBSD

Naohiro OKUBO^{1,*}, Hiromu ISHII¹, Mitsuo NOTOMI²

¹ Graduate Student, Department of Mechanical Engineering, Meiji University

² Professor, Department of Mechanical Engineering, Meiji University

*ce42017@meiji.ac.jp

Keywords: Fe-Mn-Si based alloy, shape memory effect, stress induced transformation, variant selection, single variant

1. Introduction

Shape memory alloys can recover the original shape by heating and/or unloading after deformed. Ni-Ti alloy has used practically for many applications due to the fine recovery effect. Contrast to poor workability and expensive cost of Ni-Ti alloy, ferrous shape memory alloys have good workability and reasonable cost. Fe-Mn-Si based alloy has been utilized in pipe joints, although the amount of this shape recovery is less than that of Ni-Ti alloy.

The shape memory effect (SME) in Fe-Mn-Si based alloy is associated with $\gamma \rightleftharpoons \epsilon$ martensitic transformation which is caused by motion of the Shockley partial dislocation and martensite phase can sometimes made to form variants by stress induced transformation in several conditions. The four orientations of the variants in Fe-Mn-Si based alloy could be formed according to Shouji-Nishiyama (S-N) orientation relationship between the austenite phase (A-phase) and the martensite phase (M-phase). If one direction of the variants only was formed in the transformation, what is called as the single variant formation, this alloy would have a good SME since the back way would have been limited in inverse transformation. Some authors [1][2] reported the single variant formation under stress induced transformation and the effect of variant selection in SME.

We studied the crystal orientation of M-phase in Fe-Mn-Si based alloy with electron backscatter diffraction (EBSD). The amount of shape recovery was quantified by means of bending test. The best shape recovery ratio was about 86% for the specimen annealed 873[K]. From these results, the effect of variant selection to SME was discussed and also we studied the relationship between the variant selection and the direction of the applied stress on the basis of crystallography.

2. Experimental methods

Fe-28Mn-6Si-5Cr alloy (mass%) was used as a wire, its diameter is $\phi 1.2$ [mm] and the wire was cut three pieces as the length about 5[mm]. The chemical composition is showed in Table 1. One of them is called As-received specimen. The others were annealed with a holding jig to memory the original shape. They were heated at 873[K] and 1273[K] for one hour and then cooled in furnace and these specimens are called each Ann.873 specimen and Ann.1273 specimen respectively.

To obtain the shape recovery, each specimen was bended at a constant radius of curvature using the material testing machine with strain controlled and heated them to 923[K] for 15 minutes in the purpose of shape recovery. The best shape recovery ratio was about 86% for Ann. 873 specimen as shown in Table 2. The EBSD analysis was carried out to only Ann.873 specimen and to tensile area after bending Ann.873 specimen. We cut them 5[mm] length and pile up specimens and carbon tape on aluminum die, finally embedded together in cup of $\phi 8$ [mm]. We polished the fine surface as the less roughness to measure with EBSD.

Table 1 Chemical composition (mass%)

C	Si	Mn	P	S
0.047	5.69	27.2	<0.003	<0.009
Cr	Ni	N	O	
5.02	0.033	0.012	0.002	

Table 2 Shape recovery ratio in each specimen

Specimen name	Shape recovery ratio
As-received specimen	11% (10[deg.]/90[deg.])
Ann.873 specimen	86% (62[deg.]/73[deg.])
Ann.1273 specimen	28% (28[deg.]/100[deg.])

3. Result and discussion

Table 3 shows Inverse Pole Figure (IPF) maps and Pole Figures (PF) in Ann.873 specimen. In IPF maps, each color level represents to the crystal orientation at the point for the normal direction to the polished surface according to the stereo triangle indices shown in the top right of each figures. The PF indicates the direction of crystal orientation at each position analyzed in IPF maps to a circle projected sphere by means of stereographic projection and density of crystal orientation represents the color contrast. In Table 3, the amount of M-phases (e) to (g) increases after bending instead of decreasing the amount of A-phases (a) to (c). M-phases might be formed from A-phases due to stress-induced transformation caused by bending deformation. In Table 3, tensile texture before bending, (b) is existed to the longitudinal direction due to wire drawing and variants are formed to prior orientation after bending, (h). Variants might be formed to prior orientation for variant selection changed by tensile texture and annealing (f) to (h). It found that formation of variants to prior orientation is related to variant selection and that affects the improvement of SME.

We studied particularly the relationship between prior orientation of variants and tensile stress by deformation. Fig. 1 shows PFs of each single grain enclosed color line in Table 3 (c). In Fig. 1, four color circles of each single grain correspond to the crystal orientation of A-phase. Variants were only formed to one direction of red circle after deformation and that means a single variant is formed by stress-induced transformation. Fig. 2 shows the angles of prior orientation of variants to tensile stress. The red and blue arrows in Fig. 2 represent each direction of tensile stress and prior orientation. High degree of Schmid's factor, 0.47 was calculated at the angle between red and blue arrows and shows more activation of dislocation movement. If dislocation movement is more activated, variants might be formed to prior orientation.

4. Conclusion

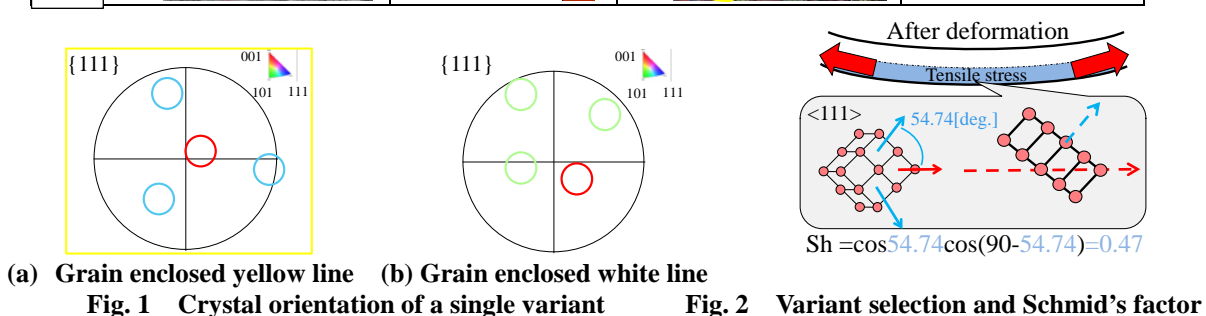
Variant selection might correspond to the activation of dislocation movement as one of the factor. The grain of high Schmid's factor produces concentrating a prior orientation in four directions and then improves SME.

References

- [1] O. Matsumura ,S. Furusako ,T. Furukawa and H. Otsuka, Formation of Surface Texture and Anisotropy of Shape Memory Effect in an Fe-Mn-Si Alloy, ISIJ Int. 36, (1996), pp1103
- [2] B.H. Jiang , X. Qi , Y.L Ren and C.Q. Wang, Effect of Annealing Texture on Shape Memory Effect in an Fe-Mn-Si-Cr Alloy Wire, Mater. Trans. JIM 41, (2000), pp1703

Table 3 Change of crystal orientation in Ann.873 specimen

	Before bending		Tensile area after bending	
	IPF map	PF	IPF map	PF
Austenite (fcc)				
Martensite (hcp)				



CHARACTERISTICS OF METAL MATRIX COMPOSITES REINFORCED WITH PALM OIL FLY ASH FABRICATED BY USING STIR CASTING AND CENTRIFUGAL CASTING METHODS

Suprianto^{1*}, Tugiman¹, Chandra Andrika², Nursuci Ade², Hiroshi Asanuma³

¹Lecturer, Mechanical Engineering Department, Faculty of Engineering, University of Sumatera Utara
Jalan Almamater Kampus USU, Medan 20155 INDONESIA

²Student, Mechanical Engineering Department, Faculty of Engineering, University of Sumatera Utara
Jalan Almamater Kampus USU, Medan 20155 INDONESIA

³Professor, Graduate School of Engineering, Chiba University
1-33, Yayoicho, Inage-ku, Chiba-shi, Chiba, 263-8522, Japan

*Corresponding author: suprianto.t@gmail.com, Tel: (061)8211236, Fax: (061)8213250

Keywords: Metal Matrix Composite, Casting, Aluminum

1. Introduction

Metal Matrix Composites (MMCs) are type of materials that have been developed in recent years to be used widely. The uses of MMCs have different goals such as reduction of mass, wear resistance, and so on. The properties of MMCs are determined by the nature of the basic constituent components [1]. Fly ash can improve the properties of MMCs such as hardness, compression strength and impact strength due to an increase in mass% fly ash together with a decrease in the density [2,3]. MMCs have been fabricated by using casting methods, where ceramic particles mixed with molten metals as a matrix [4]. Stir casting is one of the methods which have succeeded in making MMCs [5] in conjunction with centrifugal casting to obtain higher hardness of castings [6]. Most of the manufactures of MMCs for strengthening purposes use fly ash from coal, and rarely use that from palm oil as composite reinforcement. The objective of this research is to examine the opportunity of using palm oil fly ash in the manufacture of MMCs using stir and centrifugal casting methods.

2. Experimental

Variation of composition was conducted from 2.5 to 12.5 mass% palm oil fly ash, put into molten aluminum in crucible at 735°C pouring temperature and 450°C mold one. Locally produced fly ash having the typical composition showed in Figure 1(b) was used in this research. Samples obtained from this processes were tested to obtain mechanical and physical characteristics. Figure 1(a) shows a schematic of centrifugal casting that was used to fabricate them.

3. Results and discussion

The densities of the MMCs fabricated by stir casting as a function of composition are shown in Figure 2(a). Because of low density of the palm oil fly ash, density of the MMCs tends to decrease with increasing its mass%. Figure 2(b) shows hardness of the MMCs, where the hardness increases with increasing the percentage of fly ash. The results of impact testing are shown in Figure 2(c) and microstructures are shown in Figure 3(a), (b) and (c). Decrease in impact strength was found, which is thought to be caused by poor wettability and inhomogeneous distribution of fly ash. Microstructure

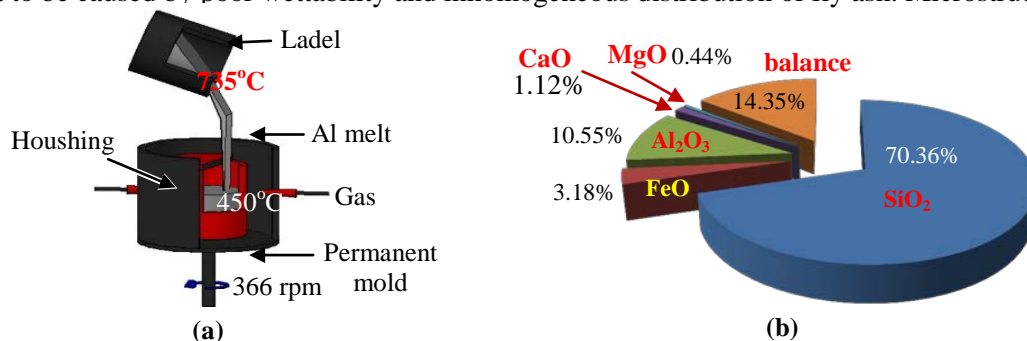


Figure 1(a) Schematic of centrifugal casting and (b) palm oil fly ash composition.

consist of a matrix of aluminum MMCs with palm oil fly ash and Si distributed among the grain boundaries. Figure 4 shows the impact energy influenced by grain size and elongation decreased than raw material, but stable as the increase in mass% fly ash.

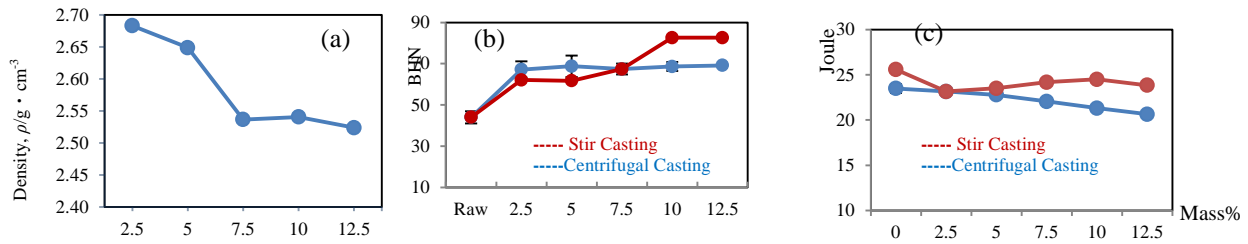


Figure 2 Effect of mass% fly ash on (a) density, (b) hardness and (c) impact energy of MMCs.

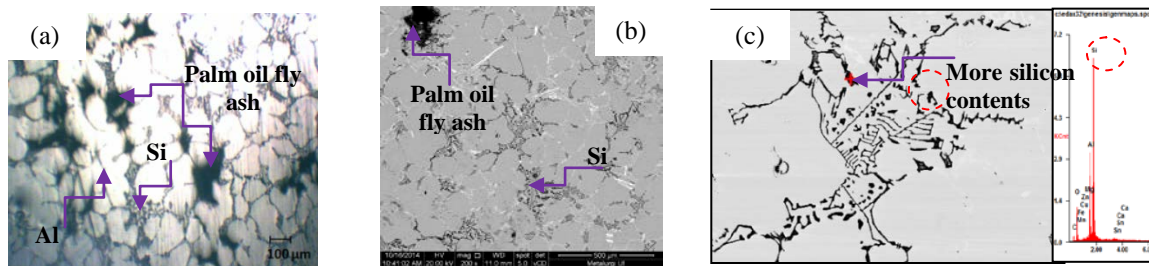


Figure 3 Microstructures of 5mass% palm oil fly ash MMC (a) optical micrograph (HF etched), (b) SEM photograph, and (c) result of EDS analysis.

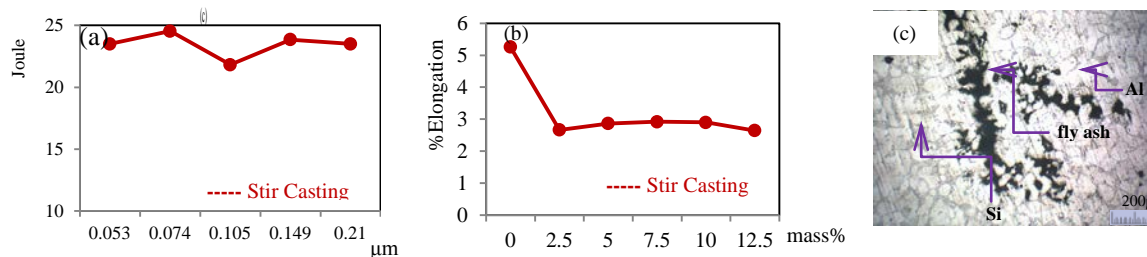


Figure 4 (a) Effect of particle size on impact energy, (b) effect of mass% fly ash on %elongation and (c) microstructure of 10 mass% fly ash.

4. Conclusions

MMCs reinforced with palm oil fly ash were tried to be fabricated in this study and the following conclusions were obtained:

- 1) Stir casting and centrifugal casting have successfully produced MMCs reinforced with palm oil fly ash, of which hardness increase with increasing mass% of palm oil fly ash in the experimented range.
- 2) The distribution of the fly ash particles tends to localize along the grain boundaries and not homogeneous.

References

- [1] K.U.Kainer, Metal Matrix Composites. Custom-made Materials for Automotive and Aerospace Engineering, WILEY-VCH Verlag GmbH & Co. KGaA, Weinheim, ISBN: 3-527-31360-5 (2006).
- [2] K.V.Mahendradan and K. Radhakrishna, Fabrication of Al-4.5% Cu alloy with fly ash metal matrix composites and its characterization, Materials Science-Poland, Vol. 25, No. 1 (2007), 57-68.
- [3] J. Babu Rao, D.Venkata Raodan and N.R.M.R.Bhargava, Development of light weight ALFA composites, International Journal of Engineering, Science and Technology, Vol.2, No. 11 (2010), 50-59.
- [4] S.Sarangidan and D. Kumar, Fabrication and Characterization of Aluminium-Fly Ash Composite Using Stir Casting Method, A Thesis, Department of Metallurgy & Materials Engineering, National Institute of Technology,Rourkel, (2009), 16-17.
- [5] J. Hashim, The Production Of Cast Metal Matrix Composite By A Modified Stir Casting Method, JurnalTeknologi, 35 (A), (2001), 9-20.
- [6] A.Jayakumardan and M.Rangaraj, Property Analysis of Aluminium (LM-25) Metal Matrix Composite, International Journal of Emerging Technology and Advanced Engineering, Vol.4,Issue 2(2014),495-501.

MECHANICAL PROPERTIES OF AMORPHOUS CARBON FILMS DEPOSITED FROM CARBON ISOTOPE MATERIALS

Yutaro Suzuki¹, Junko Hieda¹, Naoto Ohtake¹, Hiroki Akasaka*¹

¹ Tokyo Institute of Technology, 2-12-1 Ookayama, Meguro-ku Tokyo, 152-8552 Japan

*akasaka@mech.titech.ac.jp

Keywords: Amorphous carbon film, Stable isotope, Hardness, True density, Isotopic effect

1. Introduction

An amorphous carbon (*a*-C) film is mainly consisted of sp^2 and sp^3 -bonded carbons and shows interesting mechanical properties owing to mixed structures of sp^2 and sp^3 -bonded carbons. At isotopes of carbon atom, ^{13}C is stable and usable nonradioactive isotope material. ^{13}C has different characteristics from ^{12}C ; thus, the incorporation of ^{13}C into *a*-C films may lead to more advanced functions¹⁾. On studies of electrical properties on the diamond, some studies reported about ^{13}C isotopic effects^{2,3)}. On the other hand, the deposition of amorphous isotopic carbon films are few. In this study, amorphous carbon films which contained isotopes of carbon were deposited, and their structure and properties were evaluated to investigate isotopic effects.

2. Experimental

a-C and hydrogenated *a*-C(*a*-C:H) films which contained isotope of carbon were deposited on a p-type Si(100) substrate using a pulsed magnetron sputtering or a plasma chemical vapor deposition. On *a*-C deposition, Carbon (99.98%) and ^{13}C (99%) targets were used as source materials. On *a*-C:H deposition, methane(CH_4 , 99.999%), deuterated methane(CD_4 , 99%) or ^{13}C methane($^{13}\text{CH}_4$, 99 %) gases were used as source materials. These gases were introduced into the vacuum chamber and a 13.56 MHz radio frequency power of 20 W was applied to a substrate at 20 Pa.

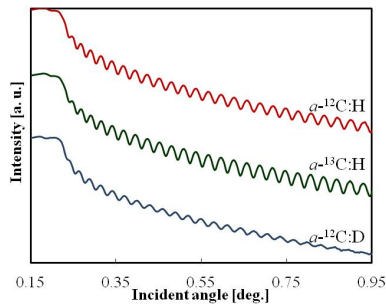
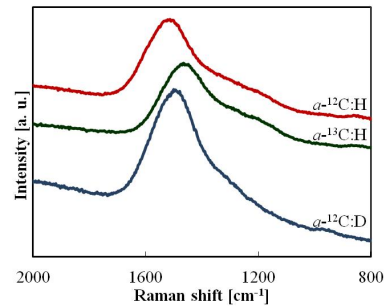
Film density was evaluated by X-ray reflectivity (XRR). The XRR pattern was obtained using a CuK_α X-ray diffractometer (X'Pert PRO MRD Phillips). The structure of the films was analyzed by Raman spectroscopy (NRS-1000 JASCO) using a Nd:YVO₄ laser (532 nm) with an aperture size of $\phi = 200 \mu\text{m}$. The hardness of the film was estimated by an indentation test using a Vickers diamond tip. To obtain the hardness of the film of nm-order thickness, a high-resolution indenter (HM500 Fischer Instruments) with a pico-meter depth resolution was used. Indentation reached maximum loads of 100 μN at 10 s. At maximum loads, the load was kept 5 s to obtain the creep rate.

3. Results and discussion

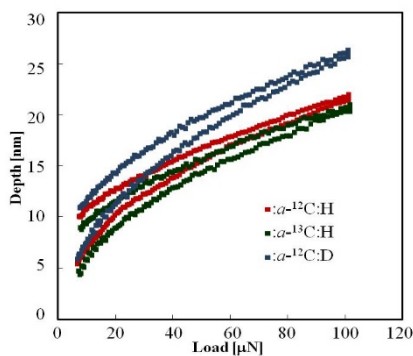
In this abstract, results about *a*-C:H films were described. Although the deposition conditions of these films were the same except for the raw material, film structure and properties indicated difference.

Figure 1 shows XRR patterns of the films. By simulation fitting, the XRR pattern densities of *a*- ^{12}C :H (1.70 g/cm^3), *a*- ^{12}C :D (1.54 g/cm^3) and *a*- ^{13}C :H (1.75 g/cm^3) films were obtained. The density of the *a*- ^{12}C :D film was lower than that of the other films. One of the possible reasons for this difference is that the plasma condition at the deposition had large difference because their dissociation and ionization energies were affected by the isotopic effect.

Figure 2 shows the Raman spectra of the *a*-C:H films. In all the Raman spectra, two broad bands appear, namely, the G (graphitic)-band at approximately 1500 cm^{-1} and the D (disorder)-band at approximately 1300 cm^{-1} . G-band peaks originate from the E_{2g} resonance oscillation in graphite structures and are due to the residual sp^2 bonds. Hence, the G-band represents the order of a graphite structure. On the other hand, Tuinstra and Koenig assigned the D-band to first-order scattering from a zone boundary phonon activated by disorder on the basis of the finite crystallite size⁴⁾. Briefly, the D-band represents the boundary of the graphite structure. To analyze data on the order of graphite cluster size, the integrated peak ratio, I_D/I_G , was calculated from the Raman spectra. The change in I_D/I_G suggests a change in the continuous order of graphite cluster size. These Raman spectra were fitted by Gaussian line shapes using curve-fitting software. Values of I_D/I_G were 0.57, 0.70 and 0.37 for *a*- ^{12}C :H, *a*- ^{13}C :H and *a*- ^{12}C :D films, respectively. The order of the graphite cluster size of *a*- ^{13}C :H is smaller than that of *a*- ^{12}C :H. The G-peak position of the *a*- ^{13}C :H film indicated a clearly lower wave number than that of the *a*- ^{12}C :H and *a*- ^{12}C :D films. This shift was reported as an isotopic effect⁵⁾. From these values of I_D/I_G , the graphite cluster


Fig. 1. XRR patterns of the a -C:H films

Fig. 2. Raman spectra of the a -C:H films

size of a - $^{12}\text{C:D}$ is larger than that of other films. Hence, the reason of low density compared with other 2 films is not graphite layer. This reason may be caused by containing of the polymer-like components at a -C:D film. Raman spectra for a -C:D indicated the gradient base line which mean containing of the uniaxially oriented conjugating polymer.


Fig. 3. Indentation depth-load profiles.
Table Results of nano-indentation tests.

	a - $^{12}\text{C:H}$	a - $^{13}\text{C:H}$	a - $^{12}\text{C:D}$
Martens hardness [GPa]	4.2	4.1	3.0
Young's modulus [GPa]	81	81	56
Creep rate [nm/s]	0.10	0.07	0.11

Figure 3 shows indentation depth-load profiles. Martens hardness, Young's modulus, and creep rates were calculated, shown in Table. The hardness and Young's modulus of the a - $^{12}\text{C:D}$ film were smaller than those of other films. This result were matched with suggestion of the containing of the polymer-like components from results of Raman measurements.

Although Martens hardness and Young's modulus showed similar values on a - $^{13}\text{C:H}$ and a - $^{12}\text{C:H}$ films, the creep rate indicated large difference. The creep rate suggests the deformation resistance, and is related to the vacancy size between the bonding networks. Domain size of sp^2 bonded carbon network is similar at these 2 films because I_D/I_G indicated little difference. One of the possible reasons for this difference is that the length of $^{13}\text{C}-^{13}\text{C}$ bond is shorter than that of $^{12}\text{C}-^{12}\text{C}$ bond.⁷⁾ Hence, it is considered that the volume of vacancy between bonding networks of $^{13}\text{C}-^{13}\text{C}$ is smaller than that of $^{12}\text{C}-^{12}\text{C}$.

4. Summary

To understand isotopic effects of amorphous carbon films, a - $^{13}\text{C:H}$ and a - $^{12}\text{C:D}$ films were deposited. Results of structural estimation by XRR and Raman spectroscopy indicated structural difference. Structure of a - $^{12}\text{C:D}$ showed large difference compared with other film because of the difference of plasma condition. On mechanical properties, the creep rate of a - $^{13}\text{C:H}$ indicated a small rate compared with that of a - $^{12}\text{C:H}$. This reasons for this difference is caused by the bonding length of ^{13}C and ^{12}C . These results indicated that a -C:H films were affected by isotope effect by the change of ^{13}C from ^{12}C .

5. Acknowledgement

This work was supported by "Planting Seeds for Research" program in Tokyo Inst. of Tech. And some parts of this work supported by JSPS KAKENHI Grant Number 15K18038.

References

- [1] N. V. Novikov, A. P. Podoba, S. V. Shmegeera, A. Witek, A. Zaitsev, A. B. Denisenko, W. Fahrner, M. Werner, Influence of isotopic content on diamond thermal conductivity, *Dia. Relat. Mater.*, 8 (1999), pp1602-1606.
- [2] H. Watanabe, C. E. Nebel, S. Shikata, Isotopic Homojunction Band Engineering from Diamond, *Science*, 324 (2009), pp1425-1428.
- [3] A. T. Collins, S. C. Lawson, G. Davies, H. Kanda, Indirect energy gap of ^{13}C diamond, *Phys. Rev. Lett.*, 65 (1990), pp891-894.
- [4] F. Tuinstra, J. L. Koenig, Raman Spectrum of Graphite, *J. Chem. Phys.* 53 (1970), pp1126-1130.
- [5] S. Karasawa, M. Mitsuhashi, S. Ohya, K. Kobayashi, T. Watanabe, K. Hirai, K. Horiguchi, F. Togashi, Crystal growth of epitaxial CVD diamond using ^{13}C isotope and characterization of dislocations by Raman spectroscopy, *J. Cryst. Grow.* 128 (1993), pp403-406.
- [6] H. Holloway, K. C. Hass, M. A. Tamor, T. R. Anthony and W. F. Banholzer, Isotopic dependence of the lattice constant of diamond, *Phys. Rev. B*, 44 (1991), pp7123-7126.

EVALUATION OF ADHESIVE STRENGTH BETWEEN Ti-29Nb-13Ta-4.6Zr ALLOY AND SOL-GEL FABRICATED HYDROXYAPATITE FILMS

Junko Hieda^{1*}, Mitsuo Niinomi², Masaaki Nakai², Ken Cho²

¹ Graduate School of Science and Engineering, Tokyo Institute of Technology

² Institute for Materials Research, Tohoku University

* hieda@mech.titech.ac.jp

Keywords: β -type titanium alloy, hydroxyapatite, adhesive strength, Ringer's solution

1. Introduction

The β -type Ti alloy, Ti-29Nb-13Ta-4.6Zr alloy (TNTZ), has been developed in order to achieve a low Young's modulus (~60 GPa) [1]. The Young's modulus of TNTZ is lower than that of stainless steel (~180 GPa) and Ti-6Al-4V ELI (~110 GPa), which are conventional alloys for biomedical applications. In addition, TNTZ consists of non-toxic and non-allergenic elements. Thus, TNTZ is a very suitable Ti alloy for implant devices. Although Ti and Ti alloys exhibit excellent hard-tissue compatibility attributed to osseointegration, it takes a long time to achieve the remodeling of the bone on the surface of Ti and Ti alloys. Therefore, to improve the hard-tissue compatibility of Ti and Ti alloys, various surface treatments have been developed for the formation of inorganic layers which exhibit the desired high hard-tissue compatibility. The most common way for providing the high hard-tissue compatibility is coating of hydroxyapatite (HAp: $\text{Ca}_{10}(\text{PO}_4)_6(\text{OH})_2$) on the surface of Ti and Ti alloys, which is a component of human bone. The investigation of the effect of the body environment on the adhesive strength of HAp films fabricated on the surface of the metallic implant is very important for biomedical applications. The adhesion between sol-gel fabricated HAp films and TNTZ before and after immersion in Ringer's solution was evaluated in this study.

2. Experimental procedures

TNTZ disks of 10 mm in diameter and 2 mm in thickness were cut from the TNTZ bar. The TNTZ disks were wet-polished using waterproof abrasive papers of up to #4000 grit and then buff-polished with a colloidal silica dispersion. Some of the mirror-polished TNTZ disks were polished using a waterproof abrasive paper of #600. These TNTZ disks are denoted by mechanically polished TNTZ disks hereinafter. The surfaces of mirror-polished and mechanically polished TNTZ disks were observed using an atomic force microscope. HAp films were fabricated on mirror-polished and mechanically polished TNTZ disks by a sol-gel process [2]. The phase constituents of the films were identified using an X-ray diffraction (XRD). Some of the samples were immersed in Ringer's solution at 310 K for 7 d in an incubator.

The adhesive strengths of HAp films fabricated on mirror-polished and on mechanically polished TNTZ disks were evaluated by adhesion tests according to ASTM F 1147-05. The samples were fixed between stainless steel rods (ϕ 10 mm) at an applied load of 0.138 MPa using a polymethylmethacrylate-based commercial dental adhesive. The samples and rods were set in the Instron-type testing machine with a maximum load capacity of 20 kN and pulled vertically with a cross-head speed of $4.17 \times 10^{-5} \text{ m} \cdot \text{s}^{-1}$. The tensile strength of the adhesive, which indicates the upper limit of the present adhesion tests, was also measured by fixing the mechanically polished TNTZ disk between the rods using this adhesive. The result is $29.7 \pm 3.5 \text{ MPa}$ (around 30 MPa). A statistical analysis of the adhesive strength was carried out by means of Student's *t*-test. After the adhesion test, the fracture surfaces of both sides of the samples were observed by scanning electron microscopy (SEM).

3. Results and discussion

The mirror-polished TNTZ disk exhibited a smooth surface and its average surface roughness was approximately 16 nm. The surface of the mechanically polished TNTZ disk had uniform asperities with heights of less than 1 μm . The average surface roughness of the mechanically polished TNTZ

disk was approximately 187 nm.

In a typical XRD pattern of the HAp film fabricated on the mirror-polished TNTZ disk by the sol-gel process, the peaks attributed to HAp were present at around 26° and 32–36°. Thus, it was confirmed that HAp was successfully formed on the TNTZ disk. Similar HAp was also obtained in the case of fabrication on the mechanically polished TNTZ disks.

Figure 1 shows the adhesive strengths of HAp films fabricated on the mirror-polished and the mechanically polished TNTZ disks before and after immersion in Ringer’s solution at 310 K for 7d. As stated above, the average tensile strength of the adhesive was around 30 MPa, which represented the limit value of the adhesive strength measurable by this test. The average adhesive strengths of the HAp films fabricated on the mirror-polished TNTZ disk before and after immersion in Ringer’s solution were about 16.0 MPa and 21.5 MPa, respectively. On the other hand, the average adhesive strengths of the HAp films fabricated on the mechanically polished TNTZ disks before and after immersion in Ringer’s solution were about 23.2 MPa and 21.2 MPa, respectively. Therefore, these values showed no significant differences ($p > 0.05$). Thus, there was no difference in the adhesive strength of HAp films with different surface morphology. Moreover, the adhesive strength exhibited similar values before and after immersion in Ringer’s solution at 310 K for 7 d. In order to evaluate the adhesion of HAp films deposited on the mirror-polished and the mechanically polished TNTZ disks, the fracture areas at the interface between HAp and TNTZ were measured on the basis of SEM images before and after immersion in Ringer’s solution as shown in Fig. 2. The average fracture areas at the interface between HAp films and mirror-polished TNTZ disks before and after immersion in Ringer’s solution were about 3.9% and 23%, respectively, revealing a significant increase after immersion in Ringer’s solution. No fracture at the interface between HAp film and the mechanically polished TNTZ disk was observed, both before and after immersion in Ringer’s solution. These results indicated that the HAp film on the mechanically polished TNTZ disk exhibited greater adhesion in comparison with the HAp film on the mirror-polished TNTZ.

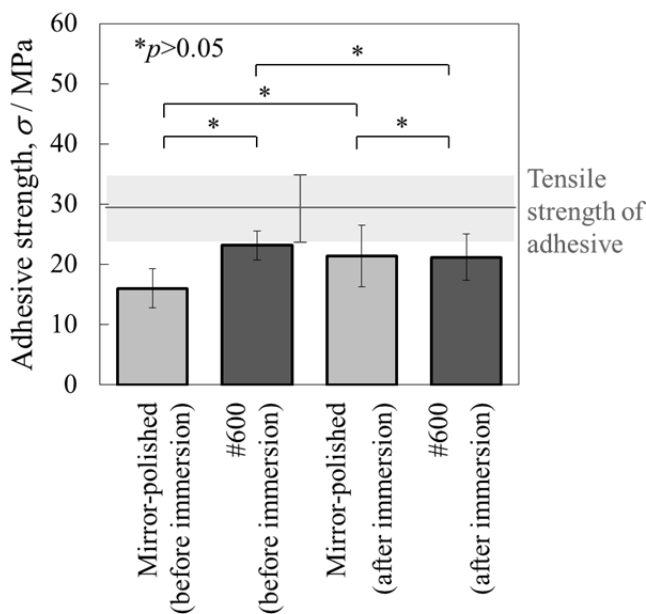


Figure 1 Adhesive strengths of HAp films fabricated on mirror-polished and mechanically polished TNTZ disks.

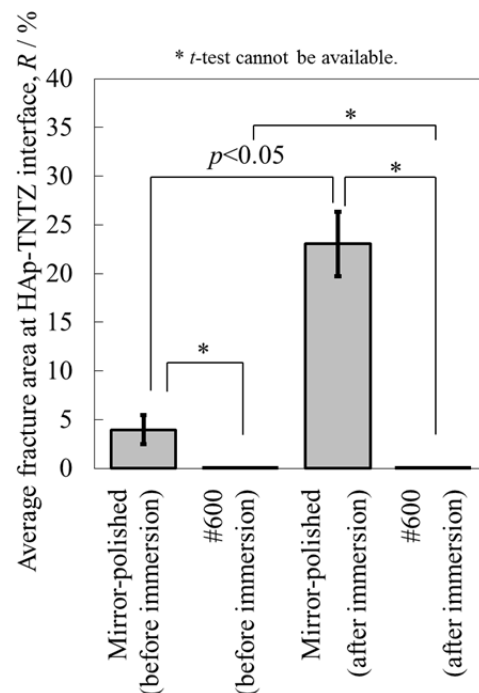


Figure 2 Average fracture areas at interface between HAp films and mirror-polished and mechanically polished TNTZ disks.

References

- [1] D. Kuroda, M. Niinomi, M. Morinaga, Y. Kato, T. Yashiro, Design and mechanical properties of new β -type titanium alloys for implant materials, *Mater. Sci. Eng. A.*, 243(1998), pp. 244-249.
- [2] L.H. Li, H.W. Kim, S.H. Lee, Y.M. Kong, H.E. Kim, Biocompatibility of titanium implants modified by microarc oxidation and hydroxyapatite coating, *J. Biomed. Mater. Res. A.*, 73(2005), pp. 48-54.

ADHESION BEHAVIOR OF MECHANICALLY JOINED PARTS OF ALUMINUM ALLOYS

Ruben Septianus¹, Murugesan Jayaprakash¹, Yukio Miyashita*¹, Tetsuri Yamada², Kiyoshi Shirato²

¹ *Department of Mechanical Engineering, Nagaoka University of Technology, 1603-1 Kamitomioka, Nagaoka, Niigata 940-2188, Japan*
² *Isuzu Motors Limited*

*Corresponding Author: miyayuki@mech.nagaokaut.ac.jp, Tel: +81-258-47-9704

Keywords: Aluminum alloy, Mechanical joint, Adhesion, Contact damage

1. Introduction

Aluminum alloys have been widely used in automotive applications, especially in automotive engine components due to their material characteristics, such as high deformability and castability, appropriate strength, light weight and good corrosion resistance, etc.[1]. In automotive engine, many parts are clamped together by using bolted joints.

Material transfer between two contact surfaces and formation of wear debris occur at the joining part due to engine vibration under the service condition, which cause surface adhesion and adhesive wear that reduces service life of the component. Therefore, it is important to understand the mechanism of adhesion behavior at the contact part in aluminum alloy. In the present study, the adhesion behavior between cast aluminum alloys was investigated.

2. Experimental Procedures

Figure 1 shows the microstructures of ADC12 and AC4C. A plate specimen of AC4C was clamped with a pad specimen of ADC12 as a bolt- nut assembly as shown in Figure 2. Both specimen and pad surfaces were polished until mirror surface. A M10 hexagonal bolt was prepared with attaching strain gage to measure the clamping force.

A servo hydraulic fatigue testing machine was used to apply cyclic loads. The experiments were conducted by varying the contact pressures (50, 60, and 70 MPa) and cyclic stress amplitude (15, 20, and 25 MPa). Cyclic loading was applied at frequency of 20Hz with 10⁵ cycles for each test.

3. Results and Discussions

Figure 3 shows the adhesive conditions for ADC12 and AC4C mechanical joint. It was observed that the strong adhesion (when bolt is removed, the pad still firmly stick to the specimen) occurred at lower stress amplitude of 15 and 20 MPa with relatively high contact pressure of 70 MPa. However, the weak adhesion (when bolt is removed, the pad still stick to the specimen, but after a few minutes it separate by itself) occurred at stress amplitude of 25 MPa with contact pressure of 70 MPa. Weak adhesion also occurred at stress amplitude of 15 and 20 MPa with lower contact pressure of 60 MPa. The adhesion did not occur at all below contact pressure of 60 MPa.

Specimen surface was observed by laser scanning microscope to study change in roughness before and after the test. Figure 4 (a) and (b) show the surface damages after the test conducted at stress amplitude of 15 MPa with contact pressure of 70 MPa for ADC12 and AC4C, respectively. It can be observed that AC4C specimen surface has more severe damage compared to ADC12 pad surface.

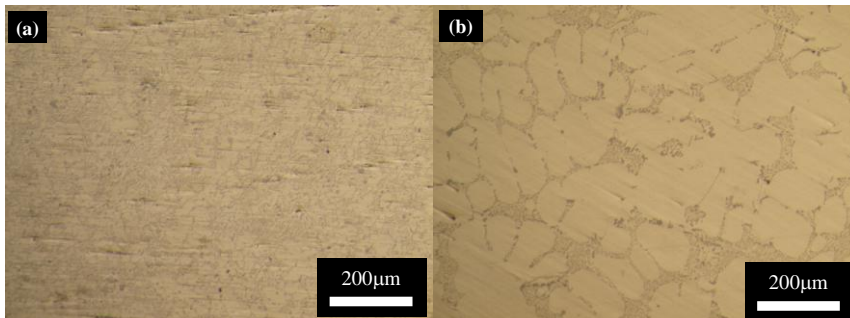


Figure 1 Microstructures of (a) ADC12 contact pad and (b) AC4C specimen.

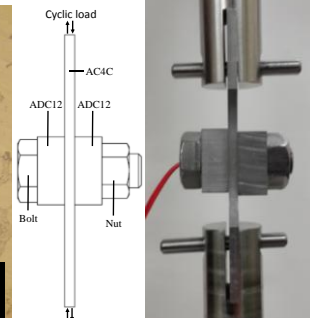


Figure 2 Mechanical joint tested.

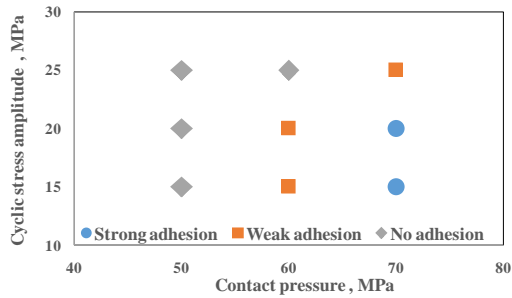


Figure 3 Adhesive conditions for ADC12 and AC4C mechanical joint.

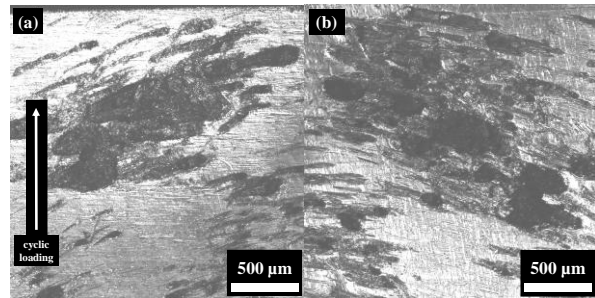


Figure 4 (a) ADC12 and (b) AC4C surfaces after the test carried out at stress amplitude of 15 MPa with contact pressure of 70 MPa.

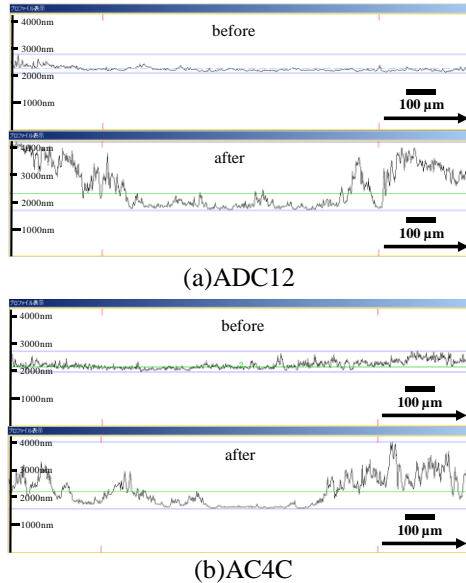


Figure 5 Surface profile of (a) ADC12 and (b) AC4C before and after the test carried out at stress amplitude of 15 MPa with contact pressure of 70 MPa.

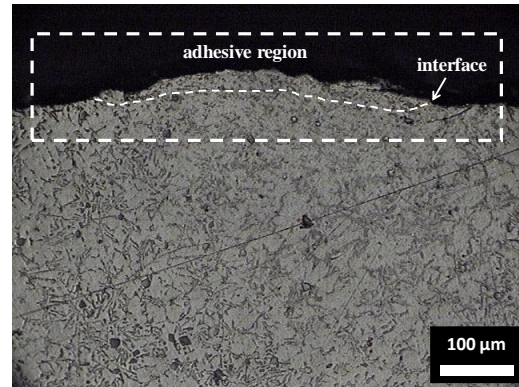


Figure 6 Cross section of ADC12 specimen after the test carried out at stress amplitude of 15 MPa with contact pressure of 70 MPa.

Surface profiles measured are shown in Figure 5. The roughness increased significantly after the test. Figure 6 shows cross section of adhesive region in ADC12 after the test. It can be observed that the metal transfer was adhered to the ADC12 contact pad surface.

The clean metallic surfaces have high surface energies and make strong metallic bonds when it contact[2]. The initial contact by clamping force may lead the plastic deformation of the surfaces asperities, which resulting adhesive bonds among the asperities[3]. When the contact pressure is high enough, the adhesion will occur.

Furthermore, when low cyclic stress amplitude is applied, the localized cold welding may occur among the asperities and resulting a strong bonding. However, when higher cyclic stress amplitude is applied, the relative slip movement between two surfaces become larger and adhesive wear will take place. In this case, the adhesion becomes weaker or may not occur.

4. Summary

Adhesion successfully occurred in the present experiment proposed. The strong adhesion occurred in the test conducted at relatively high contact pressure with lower cyclic stress amplitude. The adhesive did not occur at all below a certain contact pressure.

References

- [1] Dwivedi DK, Adhesive wear behaviour of cast aluminium–silicon alloys: Overview, *Materials and Design*, Vol. 31 (2010), pp. 2517-2531.
- [2] Bharat Bhushan, *Modern Tribology Handbook*, Vol. 1, CRC Press LLC, Florida (2001), pp. 195 – 213.
- [3] J.Halling, *Principles of Tribology*, The Macmillan Press Ltd., London(1975).

DEVELOPMENT FOR HYDROGEN STORAGE Mg-Ti SOLID SOLUTION BY MECHANICAL ALLOYING

Naoki MAEDA^{1*}, Mitsuo NOTOMI¹

¹*Department of Mechanical Engineering, Meiji University*

*ce52061@meiji.ac.jp

Keywords: *Hydrogen storage, Mg-Ti solid solution, Mechanical alloying, Stearic acid, Transformation hcp into fcc*

1. Introduction

Although hydrogen, which has high energy density and environmentally-friendly properties, is one of the alternative sources of energy to fossil fuel, its currently stored methods such as liquefaction and compression have safety issues because these require extremely low temperature or high pressure to store it. Metal hydrides have the advantage of moderate operating temperatures and pressures, compared to them, however it must need to be further improvement to put into practical use.

Mg is one of the most promising candidates for hydrogen storage material due to low cost and high hydrogen storage capacity by weight (7.6 wt.%, MgH₂). The main defect of Mg is that its hydride MgH₂ is low (de)hydrogenation kinetics because MgH₂ has high thermodynamic stability and there is some possibility to improving the defect by synthesizing with transition metals like Sc, Ti, V, Co. Ti is lightweight (4.51 g/cm³) and low cost that is advantage for hydrogen storage and it is difficult to synthesize the Mg-Ti solid solution by melting methods due to large difference of melting points between Mg (923 K) and Ti (1943 K). The mechanical alloying (MA) which is a solid-state powder processing method is capable of synthesizing such materials. Asano et al. [1] and Maweja et al. [2] had successfully synthesized Mg-Ti solution by MA and it also had made under severe milling conditions such as long milling time (more than 200 h) or high rotation speed (more than 400 rpm). The addition of process control agents (PCA) is one of the methods to enhance the MA process efficiency. It is to modify the surface condition of deformed particles by impeding the clean metal to metal contact necessary for cold welding, and promote powder fracturing [3].

The present study aims to synthesize Mg-Ti solution by MA with stearic acid as a PCA and investigate its hydrogen absorption/desorption properties.

2. Experimental

MA was performed with the planetary ball mill (LP-4, Ito Seisakusho) Powder and milling balls with a diameter of 10 mm were set in milling pot whose internal volume was 500 cm³ and it was filled with Ar gas. The milling balls and pot were made of chromium steel. Table 1 summarizes the milling conditions of all the samples in this study. Sample III was conducted hydrogenation at 573 K and 2.5 MPa with hydrogenation equipment after heat treatment at 673 K to remove stearic acid.

The X-ray diffraction (XRD) was measured with the X-ray diffractometer (MiniFlex600, Rigaku Corporation) with Cu K α radiation. The lattice parameters of the samples were calculated from the XRD peak positions. Desorption temperature was determined on detecting the exothermic reaction with the differential scanning calorimetry (DSC-60, Shimadzu Corporation).

Table 1 Milling conditions.

Sample No.		I	II	III	IV
Composition	—	Mg-30at.%Ti	Mg-30at.%Ti	Mg-50at.%Ti	Ti
Amount of stearic acid	[wt.%]	—	10	10	10
Ball filling rate	[%]	10	10	10	10
Rotation speed	[rpm]	200	200	200	200
Milling time	[h]	70	70	70	40
Powder-to-ball rate	—	1:70	1:70	1:70	1:70

3. Results and discussion

Figure 1(a)-(d) show the XRD patterns of milled sample I-IV respectively. The XRD peaks of pure Mg or Ti are visible in Figure 1(a), (b) and (d), while these can't be seen in Figure 1(c). The peaks marked by red solid circle are at the same positions as the peaks of the Mg-Ti solution with fcc phase which were reported by Asano et al. [1].

3.1 Mechanism of synthesizing Mg-Ti solution

As shown Figure 1(d), Ti was transformed hcp into fcc phase by milling with stearic acid, and at the time of the experiment, we observed some powder of sample IV was suddenly combusted and formed TiO_2 as soon as we opened the milling pot that had been finished milling, and hence the transformed Ti seems metastable. These results suggested that the Mg-Ti solution was synthesized by dissolving Mg in metastable Ti with fcc phase.

3.2 Hydrogen absorption/desorption properties of Mg-Ti solution

Figure 2(a) and (b) show the XRD pattern and the DSC results of sample III after hydrogenation respectively. As shown Figure 2(a) and (b), a part of the Mg-Ti solution was formed MgH_2 by hydrogenation and it desorbed hydrogen at approximately 637 K. The desorption temperature wasn't improved from pure MgH_2 because the formed MgH_2 wasn't dissolved Ti, and consequently wasn't achieved destabilization.

4. Conclusion

The Mg-Ti solution was synthesized by milling Mg and Ti powder with stearic acid and dissolving Mg in metastable Ti that was transformed hcp into fcc phase. It was formed MgH_2 by hydrogenation which wasn't dissolved Ti and wasn't achieved destabilization. Its desorption temperature was at approximately 673 K which wasn't improved from pure MgH_2 .

References

- [1] Kohta Asano, Hirotohi Enoki, Etsuo Akiba, Synthesis of HCP, FCC and BCC structure alloys in the Mg-Ti binary system by means of ball milling, *Journal of Alloys and Compounds*, 480(2009), pp. 558-563
- [2] Kasonde Maweja, Maje Phasha, Nic van der berg, Microstructure and crystal structure of an equimolar Mg-Ti alloy processed by Simoloyer high-energy ball mill, *Powder Technology*, 199(2010), pp. 256-263
- [3] Li Lu, Y.F. Zhang, Influence of process control agent on interdiffusion between Al and Mg during mechanical alloying, *Journal of Alloys and Compounds*, 290(1999), pp. 279-283

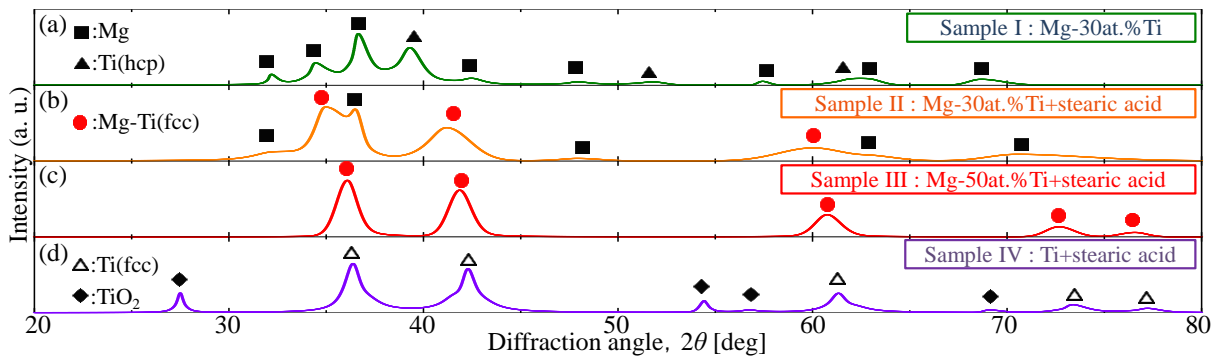


Figure 1 XRD patterns of sample I-IV.

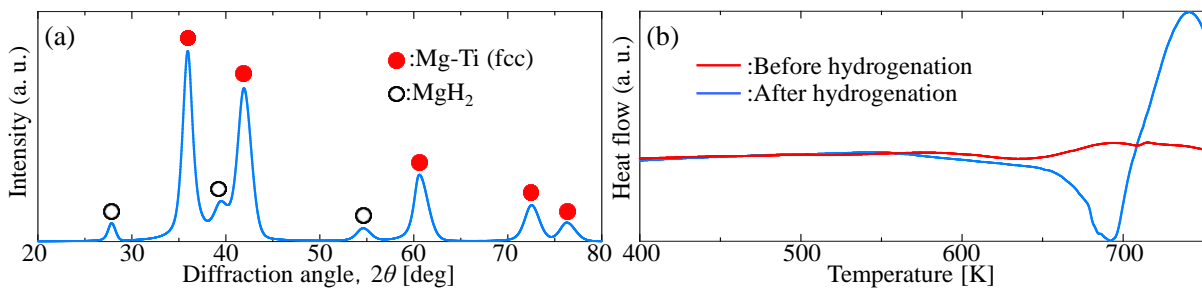


Figure 2 XRD pattern and DSC results of sample III (after hydrogenation).

DEVELOPMENT OF DAMAGE DETECTION TECHNIQUE FOR SHEET-TYPE LITHIUM-ION BATTERIES USING ACOUSTIC EMISSIONS

Hiroaki ISHII¹*, Takuma MATSUO²

¹ *Graduated Student, School of Science and Technology Meiji University*

² *Lecturer, School of Science and Technology Meiji University*

* *ce52010@meiji.ac.jp*

Keywords: Lithium-Ion Battery, Degradation, Acoustic Emission, Health Monitoring, Optical Fiber Sensor

Lithium-ion batteries have the advantages of a high energy density and reduced memory effect. They are widely used for systems such as portable devices. However, there have been some incidents due to safety problems. Therefore, a technique for detecting damage at an early stage is needed. We applied the acoustic emission (AE) technique in order to detect the degradation and damage in lithium-ion batteries. In this study, sheet-type lithium-ion batteries were monitored with an optical fiber sensor because optical fiber sensors are explosion-proof and allow for free design of the sensor shape [1].

The AE generation in sheet-type batteries was first characterized with a conventional AE sensor. Figure 1 shows experimental setup. The AE sensors were mounted onto the surface of the batteries; it was constructed from an anode electrode, a cathode electrode, a separator, and a polypropylene plate to prevent deformation of the batteries. The charging operation was carried out at a constant current of 4.16 mA, and the discharging operation was carried out at a constant current of -4.16 mA. AE signals were monitored by two sensors (PAC, R50 α) and mounted onto the surface of the batteries. The detected AE signals were first amplified (40 dB) and filtered (10 kHz high-pass filter) using a pre-amplifier and filtered (500 kHz low-pass filter) again and monitored with a digitizer (Alazartech, ATS330). The potential and current were controlled by a potentiostat (Bio-Logic, SP-50). The results obtained with a conventional AE sensor with normal charge/discharge cycles are presented below. First, AE signals were mainly detected when the potential was over 80% full. Second, the peak frequency of the AE signal was about 150 kHz. Finally, according to an analysis of the frequency spectra from the AE waveforms, the detected AE signals were caused by gas evolution [2]. Then, we repeated the charge/discharge cycles. After many cycles, the AE signals increased when the potential did not increase. We confirmed that damaged batteries generated AE signals at random intervals. The AE from the damaged batteries was 30–50 events, which was twice as many that from the normal cycles. The peak frequency of the AE signal was about 50 kHz, which changed about 150 kHz during the normal charge/discharge cycles.

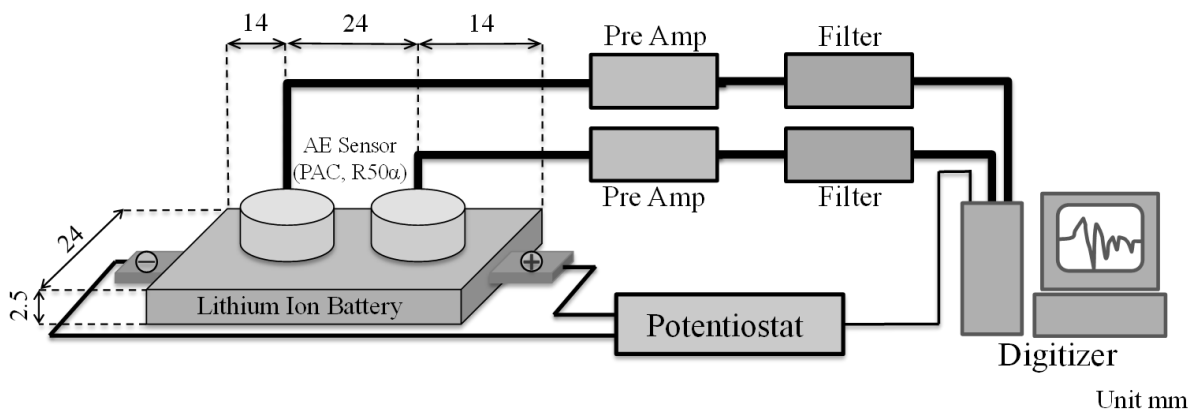


Fig.1 Experimental setup for monitoring AE signals during charge-discharge cycles utilizing PZT sensors

Then, we applied an optical fiber sensor. Experimental setup was the same shown in Fig.1, however optical fiber sensor was used. Figure 2 shows the optical fiber AE monitoring system used in this study. The optical fiber AE monitoring system was composed of an optical fiber sensor unit, a feedback circuit, and a digitizer. The digitizer recorded the AE signals detected by the sensor unit, and the feedback circuit improved the stability of the sensor. Optical fiber was wound over the aluminum cylinder and the sensor was set on the sheet-type battery. The charging operation was carried out a constant current of 0.8 mA, and the discharge operation was carried out a constant current of -0.8 mA.

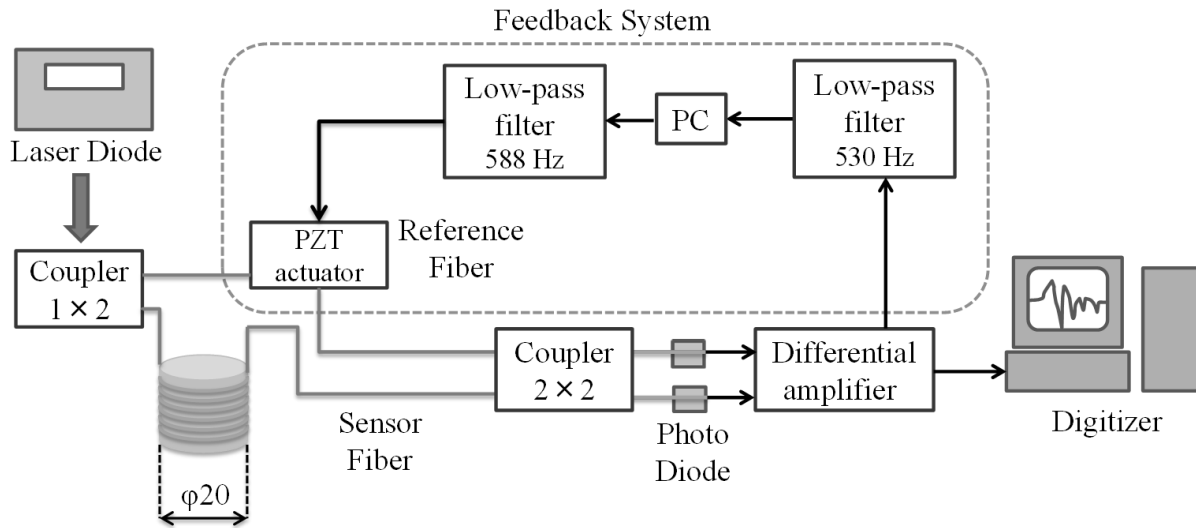


Fig.2 Optical fiber AE monitoring system used in this study

Figure 3 shows the potential and cumulative AE events as a function of time with the optical fiber sensor and the AE waveform the AE signals could be also detected with the optical fiber sensor when the signal-to-noise ratio was 30–35, as in the results obtained with the conventional AE sensor.

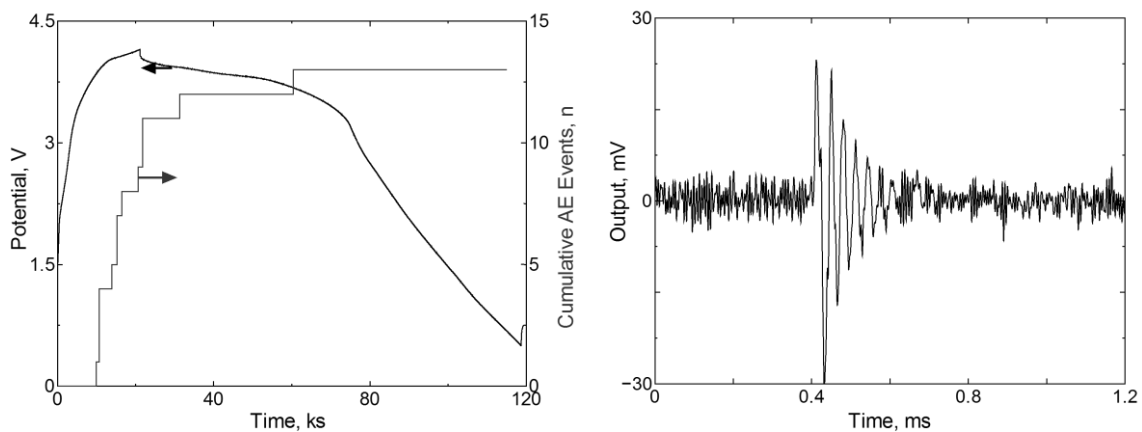


Fig.3 Potential and cumulative AE events as a function of time (left) and the AE waveform (right)

Acknowledgment

This study was partially supported by the JGC-S Scholarship Foundation, grand for young researcher.

References

- [1] Matsuo, T., Sano, K., Sakakibara, Y., and Nakayama, G., Estimate of Stress Corrosion Cracking Initiation and Propagation in High-Pressure, High-Temperature Water Environment Utilizing Acoustic Emission, *Materials Transactions of Metals and Materials*, Vol.53 No.3(2015), pp.327-332
- [2] Matsuo, T., Uchida, M., and Cho, H., Development of Acoustic Emission Clustering Method to Detect Degradation of Lithium Ion Batteries, *Journal of Solid Mechanics and Materials Engineering*, 5-12(2011), pp. 678-689.

IMPACT RESISTANCE OF THE GLASSES INSTALLED NANO-LAMIRATED FILMS AND ARAMID FIBER CLOTH

Yudai YASUMOTO^{1*}, Hikaru MASUI¹, Mitsuo NOTOMI¹ Katsumasa AOKI²

¹ Department of Mechanical Engineering, Meiji University

²SOU · SHOW CO.,Ltd.

*ce52067@meiji.ac.jp

Keywords: Glass, Nano-laminated film, Aramid fiber cloth, Impact fracture, Strain measurement

1. Introduction

Glass, which has excellent workability, production efficiency and the properties of airtightness, transparency, corrosion resistance and thermochemical stability, is used in various situation such as the windows of buildings and cars. The strength of the glass depends on the number of Griffith flaws, which is generated during the manufacturing process at the surface of the glasses and is less than its ideal strength without any cracks^[1]. In addition, if the stress over the limit of elasticity is subjected to the glass, brittle fracture is occurred instantaneously without plastic deformation, and consequently glass has a problem for impact resistance. There are many kinds of methods to reinforce glass and recently, much attention has been paid to the method of film installation on the surface of the glass.

In this study, we considered the improvement of impact resistance of glass installed nano-laminated film (Super layer URTRA600, 3M Japan Limited) and aramid fiber cloth (AW40/40, MAEDAKOSEN CO., LTD.) over its surface.

2. Experimental procedure

In this research, five sheets of glass (300×300×3.2 mm) are used as specimens (Table 1). GLASS is the specimen a glass without film and cloth. FILM-100 and ARAMID-100 are installed film or cloth (100×100) on impact surface. FILM-ALL-IMPACT and FILM-ALL-NON are installed film (300×300) on impact or non-impact surface. It takes a month for curing period of glass installed film or cloth. Their impact resistances were evaluated with the free-fall drop test mostly according to JIS R 3212. In this test, the steel ball (80 mm diameter, 2 kg weight) falls freely 2 meters high from the specimen. Fracture behaviors of all specimens are taken by high-speed camera (EX-FH25, CASIO COMPUTER CO., LTD.), whose frame rate is 240 frames per second, from the impact side of the specimen. Specimen's circumference strain is measured with strain gauge (FLA-1-11, TOKYO KEIKI INC.). A center is set as the contact point between the specimen and the ball and the virtual circle lines of which each radius are 80 and 110 mm are drawn on the impact surface. All strain gauges are attached on parallel to the lines so that circumference strain is measured. The signals from the gages translate to the bridge box (SB-121A, Tokyo Sokki Kenkyujo Co., Ltd.), dynamic strain meter (DC-97A, Tokyo Sokki Kenkyujo Co., Ltd.) and oscilloscope (DSO1024A, Agilent Technologies Inc.) in order. The range of oscilloscope is in 1 millisecond from the time the ball impacted to the specimens.

Table 1 Specimen conditions.

Specimen name	Material	Installed material	Installed area	Installed side
GLASS	Glass(300×300 mm)	×	×	×
FILM-100		Nano-laminated film	100×100	Impact side
ARAMID-100		Aramid fiber sheet		
FILM-ALL-IMPACT		Nano-laminated film	300×300	Non-impact side
FILM-ALL-NON				

3. Results and Discussions

Figure 1 shows the specimens after fractured. Figure 1 (a) shows the specimen fractured perfectly and that is penetrated by the ball. In this study this type of fracture is called All-Fractured (AF). Figure 1 (b) and (c) show the specimens fractured are also penetrated by the ball and the areas of film or cloth installed however hold the plate shape even cracked. The type of fracture is called Partially-Fractured (PF). Figure 1 (d) and (e) show the specimens are not penetrated by the ball with a lot of cracks. The type of fracture is called Non-penetration with cracks (NPC).

The resistance of impact of FILM-ALL-IMPACT and FILM-ALL-NON is improved by the installed films or cloth. This is because the impact energy diffusions caused by the film or cloth are occurred in the installed areas. In addition, the glass fragments are not scattered and remained in the area installed film or cloth and these fragments cause friction each other, and the areas remain the plate shape even cracked. In the case of PF, the load by the impact ball is concentrated to the boundary between the glass and the film or cloth, and consequently these specimens are penetrated by the ball with the areas installed film or cloth held the plate shape.

Figure 2 shows the circumference strain profile in 1 millisecond from the time the ball impacted. In this graph the vertical axis corresponds to the circumference strain of the specimen and the strain is compressive when the vertical value is negative. Figure 2 (a)-(e) shows the strains of all specimens repeat increase phase and decrease phase in compression. Table 2 shows the maximum strains of the specimens defined minimum value of the strain profile in Figure 2. The maximum strains of FILM-100, ARAMID-100, FILM-ALL-IMPACT and FILM-ALL-NON are lower than that of GLASS in the 80 mm from the center of the specimen. In Table 2 the maximum strains in 80 mm are inclined to decrease by installing film or cloth but that of FILM-100, ARAMID-100 and FILM-ALL-IMPACT are almost the same value in spite of the differences of their condition. It revealed that the maximum circumference strain is irrelevant to the penetration property.

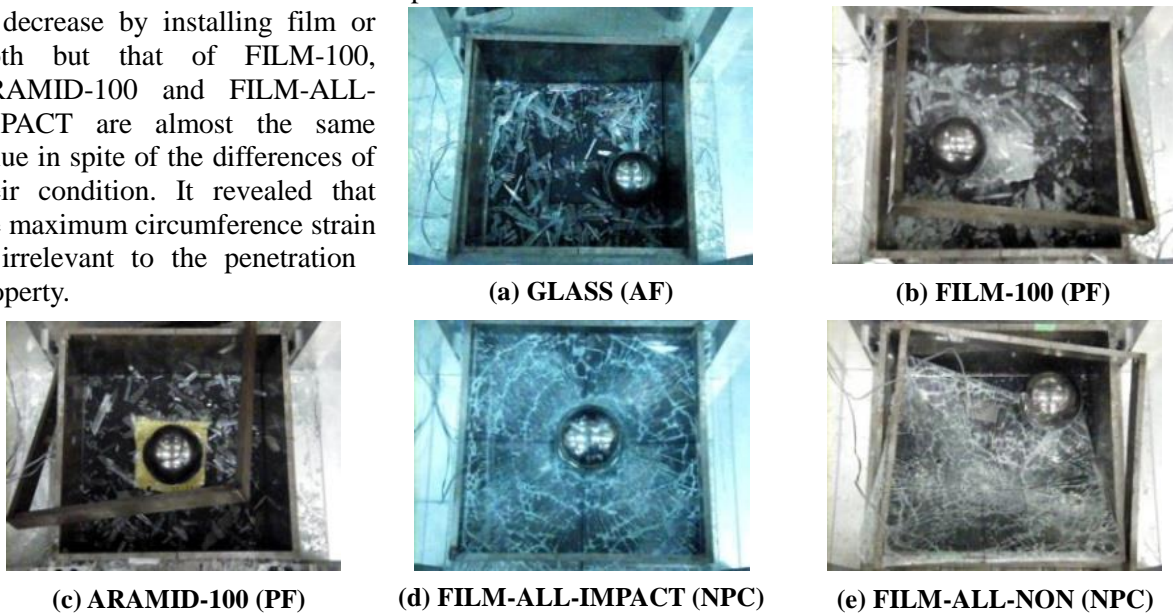


Figure 1 Specimens at the time of fractured

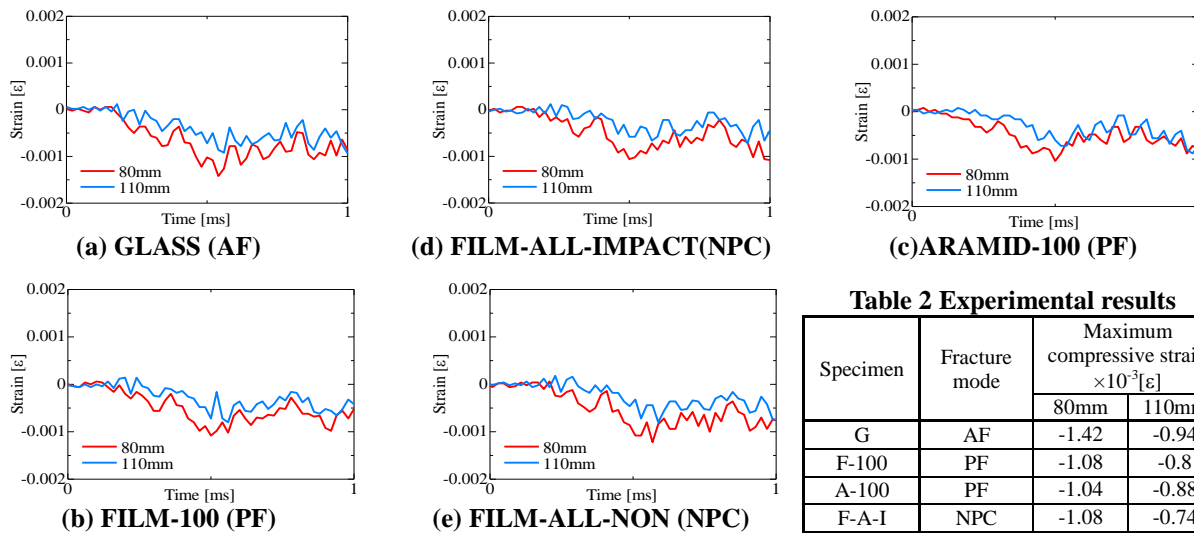


Figure 2 Circumference train profile in 1 millisecond

Table 2 Experimental results

Specimen	Fracture mode	Maximum compressive strain $\times 10^{-3}[\epsilon]$	
		80mm	110mm
G	AF	-1.42	-0.94
F-100	PF	-1.08	-0.8
A-100	PF	-1.04	-0.88
F-A-I	NPC	-1.08	-0.74
F-A-N	NPC	-1.22	-0.8

References

- [1] Hisashi HARAMORI, Relations between fracture strength of glass and Griffith flaws, The Japan Society for Precision Engineering, Volume 31(1965), pp. 807-812.

INFLUENCE OF ANNEALING ON SHAPE MEMORY PROPERTY IN FE-MN-SI BASED ALLOY

Hiromu ISHII*, Naohiro OKUBO, Mitsuo NOTOMI

Department of Mechanical Engineering, Meiji University

*ce52011@meiji.ac.jp

Keywords: *Fe-Mn-Si based alloy, Shape memory effect, Stress-induced martensitic transformation, Annealing, EBSD analysis*

1. Introduction

Fe-Mn-Si based shape memory alloys (SMAs) have attracted much attention among the numerous SMAs because these SMAs have many advantages such as high mechanical properties, fine workability and cheap cost. Although they have been expected to be utilized as large-scale products, their shape memory property is low compared with Ni-Ti alloys which have been generally used in many engineering fields, so that it has been strongly required to be improved. It is known that shape memory effect (SME) in Fe-Mn-Si based alloys is associated with stress-induced $\gamma \leftrightarrow \varepsilon$ martensitic transformation, but detail processes for improvement have been widely studied and discussed. Li et al. [1] reported that the property of the alloy was enhanced for proper annealing before deforming. The objective of this study was to clarify influences of annealing on phase microstructure, crystal structure and shape memory behavior of Fe-28Mn-6Si-5Cr alloy.

2. Experiments

The chemical composition of the alloy used for this study is listed in Table 1. The alloy which is a wire ($\phi 1.2$ mm) was manufactured by Awaji Materia Co., Ltd. and the process was cold-drawing without subsequent solution treatment. In this study, heat treatment was conducted on the conditions listed in Table 2, and the as-received alloy and the alloys annealed at 673 K, 773 K, 873 K, 973 K, 1073 K, 1173 K and 1273 K for 60 min were named specimen # 1, # 2, # 3, # 4, # 5, # 6, # 7 and # 8, respectively. The outline of the experiments was shown in Figure 1. In order to evaluate shape memory behavior, all specimens were bent by material testing machine (Autograph AGS-H, Shimadzu Corporation) with a bending punch and a jig on the condition listed in Table 3, then heated at 923 K for 15 min as a recovery treatment. Electron backscatter diffraction (EBSD) and X-ray diffraction (XRD) methods were employed to investigate the microstructural characterizations. Samples for EBSD, parts of the cut specimens embedded into resin, were mechanically polished until the specimens were halved, then the analyzed surfaces were prepared by colloidal silica nanoparticles. EBSD analysis was conducted at 20 kV acceleration voltage with a step size of 0.955 μm on a field emission gun, and scanning electron microscopy (SEM JIB-4601F, JEOL Ltd.) equipped with TSL-OIM™ EBSD set-up was used for the analysis. XRD analysis was conducted with XRD instrument (MiniFlex600, Rigaku Corporation) using Cu- K_{α} radiation ($\lambda = 0.154178$ nm).

Table 1 Chemical composition of the alloy (mass %)

Mn	Si	Cr	C	Ni
27.2	5.69	5.02	0.047	0.033
N	S	P	O	
0.012	< 0.009	< 0.003	0.002	

Table 2 Heat treatment condition in each specimen

Specimen	Heat treatment condition
# 1	No treatment
# 2	673 K \times 60 min, Furnace cooling
# 3	773 K \times 60 min, Furnace cooling
# 4	873 K \times 60 min, Furnace cooling
# 5	973 K \times 60 min, Furnace cooling
# 6	1073 K \times 60 min, Furnace cooling
# 7	1173 K \times 60 min, Furnace cooling
# 8	1273 K \times 60 min, Furnace cooling

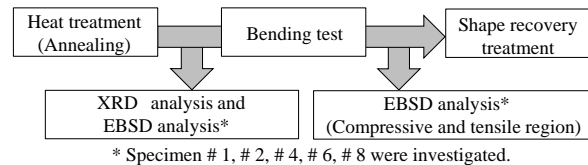


Figure 1 Outline of the experimental methods

Table 3 Bending test condition

Specimen length	50 mm
Test type	3-point bending
Maximum load	80 N
Minimum load	0 N
Test velocity	15 mm/min
Span	31 mm
Bending radius	30 mm
Hold time	3.0 sec
Temperature	Room temperature

3. Results and discussion

Table 4 shows recovery angles of the specimens after unloading and the recovery treatment, θ_{SB} and θ_{SME} , and also shows recovery ratios in SME, η_{SME} , which was calculated with a following equation.

$$\eta_{SME} = \frac{\theta_{SME}}{(180 - \theta_{max}) - \theta_{SB}} \times 100 [\%] \quad (1)$$

Where θ_{max} is 65 deg., a deformation angle in maximum loading. The results indicated that specimen # 4 and # 5 had the most recovery in SME. Table 5 shows phase distribution maps obtained by EBSD analysis, and it was found that all over austenite phases in specimen # 4 mostly transformed into ϵ martensite over the bending deformation. In contrast, specimen # 2 was formed few austenite phases by the annealing. In addition, the high temperature caused grain coarsening in specimen # 8, so it noticeably decreased the elastic recovery. Figure 2 shows quantitatively a relationship between η_{SME} and the phase transformations. A M_q/A_q is a quantitative ratio of martensite to austenite in each analyzed area, and the high M_q/A_q means that there are many martensite phases in a specimen. Figure 2 suggested ϵ martensite formed by bending led to fine SME. On the other hand, Figure 3 shows a relationship between η_{SME} and average crystallite size, D which was obtained by XRD analysis. D was most enlarged by annealing at 973 K, and that suggested the dislocation density was most decreased with the temperature [2]. Besides, the variation trend of D was similar to that of η_{SME} and then the relationship implied the decrease of dislocation density encouraged $\gamma \leftrightarrow \epsilon$ martensitic transformation.

4. Conclusions

1. Shape memory property of the alloy was enhanced by annealing at 873-973 K, which formed all over austenite phases without grain coarsening in the alloy.
2. The main factor in the fine SME was that all over austenite phases generated by the annealing temperatures mostly transformed into ϵ martensite over the bending deformation.
3. The decrease of dislocation density was caused by relatively high annealing temperatures, that would be one of the factors in encouraging the $\gamma \leftrightarrow \epsilon$ martensitic transformation.

References

- [1] Li. HJ, Dunne. D, Kennon. N, Factors influencing shape memory effect and phase transformation behaviour of Fe-Mn-Si based shape memory alloys, Materials Science and Engineering A, Vol. 273-275, No. SI (1999), pp. 517-523.
- [2] Ting C. Huang, X-ray Polycrystalline Diffraction Analysis of Thin Films, Journal of the Crystallographic Society of Japan, Vol. 34, No. 2(1992), pp. 110-117.

Table 4 Recovery angles by spring back and SME and recovery ratios in SME

Specimen	# 1	# 2	# 3	# 4	# 5	# 6	# 7	# 8
θ_{SB} [deg.]	28	49	51	41	42	36	15	10
θ_{SME} [deg.]	14	18	35	62	61	36	35	28
η_{SME} [%]	16.1	27.3	54.7	83.3	83.6	45.6	35.0	26.7

Table 5 Phase distribution maps before and after bending deformation (blue: austenite, yellow: martensite) obtained by EBSD analysis

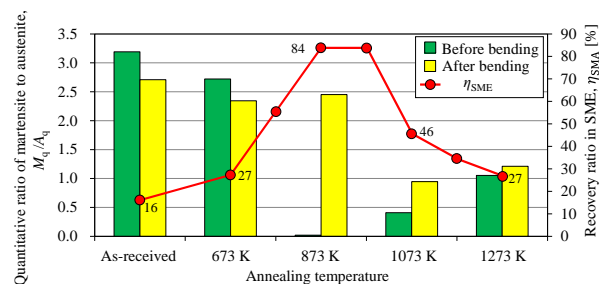
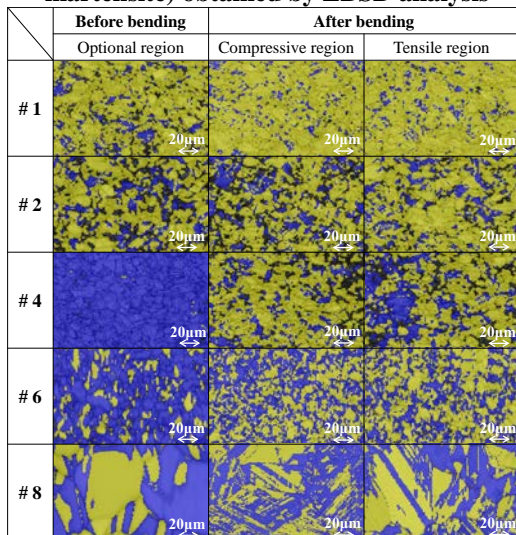


Figure 2 M_q/A_q before and after bending deformation and the variation of η_{SME} in the annealing temperatures

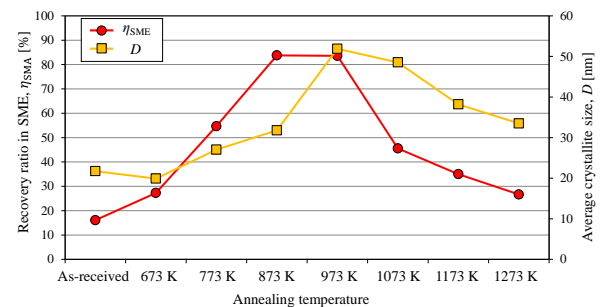


Figure 3 The Variations of η_{SME} and D in the annealing temperatures

FRICTION STIR INCREMENTAL FORMING OF ALUMINUM ALLOY SHEETS WITH BACK SUPPORT DIE

Masaaki Otsu^{1,*}, Wei Jiang², Takayuki Muranaka³, Ryo Matsumoto⁴, Masato Okada⁵

¹Professor, University of Fukui, 3-9-1 Bunkyo, Fukui, 910-8507, Japan

²Graduate Student, University of Fukui, 3-9-1, Bunkyo, Fukui, 910-8507, Japan

³Associate Professor, Fukui National College of Technology, Geshi, Sabae, 916-8507 Japan

⁴Associate Professor, Osaka University, 2-1 Yamadaoka, Suita, 565-0871, Japan

⁵Lecturer, University of Fukui, 3-9-1 Bunkyo, Fukui, 910-8507, Japan

*Corresponding Author: otsu@u-fukui.ac.jp

Keywords: Friction Stir Incremental Forming, Sheet Metal Forming, Aluminum Alloy Sheet, Back Support Die, Forming Accuracy

1. Introduction

Friction stir incremental forming (FSIF) has advantages of dieless forming and high formability for non-ferrous metals. However, forming accuracy is not so high. In conventional incremental sheet metal forming, back support die is used for improving the forming accuracy. In this study, a back support die is employed in friction stir incremental forming and formed shapes with and without back support die were compared.

2. Experimental method

The appearance of the working platform, die and tool were shown in Figure 1. The diameter of the forming tool was 6 mm and the top shape of the tool was hemispherical. AISI A5052 aluminum alloy sheets were used for specimen. The size of the sheet was 100 mm x 100 mm and the thickness was 0.5 mm. During the forming, the sheet was clamped on the upside of the die using a screw. The tool rotation rate ω feed rate v and wall angle θ were changed and formability was investigated. The tool path was shown in Figure 2. The maximum height of pyramid, which is the objective shape, was 20 mm.

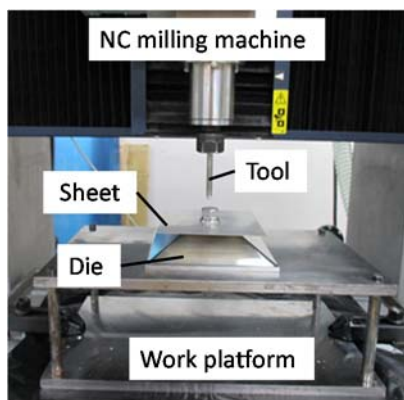


Figure 1 Appearance of working platform

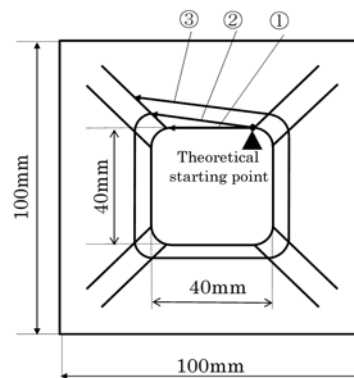


Figure 2 Tool path for forming

3. Experimental result and discussion

3.1 Classification of formed parts

The formed parts can be classified into four types. Type A is forming succeeded without any defects. Type B is forming was succeeded but burr was observed. Type C is forming was succeeded but the flange was curled up. Type D is forming failed with fracture. The formed specimens of each type were shown in Figure 3.

3.2 Formable working conditions

The feed rate of the tool was fixed, and formable wall angle was studied with changing the tool rotation rate. The experimental results when the tool feed rate was $v = 1000$ mm/min and $v = 4000$

mm/min were shown in Figure 4. In this figure, circle marks indicate that forming was completed until forming height became to 20 mm. Cross marks mean the sheet was broken during forming. Triangle marks mean that forming machine stopped by overloading.

As the tool rotation rate increased, formable wall angle became smaller and this means the formability was improved. However, as the tool feed rate increased, the minimum formable tool rotation rate was increased and the minimum formable wall angle was increased and the formability was decreased.

3.3 Cross-sectional shape

Cross-sectional shapes of ideal shape and formed parts with and without dies when the wall angle was $\theta = 45^\circ$ and , tool feed rate was $v = 1000$ mm/min and tool rotation rate was $\omega = 10000$ rpm, was were plotted in Figure 5. Although there were no significant difference between the shapes at conical surface with and without die, those at the corner and flange were different and that with die was closer to the ideal one.

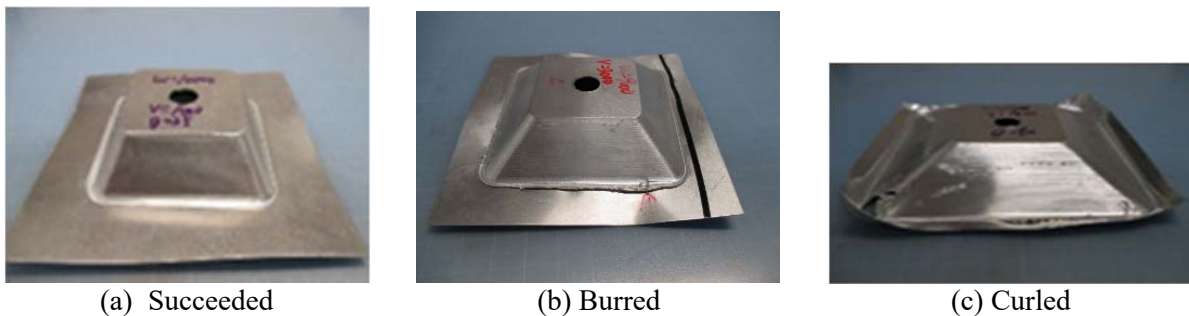
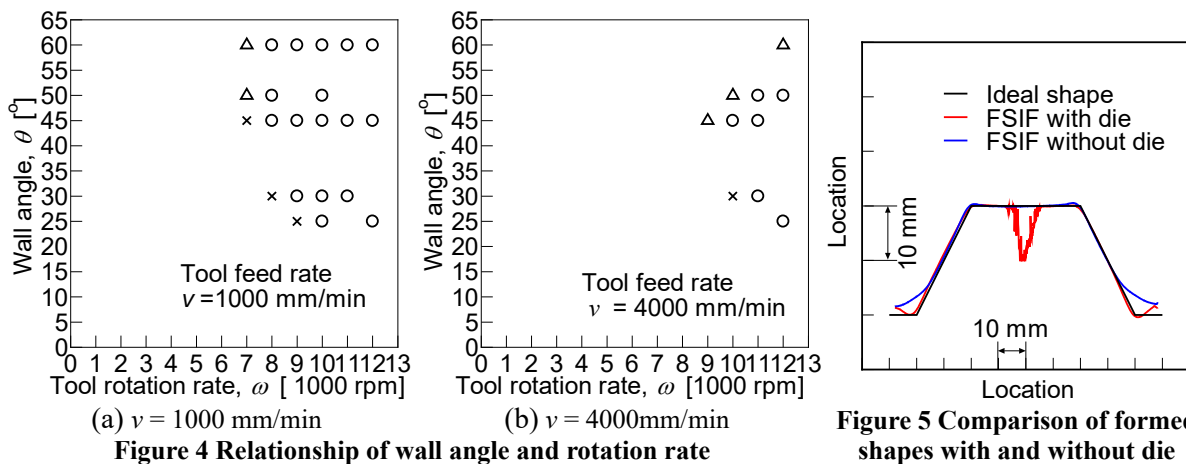


Figure 3 Appearances of formed sheets



4. Conclusions

Aluminum alloy sheets were formed by friction stir incremental forming with back support die. There were some differences between with and without die as follows.

1. In some working conditions, burr or curling up were observed although those were not observed without the back support die.
2. As the tool feed rate was increased, the minimum formable wall angle was increased with die.
3. Cross-sectional shapes at the conical surface were almost same, however, those at the corner and flange were different and that with die was closer to the ideal one.

Reference

[1] Otsu, M., Ichikawa, T., Matsuda, M., Takashima, K., Friction Stir Incremental Forming of Aluminum Alloy Sheets, Steel Research International, 81- 9(2010), pp. 942 - 945.
 [2] Ambrogio, G., Galiardi, F., Bruschi, S., Filice, L., On the high-speed Single Point Incremental Forming of titanium alloys, CIRP Annal-Manufacturing Technology 62(2013), pp. 243-246.

DEVELOPMENT OF CU-SN ALLOY WITH MECHANICAL ALLOYING

Shunsuke WATANABE^{1*}, Mituo NOTOMI²

Student, Department of Mechanical Engineering, Meiji University, 1-1-1 Higashimita Tama-ku, Kawasaki-shi, Kanagawa-ken, 214-8571, Japan

² Professor, Ditto

*Corresponding Author: ce32068@meiji.ac.jp

Keywords: Mechanical alloying, Cu-Sn alloy, Powder molding, Ductility, XRD

1. Introduction

Cu-Sn alloys have been used through ages because of good workability, high corrosion resistance and high electric conductivity in Cu-Sn solid solution. Recent research have revealed the secondary transformation and new phase for the alloys, which made it as an interesting material to substitute the graphite anodes of Lithium ion batteries, lead-free solder as well as shape memory alloy (SMA)⁽¹⁾. The Cu-Sn alloys are potential to be used in various applications because it shows good ductility under each solid solution limit. Over each solid solution limit, brittleness appears due to inter-metallic compound form such as Cu₃Sn, and Cu₆Sn₅ which made it difficult to process it using plastic forming method that is commonly used as practical method. Although the traditional Cu-Sn alloy is practically rare usage due to the occurrence of cleavage fracture under polycrystalline, the ductile Cu-Sn alloy had a potential for SMA. SMAs have drawn significant attention due to their uniqueness, i.e; they return original shape induced by heating or electromagnetic field. Cu-based SMA is a promising substitution for the Ni-Ti alloy, which is the most common SMA due to superior shape memory effect and more expensive than Cu-Sn alloy.

In this research, Cu-Sn alloy in a mixing structure of Cu-FCC solid solution and Cu₃Sn is prepared to enhance ductility for the potential of shape memory effect. The atomic ratio is fixed in reference to the new phase diagram⁽¹⁾. Also, Cu-Sn (10at.%) alloy powder were synthesized by mechanical alloying (MA) from mixtures of pure crystalline Cu and Sn powders using planetary ball mill with the weight ratio of ball to powder. The phase structure of the alloy powders were evaluated with the X-ray diffraction (XRD) and the texture and hardness of specimens were investigated with the scanning electron microscope (SEM).

2. Experimental method

In this study, elemental powder of Cu with > 99.8% of purity and < 100 μm of particle size (Niraco Corp.) and Sn with > 99.8% of purity and < 45μm of particle size (Sigma Aldrich Corp.) were mixed in planetary mills(LP-4, Ito Ltd.), to prepare Cu-10Sn (at. %). The ball-milling parameters are shown in Table 1.

Pre-alloyed powders were hot-pressed on a steel die to rectangular shape of 12 × 12 × 5 mm with compression testing machine (AYC-300P, Tokyo Testing Machine Inc.) and done heat treatment under argon atmosphere (FUA112DB, Advantec Toyo Kaisha Ltd.). Heat treatment conditions are shown in Table 2. Phase analyses were carried out on XRD (Rigaku Analix A-26L-Cu). The microstructures of the specimen were examined using a SEM (JEOL JSM-6700F) equipped with energy-dispersive X-ray spectroscopy (EDS).

Table 1 The mechanical alloying parameter

Milling material	Steel balls
Ball-to-powder ratio	30:1
Filling rate [%]	10
Rotation speed [rpm]	200
Milling time [h]	40
Milling atmosphere	Argon

Table 2 Heat treatment condition

	Hot press			Heat treatment			specimen
	Pressure [MPa]	Holding temp [°C]	Holding temp [sec]	Heat treatment [temp.]	Holding time [hr]	Cooling method	
Principal Powder	80	200	500	-	-	Furnace cooling	(a)
				200	5		(b)
				500	5		(c)
Milled powder	80	200	300	-	-	Furnace cooling	(d)
				200	5		(e)
				500	5		(f)
				-	-		(g)
				200	5		(h)
				500	5		(i)
Milled powder	80	500	300	-	-	Furnace cooling	(j)
				200	5		(k)
				500	5		(l)

3. Results and discussions

3.1 Crystal structure for Cu-Sn The structural evolution during MA, hot press and heat treatment in order of Cu and Sn is shown in Fig.1. Cu and SnO appeared in the profile of the specimen made of

principal powder as shown Fig. 1(a). The figure indicated that Sn was promoting oxidation reaction under high temperature. Also, Fig. 1(b) showed the peak of Cu, Cu-Sn solid solution and ϵ phase and the phases were caused by the melting of Sn and react Cu by heat treatment. Okabe et al.⁽³⁾ reported that Cu-10mass%Sn compact forms ϵ phase during sintering at 500°C. The ϵ phase precipitated by the heat treatment at 500°C.

Fig. 1 (2) shows the profile of the pre-alloyed powder after MA treatment. The heights of all diffraction peaks of Specimen (c) decrease while the width of the peaks increases. The lower diffraction peaks are caused by the decrease of crystallite size and the increase of micro strain due to high stresses evolving during ball milling impact. The specimen (d) that has been recrystallized by heat treatment confirmed the peak of Cu-Sn solid solution and ϵ phase, and the position of Cu peak slightly shifted to smaller angles because of the diffusion of the Sn in the Cu matrix. Lattice parameter of FCC Cu-Sn solid solution consequently varied from 0.362 nm to 0.368 nm. We confirmed Specimen (d) dissolved 7.1 at.% of Sn in Cu matrix from the results of N. Saunders et al.⁽⁴⁾ reported that the lattice parameter tends to increase by substituting or intruding Sn atoms in Cu matrix because atomic size of Sn is bigger than Cu.

Fig. 1 (3) shows the specimen of the heat treatment at 200°C with pre-alloyed powder by MA treatment. Specimen (e) shows only the peaks of Cu-Sn solid solution. However, Specimen (f) has the phase of Cu-Sn solid solution of which the peak is positioned bigger angle compared to Specimen (e) and ϵ phase. This is because the atom of Sn in Cu matrix is precipitated as ϵ phase and the lattice of Cu-Sn solid solution is shrunk with the smaller atoms of Sn in Cu matrix.

Fig. 1 (4) shows the specimen at 500°C with pre-alloyed powder by MA treatment. Both Specimen (g) and (h) show the same diffraction patterns which appear only the peaks of Cu-Sn solid solution.

3.2 Surface morphology for Cu-Sn Fig. 2 shows the images with SEM and EDS mapping of specimens. Specimen (a) and (e) can be seen porosity which leads to brittle fracture in Fig. 2 (1). On the other hand, specimen (g) is confirmed to promote densification by applying high temperatures during sintering.

From EDS mapping images of Cu and Sn in Fig. 2, segregation of Sn can be seen on specimen (a) while the specimen (e) and (g) shows that the distribution of the chemical composition is homogeneous of Cu and Sn due to be pre-alloyed by MA.

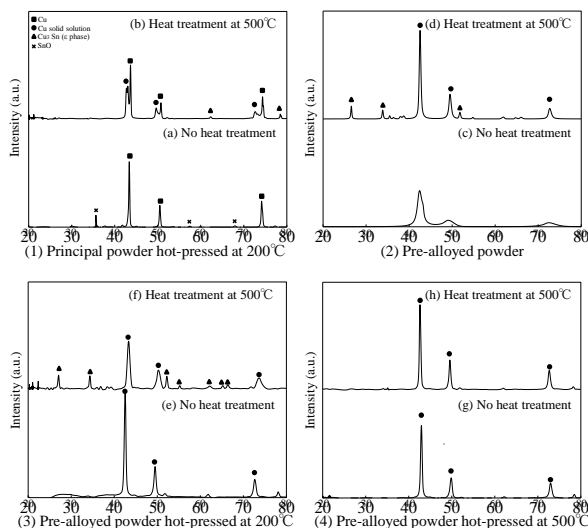


Fig. 1 XRD patterns of specimens

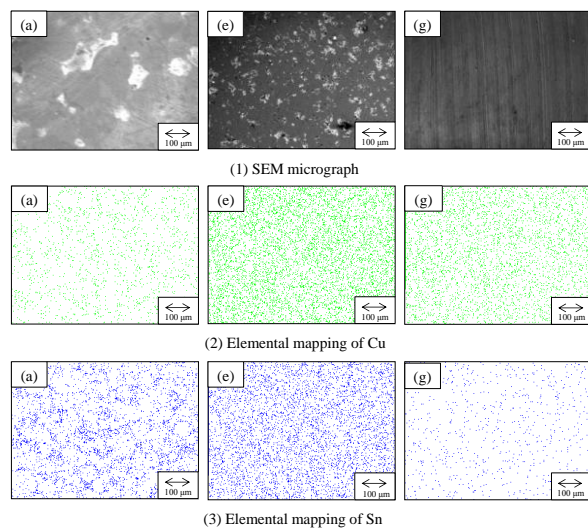


Fig. 2 Surface morphology of specimens

Reference

- [1] S.Furtauer, D.Li, D.Cupid, H.Flandorfer, The Cu-Sn phase diagram, Part 1: New experimental results, *Intermet al.lics*, Voi.34, 2013, 142-147
- [2] T.Okabe, Y.Kado, Some Aspects on the Sintering of Cu-Sn Compact, *J.Jpan.SOC.Powder Powder Met al.lurgy*, 14, 1967, 147-153
- [3] N.Saunders, AP Miodownik, The Cu-Sn (Copper-Tin) System, *Bulletin of Alloy phase diagram*, Vol.11, Bo.3, 1990, 278-287

FEM SIMULATION FOR TWO-DIMENSION CUTTING OF TITANIUM-ALLOY

Makoto Nikawa^{1,*}, Hiroki Mori², Yuki Kitagawa², Masato Okada³

¹ Associate Professor, Gifu University, 1-1 Yanagido, Gifu, Japan, 501-1193

² Graduate student, Graduate School of Engineering, Gifu University, 1-1 Yanagido, Gifu, Japan, 501-1193

³ Lecturer, University of Fukui, 3-9-1 Bunkyo, Fukui, Japan, 910-8507

*Corresponding Author: mnikawa@gifu-u.ac.jp, Tel:+81-58-293-2517, Fax:+81-58-293-2517

Keywords: Cutting, FEM, Titanium alloy, Johnson-Cook model, Ductile fracture condition

Introduction

FEM simulation is a strong means to the creation of a new processing method and the optimization of the existing processing method. There are various reports about the simulation of the cutting [1]. The simulation was actively utilized in the field of plastic working [2] such as the forging and the sheet metal forming, it had become indispensable tools for manufacturing. However, the simulation was not utilized enough in the field of the cutting. The reason, it is difficult to actually measure the phenomena during cutting due to the severe environments of high temperature, high pressure, and high strain rate. Therefore, the constitutive equation of materials was not determined.

FEM simulation for the two-dimension cutting of Ti-6Al-4V alloy was investigated in this study. The cutting force, tool flank temperature, and dimension of the chip after cutting were measured by cutting test and the parameters for the simulation were determined.

Testing methods

Cutting test

Titanium alloy (Ti-6Al-4V) of $t3 \times 100$ mm was used as workpiece. Cutting tests of the workpiece were carried out with an NC milling machine by dry cutting. Cutting was performed so that a down-cut cutting style was performed. The test conditions were shown in Table 1. The cutting force was measured with a three-component dynamometer. The cutting force in this study was obtained the maximum cutting pulse. The tool flank temperature during cutting was measured using a two-color pyrometer with an optical fiber [3].

Table 1 Experimental conditions

Cutting speed V (m/min)	25, 50, 100, 150, 200, 300
Rake angle α (deg.)	-45, -25, -9, 5
Radial depth of cut t_1 (mm)	0.1, 0.25, 0.3, 0.5

Computer simulation

Rigid-plastic analysis was carried out using DEFORM-2D Ver.9.0 which was commercial software, and Johnson-Cook's model was used for a flow stress equation of material. The equation is expressed by eq. 1.

$$\bar{\sigma} = [A + B(\varepsilon)^n] \left[1 + C \ln \left(\frac{\dot{\varepsilon}}{\dot{\varepsilon}_0} \right) \right] \left[1 - \left(\frac{T - T_r}{T_m - T_r} \right)^m \right] \quad (1)$$

where A ; initial yield strength, B ; strain-hardening coefficient, C ; strain-rate sensitivity, n ; strain-hardening exponent, m ; thermal-softening exponent, ε ; equivalent strain rate, $\dot{\varepsilon}_0$; normalized with a reference strain rate, T_m ; melting temperature of the material, T_r ; room temperature.

The parameters in this model were used a reported value by Meyer-Kleponis [4]. The friction between the chip and cutting tool was assumed the Coulomb friction. The friction coefficient that applied to simulation was calculated by the results of the cutting test.

Failure accumulation in the Johnson-Cook model was considered by applying the normalized Cockcroft & Latham law to the failure condition of materials. The equation is exposed by eq. 2.

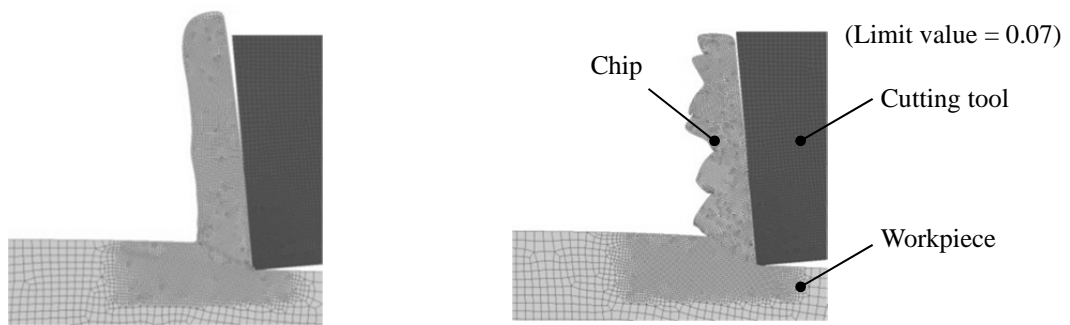
$$D_f = \int \left(\frac{\sigma_{max}}{\bar{\sigma}} \right) d\varepsilon \quad (2)$$

where D_f ; fracture limit value, σ_{max} ; maximum principal stress, $\bar{\sigma}$; equivalent stress, $d\varepsilon$; equivalent strain increment.

The validity of the calculation results was considered by comparing with the experimental results that were the cutting force, tool temperature, and chip shape.

Results

Figure 1 shows the effect of the ductile fracture condition. When a ductile fracture condition was not considered, the chip shape was calculated the flow type (Figure 1 (a)), the characteristic saw-tooth type in titanium alloy was not calculated. However, when a ductile fracture condition was considered, the chip shape was calculated the saw-tooth type (Figure 1 (b)). The chip dimensions were varied according to a limit value of the ductile fracture law.



(a) Non-consideration of the fracture condition

(b) Consideration of the fracture condition

Figure 1 Effect of the ductile fracture condition to the calculation result of chip shape

Figure 2 shows the relation between cutting force, thrust force and the limit value of ductile fracture. The cutting force was increased with increasing the limit value, the limited value was 0.1 or more, the cutting force was approximately constant value. The calculation result of cutting force was approximately 80 N lower than actual value. The thrust force was approximately accorded with experiment.

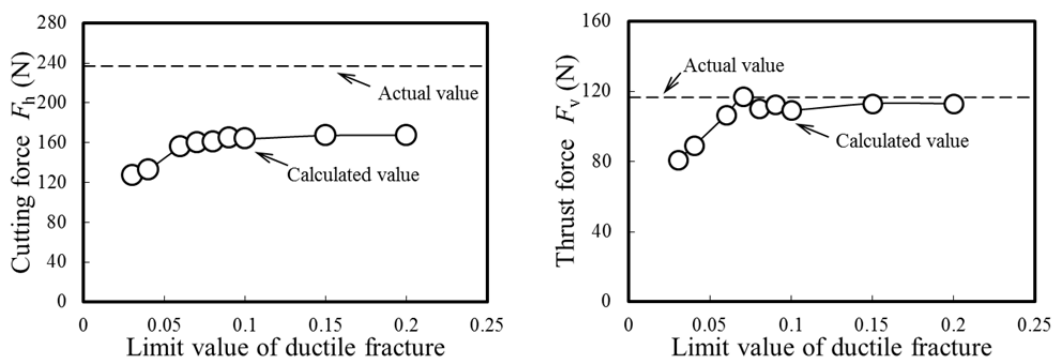


Figure 2 Effect of the ductile fracture condition to the calculation result of chip

These results were suggested that the cutting simulation of the titanium alloy was possible by the by the Johnson-Cook model that applied a ductile fracture condition.

References

- [1] P. Sartkulvanich, F. Koppka, T. Altan, Determination of flow stress for metal cutting simulation - a progress report, *J. Mater. Process. Technol.*, 146(2004), pp.61-71.
- [2] R. Neugebauer, K.-D. Bouzakis, B. Denkena, F. Klocke, A. Sterzing, A.E. Tekkaya, R. Wertheim, Velocity effects in metal forming and machining processes, *Annals of the CIRP*, 60(2011), pp.627-650.
- [3] M. Okada, A. Hosokawa, N. Asakawa, T. Ueda, End milling of stainless steel and titanium alloy in an oil mist environment, *Int. J. Manuf. Technol.*, 74(2014), pp. 1255-1266.
- [4] T. Özel and M. Sima, Finite element simulation of high speed machining Ti-6Al-4V alloy using modified material models, *Trans. of NAMRI/SME*, 38(2010), pp.49-56.

CORROSION RESISTANCE OF Si-DOPED AMORPHOUS CARBON FILMS AGAINST NITRIC ACID

Jumpei Nishikawa^{1,*}, Masayuki Nakano², Junko Hieda¹, Naoto Ohtake¹, Hiroki Akasaka¹

¹ Department of Mechanical Sciences and Engineering Tokyo Institute of Technology,

² Department of Chemical Science and Engineering Tokyo National College of Technology

*Corresponding Author: nishikawa.j.ab@m.titech.ac.jp

Keyword: Amorphous carbon film, Si-doping, Nitric acid solution, Corrosion resistance, Surface plasmon resonance

1. Introduction

Hydrogenated amorphous carbon films (*a*-C:H) are one of the functional films which consists of sp^2 and sp^3 hybridized carbon and hydrogen atoms^[1]. Typical properties of the films are high hardness and low friction coefficient^[2], and it is also known that they have high corrosion resistance against acids and alkalis such as sulfuric acid, hydrofluoric acid and ammonium hydroxide^[3]. On the other hand, these films are corroded by nitric acid because amorphous carbon films contain sp^2 bonding same as graphite^[4,5]. The film properties strongly depend on the film structure and doping of other elements into the films can also change the film properties. In this study, the effect of silicon (Si) doping on the corrosion resistance of *a*-C:H films was investigated by the precise corrosion rate measurement method.

2. Experimental method

Si-doped amorphous carbon films (*a*-C:H:Si) was deposited on Si (100) substrate by a plasma assisted chemical vapor deposition (PECVD) method. Acetylene (C_2H_2) and tetramethylsilane ($Si(CH_3)_4$) were used as raw material gases. To control Si concentration of *a*-C:H:Si films, the flow rate of $Si(CH_3)_4$ was changed while the flow rate of C_2H_2 was constant. The prepared films were soaked for 0-18 h in nitric acid solution adjusted to 2 M and flushed with distilled water. The surface of the sample was evaluated by an X-ray photoelectron spectroscopy (XPS). Furthermore, the corrosion rate in nitric acid solution was estimated by using the phenomenon of the surface plasmon resonance (SPR). A schematic illustration of the measurement apparatus is shown in Fig. 1. A 40 nm thick silver (Ag) layer was deposited on a glass substrate by magnetron sputtering method. *a*-C:H:Si films were deposited on Ag layer. The laser light incident from the back side was totally reflected on Ag layer to generate evanescent wave and excite plasmon waves on the boundary between Ag layer and *a*-C:H:Si film. Since these SPR conditions are determined by the dielectric constant of the space above the Ag layer, it is able to estimate the reduction in the thickness of the film due to corrosion as a change of the dielectric constant. The thickness was estimated in 0.3 M nitric acid solution by SPR measurement.

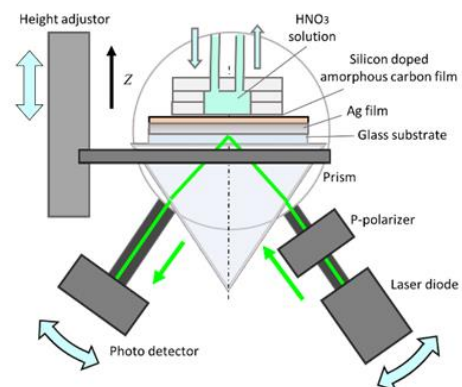


Fig. 1. Schematic illustration of SPR measurement apparatus

3. Results and Discussion

From the XPS spectrum, the proportion of sp^2 -bonding carbon in the film reduced by doping Si. The

structure of each film did not change significantly by etching in nitric acid solution.

Figure 2 shows SPR profiles at each duration after the introduction of nitric acid solution. The intensity of the reflected light was markedly attenuated at an incident angle of about 57° , which is the SPR angle. Although the total reflection angle was not shifted in these profiles, the SPR angle was shifted by an amount that increased with the duration. From these SPR angles, amount of thickness change in film thickness was calculated by fitting of SPR profiles. The results of the corrosion rate of the Si doped and non-doped *a*-C:H films in the nitric acid solution estimated by SPR measurement is shown in Fig. 3. Corrosion rate in nitric acid solution was reduced by the doping of Si into amorphous carbon films.

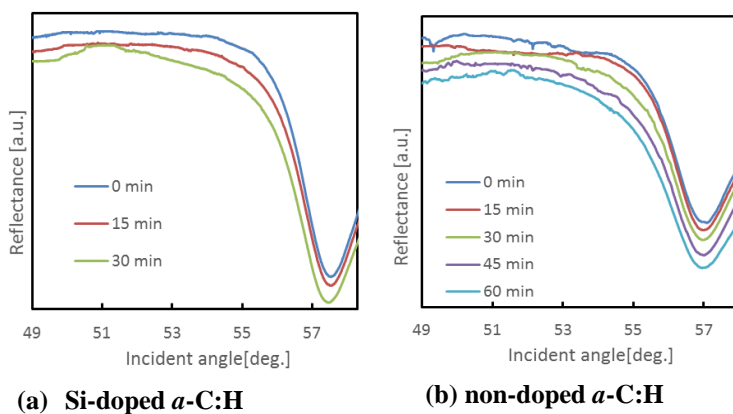


Fig. 3. SPR profiles in nitric acid solution.

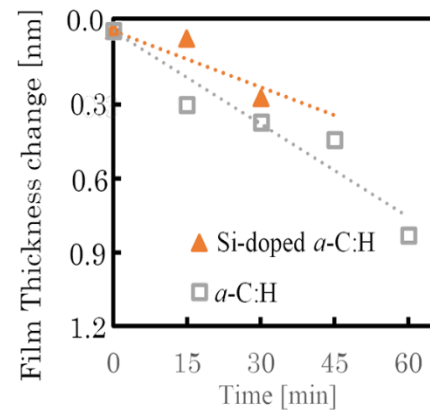


Fig. 2. Change in thickness by corrosion.

4. Conclusions

High-resistance portion and low-resistance portion against nitric acid exist in the *a*-C:H films and no significant change of the structure of *a*-C:H by oxidation occurred during etching in nitric acid solution. By doping Si into *a*-C:H films, sp^2 -bonds ratio decreased and corrosion rate was reduced. These results indicate that doping Si into *a*-C:H film increases its corrosion resistance against nitric acid.

5. Acknowledgement

This work was supported by Mitutoyo Association for Science and Technology.

References

- [1] J. Robertson, Comparison of diamond-like carbon to diamond for applications, *Phys. Status Solidi.*, 205, 9 (2008) pp233-2244.
- [2] Y. Liu, A. Erdermir, E. I. Meletis, A study of the wear mechanism of diamond-like carbon films, *Surf. Coat. Tech.*, 82 (1996) pp48-56.
- [3] R. D. Mansano, M. Massi, A. P. Mousinho, L. S. Zambom, L.G. Neto, Protective carbon layer for chemical corrosion of stainless steel, *Dia. Relat. Mater.*, 12 (2003) pp749-752.
- [4] K. Kamegawa, K. Nishikubo, H. Yoshida, Oxidative degradation of carbon blacks with nitric acid (I)—Changes in pore and crystallographic structures, *Carbon* 36, 4 (1998) pp433-441.
- [5] A. Takarada, T. Suzuki, K. Kanda, M. Niibe, M. Nakano, N. Ohtake, H. Akasaka, Structural dependence of corrosion resistance of amorphous carbon films against nitric acid, *Dia. Relat. Mater.*, 51 (2015) pp49-54.

TENSILE AND FATIGUE BEHAVIORS FOR LIP-SEAL WELDS OF LIQUID LITHIUM PIPES AT ELEVATED TEMPERATURE

Kazuyuki Furuya^{1*}, Fumio Takeo¹, Hiroshi Yokoyama¹, Tomoharu Akagaki¹

¹ Department of mechanical engineering, Hachinohe National College of Technology

*Corresponding.kazuyuki-m@hachinohe-ct.ac.jp

Keywords: Li-Flow, Lip-Seal welding, Metallurgical property, Tensile property, Fatigue property

Introduction

An intense neutron irradiation system like the International Fusion Materials Irradiation Facility is an accelerator-based D-Li neutron source designed to produce an intense high-energy neutron flux (2 MW/m²) for testing candidate materials and components to be used in the International Thermonuclear Experimental Reactor and the fusion DEMO reactor. Following a three-year key element technology phase up to the end of 2002 [1], a transition phase is being performed prior to engineering validation and engineering design activities [2]. To realize such a condition, two 40-MeV deuteron beams with a total current of 250 mA are injected into a liquid Li stream at 523 K, flowing at 20 m/s. Intense neutrons are emitted inside the Li flowing on a thin back-plate attached to the target assembly. The target assembly operates under a severe neutron irradiation condition (50 dpa/year for the back-plate). Therefore, the target assembly must be designed as a removable component to be replaced from a pipe in a loop system in which the Li flows, using a remote handling system. In the current design, the target assembly and the Li pipe are designed to have lip parts, each of which are made of an austenitic stainless steel type-316L (hereinafter known as 316L steel). Several remote cuts and re-welding between the lip parts are anticipated to be done using a fiber laser which is the most promising tool in the present design. In case of welding, the welding method is called for a lip-seal welding. The lip-seal weld operate under a corrosion/erosion condition due to the high speed Li-flow at the elevated temperature described above although the neutron irradiation damage at the weld does not exceed about 1 dpa. For that reason, it is important to elucidate metallurgical conditions and mechanical properties in the weld to select optimum welding conditions. This extended abstract presents microstructure, hardness and high temperature tensile and fatigue properties of the weld before neutron irradiation.

Experimental Methodology

Specimens of two types were prepared using a 316L steel. One specimen, which is for the metallurgical and hardness tests, simulated for lip-seal welding (hereinafter known as LSW). The other butt-joint, which is for the mechanical tests, simulated for thickness of the lip-seal part (2-mm-thick). The LSW and butt-joint were fabricated using a fiber laser tool, in the welding speed of 4000 mm / minutes and the supplied power of 1000 ~ 1100 W. Argon gas was utilized as covering gas because there is the possibility that nitrogen gas which is used normally for covering gas, reacts with Li inventory in Li pipe. As for the LSW, two 316L boards (2-mm thick each) overlapped were fixed by clamping tool, followed by lip-seal welding. Test pieces sampled from the weld were surface-finished. Some of them were followed by electrolytic etching for observation of the microstructure using an optical microscopy. Hardness distribution at the welds was measured using a Vickers hardness tester, with the testing load of 300 g and dwell time of 10 seconds. As for the butt-joint, which is specimens for tensile and fatigue tests, is 24-mm long, 16-mm wide, and 2-mm thick: the cross-section is 32 mm². A weld is located at the center of the specimen. The specimens were surface-finished for all the surfaces. Tensile and fatigue specimens of the same type were also sampled from the as-received 316L steel for reference, prepared in the same way. Tensile and fatigue tests were carried out at elevated temperatures according to relevant ISO specifications.

Result and Discussion

Figure 1 shows macroscopic and microscopic views of the LSW. As shown in [1], sound welding is visible in the weld with no harmful defects such as overlap, undercut, or macro-cracks

although there were a couple of porosities in these welded metals. Typical examples of these microscopic views are depicted in panels A and B. As revealed in those views, no micro-crack is apparent at around the bond. As for heat affected zone (HAZ), no marked change occurs in the grain size. As can be seen in the B of the figure, the LSW has small gap about 15- μm wide, and it can be seen a material like an inclusion between the gap. In result of EDX analysis for the material, BM and fusion metal, it was revealed that the material was expulsion came from fusion metal. Micro-Vickers hardness distribution of the LSW is presented in Figure 2. The minimum and maximum hardness are 150 HV in the base metal region and 200 HV in the fusion metal region, and the increment of hardness is 50 HV. Result of high temperature tensile test are portrayed in Figure 3 for butt-joint and reference material. Almost all the fracture occurred not at the welded region but at a base metal region. As can be seen in the figure, it can be said that property change of the butt-joint are almost the same trend at all temperature range. The 0.2 % off-set yield stress was decreased up to 140 MPa in accordance with temperature increases. The other properties indicated the same trend, i.e., the ultimate tensile stress, uniform elongation and total elongation were also decreased up to about 400 MPa, 7.5 % and 44 %, respectively. In result of fatigue test at RT for a reference material, the fatigue limit was 370 MPa. On the other hand for the butt-joint tested at 623 K, the fracture occurred not at the welded region but at a base metal region, and the fatigue limit was 280 MPa. Therefore it can be said that the value (280 MPa) is comparable to a fatigue limit of the reference material at 623 K. The fatigue limit of the butt-joint tested at 623 K decreased by 24 % compared to the value of the reference materials tested at RT (370 MPa). Consequently, it can be said that strength of the butt-joint are nearly equal to the reference materials, and it is thought to be that the welding condition are relevant in the range of the mechanical test condition.

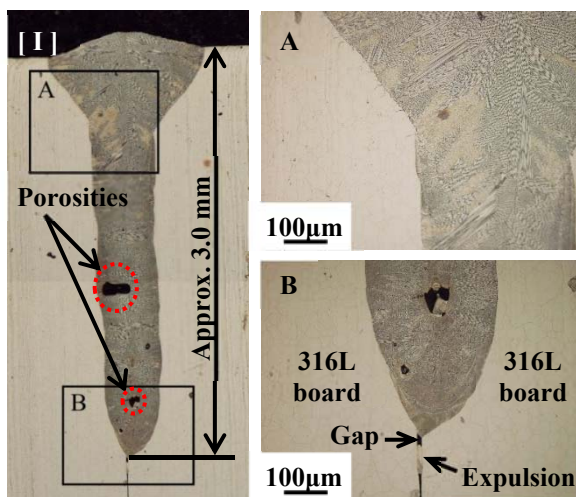


Figure 1 Macrostructure and Microstructure of LSW. [I]: Cross-sectional macrostructure of the weld. A and B: Magnified views of bond region and fusion metal

References

- [1] IFMIF International Team (Ed.), "IFMIF-KEP International Fusion Materials Irradiation Facility Key Element Technology Phase Report", JAERI-Tech 2003-005 (2003) pp. 5-16.
- [2] H. Takatsu, M. Sugimoto, S. Jitsukawa, H. Matsui, Proceedings of the 12th International Conference on Fusion Reactor Materials, J. Nucl. Mater. 329-333 (2007) pp. 178-182.

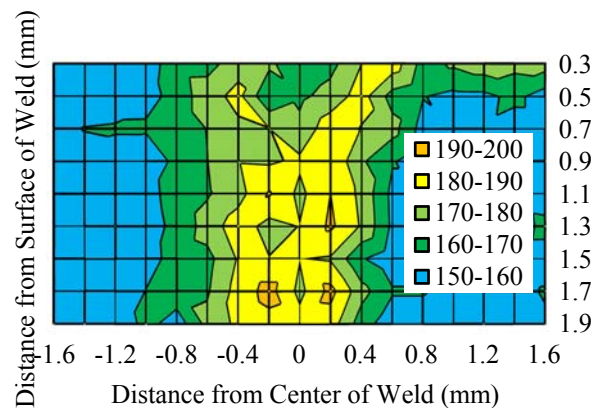


Figure 2 Micro-Vickers Hardness Distribution on Weld.

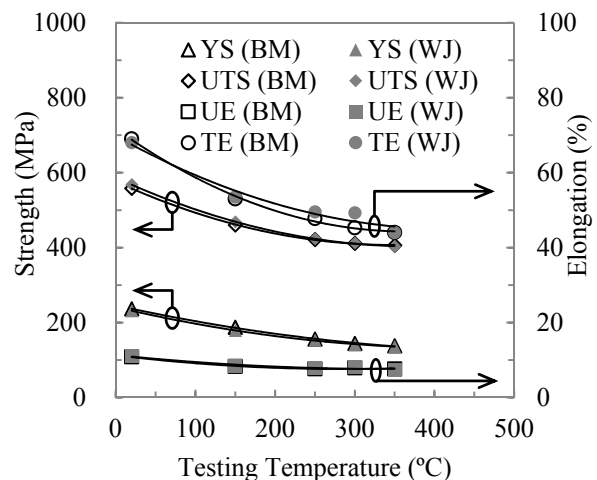


Figure 3 Comparison of Tensile Property of Reference Material and Butt-Joint.

EFFECT OF LOCAL PLASTIC PROCESSING ON FATIGUE STRENGTH OF STEEL PLATE WITH A HOLE

**Fumio Takeo^{1*}, Kazuyuki Furuya¹, Michitoshi Toyota¹, Hiroki Naomachi¹,
Daiki Yamada¹, Syogo Sasaki¹, Tomoharu Akagaki¹, Hitoshi Soyama²**

¹*Department of Mechanical Engineering, Hachinohe National College of Technology,*

²*Department of Nanomechanics, Tohoku University*

* takeo-m@hachinohe-ct.ac.jp

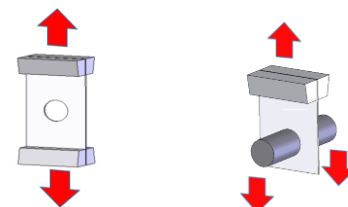
Keywords: *Fatigue Strength, Plastic Processing, Steel Plate, Circular Hole, S-N Curves*

INTRODUCTION Fatigue fracture of metallic materials has caused many serious accidents. Fatigue is easy to occur at large stress. Therefore, it is effective to improve mechanical properties in stress concentrated area of mechanical parts for enhancing the fatigue strength of them. In the previous studies, for example, the effects of local plastic deformation^[1] and cavitation peening^[2] on the bending fatigue strength of the metallic plate with a hole have been reported. In this study, the effect of the local plastic processing on tensile fatigue strength of steel plate with a circular hole which is often used for fastener was examined. Tensile fatigue tests were carried out with two types of loading methods. Based on the S-N curves, the effects of two types of local plastic processing on fatigue strength were compared and discussed.

EXPERIMENTAL APPARATUS AND PROCEDURES The fatigue strength of steel plates having a circular hole was examined. As shown in Figure 1(a) and (b), the cyclic tensile load was applied to the specimen by two methods; we call them the uniform loading type and the pin loading type respectively. In the uniform loading type, tensile load was applied by gripping both ends of the specimen. In the pin loading type, tensile load was applied to the pin which was inserted into the specimen's hole, while the other end of the specimen was gripped. This pin was made of quenched alloy steel and was 19.5mm in diameter. The material used for the specimen was cold-reduced carbon steel sheets of JIS G 3141 SPCC-SD. Figure 2 shows the shape and size of the specimen for two loading types. The specimens were 300 mm or 200 mm in length, 50 mm in width and 3.2 mm in thickness with a hole of 20 mm in diameter.

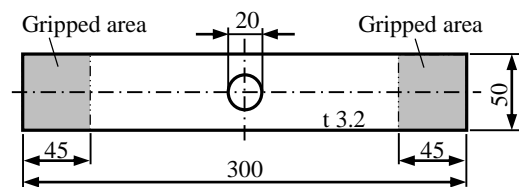
The plastic processing was introduced by pressing the edge of the hole using two types of punches as shown in Figure 3. The flat type punch was 30 mm in diameter, so the region within 5 mm from the hole-edge was deformed. Compressive load of 180 kN was applied with the punch for 30 seconds, then the thickness of processed area was reduced by about 5.4 %. On the other hand, the load of 60 kN was applied with the cone type punch, and the region within about 1 mm from the hole-edge was deformed like the chamfered shape as shown in Figure 3(b).

Tensile fatigue tests were carried out for all combinations of plastic processing types and loading types. The stress ratio of the minimum tensile stress σ_{min} , to the maximum tensile stress σ_{max} , was 0.1. In this paper, σ_{max} and σ_{min} were calculated from the applied load and the cross sectional area perpendicular to the loading direction through the shorter dimension of the specimen that passes through the center of the hole.

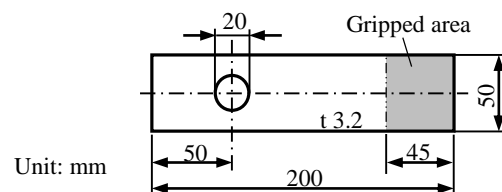


(a) Uniform loading (b) Pin loading

Figure 1 Types of loading



(a) For uniform loading



(b) For pin loading

Figure 2 Geometry of specimen

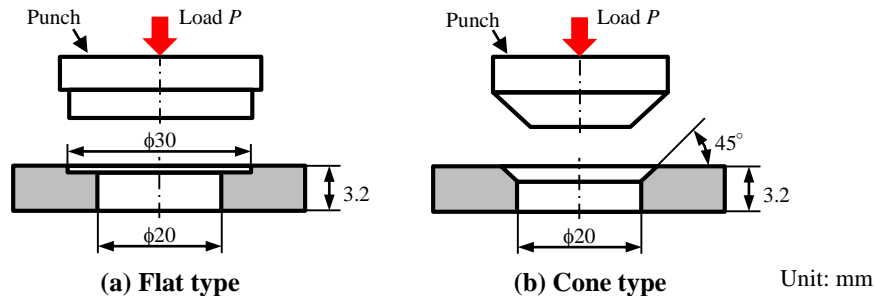


Figure 3 Schematic diagram of plastic processing

Frequency of stress cycle was 30 Hz. When the specimen was not fractured until 10^7 cycles, the test was discontinued.

EXPERIMENTAL RESULTS Figure 4 shows S-N curves obtained by fatigue tests. Blank and solid plots show the results for uniform loading type and pin loading type, respectively. Arrows in Figure 4 mean that the specimen does not fracture at 10^7 cycles.

Compared with two loading types about unprocessed specimen, the fatigue limit for pin loading type was about 6 % lower than that for uniform loading type. As to the effects of local plastic processing on the enhancing of fatigue limit, it can be found that fatigue limit of processed specimen for the uniform loading type was improved by about 20 % than that of unprocessed specimen. Considering with the magnitude of required load for plastic processing, the cone type processing seems to be more effective than the flat type. On the other hand, the effect of plastic processing for the pin loading type was lower than that for the uniform loading type. Improvement of fatigue limit was about 10 % for the flat type processing. Especially in the case of cone type processing, fatigue limit was slightly lower than unprocessed specimen. As one of the reason for this result, the friction between the pin and the inner wall of the hole could be considered. In the case of the pin loading type, fretting might contribute to the fatigue strength reduction. For the cone type processed specimen, fatigue strength would be more affected by fretting because of its small contacting area.

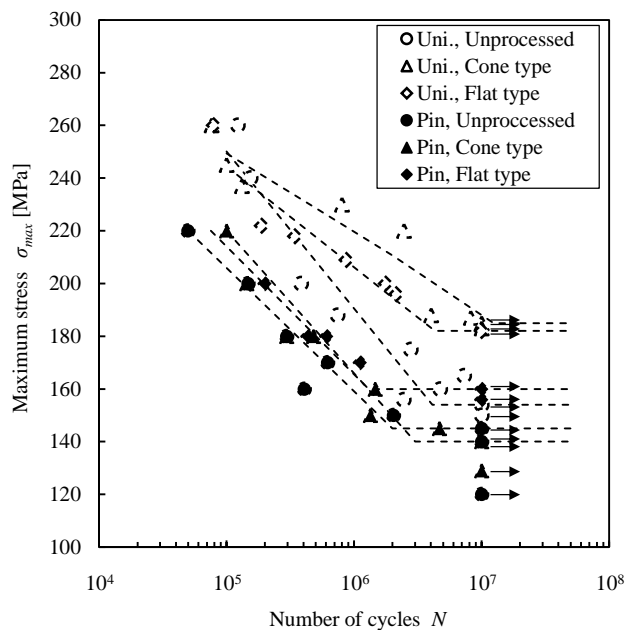


Figure 4 S-N curves obtained from fatigue tests

CONCLUSIONS The effect of local plastic processing on fatigue strength of a steel strip with a hole was examined. It was found that fatigue limit could be improved by about 20 % by plastic processing around the hole-edge for the uniform loading type. In contrast, the improvement effect for the pin loading type was low. In the case of pin loading type, fatigue strength might be affected by friction between the pin and the inner wall of the hole.

References

[1] Sheng-wu Wang, Shinich Nishida, Nobusuke Hattori and Norikazu Nakamura, Improvement in Fatigue Strength of Notched Plate-Specimen by Local Plastic Deformation, Trans. JSME, **67(A)**-664(2001), pp. 1996-2001.
 [2] Hitoshi Soyama, The use of cavitation peening to increase the fatigue strength of duralumin plates containing fastener holes, Mater. Sci. Appl., **5-6**(2014), pp. 430-440.